Beyond mere flexibility: Functional Peptide Linkers in Engineered Nanosensors and -switches

Gräwe, Alexander

(2020)

Beyond mere flexibility: Functional Peptide Linkers in Engineered Nanosensors and -switches

Dissertation von

Alexander Wilhelm Johannes Gräwe

Zur Erlangung des angestrebten akademischen Grades

eines *Doctor rerum naturalium* (Dr. rer. nat.)

Technische Universität Darmstadt

Fachbereich Biologie

Erstgutachter: Prof. Dr. Viktor Stein

Zweitgutachter: Prof. Dr. Gerhard Thiel

Gräwe, Alexander Wilhelm Johannes: Beyond mere flexibility: Functional Protein Linkers in Nanosensors and -switches
Darmstadt, Technische Universität Darmstadt
Jahr der Veröffentlichung der Dissertation auf TUprints: 2020_____
Tag der mündlichen Prüfung: 25.09.20_____
URN: urn:nbn:de:tuda-tuprints-145355

Table of contents

Summary

Human health monitoring, disease diagnosis and therapeutics rely on the detection of biomolecules. In this regard, Synthetic Biology approaches based on tailored molecular receptors and actuators can create powerful biosensing platforms. To achieve an optimal biosensor, the composition of such receptor/actuator scaffolds requires both careful design and thorough screening. Thus, my PhD studies focused on construction principles that render modular fusion proteins powerful biosensors.

Central to the functionality of fusion proteins are the domain-connecting peptidic linkers. While the importance of linkers is known, methods to systematically screen the underlying amino acid space are scarce. Therefore, a novel DNA assembly method was devised that enables straightforward cloning of large and diverse linker libraries. By applying the strategy to synthetic protein switches, I identified multiple potent ligand-responsive proteases.

The importance of linkers was further assessed by investigating the behaviour of nanopore scaffolds based on the β-barrel transmembrane protein FhuA ΔcΔ5L. The linker between the transmembrane domain and engineered terminal receptor tags emerged as a crucial parameter, impacting both open probability and intermolecular interaction ability of the nanopore in artificial lipid bilayers. An engineered ΔcΔ5L variant could irreversibly catch a second fusion protein while embedded into the bilayer, demonstrating biosensing at the single molecule level.

While biological nanopores are highly specific, their lack of stability complicates their use in application-oriented biosensors. Considering this, a strategy to stably immobilize fusion protein receptors in solid-state nanopores was developed in collaboration with Ivana Duznovic from the Materials Analysis group. Highly specific nanobodies attached to conical nanopores in track-etched poly(ethylene terephthalate) (PET) membranes allowed sensitive discrimination of analytes by current-voltage (I-V) measurements. The developed nanobody-nanopore platform constitutes a highly modular biosensing system and can potentially be combined with lab-on-chip devices.

In the first chapter, I embed my dissertation in the context of Synthetic Biology and Nanosensors while outlining the content of the following chapters. The second chapter describes the development of a cloning strategy for protein linkers and its application to synthetic protein switches. The third chapter deals with the biological nanopore scaffold ΔcΔ5L, while the fourth chapter describes the development of solid-state nanopore biosensing platform.

Zusammenfassung

Die Detektion von Biomolekülen ist von entscheidender Bedeutung sowohl in der Diagnostik von Krankheiten wie auch in der Therapeutik und bei Vorsorgeuntersuchungen. In diesem Sinne ermöglicht die Synthetische Biologie die Konstruktion wirkungsvoller Biosensorik-Plattformen auf Basis von molekularen Rezeptoren und Aktuatoren. Ein optimaler Biosensor lässt sich nur durch umsichtiges Design und nach umfassendem Screening identifizieren. In meiner Promotion habe ich mich daher intensiv mit Konstruktionsprinzipien befasst, die es ermöglichen, aus modularen Fusionsproteinen wirkungsvolle Biosensoren zu generieren.

Die Proteinlinker zwischen den einzelnen Domänen von Fusionsproteinen sind für die Funktionalität Letzterer zentral. Obwohl diese Bedeutung bekannt ist, existieren bisher nur wenige Methoden, die eine systematische Untersuchung der Linker erlauben. Daher wurde eine neuartige Strategie zur DNA-Assemblierung entwickelt, die das Klonieren umfangreicher Linker-Bibliotheken ermöglicht. Bei der Anwendung dieser Strategie auf synthetische Proteinschalter habe ich mehrere schlagkräftige Proteasen identifiziert, die auf Liganden reagieren.

Dass Linker auch in einem anderen Kontext von entscheidender Bedeutung sind, wurde durch die Charakterisierung verschiedener Varianten der β-Fass Transmembran-Nanopore FhuA ΔcΔ5L gezeigt, die in artifiziellen Lipid-Bilayern vermessen wurden. Der Linker zwischen der Transmembran-Domäne und maßgeschneiderten terminalen Rezeptorpeptiden stellte sich als entscheidender Parameter heraus, der sowohl Offenwahrscheinlichkeit als auch die Fähigkeit der Pore, mit anderen Molekülen zu interagieren, beeinflusste. Eine maßgeschneiderte ΔcΔ5L Variante verknüpfte sich irreversibel mit einem zweiten Fusionsprotein, während sie im Bilayer verankert war. Dadurch wurde aufgezeigt, dass das System als Biosensor im Einzelmolekülmaßstab funktioniert.

Biologische Nanoporen sind zwar hochspezifisch, aber strukturell anfällig. Daher ist ihr Einsatz in anwendungsorientierten Biosensoren mit Schwierigkeiten verbunden. Als Alternative wurde eine Strategie zur stabilen Immobilisierung von Fusionsprotein-Rezeptoren in ionenspur-geätzten PET-Folien entwickelt, in enger Zusammenarbeit mit Ivana Duznovic aus der Arbeitsgruppe Materialanalytik. Die Anbringung hochspezifischer Nanobodies an konische Nanoporen erlaubte die sensitive Unterscheidung von Analyten durch Strom-Spannungs-Messungen (I-V Messungen). Die entwickelte Nanobody-Nanoporen-Biosensor-Plattform ist hochmodular und potentiell kombinierbar mit der Lab-on-Chip Technologie.

Im ersten Kapitel setze ich meine Dissertation in den Kontext von Synthetischer Biologie und Nanosensoren und gehe auf die entsprechenden Berührungspunkte ein, die in den folgenden Kapiteln beschrieben werden. Das zweite Kapitel beschreibt die Entwicklung einer Klonierungsstrategie für Protein-Linker und deren Anwendung anhand synthetischer Proteinschalter. Das dritte Kapitel behandelt die biologische Nanopore ΔcΔ5L, während sich das vierte Kapitel der Entwicklung einer Biosensorik-Plattform auf Basis von Festkörper-Nanoporen widmet.

Chapter 1
Nanosensors in Synthetic Biology

1. Synthetic Biology

Synthetic Biology has grown to an independent research branch, rooted in multiple Life Science and Engineering disciplines. It combines principles from both Engineering and Biology worlds and shares large interfaces with Bioinformatics, Medicine and Metabolic Engineering. Due to its broad scope, attempts to precisely define Synthetic Biology are always biased towards a certain research area, for instance creation of synthetic minimal cells [1], implementation of sophisticated (bio-)logic circuits [2,3] or strain development [4]. Yet, it is possible to broadly summarize the activities of the researcher working in this discipline: A Synthetic Biologist aims to construct useful bio-inspired functionalities in a systematic fashion.

In this regard, the workflow of a Synthetic Biology project follows the omnipresent pattern that is known as the Design-Build-Test or Design-Build-Test-Learn cycle (Figure 1) [4]. An initial concept or idea is carefully designed based on available knowledge. This includes available data, for instance crystal structures (in case of fusion protein design) [5] or bioinformatic models [6,7], but can also be guided by a specific research question [3]. The following implementation or "building" is mostly performed by means of biochemical and molecular biology methods. When the constructed system is tested, it produces data that can directly be used for an improved design, which is often the case in directed evolution approaches [8]. Moreover, the gathered data is always linked to an insight or learn effect that can help to improve the initial design (Does the system behave as expected? Are there any bottlenecks or drawbacks in the current design?). Eventually, new designs based on the gained knowledge will be developed.

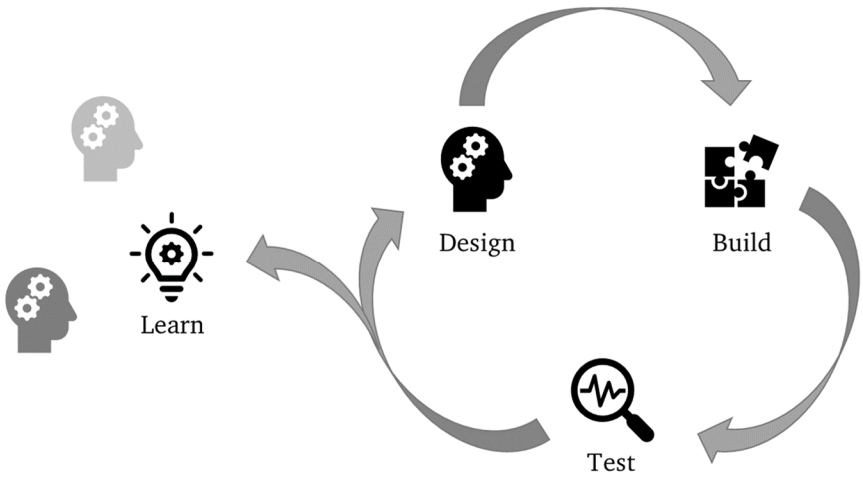

Figure 1 *The Design-Build-Test-(Learn) cycle.*

2. The Nano-Prefix in Synthetic Biology

A recurring motif in many Synthetic Biology areas is the “nano” prefix or -tag. Mostly, this prefix relates only briefly to the order of magnitude 10^{-9}. Rather, it refers to the molecular environment and aims to stress the small nature of a system. This is highlighted by a compilation of nano-tagged words found in titles and abstracts of the Synthetic Biology literature (Table 1).

My PhD studies focused on two of these nano-tagged concepts: **Nanobinders** (Chapters 2-4) and **Nanopores** (Chapters 3 & 4). Additionally, nanolight designs were included to visualize important project milestones. All concepts are part of the larger nanosensor framework that spans the bridge from basic research to application.

Table 1 *Synthetic Biology related, nano-tagged keywords appearing in the PubMed database [9].*

Keyword	Description	Example References
Nanobodies	Minimalized single-domain antibody scaffolds with high affinity for various target molecules	[10]
Nanocages	Related to nanoreactors; Self-assembling, hollow protein compartments	[11]
Nanodiscs	Artificial lipid environment for cell free expression, purification and characterization of membrane proteins	[12]
Nanoghosts	Artificial membrane-enclosed compartments used to study therapeutic approaches	[13]
NanoLuc	Smaller, engineered version of a natural occurring bioluminescent luciferase with broad applications in cell imaging and diagnosis	[14]
Nanomachines	Higher-order functionalities; combine multiple modules and concepts into a larger assembly with a complex purpose	[15]
Nanopores	Membrane proteins that connect two separated volumes, e.g. ion channels and toxins; often engineered for specific purposes like stochastic sensing	[16]
Nanoreactors	Related to Nanocages; three dimensional scaffolds designed to improve biochemical reactions by increasing local concentrations	[11]
Nanostructures	Assembled from nanobuilding blocks; umbrella term for artificial complexes of biological entities	[15]
Nanoswitches	Keyword mainly applied for DNA-based scaffolds; Generate a detectable output in response to an input; subcategory of nanosensors	[17]
Nanowires/-tubes/ -fibers	Protein- or DNA-based elongated architecture; Potential in electronics; Includes peptoid nanosheets	[18–20]

3. Nanobinders

3.1 Nanobodies

A prominent example of "nanobinders" are Immunoglobulins (Ig), also termed antibodies. Y-shaped antibodies form the backbone of our powerful immune system, as they bind their target antigens with high affinity and specificity [21,22]. In contrast to humans, Immunoglobulins of Camelids and Chondrichthyes consist of only one polypeptide chain [10]. This evolutionary phenomenon allowed the development of single-domain antibodies also known as nanobodies, V_HHs (camelids) or $V_{NAR}s$ (Chondrichthyes) [10,23]. When compared to classical hetero-tetrameric IgG-like architectures, these nanobodies offer many advantages: They are considerably smaller, can be tuned to a larger number of epitopes and can be recombinantly produced at high yields [10].

Nanobody development involves multiple steps. Most studies start with a camel, dromedary or llama immunization to obtain a first V_HH library against a target antigen [10,24]. The best binders are identified *via* phage or yeast display [24,25] and their affinities can be further improved for instance *via* directed evolution [26]. The obtained nanobodies are useful tools especially in biosensor technologies, with potential applications also in therapeutics [10]. Examples include biosensors for viral infection [27] and enzymatic activity [28,29], but also for small molecules like toxins [30] and hormones [31]. Nanobodies are also employed as stabilizers in hard to crystallize membrane proteins [32].

In my PhD studies, I prepared multiple nanobodies for surface immobilization (Chapter 4). In cooperation with Ivana Duznovic from the Materials Analysis group at TU Darmstadt, we devised a nanosensing strategy based on the combination of solid-state nanopores and nanobodies.

3.2 Bioconjugation

An extreme example of "nanobinding" is bioconjugation, which describes the covalent linking of a biomolecule and second molecule. Various bioconjugation strategies rely on chemical linkage of disulfide bonds or the use of unnatural amino acids (*aa*) [33]. To facilitate covalent protein-protein linkage, protein engineers developed a variety of enzymatic methods. From the large number of strategies, two that I used during my PhD studies are introduced here.

3.2.1 Sortase A

Sortase A is a Ca^{2+}-dependent protein-sorting transpeptidase found in the gram-positive bacterium *Staphylococcus aureus*. It naturally acts as a "sorting" protease, cleaving between T and G of the motif LPXTG (where X could be any *aa*) and forming a new peptide bond between the T moiety and the N-terminus of a poly-G tail in peptidoglycan [34]. *In vitro*, this reaction is often exploited for protein immobilization [35,36]. Moreover, protein engineering studies generated Sortase A variants that are no longer Ca^{2+}-dependent [37], have superior catalytic activity [38] and allow specific conjugation of primary amines [39].

3.2.2 SpyTag/SpyCatcher

In nature, microorganisms use isopeptide bonds between proteins to establish highly stable architectures, for example pilins and adhesins [40]. The group of Mark Howarth minimalized and optimized a system from *Streptococcus pyogenes* for usage in biotechnological applications and named it SpyTag/SpyCatcher [41,42]. Over time, other examples with the same principle, like the SnoopTag/SnoopCatcher system [43], were established.

The main advantage of these Tag/Catcher system is the spontaneous, self-catalyzed isopeptide bond formation between the respective interaction partners. In case of the Spy-system, the 13 *aa* SpyTag is bound by the 15 kDa SpyCatcher (K_D = 0.2 μM) and an isopeptide bond is formed between the ε-amino group of a lysine (SpyTag) and the β-carboxyl group of an aspartate (SpyCatcher) at a rate constant of $1.7 \pm 0.4 \times 10^3\ M^{-1}s^{-1}$ [42,44]. Further protein engineering yielded a 12 times faster version SpyTag002/SpyCatcher002 [44].

The genetically encoded SpyTag/SpyCatcher system has found countless applications in Synthetic Biology and Material Sciences, as it is modular [43,45], facilitates protein conjugation [16], but also enables the assembly of bioactive gel-like structures [46,47]. In my PhD studies, I employed the system for nanopore conjugation (Chapter 3) as well as for protein immobilization (Chapter 4).

3.3 Triggered Binding and Proteases

In the cellular context, a simple ligand binding event at the cell membrane can result in vast and multiple reactions inside the cell [22]. Such signal amplification is mediated by timed or triggered binding, meaning that a certain response – for instance enzymatic activity – is only generated if a specific input – for instance a phosphorylation – is present. In the Synthetic Biology world, the implementation of signal amplification remains one of the key aspects for successful biosensor design, as has been shown for both whole-cell [48] and *in vitro* biosensors [28,49].

Importantly, signal amplification systems require tightly controlled ON- and OFF-states. One link in the cascade generating an output without the input generally renders the whole amplification chain unstable. Thus, the chain should ideally consist of bistable switches that are switched either completely ON or OFF. In Synthetic Biology, many bistable switches have been realized on the genetic level, for instance in gene circuits [50], while bistable protein switches remain a major challenge. Yet, recent progress has been achieved by using autoinhibition concepts [5], split-proteins [51] and dimerization domains [2].

In this regard, proteases are considered the most useful enzyme class for post-translational signal amplification [51,52]. In the context of this chapter, proteases can be described as “nano-scissors”, as they cleave peptide bonds between amino acids. Sequence-specific proteases like the Nuclear Inclusion protein A (NIa) proteases from the *Potyviridae* family cleave very distinct motifs [53]. For instance, the TVMV protease recognizes the motif ETVRFQS and cleaves between Q and S [54]. In my PhD studies, I constructed several synthetic protease switches that respond to small molecules (Chapter 2). As outlined, these switches can serve as potent amplifiers in artificial signaling cascades that can be integrated into sensitive biosensor designs.

4. Nanopores as Biosensors

The term nanopore is widely used both in (Synthetic) Biology and Material Science. For instance, the term refers to protein channels embedded in lipid bilayer membranes (Chapter 3), but also to nanometer-wide apertures in solid materials (Chapter 4) [55]. In the biological context, nanopores are highly important for cellular life, as they transfer information from the environment into cells and *vice versa* (examples in Chapter 3).

Since pioneered by Hagan Bayley and coworkers [56], genetically engineered nanopores have become powerful biosensing tools. A prominent example is the rise of the nanopore sequencing technology [57]. A few decades after the initial idea was formulated, nanopore sequencing is now routinely used for DNA analysis in diagnostics [58], epidemics [59] and genome mapping [60]. Nanopore sequencing is based on the concept of stochastic sensing, where the conductivity of a given pore responds to an analyte that either blocks, enters or passes the pore lumen [61]. Importantly, the duration and shape of the blocking event can be directly linked to the identity of the analyte [61–63]. For the nanopore sequencing technology, many optimization steps – for instance retardation of the DNA translocation – were necessary to allow proper discrimination of the nucleobases [57].

The heptameric protein toxin α-hemolysin (aHL) was the first nanopore of choice as it has multiple superior properties (described in Chapter 3). In the last decade, other useful scaffolds like the *Mycobacterium smegmatis* porin A (MspA) have emerged [64]. In short, the large variety of known transmembrane pores, combined with genetic engineering approaches, offers nearly unlimited possibilities of molecular sensors. In my PhD studies, I focused on the well-studied *Escherichia coli* outer membrane protein FhuA, precisely on one of its minimalized scaffolds, ΔcΔ5L, and investigated the role of attached tags (Chapter 3).

Chapter 2
Functional Linkers in Fusion Proteins

1. Introduction & Background

Fusion proteins – also called “chimerics” or “chimeras”– form indispensable tools in the field of synthetic biology and beyond. Since the late 1980ies it is known that genetic fusion of coding sequences that translate into distinct protein domains can result in proteins with higher stability or improved function [65,66]. By combination of well characterized protein domains, it became possible to construct completely new functionalities, to create artificial response functions and to control protein behaviour precisely.

At the DNA level, genetically encoded fusion proteins are constructed by in-frame connection of C- and N-terminal regions. For this task, only two options exist: Either a direct connection of the domains or the inclusion of a bridging sequence, named **linker** or **spacer**. Direct fusion or even truncation of domains can be advantageous for certain applications (see e.g. GluSnFR [67] and other FRET sensors [68,69]), especially regarding the fact that many proteins have unstructured termini [70]. These termini may even provide enough flexibility that additional spacers have no measurable effect [71]. For most fusion proteins to function properly, however, linkers are preferred.

Although primary without function, linkers are far more than simple spacers between two protein domains, and this has been emphasized early on in studies on sFvs and related fusion proteins [72]. Linker sequences can have severe effects on fusion protein stability, folding efficiency and functionality, as highlighted throughout this chapter. Yet, despite recent progress, there is still a lack of understanding regarding the relationship of linker structure and -function.

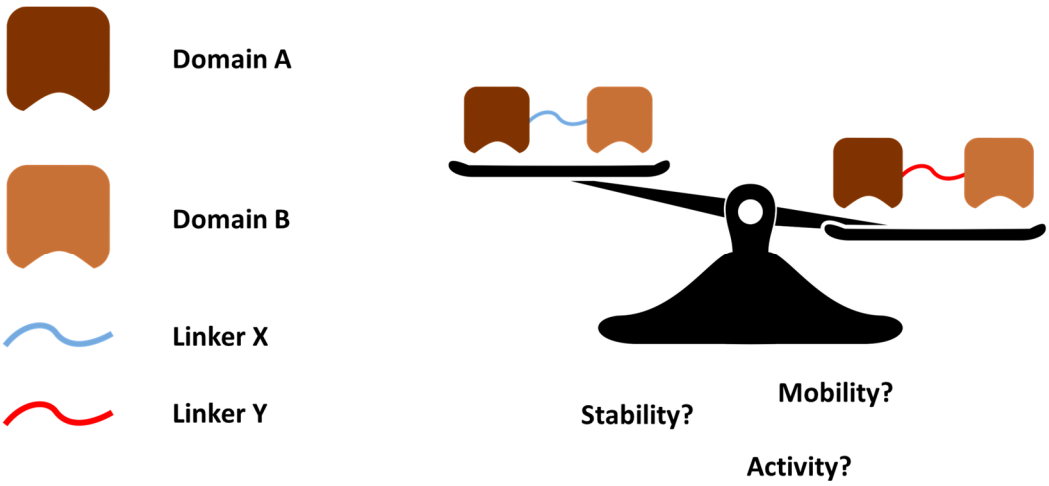

Figure 2 *Comic representation of the building blocks of synthetic fusion proteins and the dilemma of linker choice.*

1.1 Linker Properties

As Kaczmarski and co-authors precisely point out, "(l)inker choice is highly system dependent" [73]. When a multi-domain synthetic fusion protein is designed and a linker is needed, researchers can choose from a variety of well-known sequence motifs or "templates", even with the help of internet databases [74,75]. The most fundamental criteria when choosing a linker are **amino acid composition** and **length**, both affecting other important aspects like hydrophobicity and secondary structure.

1.1.1 Amino Acid Composition

In natural multi-domain proteins, linkers play important roles in enzymatic processes and allosteric signalling [76,77]. The use of amino acids (*aa*) in natural linkers is biased towards small, polar uncharged or charged residues, mainly G, S, E, P, A and T [74,78,79]. The study of natural linkers laid the foundation for the creation of reliable artificial ones.

Small amino acids are preferred over large ones as they neither compromise the folding nor the structure of the target protein [74]. Especially G-based linkers maintain the mobility of the attached domains, as G has no β-carbon and thus is less conformationally restricted than other *aa* [74,80,81]. Although linkers constructed solely of G have been successfully used, long polyG chains collapse into globular structures in aqueous solutions [82]. Furthermore, studies show that polyG linkers – as well as longer linkers in general – tend to be non-specifically cleaved by endopeptidases [83,84]. Therefore, polar moieties are introduced to achieve better solubility [74].

The most frequently used artificial **flexible linkers** are based on G/S motifs, for example GGS, GGGS or GGGGS repeats [2,5,85–93]. Flexibility of these repeats decreases with increasing S content [87,94]. Incorporation of A and T→S substitutions are common [8,69,95–98], and other *aa* may be added as well. For instance, Sørensen and Kjaergaard showed that G/S linker expansion increases with increasing E or D content due to favourable solvent interactions of these charged residues [99,100]. The authors also studied the impact of hydrophobic and aromatic *aa* as well as polyampholyte regions, but the effects on expansion or contraction of the linker sequence were negligible.

Interactions between homopolymeric amino acid stretches have been investigated [101], and in contrast to polyG, most of these sequences do not form reliable linkers. For instance, polyA, polyQ and hydrophobic stretches in general are prone to aggregation [101–104], whereas polyE and polyS adopt disordered and unstructured conformations [102,105]. There are, however, few exceptions. PolyN is a shield against unspecific proteolysis [83] and seems to prevent linker collapsing, as recent fusion proteins with Green Fluorescent Protein (GFP)-reporters suggest [106]. In general, the molecular environment greatly affects the overall structure of homopolymeric stretches [102,105].

Another special case is **polyP**. Proline itself influences the folding kinetics of the nascent protein chain to a great extent [107] and is often found in hinge regions or turns due to its helix-breaking properties [107,108]. In aqueous solution, poly-L-proline mainly folds into a left handed PPII-helix [80,109] that acts like a rigid "ruler" [108,110]. An idealized PPII-helix (Figure 3) spans 3.1 Å per residue and 3 residues per turn, in contrast to α-helices with 1.5 Å per residue and 3.6 residues per turn [110]. Because of this behaviour, researchers use polyP stretches as rigid linkers to tightly control the spacing of distinct domains [111–115]. Caution is needed when adding such rigidity to a system, as this may disturb the mobility of attached domains [116]. Also, it has to be considered that stretches of consecutive prolines can result in ribosome stalling during translation [117]. To circumvent this but still maintain stiffness, residues of polyP can be substituted with A, E, K or T in an alternating manner [74,76,118,119].

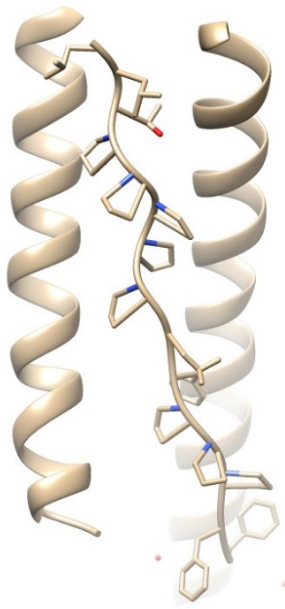

Figure 3 *Example of a left-handed PPII helix (middle) with the sequence LLTPPPPPLFPPPFF. Adapted from PDB 1VZJ using UCSF Chimera [120].*

Generally, stiffness and expansion of the linker sequence increase with increasing P content [100,121]. By combination of flexible G/S or G/S-like elements with P, **semi-flexible linkers** can be constructed. These include for example stretches of G, S and P [122] or G, S, A and P [123,124], but also alternating polyP and G/S "hinges" [125]. PASylation motifs – stretches composed solely of P, A and S – have also been proposed as linkers [126,127]. The term PASylation is derived from PEGylation, a technology that improves the pharmacokinetic properties of therapeutic peptides or proteins but relies on PEG instead of *aa* [126,128]. PASylation motifs are chemically inert and do not aggregate; hence, they have been established as fully genetically encoded alternatives for PEGylation [13,129,130].

Another P containing motif, $(GPGGA)_n$, forms semi-flexible, elastic "spring"-like linkers and was derived from the spider silk protein flagelliform [131]. In a FRET-biosensor study from Jones *et al.*, $(GPGGA)_8$ proved superior than both flexible and rigid α-helical linkers [98]. Interestingly, the rigid linkers used in this study were based on $(MALEK)_n$, a newly devised motif that incorporates *aa* that are entropically less affected than others when folded into a rigid helix [132].

However, the most common rigid protein spacer apart from polyP is the **$(EAAAK)_n$** motif, originally introduced as a linker by Arai *et al.* [133,134]. Between pH values of 4-9, E and K are ionized and thus able to form salt bridges based on their electrostatic interactions, whereby the structure folds into a monomeric, elongated α-helix [133,135,136], resembling natural occurring rigid helices (Figure 4). For n=3, the motif has about 80 % helicity [133,135]. The motif starts with E rather than K because negatively charged *aa* at the N-terminus have been shown to improve α-helix formation in isolated α-peptides [136,137]. Although there is evidence that $(EAAAK)_n$ linkers are prone to hydrolysis at pH 6-7 [119,138], they have been

used in countless applications in synthetic biology and protein design, in particular as donor/acceptor separator in FRET-based biosensors [73,114,139–144], but also in therapeutic proteins [74,119,145]. Similar to P and G/S mixtures, combinations of rigid $(EAAAK)_n$ stretches with flexible G/S-sequences result in semi-flexible linkers [141–144].

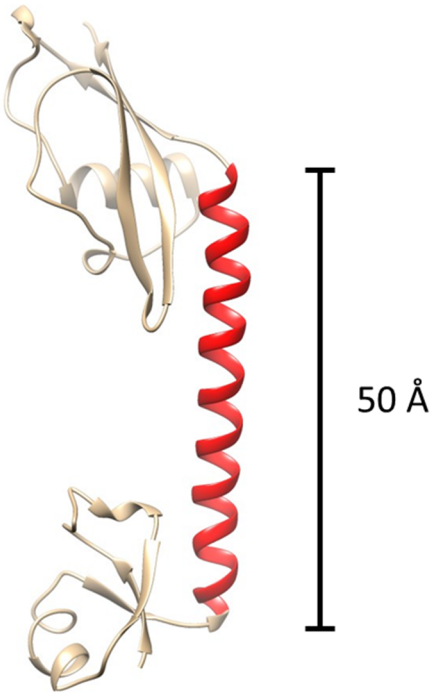

Figure 4 *Example of a natural α-helix that spans 50 Å, found in ribosomal protein L9 (PDB: 1DIV) [136]. Visualized with UCSF Chimera [120].*

Other rigid α-helices apart from $(EAAAK)_n$ include **ER/K helices** [136]. In less "strict" patterns, these also occur in natural proteins, for example in myosin X and VI [136,146]. Like in $(EAAAK)_n$, the spacing (i, i+4) is important, and E_4K_4 repeats form stable helices while E_2K_2 repeats do not [136,147]. ER/K linkers have mainly been employed by the Sivaramakrishnan group in FRET-based sensors and to modulate the effective concentration of binding partners, e.g. GPCRs and G-proteins [146,148,149]. Interestingly, "pure" EK-based sequences share the anti-fouling properties of PASylation motifs and can stabilize target proteins [150]. An extensive experimental analysis of the behaviour of E_4K_4, K_4E_4 and similar α-helices – also regarding flanking sequences – was performed by the Woolfson lab in 2015 [147], leading to a large collection of *de novo* designed helical peptides [151]. Recent bioinformatical analysis of natural occurring single α-helices complemented these experiments [152].

A rigid motif based on a natural epitope is the sequence KLYPYDVPDYA [153]. *Via* MD-simulations, the YPY stretch in this motif was found to act as a stiff turn element, and since then the 11 *aa* helix has been integrated in FRET sensor scaffolds for cAMP [153], L-lysine [154] and glucose [155].

As linkers are increasingly recognized as important fusion protein features, unusual sequences emerge or are proposed. These include repeat motifs like polyGQ, claimed to be semi-flexible [156], and polyNQ, showing anti-fouling behaviour similar to polyEK and other zwitterionic peptides [157,158], but also large, structured "linker domains" as part of a separation strategy [159,160]. The artificial motif $(EAQA)_n$ for instance has pH responsive properties and was introduced into a maltose-dependent β-lactamase switch [161].

1.1.2 Linker Length

With a plethora of different linker motifs to choose from, the question arises: What is the optimal length to connect the domains in a fusion protein?

In natural proteins, linkers have an average length of 5 to 15 *aa* [78,79]. Average needs to be stressed here, as for instance linkers in very large natural multi-enzyme complexes range from 5 to over 700 residues [162]. Longer linkers appear to be generally more hydrophilic than shorter ones [74,78]. Again, it must be emphasized that many interdomain linkers fulfil crucial roles in natural proteins [163].

In artificial fusion proteins, the length of the linker is at least equally important as its sequence. Although there are few exceptions where linker length has little effect on the fusion proteins performance [71,164], in general, small modifications lead to drastic changes in activity [95,115,119,124,165,166] and/or stability [2,92,121,165]. Length plays a less important role for flexible G/S-linkers than for rigid ones, as a recent study on GFP fusion nanobodies suggests [93]. Linker length is especially important for efficient labelling an coupling [94] as well as in the area of synthetic protein switches, where structural changes of receptor domains must be transferred to other parts of the fusion protein [5,90,123,167].

Most of the time, finding the optimal linker length and composition is a screening process rather than a result of *a priori* design [5,84,122,140,168,169]. Protein modelling has the potential to aid in this perspective, as recent progress suggests [6,16,96]. However, the difficulty regarding modelling is the high flexibility of linker stretches, which lets them behave as unstructured polymers [82,87,100]. For instance, simulations showed that beyond the size of a dodecamer (12xP), polyP is better compared to a worm-like chain rather than a stiff rod [111,162]. Also ER/K helices behave as worm-like chain modules [146], however, helicity increases the more EK repeats are present [147].

In one particular case, the FRET efficiency of a fusion protein was only enhanced after an accidental 22-*aa* insertion [170]. In another case, one single linker-optimized construct was unpredictably superior to 175 other fusion proteins [67]. To conclude, high-throughput screening remains the method of choice when searching for the optimal linker or linker combination, especially for complex systems with more than two functional domains.

1.2 How Linkers Affect Stability and Mobility of Fusion Proteins

1.2.1 Linker Effects on Fusion Protein Stability

The structural modularity of chimeric proteins creates the impression that protein domains can be handled as “building blocks” or LEGO pieces [171]. Per this rationale, the properties of one subunit would be unaffected when tethered to another subunit. However, this only holds true for few examples [171]. In the majority of cases, protein fusion leads to complex changes in thermodynamics and folding behaviour, resulting in both stabilization and destabilization, depending on the fusion partners and the linkers [171–173].

As the protein subunits experience constraints on their mobility due to tethering, they may thermodynamically prefer an unfolded state over a folded state [171,172]. Although this intrinsic destabilization may be “rescued” or even surpassed by the stabilizing effects of the interface between neighbouring domains [171–173], this is rather the exception than the rule [74,122,127,174].

Linkers can efficiently reduce strain caused by inter-domain vicinity. Thereby, fusion protein expression may be increased, as independent folding is enabled [74,127,175]. However, the effect of linkers on fusion protein stability is highly system dependent, since both linker length and composition are important parameters influencing domain interfaces and domain folding kinetics [81,176].

Some design recommendations – rather than strict rules – can be considered. For instance, hydrophilic *aa* in linker sequences effectively prevent unfolding and aggregation, both in flexible as in rigid α-helical linkers [81]. As proline is a secondary amino acid and lacks the amide proton, PolyP linkers form an exception; they are less prone to aggregation [109]. Regarding linker length, extremely long linkers tend to be unstable [100], although linkers exceeding 100 residues are useful for certain applications [97,143,146]. In cases where such long linkers are needed, structured "linker domains" also hold potential [159,160].

Linkers constitute domain-bridging elements that are generally solvent exposed, which makes them accessible targets for unspecific cleavage by endopeptidases *in vivo* and proteolysis in general [119]. Especially for G/S based flexible motifs, the propensity to be cleaved increases with linker length [83,84]. Nevertheless, sometimes it is key that fusion proteins can be irreversibly splitted into distinct domains, either by the action of proteases or changes in the proteins environment. From this perspective, linkers provide a perfect frame for **designed cleavage sites** due to their accessibility. Applications include, but are not limited to, synthetic amplification cascades and programmable protein circuits [28,51,177] as well as *in vivo* drug delivery [74,178].

Some reviews pooled cleavable linkers into a separate linker class [74,76]. Yet, if protease recognition sites and similar responsive sequences are treated as domains – as they clearly fulfil a distinct function other than spacing –, only the residues connecting these sites with other domains would act as linkers. For the sake of clarity, the term "cleavable linker" should thus be avoided and instead named "cleavage site" or "cleavable domain" when speaking of purely genetically encoded fusion proteins.

1.2.2 Linker Effects on Domain Mobility

It is important to notice that proteins in solution always exist in forms of conformational ensembles rather than single states [82,179]. All possible conformational states are given *a priori* (they are "pre-encoded") by the sequence, and the probability of each state is determined by statistical thermodynamics [179]. The distribution within the conformational ensemble changes if the protein backbone is perturbed, for example by ligand binding [180]. In this regard, binding can have allosteric effects on protein conformation or electrostatics as a result of favourable changes in enthalpy or entropy, or both [179–181].

Acting as transducers, linkers mediate between the aforementioned forces of stabilization and destabilization and translate structural changes caused by perturbations between tethered domains [179,182]. Linkers with higher flexibility can more easily change between different structural states and therefore propagate forces acting on the protein backbone faster [76,179].

Molecular simulations suggested that the impact of a linker's length on its dynamics, stiffness and its neighbouring domains appears to be larger than the impact of its amino acid sequence. For instance, Arviv and Levy observed that the folding behaviour of two connected domains gets coupled more pronouncedly when linker rigidity increases [172]. Their results were later complemented by the Cieplak group, whose all-atom and coarse-grained molecular dynamics

simulations revealed a clear inverse proportionality between linker size l and elastic stiffness κ, while the overall sequence identity had minor impact – with exception of the rigid polyP [162].

Experimental studies relativized these *in silico* findings. Ruiz *et al.* showed that both linker length and composition are highly important for optimal catalytic activity of cellulases, demonstrating that protein mobility can be governed by specific *aa* inside the linker [77]. Adamson *et al.* screened both linker identity and length in affimer-based enzyme switches and identified a medium length, flexible $(GSG)_7$ linker as the optimal solution [183]. Another example is a study on sFvs by Klement *et al.*, where changes in *aa* composition had a greater effect on the proteins functionality than changes in linker length, as P-rich linkers outperformed flexible G/S-linkers [121].

In a fusion protein, the strong interplay between linkers and domains must not be underestimated. Kirubakaran *et al.* examined five different linkers and their influence on the properties of the linked domains PDZ and SH3 *via* molecular dynamics simulations [184]. They showed that linker identity and size is similar important to the fusion proteins behaviour as the domain order (PDZ3-SH3 or SH3-PDZ3). This dependency adds an additional layer of complexity to *a priori* fusion protein design.

To conclude, both stiffness and *aa* composition affect the mobility of linkers and thus of the whole protein. Linkers with higher flexibility can facilitate conformational transitions by lowering the respective energetic barriers [76,179]. The consequences of allosteric force propagation within a fusion protein can be manifold, ranging from small amino acid reorientations to structural rearrangement of whole domains. Considering these aspects, the Nussinov group suggested a paradigm shift in linker categorization to bring into focus the dynamic role of linkers [179]. A summary of the properties of *aa* and motifs in linkers is given in Figure 5.

1.3 Beyond Simple Peptidic Linkers

In the previous paragraphs, all discussed linkers are formed by “raw” amino acid stretches. In other words, no additional step other than protein translation is required to render the linker a functional unit. However, these linkers can be further modified. For example, disulfide bridges formed by cysteines can be exploited [74,178], and chemical cross linkers can be used to stabilize rigid α-helical linker motifs [185].

The use of non-peptidic linkers in fusion proteins is a well-studied alternative to genetically encoded linkers. Non-peptidic linkers include for instance PEG [186] and DNA [187]. In the latter case, the rigidity of DNA linkers can be adjusted by ssDNA (behaving flexible) and dsDNA (behaving rigid). As in multi-domain proteins with simple *aa* linkers, the performance of a given fusion product/molecule is also highly dependent on linker length [186–189]. This is both true in solutions and near surfaces (described in Chapter 4).

Non-peptidic linkers offer more possibilities to add functionalities to a fusion protein than simple *aa* linkers. However, considering that linker space can be unpredictably peaked [67], high-throughput screening of genetically encoded linkers is preferred if the application does not rely on a specific, unusual functionality in the linker.

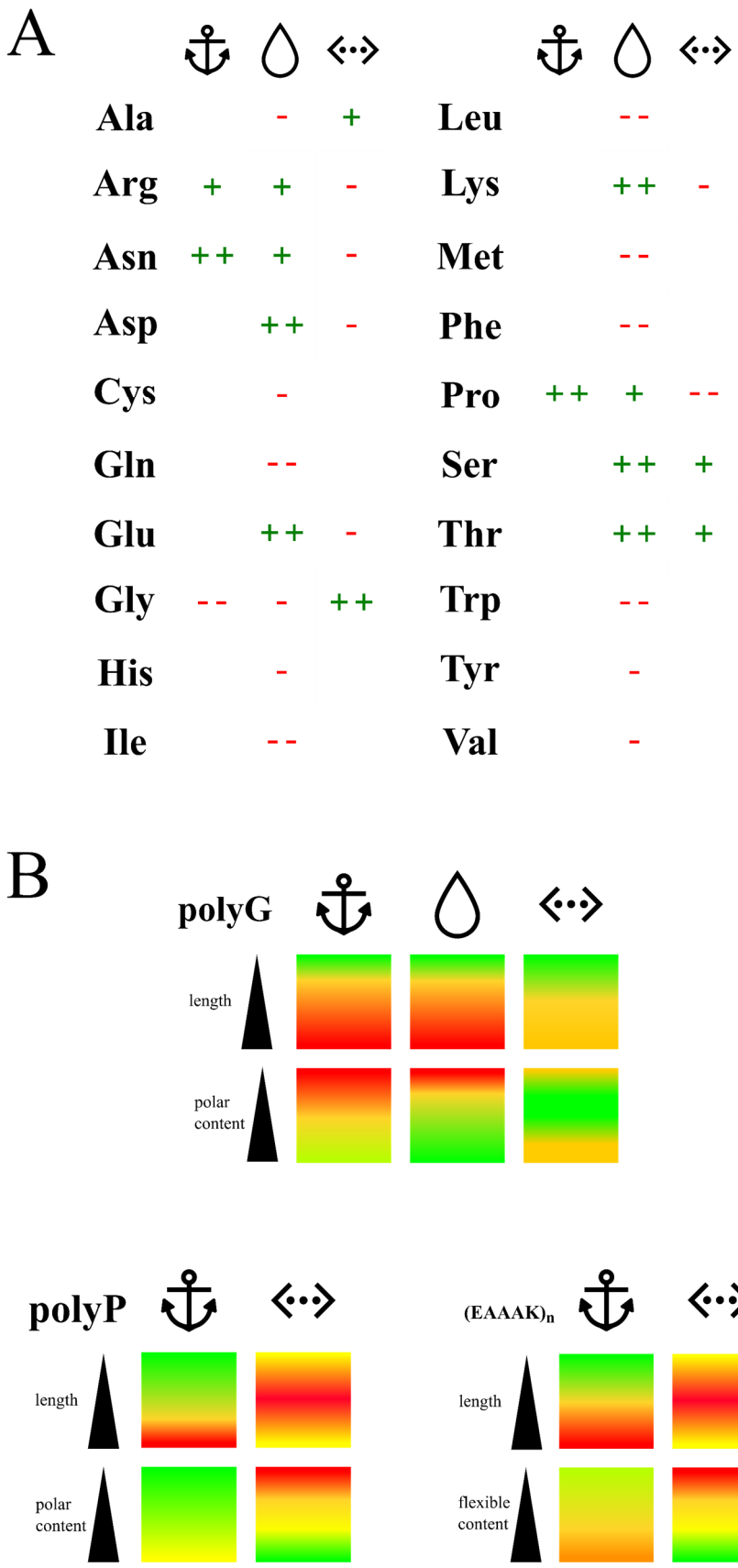

Figure 5 *Qualitative amino acid effects on linker properties summarized from sections 1.1 and 1.2. A: Individual amino acid properties; Anchor: Stability; Drop: Solubility; Dotted arrows: Flexibility. B: Heat map of motifs as a function of length or content variation on a qualitative scale from beneficial/unaffected (green) to problematic (red).*

1.4 Assembly Strategies

One particular example for an extensive linker characterization study has been published by the Tsien group [67]. In this work, 176 linker variants were systematically screened to optimize a FRET-based sensor. However, only one single linker gave superior results, leading the authors to conclude there could be no clear *a priori* prediction of the optimal linker composition.

Considering this, it is desirable to screen the linker space of a given fusion protein. A variety of cloning strategies have been proposed or have the potential to be employed for the cloning of linker coding regions. These strategies range from restriction enzyme based to completely enzyme-free. To anticipate the following overview, linker cloning is a demanding task due to the inherent properties of those *aa* that are mostly used as bridging elements. The repetitive codon pattern of prominent linker *aa* like G, S, E, P, A and K, may lead to complications during cloning.

1.4.1 Restriction Enzyme-based Strategies

The concept of the **BioBrick assembly** marked a milestone in standardization attempts, allowing linking of basic genetic parts into larger composite parts [190]. Variants thereof have been developed to generate fusion proteins, in particular the Freiburg standard (BBF RFC 25) and the BglBrick standard [191]. Due to the chosen restriction enzymes, domains are separated either by T-G (Freiburg) or by G-S (BglBrick). While both scars comprise small and hence unproblematic *aa*, they pose constrains regarding the screening of very small linkers. Apart from the special case of two connected domains (linker length: 2), the smallest possible linker would contain five *aa*.

In a straightforward approach, Li *et al.* constructed a 32-linker library consisting of EAAAK and GGGS repeating units to analyse linker flexibility and FRET efficiencies between CFP and YFP [141]. The units were assembled using two restriction sites, for Not1 and BamH1, resulting in 25-*aa* long linkers. In a similar study, BamH1 was used by Evers *et al.* [85] to partial digest a long GGSGGS-based linker, thereby generating a small library of nine fusion proteins. However, both strategies are limited to restriction sites within the linker sequence, limiting the possible sequence space for linker screening.

PCR-free assembly of long, repetitive sequences has also been described, for example by Scior *et al.* [192]. They achieved cloning of poly-Q, poly-A and poly-N by combining the use of synthetic oligonucleotides with the advantages of Type II S restriction enzymes, thereby enabling seamless cloning. Starting from Q_{11}, repetitive sequences coding for up to Q_{110} were cloned by the authors. Briefly, the plasmid is linearized *via* a unique BsmB1 site following the poly-Q sequence, thereby generating fitting overhangs for annealed oligonucleotides that code for another poly-Q building block. After ligation of the backbone and the oligonucleotides, the original poly-Q sequence becomes elongated and can be reused for another round of cloning. This method has the potential to assemble longer linkers composed of a strict pattern before subcloning them between domains of interest. Moreover, with a PCR-free strategy, recombination or annealing issues may be circumvented that arise due to the high Guanine/Cytosine content of G, A and P codons.

However, for higher order protein fusions, e.g. linker-based fusions of more than two domains, a modular strategy is more straightforward. Such a modularity is especially useful for plasmid and expression optimization.

One recent example of such a strategy is the Modular Protein Expression Toolbox (**MoPET**) proposed by Weber *et al.* [193] and based on Golden Gate assembly [194]. The main advantage of MoPET is that the specific sequence linking different functional modules can be as short as one amino acid. Nevertheless, the overlaps resulting from Type II S restriction must be distinct from each other, meaning that the succession and place of modules in the coding region must be clearly defined.

Although it was not proposed to clone linkers, the **PRe-RDL** method (recursive directional ligation by plasmid reconstruction) [195] offers many advantages: Originally used to assemble oligomers of elastin-like polymer sequences, it is in principle seamless and sequence-independent. Again, the strategy heavily relies on Type II S restriction enzymes, in this case BseR1 and Acu1. As the method is non-hierarchic, it may also be employed for higher order protein fusions, for example four domains with three linkers. PRe-RDL involves multiple cloning rounds with gel band excision steps and is therefore somewhat more time-consuming compared to other strategies.

1.4.2 PCR-based Strategies

To screen for the optimal length of a defined linker between two domains, PCR-based methods work faster than PCR-free strategies, as the "length library" can be generated during the amplification of the sequence. To mention a recent example, Norris and co-workers [84] have described the **protaTETHER** method. The method intentionally exploits the promiscuous binding of a short forward primer having only one repeat of linker codons to a longer complementary reverse primer having four to eight repeats of the respective linker codons. Thereby, a PCR produces a variety of products with different linker lengths. These products overlap with the vector containing the domains to fuse. Thus, after annealing and transformation, the resulting library of fusion proteins can be screened for the best candidate depending on the application. Yet, a new set of specific oligonucleotides must be designed for every new construct, somewhat limiting the modularity.

The **PATCHY** method (primer-aided truncation for the creation of hybrid proteins) introduced by the Möglich group relies on a one-pot PCR with a mix of staggered primers to generate a gene library with sequence truncations between the coding sequences of two functional domains [196]. While this approach is systematic, it is limited to a certain linker position. As in other approaches, it is likely that screening of repetitive Guanine/Cytosine stretches in the classical linker space could lead to problems during assembly.

1.4.3 Combination of PCR and Restriction

An approach to circumvent the step by step optimization of linker cloning was performed by Ibraheem *et al.* [95]. To improve FRET-based biosensors, they generated linker libraries with length from 0 to 20 based on G, A and S *aa*. Theoretically, 640 variants were constructed using an approach that combined PCR and restriction digest. Because specific restriction enzymes are needed to unite linkers and domains following PCR, small "scars" remained, flanking the insertion sites of the linkers.

1.5 Perspectives

The functionality of a multi-domain fusion protein is highly dependent on the domain-connecting linker(s). Inspired by naturally occurring motifs, artificial linkers have been developed that ensure separation, solubility, stability and mobility of single domains. New motifs have been proposed that could become useful linkers in the future, for instance the EK-helices or polyampholytic stretches [147].

The assembly of multi-domain fusion proteins and their linkers remains a challenge due to the repetitive nature of conventional linker amino acid codons. Considering this, the Synthetic Biology community would benefit from a reliable fusion protein assembly method that allows (nearly) full factorial linker space coverage. To meet this need, my colleagues and I developed a cloning strategy that I applied to construct potent protease switches. The workflow and results are presented hereafter in section 3 and have been published in condensed form in [123].

2. Methods

2.1 Standard Methods

Liquid *Escherichia coli* cultures were routinely grown in LB medium at 37 °C and 180 turns/min in appropriate shakers for plasmid amplification. For long term storage of *E. coli* strains, glycerol cultures were generated. To do so, 500 μl of 50 % (w/v) sterile glycerol solution and 500 μl of the respective overnight culture were gently mixed, flash frozen and stored at -80 °C.

To transform chemically competent *E. coli* cells via heat shock, the cells (100 μl aliquots) were thawed on ice and 0.2-2 μg of the desired plasmid DNA was added. The mixture was stored on ice for 30 min, incubated at 42 °C for 45-60 s and stored on ice for another minute before pre-warmed (30 °C) SOC medium was added. The cells were grown for 1 h at 37 °C and then plated on LB-agar with the respective antibiotic.

PCRs were routinely performed in 50 μl reactions using in-house purified proofreading polymerase (Sup Table 1). Gibson assembly [197] either with commercially synthesized DNA (IDT or GenScript) or in-house DNA was executed according to the manufacturer (NEB). Plasmid preparations were performed with M&N NucleoSpin® Plasmid Kits. Ligations were performed in 12 μl reactions overnight at 16 °C or at 30 °C for 3 h.

For agarose gel electrophoresis, 0.5-1.5 % (w/v) melted agarose in TAE buffer was supplemented with Midori Green Advance (Nippon Genetics). Samples were loaded after dilution with loading dye (6x) and run at 110-120 V for 30-45 min in Gelsystem Mini M chambers (VWR) before recording *via* E-BOX (Vilber).

Successfully cloned plasmids were routinely sequence-verified by commercial DNA sequencing at Microsynth Seqlab.

SDS-PAGE after Laemmli [198] was performed using either precast 4-20 % gradient gels (Bio-Rad) or self made gels with 5 % stacking gel and 12 % running gel unless stated otherwise. Running buffer was always prepared as 10x stock (250 mM Tris, 1.92 M Glycine, 1 % (w/v) SDS). Sample loading dye was prepared as 2x or 5x stock. In case of precast gels, runs were performed at max. 200 V for 35-40 min. In case of self-prepared gels, runs were performed at max. 140 V for 45-75 min.

2.2 Library Cloning

All cloning enzymes were purchased from New England Biolabs (NEB). For cloning of fusion protein libraries, the developed iterative Functional Linker Cloning (iFLinkC [123], section 3.2) was performed. Functional domains (FDs) in plasmid backbone pFD, and peptide linkers in plasmid backbone pL2 comprise the starting point of iFLinkC. Functional domains and linkers were cloned into the respective backbones using standard cloning strategies, e.g. hybridization of annealed oligos, restriction and ligation, and Ligase Cycling Reaction (LCR) [199,200] as described in Table 8 in the result section. For combining Linkers and FDs, restriction digestion was performed depending on the desired direction of the parts (e.g. N-terminal linker and C-terminal domain or vice versa). iFLinkC relies heavily on 2 bp overhangs generated by the unusual Type II S enzymes Bts1 and BsrD1 [201]. The minimal linker formed by iFLinkC is comprised of one G only. Unless the last functional domain that is cloned to the C-terminus of the fusion protein has a stop codon, the translated protein ends with the final three *aa* GIA. Bbs1 and Bsa1 restriction sites were used for additional linearization to inhibit religation of the

donor plasmid. Sequences of empty pFD, pL2 and pFlinkC-XE (work name: pDEST) plasmids are attached to the supplement.

The restriction digestion strategy is described in detail in section 3.2. The addition of rSAP (recombinant shrimp alkaline phosphatase) to one of the restriction reactions is recommended to avoid religation events (Table 2). The subsequent separation of plasmid fragments was performed *via* agarose gel-electrophoresis for optimal results. After gel extraction and clean-up, ligation was performed at 16 °C overnight using T4 ligase. Heat-competent *E. coli* Dh10β were transformed with 2-3 μl of the ligation reaction. In the case of libraries, 40 μl aliquots were plated on agar plates to assess cloning efficiency and while the remainder of the transformation reaction was used to inoculate 10 ml of overnight culture.

Assembled libraries were cloned into pFLinkC-XE *via* Bts1 and Spe1/Nhe1 following the same pipeline of restriction digest, gel extraction and ligation. *E. coli* Dh10β were transformed with the assembled libraries for storage purposes while ultracompetent *E. coli* BL21(DE3) were transformed with the libraries *via* electroporation for screening purposes. Details regarding restriction digest are given in Table 3.

Table 2 *Step-by-step cloning table for restriction digest of FDs and linkers. BsrD1 digest was performed in PCR cyclers to prevent lid condensation. rSAP should only be added to one of the reactions. All restriction enzymes and buffers were purchase from New England Biolabs (NEB).*

Component	Amount / Volume	Incubation	Add	Incubation
pL2 containing Linker(s)	Up to 2 μg total DNA*	1 h 65 °C	1 μl Spe1/EcoR1**	1 h 37 °C
BsrD1	1 μl		1 μl Bsa1	
NEB Buffer 2.1 (10x)	5 μl		(1 μl rSAP)	
ddH_2O	to 50 μl			

Component	Amount / Volume	Incubation	Add	Incubation
pFD containing Functional Domain(s)	Up to 2 μg total DNA*	1.5 h 37 °C	1 μl Bbs1	0.5 h 37 °C
Bts1	1 μl		(1 μl rSAP)	
Spe1/EcoR1**	1 μl			
CutSmart buffer (10x)	5 μl			
ddH_2O	to 50 μl			

* If libraries are to be generated, plasmids are used in equimolar amounts
** FDs larger than 300-350 bp are best cloned *via* Spe1, smaller FDs should be cloned with EcoR1 to facilitate downstream agarose gel excision

Table 3 *Step-by-step cloning table for final cloning of a fusion protein (library) into the expression vector pFLinkC-XE.*

Component	Amount / Volume	Incubation	Add	Incubation
pFLinkC-XE	Up to 2 μg	1.5 h 37 °C	1 μl rSAP	0.5 h 37 °C
Bts1	1 μl			
Nhe1	1 μl			
CutSmart buffer (10x)	5 μl			
ddH_2O	to 50 μl			

Component	Amount / Volume	Incubation
Fusion protein (library) in pL2/FD	Up to 2 μg	1.5 h 37 °C
Bts1	1 μl	
Spe1	1 μl	
CutSmart buffer (NEB) (10x)	5 μl	
ddH_2O	to 50 μl	

2.3 Ligase Cycling Reaction

LCR primers were phosphorylated following the protocol from [200] (Table 4), followed by adapted PCR (Table 5). PCR products were purified *via* agarose gel electrophoresis and respective kits. A Dpn1 digest was performed for 30 min at 37 °C, combined with the dilution of the PCR products to 12 nM. Scaffold oligonucleotide connector (SOC) mix was prepared with 100 nM SOC primer each, and LCR was prepared (Table 6) and performed in a PCR cycler (Table 7), followed by *E. coli* transformation.

Table 4 *LCR Primer phosphorylation*

Component	Amount (μl)	Final Concentration
100 μM Forward Primer (Stock)	1,5	3 μM
100 μM Reverse Primer (Stock)	1,5	3 μM
10 U/μl T4 Polynucleotide Kinase (T4 PNK)	1	0.2 U
10X T4 Ligase Buffer	5	1X
dH_2O	41	
Total	50	
Incubation: 37°C for 30 minutes		

Table 5 *Adapted PCR for LCR cloning. Top row: Number of reactions. All other numbers in μl.*

PCR reactions	1	2	4	6	…
DNA-Template (Plasmid) 20 ng/μl	1	2	4	6	
Phosphorylated primer mix	8	16	32	48	
dNTPs	1	2	4	6	
GC Buffer	10	20	40	60	
dH_2O	29,5	59	118	177	
Phusion Polymerase	0,5	1	2	3	

Table 6 *LCR reaction adapted from [199,200].*

Component	Amount (μl)
12 nM DNA-Parts (backbone, inserts)	4
100 nM SOC Mix	6
10x Taq Ligase Buffer	2
40 U/μl Taq DNA Ligase	2
H_2O	6
Total	20

Table 7 *LCR program.*

Temperature	Time	
1. 95°C	2 min	
2. 95°C	30 s	Repeat 30x
3. 60°C	2 min	
4. 55°C	10 min	
6. 10°C	Standby	

2.4 Electrocompetent *E. coli* BL21(DE3)

100 ml SOB medium are inoculated with BL21(DE3) to $OD_{600} \approx 0.15$ and grown to $OD_{600} \approx 0.5$ before cells are stored for 15 min on ice. Cells are centrifuged at 4000 xg, 4 °C, 15 min, resuspended in 50 ml cold H_2O. These steps are repeated once, before cells are resuspended in 25 ml cold glycerol (10 % w/v). After a final centrifugation step as before, pellets are resuspended in 300-400 μl cold glycerol (10 % w/v), flash frozen in $N_{2(l)}$ and stored at -80 °C.

For transformation *via* electroporation, 1 μl plasmid DNA (50 ng/μl) was mixed with 50 μl cold glycerol (10 % w/v), mixed with 50 μl competent cells and incubated for 5 min on ice, followed directly by ≈ 7 ms electro-shock at 1.81 kEV, 300 Ω and 25 μF. 1 ml of SOC medium was added. After 1 h at 37 °C, cells were plated on agar plates with the appropriate antibiotics.

2.5 Chemically competent *E. coli*

200 ml of SOB medium were inoculated with 4 ml of an overnight *E. coli* culture and stirred at min. 180 rpm at ≈ 20 °C. When the OD_{600} reached 0.5-0.6, the culture was incubated on ice for 10 min, followed by centrifugation at 2500 xg, 4 °C, 15 min. Pellets were resuspended in 5 ml TB buffer (4 °C) and centrifuged a second time. Pellets were resuspended in TB buffer supplemented with 7% DMSO, incubated on ice for 10 min, aliquoted, flash-frozen in liquid nitrogen ($N_{2(l)}$) and stored at -80 °C.

2.6 Protein Purification

Protein switches were expressed from respective pFLinkC-XE (pDEST) plasmids as MBP-fusion in *E. coli* BL21(DE3) at 1 l LB scale, containing the appropriate antibiotic (100 μg/ml ampicillin). IPTG was added at an OD_{600} of 0.5, and expression continued for 4.5 h at 30 °C. Cultures were harvested via centrifugation and stored at -20°C. At the day of purification, the cells were resuspended in 40 ml of buffer W each (150 mM NaCl, 100 mM Tris-Cl, 1 mM EDTA pH=8) and crushed via four passes through an Emulsiflex C3 (Avestin). After centrifugation at 25000 xg for 1 h at 4 °C, the sample was filtered through a 0.45 μm syringe filter. An ÄKTApure system and a 1 ml StrepTrap HP column (GE Healthcare) was used to purify the proteins. The columns were equilibrated with 8 CV of buffer W. After protein loading, the columns were washed with 8 CV of buffer W. The protein was eluted with 5 CV buffer E (150 mM NaCl, 100 mM Tris-Cl, 2.5 mM desthiobiotin, 1 mM EDTA, pH=8) at 0.5 ml fractions and the concentration estimated *via* nanodrop-measurement. Protein aliquots were flash frozen in $N_{2(l)}$ and stored at -80 °C until needed.

2.7 Fluorogenic Protease Substrate Peptides and Affinity Clamp Peptide Ligands

Protease substrate ANA-peptide (see [5]) and affinity clamp peptide ligand were synthesized by GenScript. ANA-peptide was dissolved in DMSO to a final concentration of 8 mM and stored at -80 °C, affinity clamp peptide ligand was dissolved in DMSO to a final concentration of 10 mM and stored at -20 °C.

2.8 Reverse ITC

Reverse ITC was performed on a Malvern MicroCal PEAQ-ITC at the Hausch research group (TU Darmstadt). Freshly purified protein switch 2_B3 was concentrated to 70 μM with Vivaspin 500 centrifugal filters (Sartorius). 10 μM rapamycin solution in buffer E with 0.05 % DMSO was titrated with the protein in the same buffer. Data were analyzed using MicroCal PEAQ-ITC analysis software.

2.9 Ligand Titration Experiments

Apparent K_ds of TVMV protease-based switches were measured by means of ligand titration. In case of the best rapamycin switch 2_B3, 10 nM of 2_B3 were sufficient to determine ANA-peptide cleavage induced fluorescence using the TECAN Spark platereader. Initial rates extraction, plotting and non-linear regression fit was performed according to [5]. The derivation of the regression fit equation is attached in the supplement of this chapter (Sup Text 1).

2.10 Library Assay

Fusion protein libraries in pFLinkC-XE were transformed into *E. coli* BL21(DE3) cells (NEB) by means of electroporation and plated on LB plates with 100 μg/ml ampicillin. Resultant colonies were used to inoculate 500 μl of modified minimal autoinduction medium (N-5052) made of 0.5% glycerol, 0.05% glucose, 0.2% lactose, 50 mM KH_2PO_4, 50 mM Na_2HPO_4, 10 mM $(NH_4)_2SO_4$, $MgSO_4$, and 1x trace metal solution [202] with antibiotics in 96-deepwell plates (Faust). Depending on addition of casaminoacids, cells were cultivated for 48 or 72 h at 37 °C in a microwellplate shaker (Heidolph) at 1200 rpm. 100 μl of each culture were saved in form of glycerol stocks. The remaining cells were spun down, and the plate stored at -20 °C until used.

Lysis was performed according to [203] with modifications. Briefly, pellets were thawed and resuspended in 100 μl buffer W with 1 mg/ml lysozyme and 1 μg/ml DNase. This suspension was incubated for 2 h at 1200 rpm and 30 °C. After centrifugation (2500 xg, 4 °C, 20 min) the supernatant was used for the following assay.

The lysate-based library assay was performed in 150 mM NaCl, 100 mM TRIS-Cl pH=8, 4 mM DTT, 5 mM EDTA and rapamycin. 20 μl of protein-containing lysis supernatant were added to 90 μl of assay buffer containing no or 5 μM rapamycin, respectively, in black 96-flat bottom plates. Proteins were incubated in these buffers for 5 min at RT under slight shaking, before addition of 90 μl assay buffer containing 5 μM ANA-peptide. ANA-peptide contains a fluorophore (a 7-methoxycoumarinyl-4-acetyl group) that is quenched by an intramolecular 5-amino-2-nitrobenzoyl group unless the latter is cleaved off *via* TVMV protease, leading to a measurable increase of fluorescence. Fluorescence increase was measured in a TECAN Spark platereader (Tecan) at gain 80, Z-position 20000 μm, 30 °C, excitation 330 nm and emission 405 nm in appropriate time intervals.

3. Results

3.1 Protein engineering – Starting Point Rapamycin-switch

Synthetic protein switches share a modular pattern. Both receptor and actuator domains of such fusion proteins can in principle be exchanged by others, leading to new switching behaviours. One known protease switch is the module TVMVp^{E217}-PDZ^{G37}-FN3^{GPG}-AI$_{TVMV}$ [5]. In this switch, the two-domain affinity clamp receptor module PDZ^{G37}-FN3^{GPG} can recognize and bind small peptide ligands, leading to structural rearrangements within the protein backbone [90,204]. In the OFF-state, the activity of the N-terminal actuator TVMV protease (TVMVp) is tightly repressed by its autoinhibitory domain (AI$_{TVMV}$) at the C-terminus of the fusion protein. In this switch, ligand binding by the receptor module releases the AI$_{TVMV}$ from TVMVp, thereby activating the protease.

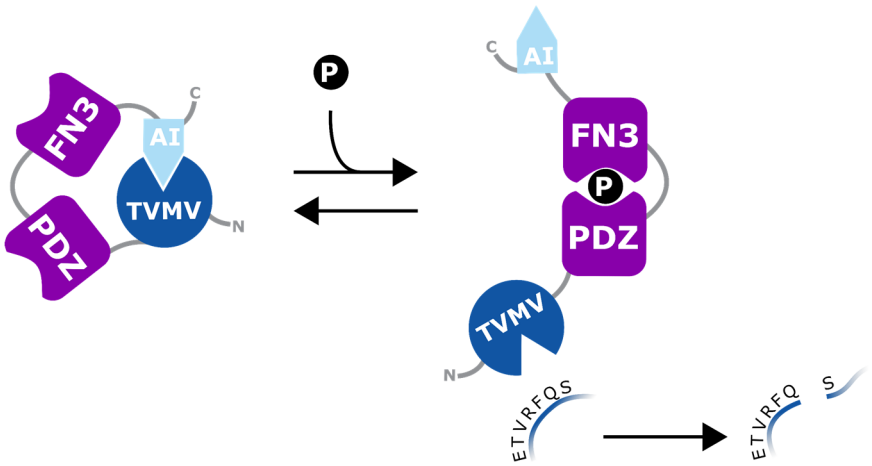

Figure 6 *Comic representation of the autoinhibited protease switch TVMVp^{E217}-PDZ^{G37}-FN3^{GPG}-AI$_{TVMV}$ from [5].*

Following the architecture of this prototype scaffold, a new protein switch was designed in the first months of my PhD studies. While the actuator TVMVp and its autoinhibitory domain AI$_{TVMV}$ were maintained in the construct, FKBP12 and FRB were chosen as receptor domains. Both domains have been used before in artificial protease cascades [5], but not as part of a single chain switch. FKBP12 (hereafter abbreviated as FKBP) is a 12 kDa FK506 binding protein that binds the small immunosuppressant rapamycin with extraordinary affinity (K_D = 0.2 nM) [205]. The complex is then bound by FRB (FKBP-rapamycin binding domain), a protein derived from a domain of mTOR, forming a ternary complex [205].

Additional changes were made to improve the architecture and increase success chances. The domain order of TVMVp and AI$_{TVMV}$ was reversed, leaving AI$_{TVMV}$ closer to the N-terminus than the protease to prevent background activity that might be caused by incomplete translation or non-specific proteolysis of the large fusion protein [5,123]. The MBP gene was included upstream (5') of the switch coding region as a solubility enhancer [206], separated from the switch by a TEV protease cleavage site. Additional affinity tags were included for purification purposes. The initial domain orientation FKBP-FRB was chosen after structural analysis in UCSF Chimera [120]. The main criteria for the design were the vicinities of the respective domain termini. Using UCSF Chimera [120] and the available crystal structures of the distinct domains, first approximations of the appropriate linker lengths were made.

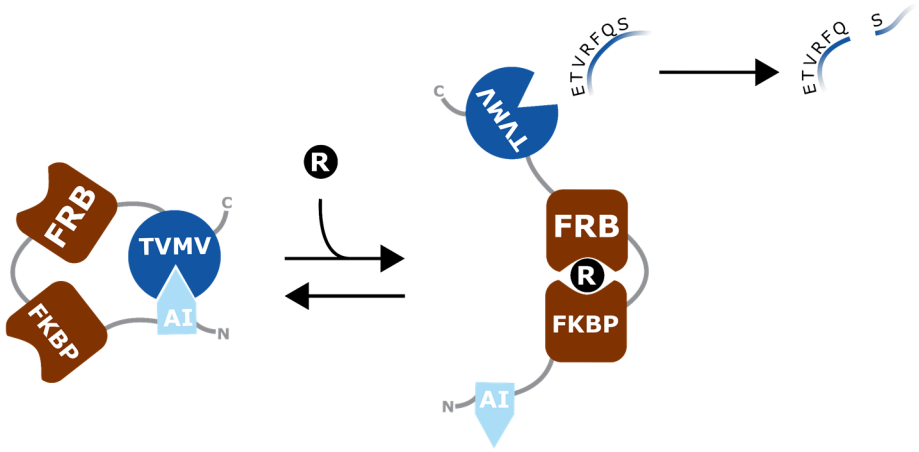

Figure 7 *Comic representation of the proposed autoinhibited protease switch AI_{TVMV}-FKBP-FRB-TVMVp.*

Thus, the starting point for the rapamycin inducible protease switch was designated as MBP-TEV_{site}-strep-^{SGG}-AI_{TVMV}-^{GPGAS}-FKBP-$^{GL(GGGS)3ET}$-FRB-^{SGGRGS}-TVMVp-^{GGS}-6xHis (linkers in superscript). Restriction enzyme sites were introduced in the initial linker coding sequences to enable fine-tuning of the switch later. The sequence was ordered as a gblock (IDT) named gAG6 and inserted into pASK-IBA3 *via* Gibson assembly.

The corresponding AG6 protein was expressed in *E. coli* BL21(DE3) and purified *via* its StrepTagII. The respective SDS-PAGE is shown in Figure 8. The additional bands in the elution fraction indicate either incomplete translation or unspecific hydrolysis. This phenomenon recurred in purifications of other large multi-domain proteins used in this work.

In a first proof-of-concept experiment, 400 nM of AG6 were mixed with 5 μM of TVMVp substrate (ANA-peptide) and 0 or 5 μM of rapamycin, respectively. ANA-peptide contains a fluorophore (a 7-methoxycoumarinyl-4-acetyl group) that is quenched by an intramolecular 5-amino-2-nitrobenzoyl group unless the latter is cleaved off *via* TVMVp, leading to a measurable increase of fluorescence. The slopes of the resulting RFU/min graph were 4.08 ± 0.04 for 5 μM rapamycin and 1.13 ± 0.02 for 0 μM rapamycin, respectively (Figure 8).

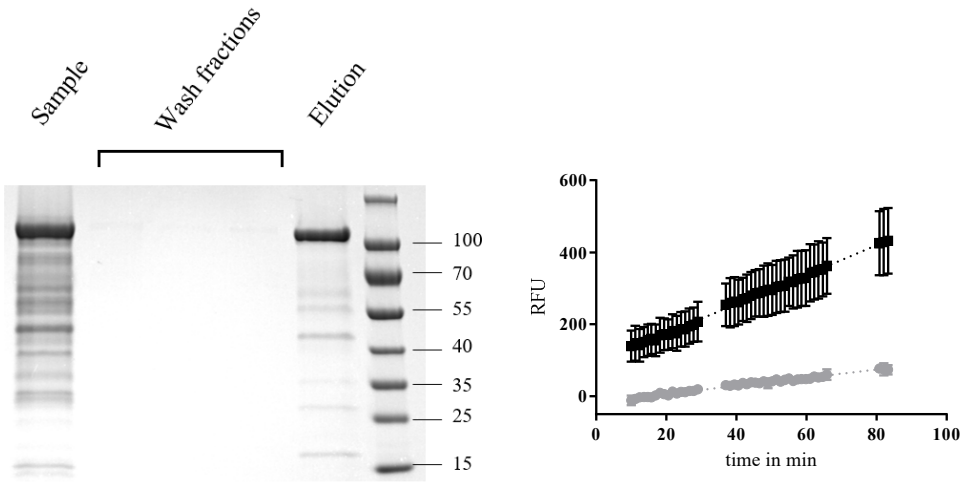

Figure 8 *Purification and characterization of AG6. Left: SDS-PAGE of ÄKTA purification. A discrepancy to the expected size of AG6 (97.2 kDa) is likely caused by insufficient heating. Marker in kDa. Right: TECAN measurement of ANA-peptide conversion by AG6 in absence (grey) or presence (black) of rapamycin. Error bars represent standard deviation of triplicates.*

These results demonstrate twofold. Firstly, the architecture of the rationally designed fusion protein switch allows for a repression of TVMVp by AI_{TVMV} in the basal state. Secondly, they showed that upon rapamycin binding by the affinity clamp module FKBP/FRB, AI_{TVMV} is to some extent released from the active center of the protease, leading to higher turnover of ANA-peptide. Thus, AG6 constitutes a first single chain rapamycin-inducible protease switch.

3.2 Conceiving a Linker Cloning Strategy

Considering the role of linkers in fusion protein mobility (section 1.2.2), further optimization of the AG6 switch at the linker sites could potentially lead to improved switches with respect to activity and inducibility. However, while it is possible to rationally design a fusion protein scaffold using available crystal structures, rational design of a fusion protein's mobility represents a task considerably more demanding. As discussed in the introduction (section 1.2), there is still a lack of understanding how allosteric forces or structural changes are propagated through the protein backbone, in particular for multi-domain fusion proteins.

Therefore, a generalizable method was developed that enables high-throughput screening of linker space in multi-domain fusion proteins to accelerate the process of finding improved switch variants. The method was termed iterative Functional Linker Cloning (**iFLinkC**). It relies on Bts1 and BsrD1, two unusual Type II S restriction enzymes that generate two-nucleotide overhangs close to their binding site [201]. When the sites are placed correctly, linker libraries – starting from a minimal linker of one glycine – can be fused to protein domains in a modular fashion *via* restriction and ligation (Figure 9). Importantly, iFLinkC is not limited by linker identity, and e.g. proline-helices or PASylation motifs [126] can be treated the same way as GS-rich sequences.

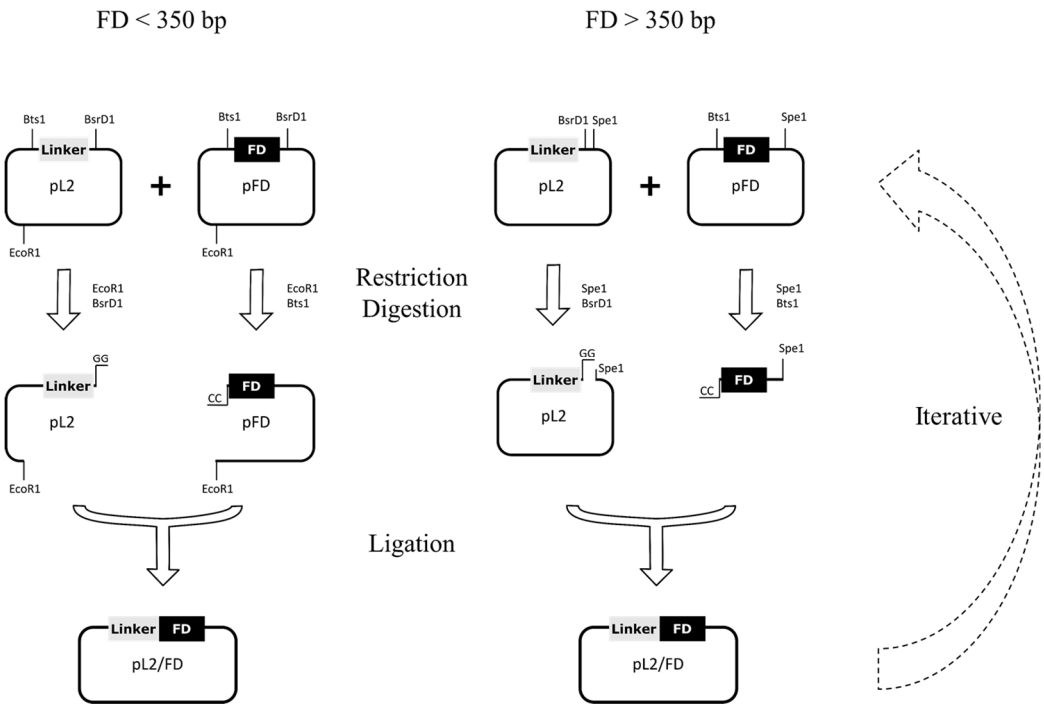

Figure 9 *Overview of the iFLinkC method to generate multi-domain fusion proteins. Depending on the size of the functional domain (FD), two cloning workflows are possible, both resulting in the same plasmid with a linker-FD combination that carries the identical restriction sites as the initial plasmids. This allows to attach additional linkers / FDs in an iterative and combinatorial manner. The cloning process can be performed in parallel to save time during the construction of large fusion proteins and/or libraries. A comparable figure was published in [123].*

It is important to notice that by design, linkers can only be attached to FDs and *vice versa* due to the nature of the two-nucleotide overhangs. For instance, fusion of two FDs without at least the 1xG linker in between results in a 1 bp frameshift (Figure 10). After construction in pL2/pFD, the fusion protein or fusion protein library is cloned into an iFLinkC compatible expression vector that contains a promoter, ribosome binding site, start codon and terminator, for instance iFLinkC-XE, *via* restriction digest with Bts1 and Nhe1/Spe1 and subsequent ligation.

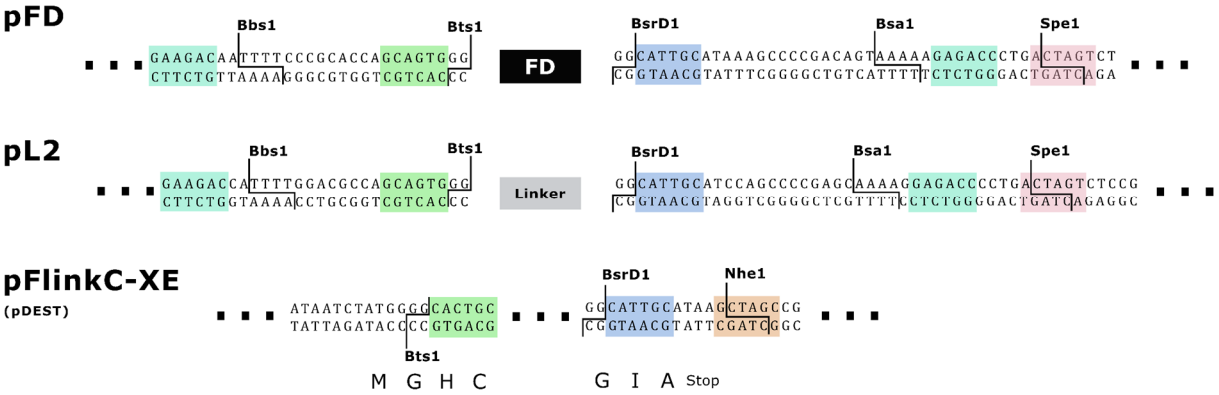

Figure 10 *Cloning sites of the respective iFLinkC plasmids. Binding sites of restriction enzymes are colored. The first and last aa of pFlinkC-XE are indicated. After insertion of a fusion protein library, aa MG remain at the N-terminus and GIA at the C-terminus unless a stop codon is explicitly introduced at the end of the last functional domain.*

3.3 Generation of iFLinkC Backbones

The original pFLinkC-XE plasmid (working name: pDEST) was designed to be essentially a pET32a(+) backbone with a new multiple cloning site and an mRFP insert as an additional selection marker. The important modifications from the pET32a(+) backbone are:

- Removal of all Bts1, BsrD1, Bbs1 and Bsa1 sites from the backbone
- Removal of f1 bacteriophage ori
- Insertion of an EcoR1 site between KanR and ori
- Insertion of an Mfe1 site between pBR322 ori and cloning site

In the scope of her master thesis, Anastasia Weyrich optimized pFLinkC-XE to contain the coding sequence for the green fluorescent fusion protein mNeongreen-$(GGS)_2$-CfaN as a selection marker, as the mRFP coding sequence lead to unexpected difficulties during cloning. The pFD and pL2 plasmid were designed to be essentially pET24(+) backbones with a new multiple cloning site. The important modifications from the pET24(+) backbone are the same as for pFLinkC-XE, with the additional removal of the T7 promoter sequence. The sequences of the empty plasmids are available in the supplement of [123]; the cloning sites are depicted in Figure 10.

Linkers and functional domains were cloned into the respective plasmids by means of Gibson assembly, oligo annealing, Ligase Cycling Reaction (LCR) or restriction cloning (partial digestion from larger linkers) as listed in Table 8.

Table 8 *Shown are the functional linkers (italic) and domains used in the first libraries of iFLinkC and the respective method that was used for cloning into pFD / pL2. LCR: Ligase Cycling Reaction; oligo: Oligo cloning; Gibson: Gibson Assembly.*

insert	method	insert	method	insert	method
G	LCR	*GGSGGSG*	Restriction from larger linker	AI_{TVMV}	LCR
GG	LCR	*(GGS)$_3$G*	oligo	FKBP	Gibson
GGG	LCR	*(GGS)$_4$GSG*	oligo	FRB	Gibson
GGSG	LCR	*G(P)$_7$G*	oligo	TVMVp	Gibson
GPG	LCR	*G(TP)$_4$TG*	Restriction from larger linker	MBP-TEV_{site}-strep-AI_{TVMV}	Gibson
GPPPG	oligo	*GGASPAGG*	Restriction from larger linker	ePDZ-B1	Restriction (A. Weyrich)
GSPAG	LCR	*GGASPAAPAPAG*	oligo	FN3	Restriction (A. Weyrich)
		GGA(EAAAK)$_2$AGG	Restriction from larger linker	StrepTag-II	oligo

3.4 iFLinkC Optimization

Prior to the generation of a large rapamycin-switch library, efficiency tests were performed. As described in the method section, restriction with Bsa1 in combination with BsrD1 as well as restriction with Bbs1 combined with Bts1 enable the excision of small ≈ 20 bp fragments during the iFLinkC procedure. This in principle allows “one pot reactions” by sequential action of ligase and Exonuclease III (ExoIII) after separation of the desired DNA from the small fragments *via* magnetic beads or PEG precipitation instead of agarose gel excision. Consequently, iFLinkC should be automatable. The efficiency of these alternatives (PEG precipitation, magnetic beads, “one pot reaction”) was compared to gel extraction of cleaved DNA substrates. Albeit less time consuming, none of these strategies came close to the superior efficiency of the agarose gel extraction method.

The reasons for this are manifold. For instance, neither restriction nor ligation reactions achieve 100% efficiency, therefore original plasmid remains in the reaction up until transformation. Furthermore, the small ≈ 20 bp fragments may not be completely removed and cause ligation artifacts. For the one pot reaction, trace amounts of linear side products – despite the usage of ExoIII – may interfere with plasmids during transformation or may be otherwise processed to plasmid artifacts in *E. coli*. On the contrary, agarose gel extraction allows evaluation of restriction efficiency during the cloning procedure, while simultaneously separating desired DNA fragments from undesired. Thereby, ligation artifacts are minimized, leading to an overall higher number of correct clones after transformation. Downscaling of the reactions to very small volumes, for instance in suitable robotic platforms, might improve the efficiency of the alternative methods.

After thorough optimization of the workflow and the material mainly performed by Anastasia Weyrich in the scope of her master thesis, the described iFLinkC method was applied for a fusion protein library cloning. A rapamycin switch library was generated in four steps as depicted in the following scheme (Table 9, Table 10). In the last step, the assembled library was cloned into pDEST (pFLinkC-XE).

In the library, the domain orientation of the original AG6 switch was maintained (AI_{TVMV}-FKBP-FRB-TVMVp). As described in the introduction, linker lengths can have extreme effects on fusion protein performance, therefore the "allowed" lengths of the three library linkers were chosen based on the successful AG6 switch (L1: 5 *aa*, L2: 16 *aa*, L3: 6 *aa*). Seven small linkers were allowed for the "outer" positions L1 (AI_{TVMV}-FKBP) and L3 (FRB-TVMVp), while 15 linkers with up to 16 *aa* were allowed for L2 (FKBP-FRB) (Table 9). Thus, the library had an overall diversity of 735 variants. The C-terminal 6xHis-tag that was part of the initial AG6 was omitted in the library.

Table 9 *Linker sub-libraries used in the rapamycin-switch library.*

Notation	Linkers included
Linker (7)	G, GG, GPG, GGG, GGSG, GPPPG, GSPAG
Linker (15)	Linker (7), $(GGS)_2G$, $(GGS)_3G$, $(GGS)_4GSG$, GGASPAGG, GGASPAAPAPAG, $G(P)_7G$, $G(TP)_4TG$, $GGA(EAAAK)_2AGG$

Table 10 *Assembly scheme of the rapamycin switch library.*

Cloning Step 1 (parallel)

Substrate	Processed with enzymes
Linker (7) in pL2	BsrD1 + Spe1 + rSAP
TVMVp in pFD	Bts1 + Spe1
Linker (15) in pL2	BsrD1 + Spe1 + rSAP
FRB in pFD	Bts1 + Spe1
Linker (7) in pL2	BsrD1 + Spe1 + rSAP
FKBP in pFD	Bts1 + Spe1

Cloning Step 2 (parallel)

Substrate	Processed with enzymes
MBP-(TEV_{site})-strep-AI_{TVMV}	BsrD1 + EcoR1
Linker (7)-FKBP	Bts1 + EcoR1
Linker (15)-FRB	BsrD1 + Spe1 + rSAP
Linker (7)-TVMVp	Bts1 + Spe1 + Bbs1-HF

Cloning Step 3

Substrate	Processed with enzymes
MBP-(TEV_{site})-strep-AI_{TVMV}-Linker (7)-FKBP	BsrD1 + EcoR1 + Bsa1-HF
Linker (15)-FRB-Linker (7)-TVMVp	Bts1 + EcoR1 + Bbs1-HF

Cloning Step 4 (to pDEST / pFLinkC-XE)

Substrate	Processed with enzymes
Assembled Library	Btsa1 + Spe1
pDEST-T7-UTR-mNeongreen-$(GGS)_2$-CfaN	Btsa1 + Nhe1 + rSAP

3.5 Library Screening Procedure

High-throughput screening of protein libraries in 96-well format can be performed with *E. coli* lysates. A procedure was developed based on the assay described by Santos-Aberturas *et al.* [203] (section 2.10). As before, protease activity was measured by fluorescence increase resulting from the processing of initially quenched ANA-peptide.

First, the assay was tested with the AG6 protein. 10x 300 μl LB medium in a 96 deep-well plate were inoculated with 30 μl of BL21(DE3) carrying the AG6 expression plasmid and induced manually with 0.75 mM IPTG after 4 h. Expression occurred overnight, and on the next day the protocol described in section 2.10 was used to harvest and lyse cells. Although in the first experiment over the course of 80 min, the presence of 5 μM rapamycin had no significant effect on ANA-peptide turnover, as determined from the slope in RFU/min, protease activity was observed, showing that expression of the protein and the activity assay work in principle.

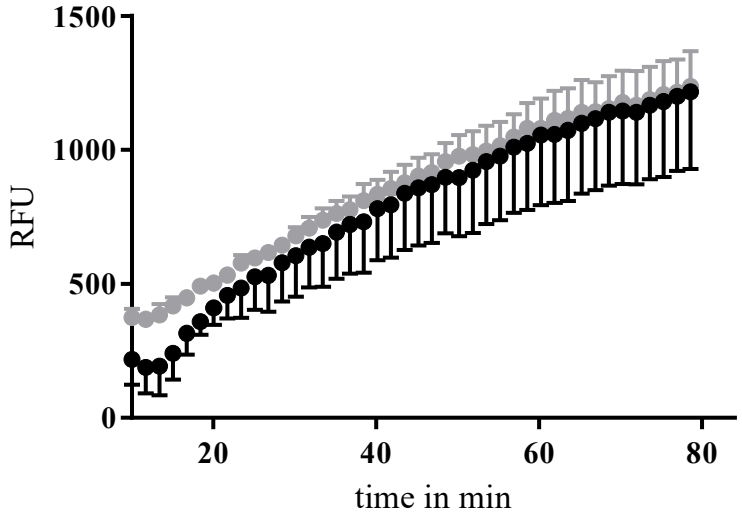

Figure 11 *First 96-well plate test of AG6 rapamycin switch with (black) or without (grey) rapamycin added. Shown are the relative fluorescence units (RFU) that increase over time due to the TVMVp domain cleaving the ANA-peptide substrate. Presence of rapamycin yielded no significant higher ANA-peptide turnover. Error bars represent standard deviation of triplicates.*

The assay was optimized by Anastasia Weyrich during her Master thesis. In particular, the addition of 5 mM EDTA in the final assay buffer proved to be important to prevent unspecific cleavage of the assay substrate ANA-peptide. Moreover, the usage of modified minimal auto-induction medium N-5052 simplified the overall workflow.

A figure with plotted RFU/min slopes is given in the supplement (Sup Fig 1), while the library lysate screening results are summarized in Table 11. Among 233 screened variants, about 30 % showed higher protease activity by the addition of rapamycin. About 6 % showed very little basal protease activity and were denoted as “tight”. In Figure 12, example traces for selected variants are shown. It must be emphasized that the library has a high plasticity (Sup Fig 2), ranging from variants with poor inducibility to very powerful rapamycin switches, and that this plasticity is generated solely by the domain-connecting linkers.

Table 11 *Summary of rapamycin-switch library screening*

Parameter	*Quantity*
Possible variants	735
Screened colonies	233
Religands	47
Inducible variants	69
→ Thereof: tight	14
Sequenced variants	35

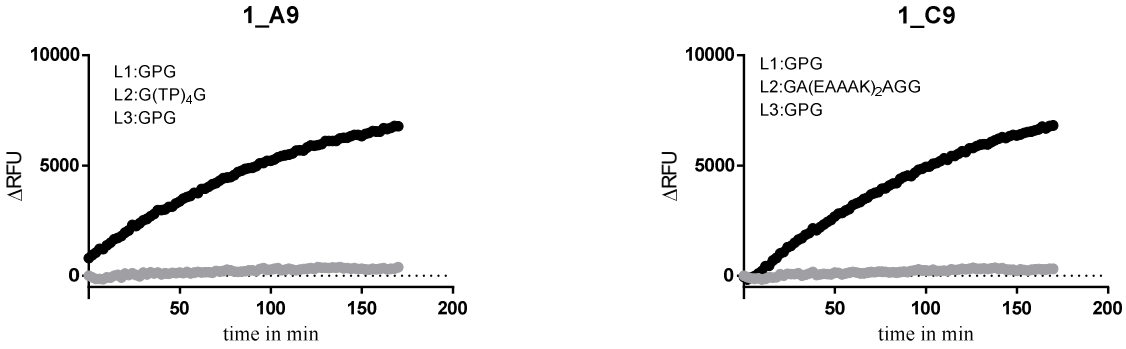

Figure 12 *Example traces of lysate screening experiments. Shown are ANA-peptide conversions for switches 1_A9 and 1_C9 respectively in absence (grey) or presence (black) of 5 µM rapamycin. Linkers of the respective switches are indicated as insets. Values were normalized to negative control. Similar figures were included in the publication [123].*

The first library contained a considerable number of pFLinkC-XE religands which could be identified prior to screening due to the expression of mNeongreen-$(GGS)_2$-CfaN (Figure 13). The high number might be caused by insufficient time of enzymatic cleavage in the last cloning step or lack of rSAP activity.

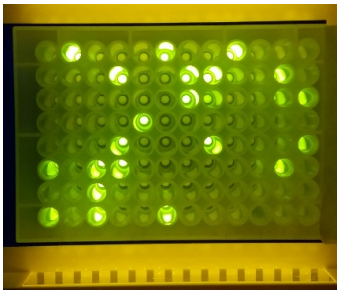

Figure 13 *96-deep well plate of screening #1 under blue light after centrifugation. Religands of pFLink-XE could be identified as they expressed the fluorescent control protein mNeongreen-$(GGS)_2$-CfaN.*

Selected inducible variants were expressed in larger scale, purified *via* StrepTagII and measured at defined concentrations. For some proteins, the deviations from the lysate assay were considerable (see 3-A1 in Table 12), however, the tendency of the lysate screening could be reproduced for all purified proteins. Reasons for deviations may be caused as well by the lysate screening assay (cell growth in deep well plates, expression and cell lysis variations), but also

by instability of the large multi-domain proteins during purification, as can be seen for 3_F3 in Figure 14.

Table 12 *Summary of FKBP-library screening experiments; comparison of lysate screening and purified screening results. Maximum x-fold induction was calculated from the initial linear range. The initial linear range was variant-specifically chosen and dependent on the moment the fluorescence signal exceeded background noise.*

Variant	L1	L2	L3	x-fold induction (Lysates)	x-fold induction (Purified)
1_A9	GPG	$G(TP)_4G$	GPG	> 80	150.6 ± 5.1
2_B3	GPG	$G(P)_7G$	GPG	72.5 ± 13.7	87.1 ± 6.0
3_F6	GPPPG	$G(TP)_4G$	G	68.3 ± 17.0	69.7 ± 8.9
3_A1	GPPPG	GPPPG	GG	64.4 ± 21.0	18.7 ± 1.0
1_C9	GPG	$GGA(EAAAK)_2AGG$	GSPAG	> 60	36.9 ± 0.7
3_C9	GPG	GGG	GSPAG	53.9 ± 9.2	
2_E7	GPG	$G(P)_7G$	G	41.0 ± 6.6	
3_F3	GPG	GSPAG	GGG	38.5 ± 7.5	
3_H4	GPG	$(GGS)_4GSG$	GPPPG	21.6 ± 3.4	
2_G2	GPPPG	$GGA(EAAAK)_2AGG$	GG	16.8 ± 1.9	
2_E3	GSPAG	$GGA(EAAAK)_2AGG$	GSPAG	11.9 ± 0.9	
1_A7	GPPPG	GG	GGSG	5.0 ± 0.4	
2_G1	GSPAG	$GGA(EAAAK)_2AGG$	GPPPG	4.2 ± 0.5	
1_A8	GGSG	GPG	GGSG	4.1 ± 0.5	
1_D11	GPPPG	GG	GSPAG	3.6 ± 0.5	
1_C11	GPPPG	$(GGS)_4GSG$	GSPAG	3.6 ± 0.3	
1_D7	GSPAG	GGASPAAPAPAG	GSPAG	3.2 ± 0.1	
1_D10	GPPPG	GPG	GSPAG	3.0 ± 0.2	
3_A3	GSPAG	GGSG	GPPPG	2.8 ± 0.4	
3_D6	GSPAG	GGG	GPPPG	2.6 ± 0.1	
1_D4	GPPPG	GPG	GSPAG	2.6 ± 0.1	
1_E8	GSPAG	$(GGS)_4GSG$	G	2.4 ± 0.2	

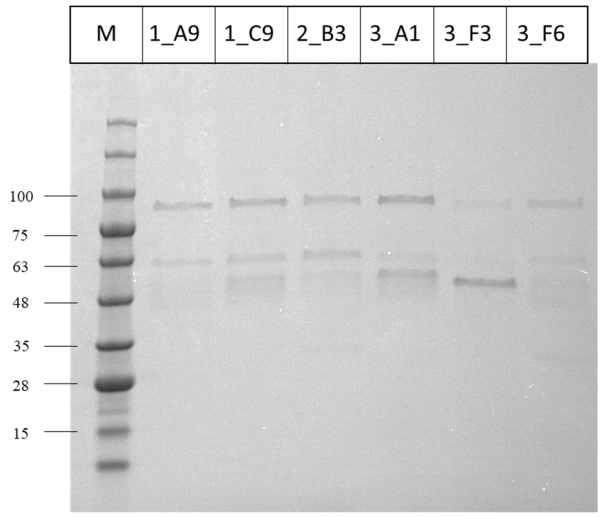

Figure 14 *SDS-PAGE of six purified rapamycin-switches with expected sizes of about 95 kDa. Bands at 48-63 kDa indicate instability of the large multi-domain proteins, in particular in the case of 3_F3. M: Marker BlueStar Prestained (Nippon Genetics). Size in kDa.*

An important question concerns the reproducibility of the lysate screening results. When LB medium was used and manual induction was performed, the data showed the same trend as in the original screening but nonetheless differed considerably (Table 13). This once again underlines the variance caused by using lysozyme as high-throughput screening lysis reagent and *E. coli* in general, and shows the importance of additional characterization of single variants in purified form. However, the assay is sufficient to identify well performing switches that can be characterized in detail in purified form.

Table 13 *Lysate screening reproduction results. Error calculated using Gaussian error propagation. In contrast to the induction ratios in Table 12, the linear fit considered all data points from the range 10-40 min objectively.*

Variant	x-fold induction n=2	Variant	x-fold induction n=2
1_A9	21.3 ± 1.4	2_E3	5.1 ± 0.2
2_B3	18.2 ± 1.1	1_D7	4.9 ± 0.1
2_E7	17.8 ± 0.9	3_F6	4.9 ± 0.2
3_A3	14.9 ± 12.3	2_G2	4.1 ± 0.3
1_C9	11.9 ± 0.6	1_D11	4.1 ± 0.3
3_F3	10.4 ± 0.3	1_A7	4.1 ± 0.3
3_H4	8.9 ± 0.6	2_G1	3.8 ± 0.1
1_C11	8.8 ± 1.7	1_E7	3.2 ± 0.1
3_C9	8.0 ± 0.6	1_A8	2.9 ± 0.2
3_A1	7.0 ± 0.8	3_D6	2.6 ± 0.1
1_E8	5.5 ± 0.2	1_D4	2.4 ± 0.1
1_D10	5.2 ± 0.3		

3.6 Biophysical Characterization of Switch Behaviour

The switch variants with the highest fold-induction were examined closer. Sequencing identified a recurring GPG linker at the position L1 directly downstream of AI_{TVMV}. Combined with the observation that those switches were exceptionally repressed in the OFF-state, this lead to the assumption that the GPG motif serves as an elongation of AI_{TVMV}, improving its affinity towards TVMVp.

To test this hypothesis, AI_{TVMV} was ordered as a peptide along with three C-terminal elongated variants (+G, +GP, +GPG). These peptides were titrated against 200 nM SH3-TVMVp (a TVMVp variant with an N-terminal SH3-domain) in presence of 5 μM ANA-peptide substrate. Titration curves were fitted by a non-linear regression per

$$V = V_{max} \cdot \frac{c_s}{c_s + K_M \cdot (1 + \frac{c_i}{1 + K_i})} \quad (1)$$

which describes the enzyme kinetics for a competitive inhibitor [22] to obtain K_i values, where V (=Y) denotes the reaction velocity, V_{max} the maximum reaction velocity, c_s the substrate concentration and c_i (=X) the inhibitor concentration. K_M was fixed at 65 μM as in [5].

The K_i of unmodified AI_{TVMV} (REYVRFAP) was determined as 133 μM ± 12 μM (Sup Fig 3), a value that approximates the originally reported K_i of 196 μM ± 26 μM [5]. For AI_{TVMV}+G, the K_i was in the same order of magnitude (186 μM ± 15 μM). However, AI_{TVMV}+GP and

AI_{TVMV}+GPG showed a K_i of 4.5 μM ± 0.3 μM and 3.0 μM ± 0.2 μM, respectively (Figure 15). Thus, the elongation of AI_{TVMV} by these two residues improves its affinity towards TVMVp by nearly two orders of magnitude. This explains the strongly repressed OFF-state and the high fold-induction. This phenomenon may be caused by an additional interface between the motif and the protease, generated by the additional proline. In this regard, a molecular docking simulation and/or a crystallographic study could elucidate the underlying principle and could facilitate development of future autoinhibitory modules for other proteases.

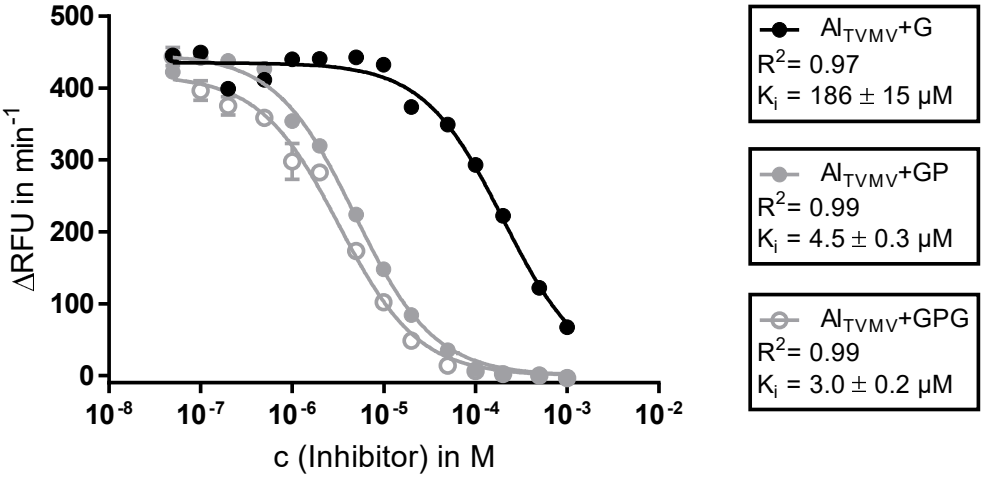

Figure 15 *AI-peptide inhibition. SH3-TVMVp (200 nM) was titrated with three different AI-peptides. The legend depicts the R^2 values of the corresponding fits together with the determined K_is. Standard errors derive from duplicate measurements. A similar figure was included in the publication [123].*

3.7 Apparent Rapamycin Affinity

The tested multidomain switches comprise two separate modules: The receptor module (FKBP/FRB) and the actuator module (AI_{TVMV}/TVMVp). Banaszynski *et al.* have thoroughly investigated the affinities involved in the assembly of the ternary FKBP/FRB/rapamycin complex [205]. Briefly, rapamycin first binds with high affinity to FKBP (K_D = 0.2 nM), together forming a complex that is then bound by FRB (K_D = 12 nM). In case of the large multidomain switch, this binding induces large conformational changes throughout the protein backbone. However, the biophysical forces behind this reorganization work against the stable complex of the actuator module. As shown in the previous paragraph, AI_{TVMV}+GPG for instance is bound by TVMVp with an affinity in the low μM range.

The phenomenon of this "conformational conflict" was observed when switch 2_B3 was titrated with rapamycin. The initial reaction rates were plotted as a function of rapamycin concentration and an apparent K_D of 20.7 ± 2.6 nM was determined (Figure 16). Importantly, the data had to be fitted to a quadratic equation (Sup Text 1) because rapamycin is depleted from the system during the reaction due to its high affinity towards FKBP [205,207].

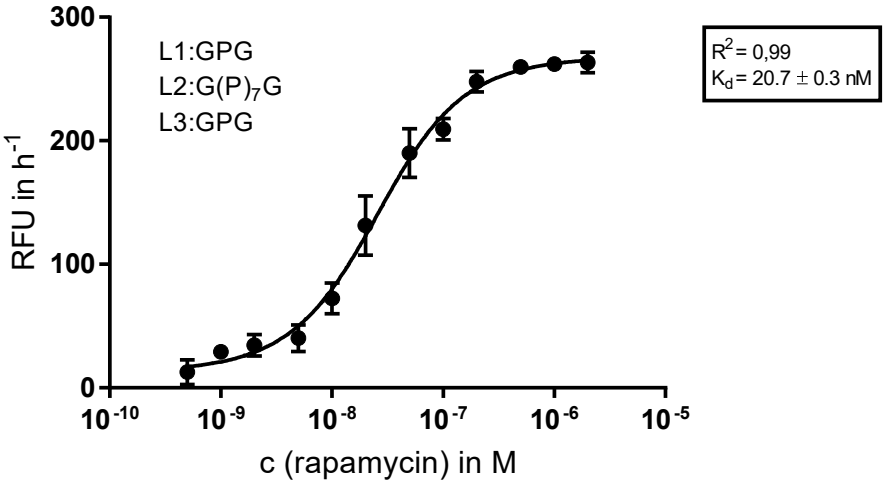

Figure 16 *Titration of 10 nM 2_B3 switch with rapamycin in presence of 5 μM ANA-peptide revealed an apparent K_D of 20.7 ± 0.3 nM for the rapamycin-switch interaction. Linkers of 2_B3 are indicated as inset. Standard errors derive from duplicate measurements. A similar figure was included in the publication [123].*

Thus, binding of rapamycin by the switch is *seemingly* twice as weak as FRB binding to the FKBP/rapamycin complex, which is the rate limiting step in the original receptor module. To investigate if the switch architecture constrains FKBP mobility and thereby weakens rapamycin recognition, a reverse isothermal titration calorimetry (ITC) experiment was performed. 2_B3 fusion protein at 68 μM was dissolved stepwise into 10 μM rapamycin solution, and the K_D along with the molar binding enthalpy ΔH were calculated using the MicroCal Analysis software. For N=1 binding pocket, values were determined as K_D = 0.86 ± 1.25 nM and ΔH = -95.7 ± 3.82 kJ/mol (ΔG = -51.8 kJ/mol). This underlines that the binding of rapamycin by FKBP is not hampered by the switch architecture. The discrepancy between the obtained ΔH and literature values for FKBP/rapamycin binding (ΔH ≈ -60 kJ/mol [208]) is most likely caused by the conformational reorganization of the fusion protein backbone or differences in the buffers used.

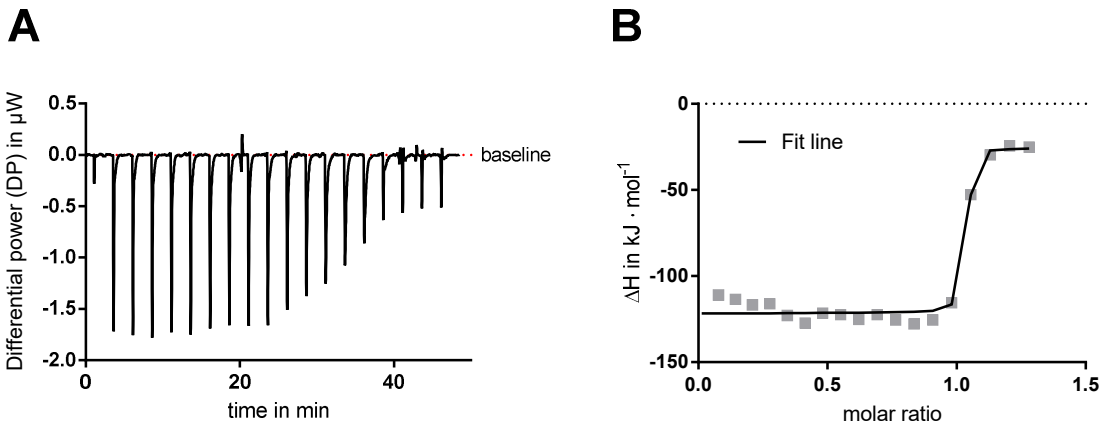

Figure 17 *Reverse ITC measurement of rapamycin-switch 2_B3. A) Raw data trace with adjusted baseline. B) ΔH as a function of molar ratio, calculated in MicroCal Analysis. I acknowledge Christian Meyners for support during the experiment and analysis.*

3.8 ePDZ-b1/FN3 Protease Switch

To prove the modular principle of the iFLinkC method and to develop a single chain protease switch with a second receptor module, FN3 and ePDZ-b1 were employed. As FN3 domains can be evolved to bind various peptide targets [204], the PDZ-FN3 affinity clamps constitute highly modular receptors, rendering them useful for the development of synthetic protein switches that react to a variety of peptide inputs.

In contrast to the known switch TVMVp^{E217}-PDZ^{G37}-FN3^{GPG}-AI$_{TVMV}$ [5], the orientation of AI$_{TVMV}$ and TVMVp was reversed in the design of this work. The orientation of PDZ and FN3 was maintained for structural reasons, as in reverse order, the affinity clamp would not be able to form [90,204]. Thus, the overall structure of the library is MBP-TEV$_{site}$-strep-^{SGG}-AI$_{TVMV}$-^{L1}-ePDZ-b1-^{L2}-FN3-^{L3}-TVMVp.

The same linker space was screened as in the rapamycin switch library. Seven short linkers were allowed at positions L1 and L3 and 15 linkers with up to 16 *aa* at position L2. Due to a misinterpretation of the protein sequences [5], the FN3 domain started with an additional glycine, meaning that in all screens, L2 was one *aa* longer than intended (for instance, GPGG instead of GPG).

Although twice as many colonies were screened as in the rapamycin library, no reproducibly inducible variant was found. Strikingly however, in 156 cases the addition of the peptide ligand led to a repression of protease activity (Table 14). In 17 cases, the activity was repressed down to 25 % of the initial value without ligand, meaning a 4-fold repression. Example ANA-peptide conversion traces of purified repressible switches are shown in Figure 18, while details of the 10 sequenced variants are given in Table 15.

In a second library screening performed by Luca Brenker during his bachelor thesis, another 178+206 variants were tested with slight modifications regarding the linker space. Variants that seemed inducible did not yield the same result when tested again or in purified form.

Table 14 *Screening results of ePDZ-b1/FN3 protease switch library.*

Parameter	***Quantity***
Possible variants	735
Screened colonies	467
Religands	0
Repressible variants	156
Thereof: up to <0.25 repressible	17
Sequenced variants	10

Table 15 *Summary of ePDZ-b1/FN3-library screening experiments; comparison of lysate screening and purified screening results. Maximum x-fold induction was calculated from the initial linear range. The initial linear range was variant-specifically chosen and dependent on the moment the fluorescence signal exceeded background noise.*

Variant	L1	L2	L3	x-fold repression (Lysates)	x-fold repression (Purified)
5_H8	GG	GPGG	GG	16.6 ± 9.9	
5_F7	GG	GPGG	GGSG	10.3 ± 2.5	
2_H7	GG	GPGG	GG	7.9 ± 1.2	8.3 ± 1.0
2_A5	GGG	GPGG	GGSG	6.1 ± 1.3	14.3 ± 1.5
5_A12	GG	GPGG	GGG	5.5 ± 1.2	7.6 ± 0.4
2_F6	GGG	GPGG	GGG	5.2 ± 0.3	
5_C6	GGG	GGGG	GGSG	3.4 ± 0.5	

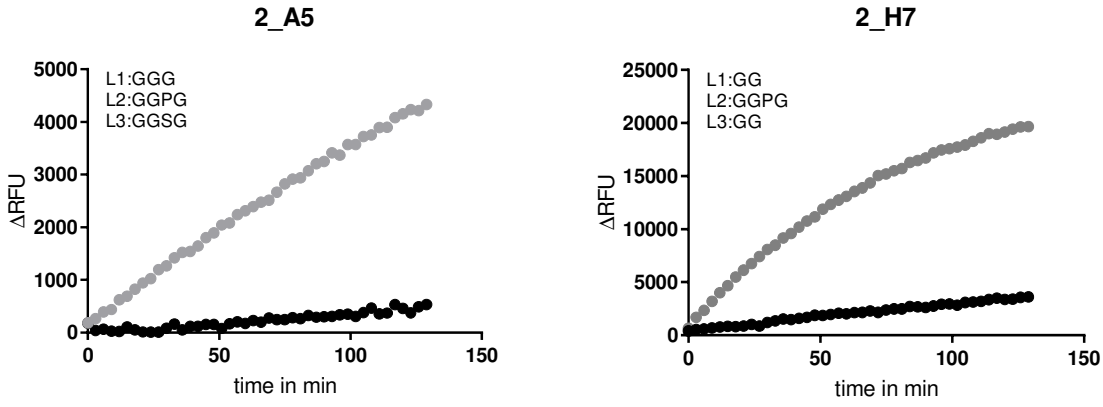

Figure 18 *Example traces of strongly repressible ePDZ-b1/FN3 single chain protease switches. Shown are ANA-peptide conversions by switches 2_A5 and 2_H7 respectively in absence (grey) or presence (black) of peptide ligand. Linkers of the respective switches are indicated as insets. Purified switches were present at 200 nM. Values were normalized to negative control.*

3.9 Effects of N-terminal MBP are negligible

All multidomain-protein switches contain an N-terminal MBP as solubility enhancer that is separated from the switch by a TEV protease site. This large protein may influence the switch behaviour due to surface clashes or constraints on the proteins mobility.

In two independent experiments, of which one was conducted by Anastasia Weyrich, purified rapamycin switches were incubated with or without TEV protease and subsequently assayed with ANA-peptide. For all switches except one (clone V1, AI_{TVMV}-^{GGASPAGG}-FKBP-$^{(GGS)2G}$-FRB-$^{(GGS)2G}$-TVMVp), removal of MBP had neither an effect on activity nor inducibility. For clone V1, MBP removal slightly decreased rapamycin inducibility, however, within the experimental error. Therefore, the stabilization introduced by MBP appears to outweigh possible constraints on mobility of the multidomain architecture.

3.10 Construction of a FRET-based TVMVp Sensor Protein

In all described experiments, commercial ANA-peptide was used as a substrate to assay TVMVp activity. For future applications of TVMVp-switches, however, other substrates must be

considered and developed. As a first alternative for protease activity sensing, a protein FRET-sensor based on the fluorescent proteins YPet and CyPet was devised, with the structure CyPet-FKBP-TVMV$_{site}$-FRB-Ypet. In presence of TVMVp, the protein gets cleaved into CyPet-FKBP and FRB-YPet, resulting in a reduced FRET effect (ex. 415 nm, em. 527 nm). Rapamycin addition restores the FRET effect by reassembly of the architecture *via* FKBP-FRB interaction.

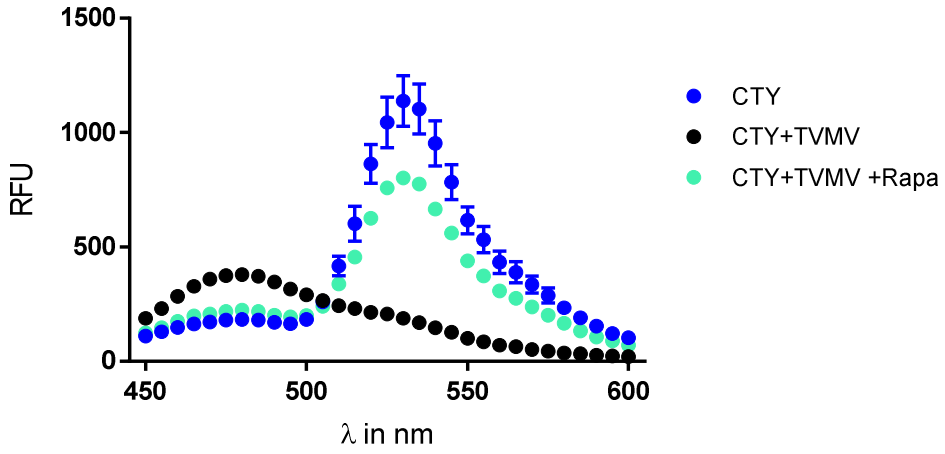

Figure 19 *Validation of FRET-based TVMVp sensor CyPet-FKBP-TVMV$_{site}$-FRB-Ypet (CTY). Shown are emission spectra of 100 nM CTY (dark blue), 100 nM CTY with 500 nM TVMVp (black) and 100 nM cleaved CTY with 100 nM rapamycin (turquoise).*

The sensor was constructed, and the concept successfully verified by Anastasia Weyrich and Lisa Gertig in the scope of a practical course. While the protein is useful for testing TVMVp activity, it was not cleaved by FKBP-FRB-TVMVp-switches. As an experiment with modified FRET-sensors suggested, this is most likely caused by sterical hindrance and/or inaccessibility of the cleavage site or TVMVp active center, respectively. This hypothesis is supported both by a control experiment where TVMVp was not able to cleave CyPet-^{GPGAS}-TVMVsite-^{GGRGSS}-YPet, while it cleaved a sensor with an additional internal FRB domain, CyPet-^{GPGAS}-TVMVsite-^{KLGG}-FRB-^{SGGRGSS}-YPet (cloned by Tim Maier) (Figure 20), and by studies of Anastasia Weyrich on different linkers between TVMV$_{site}$ and the two fluorescent proteins.

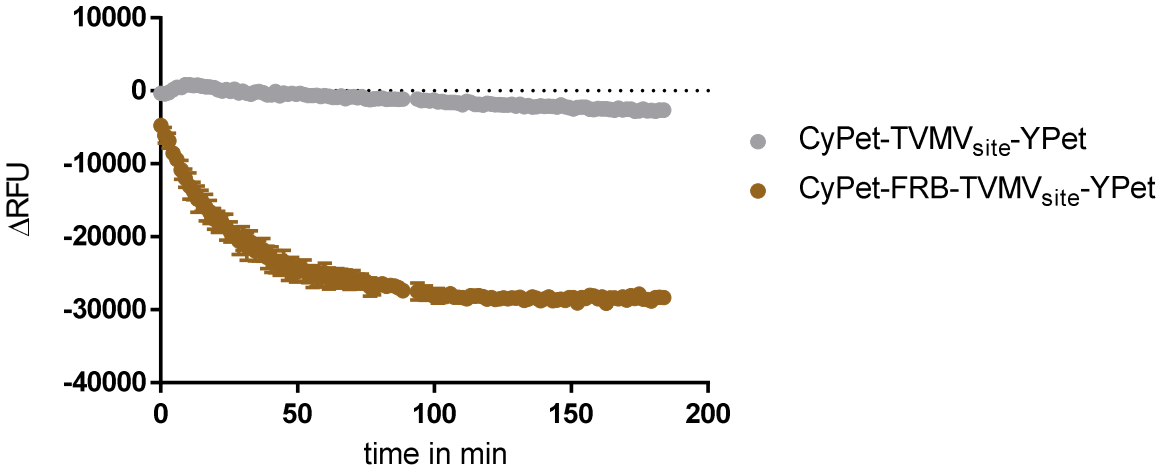

Figure 20 *Cleavage of TVMV$_{site}$ is affected by protein architecture. Shown are the ΔRFU values at 527 nm (extinction: 415 nm) as a function of time. Fluorescent proteins were added at the same concentration.*

3.11 Summary and Discussion

By rational design based on crystal structures and published scaffolds, a rapamycin-inducible protease switch was successfully constructed and validated. Yet, the initial switch showed only marginal inducibility that could only be observed with purified protein and not in *E. coli* lysates (Figure 8, Figure 9). This was attributed to the interdomain linkers, as the domain order was apparently appropriate for transferring rapamycin-induced conformational changes in the FKBP-FRB receptor module to the protease and AI_{TVMV} domain.

While some modular cloning strategies exist to alter a single linker between two domains of a fusion protein (as discussed in section 1.4), none of them allow differentiated and thorough screening of multiple linker positions. Thus, a new method was devised based on classical restriction and ligation, however with the use of specialized Type II S restriction enzymes (section 3.2).

With the developed iFLinkC strategy, a large linker space both in terms of identity and length can be screened in short time [123]. Linkers can be treated as modular building blocks and combined to linker libraries, as they are stored in plasmid backbones that allow construction of desired fusion proteins in an iterative and parallel fashion. Moreover, it is possible to exchange the current minimal linker of one glycine to another amino acid (pair) if the cleavage sites of BsrD1 and Bts1 are adapted, yet, this would lead to a second set of storage and assembly plasmids incompatible to the current pL2 and pFD.

Although the available linker space was not screened to completion, I identified many rapamycin-inducible variants showing x-fold induction of >40 in bacterial lysate assays, some of them performing even better in purified form (Table 12). The discrepancy between lysate screening and purified protein screening can have several reasons. For example, residual *E. coli* proteins may tend to unspecifically interact with the switches in lysate-based experiments, reducing their overall activity. Generally, the proteins mobility – both in terms of diffusion and conformational flexibility – is likely reduced in the highly crowded *in vivo* environment that the lysate adopts [209]. For instance, molecular crowding conditions can even render the reverse reaction of a protease-catalyzed process favourable, leading to an equilibrium shift from proteolysis towards peptide bond synthesis [210]. The occurrence of this phenomenon in the TVMVp switch studies is unlikely, especially as the substrate is small. Nevertheless, it should be considered that the results from less crowded *in vitro* environments resemble the switch activity under idealized conditions.

In the best FKBP-FRB protease switches, the AI_{TVMV} motif was extended by GP *via* the L1 linker. This extension proved to lower the K_i of the autoinhibitory motif more than one order of magnitude (Figure 15), leading to a highly repressed OFF-state which in turn explains the high x-fold induction in presence of rapamycin. While the exact reason for the improved inhibition remains uncertain, the findings underline the importance of a tight OFF-state for molecular switches in general.

The second switch library based on a PDZ-FN3 affinity clamp did not yield an inducible variant despite exhaustive screening. This was unexpected, as an inducible single polypeptide TVMVp PDZ-FN3 switch has been published [5]. By comparing the designs of this work and [5], an explanation can be derived. The switch from Stein and Alexandrov was based on an N-terminal protease and a C-terminal AI_{TVMV}, while this respective orientation was reversed in my design to prevent residual protease activity caused by incomplete translation. Moreover, both heavy truncation of L1 between the N-terminal protease and ePDZ-b1 together with a precisely tuned L2 between ePDZ-b1 and FN3 were necessary to yield an inducible variant [5]. Strikingly, the

same domain orientation but different linkers created a repressible variant, comparable to the ones identified here (Table 15). This demonstrates twofold: Firstly, the domain orientation in synthetic protein switches can have fundamental impact on switch behaviour. Secondly, some cases demand very short linkers (like ESG in [5]) or even a direct domain fusion [67].

The TVMV protease served as a potent actuator module in all experiments. While it successfully cleaved the quenched substrate upon activation by an allosteric ligand, the additionally gathered data (Figure 19, Figure 20, also Master thesis Anastasia Weyrich) call for caution. Processing of the relatively small ANA-peptide does not necessarily compare to processing of a TVMVp cleavage motif that is embedded into a larger fusion protein. In the latter case, the cleavage site can be sterically blocked, both by the substrate protein or the protease fusion protein, leading to an apparently reduced catalytical activity. Importantly, these results were all obtained from *in vitro* experiments. The mentioned molecular crowding situation could further impact the potential of protease switches *in vivo*.

Altogether, the results of this study highlight the importance of high-throughput and fractional factorial linker screening approaches. For the tested architecture AI_{TVMV}-^{L1}-ePDZ-b1-^{L2}-FN3-^{L3}-TVMVp, an inducible variant may be found if the lengths of all linkers are screened in a full factorial fashion (e.g. from 1 up to 15). However, there is no guarantee that the chosen domain orientation allows a switch-ON behaviour at all. Yet, the identified repressible PDZ-FN3 protease switches comprise useful tools for multiple applications, for instance programmable protein circuits [51,177] or responsive biohybrid materials [3].

As a perspective, the developed iFLinkC strategy could be applied to screen and characterize unusual linker motifs, like the mentioned $(EAQA)_n$, E/RK helices or even larger “linker domains” (see section 1.1). The large potential of the still not fully explored linker space will allow the construction of powerful synthetic fusion proteins and thus pave the way for novel and improved switches, biosensor scaffolds and alike.

4. Supplement Chapter 2

Sup Table 1 *PCR calculator. All numbers in µl.*

	PCR reactions						
Component	1	2	4	6	8	10	12
DNA template (10-30 ng/µl)	1	2	4	6	8	10	12
Forward Primer (10 µM)	2,5	5	10	15	20	25	30
Reverse Primer (10 µM)	2,5	5	10	15	20	25	30
dNTPs	1	2	4	6	8	10	12
GC buffer	10	20	40	60	80	100	120
ddH_2O	33	66	132	198	264	330	396
Phusion Polymerase	0,5	1	2	3	4	5	6

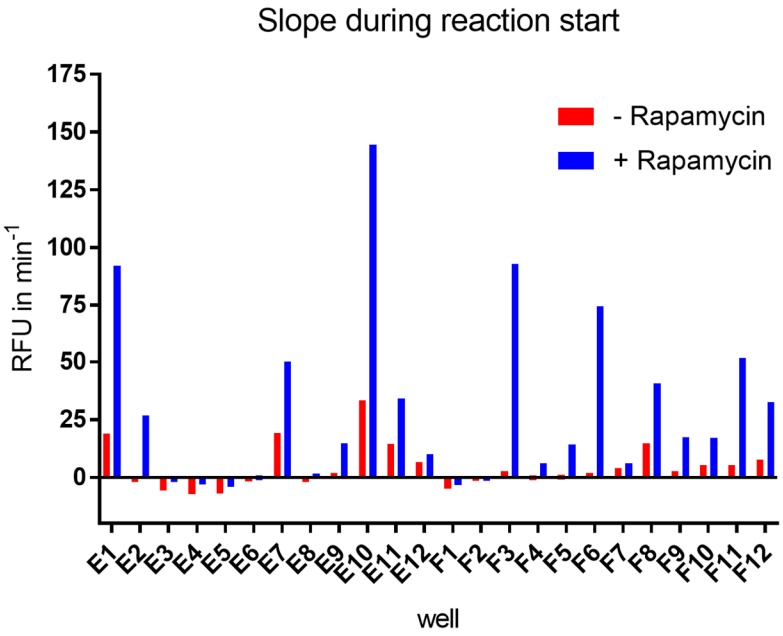

Sup Fig 1 *Example for raw results from high-throughput lysate screening. Shown are the slopes in RFU/min during reaction start (10 min) of rows E and F of a screened plate. Inducible variants with tight basal state like F3 are clearly discriminated from inactive ones like E8.*

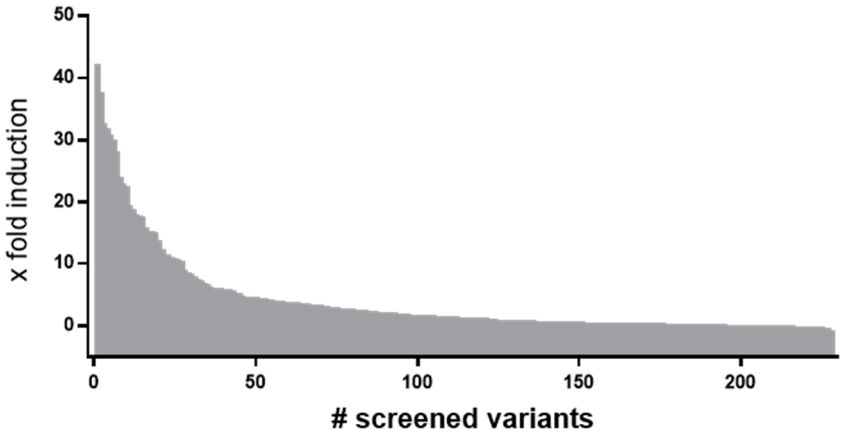

Sup Fig 2 *Global plasticity of the FKBP-FRB rapamycin switch library screening (lysate experiments). The 233 variants that were screened are plotted from the one showing the highest x-fold induction to the lowest.*

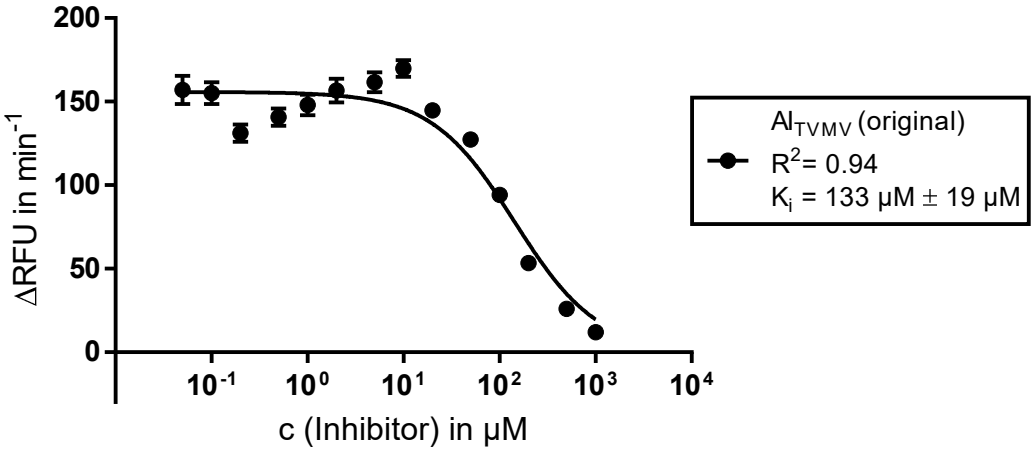

Sup Fig 3 *AI-peptide inhibition. SH3-TVMVp (200 nM) was titrated with REYVRFAP. The legend depicts the R^2 value of the corresponding fit together with the determined K_i. Standard errors derive from duplicate measurements.*

Sup Text 1 *Derivation of the Fit-function applied in Figure 16.*

Symbol	Meaning
v_{max}	Maximal reaction rate
v	Reaction rate
k_{cat}	Turnover number
$[E_T]$	Total enzyme concentration in steady state
K_D	Equilibrium dissociation constant
[ES]	Enzyme-substrate-complex concentration in steady state
[RL]	Receptor-ligand-complex concentration in steady state
[L]	Free ligand concentration in steady state
$[L_T]$	Total ligand concentration in steady state
$[R_T]$	Total receptor concentration in steady state
v_0	Initial reaction rate

The maximal reaction rate of an enzymatic process is defined [22] as

$$v_{max} = k_{cat}\,[E_T],$$

while the actual reaction rate is

$$v = k_{cat}[ES].$$

Combination of both equations gives

$$v = v_{max}\frac{[ES]}{[E_T]} \tag{S1}$$

Assuming that the rate limiting step of the ANA-peptide reaction is the cleavage by the TVMVp domain, [ES] of this reaction equals [RL], the concentration of the receptor-ligand complex build by rapamycin and the switch. Under idealized conditions and with a 1:1 interaction between a single ligand and a single receptor site, [RL] can be expressed [207] as

$$[RL] = \frac{[L][R_T]}{[L] + K_D}$$

However, due to the high affinity of FKBP to rapamycin, free rapamycin is depleted during the reaction, hence the idealized condition $[L] = [L_T]$ is not met. Thus, [RL] has to be written [207] as

$$[RL] = \frac{([R_T] + [L_T] + K_D) - \sqrt{([R_T] + [L_T] + K_D)^2 - 4[R_T][L_T]}}{2} \tag{S2}$$

Considering the initial background activity of the switch in absence of rapamycin, the final fitting function – substituting [ES] with [RL], $[E_T]$ with $[R_T]$ and combining equations (S1) and (S2) – thus reads as

$$v = v_0 + (v_{max} - v_0)\frac{([R_T] + [L_T] + K_D) - \sqrt{([R_T] + [L_T] + K_D)^2 - 4[R_T][L_T]}}{2[R_T]} \quad ,$$

where v is plotted as a function of $[L_T]$ in Figure 16 to determine the apparent K_D of the rapamycin/switch interaction.

Page intentionally left blank

Chapter 3
Investigations on FhuA-based Nanopores

1. Introduction & Background

The molecular switches developed and discussed in the previous chapter could convert environmental inputs into orthogonal signals and reactions. Such conversion is one of the key principles that allow microorganisms to interact with their environment. Receptors in cell membranes forward information from the outside of a cell to its interior, leading to a variety of responses. Generally speaking, compartmentalization of a given volume by a lipid bilayer membrane counts as one of the main features of cellular life [211].

During evolution, cells have developed many strategies to react to environmental inputs. An exceptional example is the alternation of current flow by membrane-anchored proteins. For instance, small ion channels that are embedded in the membranes of axons are responsible for the propagation of an action potential through neurons [22]. The unique properties of transmembrane protein pores have made them great templates for biosensors. These proteins are also named "**nanopores**" [212], although this term is ambiguous as it is also used in solid-state material science [213,214].

Nanopore sensing allows single-molecule analytics in real time, converting complex processes into readily detectable signals [62,215]. When embedded in artificial lipid bilayers, polymer membranes [64,216] or combinations thereof [217], a binding event or a passage of a molecule triggers changes in its conductance, leading to a change in electrical current, blocking frequency or similar [218,219].

As discussed earlier (Chapter 1), one of the most prominent examples is the evolution of the nanopore sequencing technology. The simple concept of DNA or RNA translocation through the aperture of a protein nanopore lead to multiple successful products in point-of-care diagnostics [212,220,221]. Nanopore sensing is however not limited to nucleic acids. Its applications range from characterization of enzyme activities [63,219,222–224], antibodies [225,226] and analytes like toxins [227] to the detection of proteases [63,189,223], peptides [228,229] and even conformational changes of single molecules [230].

For the sake of clarity, I will concentrate on peptide and protein nanopore scaffolds that can be recombinantly produced in microorganisms and are composed of canonical amino acids (*aa*). "Non-natural" nanopore scaffolds that resist easy recombinant production, including gramicidin [231], melittin [232] and peptide nanotubes [233,234] are omitted from this overview. Solid state nanopores and solid/biological chimeras are discussed in Chapter 4.

1.1 Nanopore examples – bottom up

Bottom up nanopore engineering is driven by the aforementioned need of new biosensors, but also by the search for new antibacterial and anticancer compounds [235]. However, *de novo* design of not only nanopores, but integral membrane proteins in general, is challenging due to the complexity of protein folding as well as lipid/protein and protein/protein interactions and interfaces, respectively [236,237].

1.1.1 Antimicrobial peptides

While the potential of antimicrobial peptides in clinical applications is considered high [235], efforts to generate controllable and stable "minimal" nanopores are still hampered by a lack of structure-function relationship understanding [238]. This is intriguing, since artificial, minimal pore forming peptide sequences based on the gramicidin scaffold have been investigated since 1973 [236,239,240]. Today, new active pore-forming peptides are mainly found by high-throughput-screening of peptide libraries [235,241] or with the help of simulations [242]. Yet, it remains obscure to assess how to engineer completely new, stable nanopores out of antimicrobial peptides.

1.1.2 cWza

A strong driving force behind the *de novo* design of nanopores are computational approaches, for example from the Woolfson lab. In cooperation with the Bayley lab, they derived a 35-*aa* consensus peptide sequence from the transmembrane spanning domain D4 of the *E. coli* polysaccharide transporter Wza. This artificial scaffold, named cWza, inserted as a parallel oriented octamer into lipid bilayers. Depending on the applied membrane potential, cWza showed different conductivity states, which the authors proposed to be due to different octamer structures cWza can form in the membrane. It was possible to introduce certain mutations to the scaffold. Put together, these experiments are a successful minimalization approach based on artificial peptides. [243]

1.1.3 Holins

dsDNA bacteriophages that infect gram-negative bacteria lyse their hosts by the help of three protein families: Holins that form "holes" or pores in the inner membrane, endolysins or murein hydrolases that degrade the peptidoglycan layer, and spanins that disrupt the outer membrane [244]. Membrane permeabilization by holins is preceded by their accumulation in the cytoplasm, followed by induction of membrane lesion [244].

Holin engineering was pioneered by Lella and Mahalakshmi in 2016. By reversing nearly the whole 28-*aa* sequence of the first transmembrane domain (TM1) from the mycobacteriophage D29 holin, they created the functional ion-conducting channel rTM1 [245]. Its behaviour could be further altered by small sequence modifications. However, the exact mechanism of pore forming as well as the pore stoichiometry remained unclear. Such data would support further nanopore engineering of holins.

1.2 Nanopore examples – Top down

Engineering of natural existing nanopores is mandatory for achieving a desired function and thus a functional biosensor. The engineering scope can range from very small changes in the protein backbone to complete redesign. For instance, translocation and sensing of analytes is fine-tuned by the addition of charges [228,246–248] or adapters [249–251]. Flexible protein loops outside the membrane lumen may impact the nanopore behaviour [252], however, they can be exploited [186,253,254] or deleted [228,255] to gain desired functionalities. Extreme alterations in the structure of the nanopore itself include enlargement [250,256,257] and diminution [258–261] by mutation, addition or deletion of subunits or beta-strand, respectively. Combinations of nanopores and large sensing domains outside the membrane represent particular challenging tasks [16,262]. In the following, a review of some of the best characterized nanopores to date is given, categorized by their structural identity. This overview is not exhaustive, especially as companies are currently heavily screening and optimizing nanopores [263].

1.2.1 Artificial scaffolds

1.2.1.1 phi29 connector

The phi29 connector protein was the first example for an engineering approach in which a nanopore protein was created from an otherwise not membrane-bound protein [264]. It assembles into a homododecamer with its narrowest constriction 3.6 nm in diameter [265]. Phi29 connector served as a platform for DNA translocation [264] and small molecule sensing [266]. However, phi29 connector does not insert spontaneously into lipid bilayers [265].

1.2.2 Beta-pore-forming toxins

1.2.2.1 α-hemolysin

The concept of nanopore sensing points back to the characterization of the homo-heptameric, beta-pore-forming toxin α-hemolysin (aHL) from the human pathogen *Staphylococcus aureus*. It was originally named after its property to lyse erythrocytes [267]. Since its structure has been solved in 1996 [268], aHL served as a scaffold for countless biosensor concepts [16,56,189,246,249,251,262,269,270] and has been used as a standard pore-forming channel during device development studies [271,272].

In its active heptameric form, aHL has a characteristic mushroom-like shape, with a crown-like outer-membrane part and a transmembrane beta-barrel containing the main constriction (2.6 nm diameter) [265,268]. Experiments with aHL and its rationally designed variants are straightforward, as they are stable and insert spontaneously into lipid bilayers [265,271]. Furthermore, aHL can be precisely genetically engineered to recognized diverse target molecules [56,189]. Nevertheless, aHL has limitations. Purification of heteroheptamers is laborious [16,262] and the relatively narrow constriction of 2.6 nm limits sensing applications based on translocation.

1.2.2.2 Aerolysin

Aerolysin is a beta-pore-forming toxin from *Aeromonas hydrophila* and, similar to aHL, forms heptameric pores [248,273]. The 3D structure of its active pore complex by means of Cryo-EM shows a channel with a constriction of 10-17 Å [248,273]. When compared to aHL, aerolysin

offers the advantage of a broad cap that does not block the transmembrane pore like the crown/vestibule domain of aHL [227], however, the channel is considerably longer (10 nm compared to aHLs 8.5 nm) and its interior is largely charged [248,273].

Although lipid bilayer experiments with aerolysin date back to 1990 [274], engineering efforts regarding this scaffold are still young, owed to the fact that its high resolution structure was solved only in 2016 – 20 years after that of aHL [273]. In a study where the "blank" aerolysin pore has been used to sense peptide translocation, it was demonstrated that the pore is relatively insensitive towards serum components [227]. Recently, rational design of aerolysin allowed investigations about selectivity and translocation processes, suggesting that aerolysin will emerge as a tuneable biosensor scaffold [248,275].

1.2.3 Alpha-pore-forming toxins

1.2.3.1 Cytolysin A

Among the largest protein nanopores characterized to date is the dodecameric alpha-pore-forming toxin ClyA found in *E. coli* and *Salmonella entera* strains [276,277]. Its structure was solved in 2009 [277]. One ClyA subunit – mainly a-helical – has a size of about 34 kDa and undergoes extreme structural changes when assembling into pore complexes [276]. The pore-forming homododecamer forms a hollow cylinder sitting on the lipid membrane, with a diameter of 35 Å at the narrowest constriction [276]. As aHL, ClyA has been used to probe new membrane-based devices [278].

Proteins larger than 20 kDa can be electrophoretically trapped inside the ClyA lumen [250,257,279]. This phenomenon has been used to analyse protein interaction and analyte recognition at a single-molecule level [230,280,281]. A directed evolution approach has led to ClyA variants that assemble into nanopores of varying diameter, thus broadening the possibilities of analyte recognition and characterization [257]. Recent progress in understanding its assembly and pore-forming mechanism [282] paves the way to improved rational design of ClyA.

1.2.3.2 Fragaceatoxin C

The crystal structure of FraC, an alpha-pore-forming toxin produced by sea anemones, was published in 2015 [283], yet its conical shape and beneficial single constriction of 16 Å has already drawn the attention of nanopore engineers. FraC monomers consist of two parts, an a-helical transmembrane domain at the N-terminus in combination with a C-terminal, beta-sheet rich domain called the beta-core [283]. They assemble into pore-forming homooctamers [283]. Like ClyA, FraC has been engineered through directed evolution approaches. Its potential applications range from DNA analysis [247] to peptide length analysis [261] and protein-fingerprinting [229].

1.2.4 Inner membrane proteins

1.2.4.1 MspA

The monomeric porin A of the gram-positive *Mycobacterium smegmatis* (MspA) was chosen as candidate nanopore scaffold for DNA sequencing mainly due to its geometry [284]. With a central constriction of about 1 nm length and width it forms the perfect aperture for ssDNA, and in contrast to aHL it lacks any additional crown-like constriction. MspA is extremely robust

to environmental conditions and amenable to genetic engineering [284], and evolved as one of the most promising DNA sequencing nanopore scaffolds [285].

1.2.5 Outer membrane proteins

1.2.5.1 Interlude – Outer membrane protein biogenesis

In gram-negative bacteria like *E. coli*, the biogenesis – simply put: the journey – of outer membrane proteins (Omps) to their target is a highly complex process [286]. It involves translocation of the peptide chain over the inner membrane, chaperone-assisted transport through the periplasm, and assembly of the protein into the asymmetric bilayer that forms the outer membrane [286].

Firstly, the unstructured Omp peptide chain is transported actively across the inner membrane by the general secretory system (Sec translocon). The SecYEG complex serves as the translocation channel, and translocation is mediated by the ATPase SecA as well as the proton motive force [287,288]. Omp recognition and targeting is mediated by an N-terminal signal sequence that gets cleaved off during this process [288–290]. These particular signal sequences contain three distinct motifs but are otherwise not conserved [289].

Following translocation, chaperone proteins like SurA and Skp bind the Omp chain in the periplasm, by this means creating a dynamic chaperone-substrate ensemble that prevents misfolding [291–293] [320–322]. Finally, the Omp folds into its correct structure in the outer membrane, heavily assisted by the beta-barrel assembly machinery (BAM)-complex [286,294]. Similar to the N-terminal signal sequence important for SecYEG translocation, a species-specific motif at the C-terminus allows the Omp to be recruited by the BAM-complex [294–296].

1.2.5.2 OmpG

Multiple structures of the monomeric porin OmpG from *E. coli* were described in 2006 and 2007, revealing a 14-stranded beta-barrel with an inner constriction of 12x15 Å [297]. Pioneered by the work from Min Chen, who became a leading expert on this scaffold, and Syma Khalid [298], the OmpG architecture was successively optimized and engineered into a quiet and stable nanopore [252,297,298]. To date, OmpG has proven a reliable biosensor for small molecules [186,298], antibodies [186,225] and protease activity [63]. OmpG has been amenable to large changes in its structure, like minimalization [260] and re-combination [299].

In contrast to other nanopores, analyte sensing is translocation-independent and identified by changes in current fluctuation (gating) events [186]. Therefore, the impact of the beta-sheet connecting loops has been investigated in detail experimentally and *in silico* [252,297,300].

1.2.5.3 FhuA

FhuA and its derivative scaffolds are discussed in detail in the following section.

1.3 FhuA based nanopores

1.3.1 The FhuA scaffold

FhuA belongs to one of the first studied membrane proteins, dating back to experiments from Max Delbrück in the 1940ies [301]. Until 1980, it was known as the TonA protein, after phage T1 (*T one*) that exploits the protein to infect *E. coli*, while the "A" stands for a specific phenotype [301]. In 1980 its name was changed to FhuA, as it is involved in *f*erric *h*ydroxamate *u*ptake [302]. Specifically, it is responsible for siderophore uptake in general and serves as a target and/or receptor for many phages (e.g., T1, T5 and φ80), toxins (Colicin M) and some antibiotics [301,303].

FhuA is located in the outer membrane of the gram-negative *E. coli*. Two crystal structures of natural FhuA solved in 1998 presented a barrel-shaped protein consisting of 22 antiparallel beta-sheets with surface-exposed connecting loops and an N-terminal, globular cork (or plug) domain filling the barrel [304,305]. With its dimensions of 69 Å height, 46 x 39 Å cross section, 714 *aa* and about 79 kDa (without the signal sequence), FhuA ranks among the largest known beta-barrel proteins [304,306]. In *E. coli*, native FhuA (wtFhuA) is expressed with an N-terminal 33-*aa* signal sequence (+sig) that ensures its export from the cytoplasm to the periplasm via the SEC pathway (section 1.2.5.1). During further biogenesis, this signal sequence is cleaved off. The hydrophobic membrane region has a height of 25 Å [306].

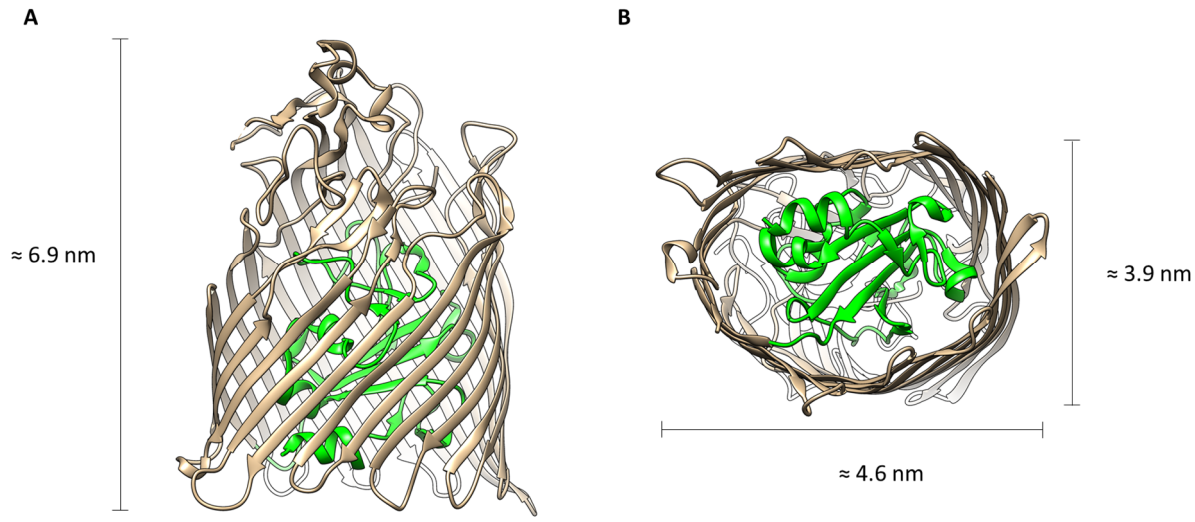

Figure 21 *Ribbon representation of the wtFhuA structure. A: Side view; B: View from the periplasmic side. The β-barrel is depicted in beige, the cork domain is highlighted in green. Images were generated using UCSF Chimera [120] and PDB file 4CU4 [307].*

Ligand interaction and translocation is mediated by an interface between the loops, the barrel itself and the cork [304,308]. The cork domain shares a large inner surface with the barrel [303,304]. During ligand uptake, the cork is rearranged and pulled out of the barrel in a concerted motion involving the action of TonB, a key cytoplasmic membrane-anchored protein [309–313]. The relation between the FhuA cork and barrel domain deserves a special remark, as they can reconstitute into functional FhuA when expressed separately [314,315]. However, the cork itself is unstructured and fairly unstable in solution [315,316]. Moreover, MD

simulations revealed that the cork is not important for stabilizing the beta-barrel architecture, in contrast to the hydrogen bond network formed by neighbouring beta-sheets [317,318].

Artificial bilayer (black lipid membrane, BLM) experiments with wtFhuA date back to 1993, even before its 3D structure was solved [319]. wtFhuA does not show channel activity when inserted into artificial lipid bilayers unless a ligand is added [320] or the protein is stressed by urea [312,315]. However, deletion of the cork domain as well as deletion of certain loops transform FhuA into an ion-conducting nanopore. While deletion of the cork domain alone is not sufficient to create stable channels in artificial bilayers [321], additional deletion of loop residues leads to stable channels with conductance between 1.5 and 3 nS in 1 M KCl [319,322].

There are diverging opinions regarding the tendency of FhuA and its variants to insert spontaneously into artificial lipid bilayers. While the Finkelstein group states that an osmotic gradient is important for proper FhuA insertion[1] [312,315], experiments by the Braun [319,322] and Movileanu [255,323] groups claim the insertion process to be spontaneous. This contradiction might result from different purification protocols, or – even more likely – from different FhuA scaffolds used. For instance, the Movileanu group demonstrated evidence that their variant ΔcΔ5L always inserts with the periplasmic loops first [226,323,324].

1.3.2 FhuA ΔcΔ5L

The Movileanu group successively transformed FhuA into a quiet nanopore scaffold. They deleted the cork and replaced loops 3, 4, 5, 10 and 11 with a short, flexible 5 *aa* motifs, creating the FhuA ΔcΔ5L variant as a result [255,323] (mislabelled ΔcΔ4L in the original publications according to [228]). Since then, this engineered nanopore scaffold has been employed in various membrane protein investigations and biosensing studies [226,228,324–327].

As a nanopore scaffold, ΔcΔ5L offers reasonable advantages: It is monomeric and stable, has a quiet electric signature with high open probability and an exceptional high conductance – leading to a favourable signal-to-noise ratio [228,255,323]. Its size is 44 x 31 Å, with internal average dimensions of 26 x 39 Å [323]. The interior channel walls of ΔcΔ5L are mainly acidic, hence the pore is cation-selective [228,255,323]. Although the N-terminal 33-*aa* Omp signal sequence is still present in ΔcΔ5L, it was claimed that it does not influence the open state of the nanopore to a relevant degree [228].

1.3.3 Other FhuA scaffolds

ΔcΔ5L is not the only FhuA scaffold constructed by the Movileanu group. Wolfe and colleagues created ΔcΔ5L-25N and dcd7L-30N to render the scaffold weakly anion-selective, without negative effects on stability and other biophysical properties [228]. In their nomenclature, 25N and 30N correspond to the numbers of charge neutralising mutations in the ΔcΔ5L scaffold. In follow-up studies, Thakur and colleagues created $H_6[PA]_3$FhuA, which is basically ΔcΔ5L with a 6xHis tag and a rigid linker at the N-terminus instead of the 33-*aa* Omp signal sequence [226]. $H_6[PA]_3$FhuA was used to investigate antibody binding at the single molecule level [226]. The minimal scaffold, tagless (TL or t)-FhuA, was characterized in detail and served as a platform for additional biosensor constructs (Table 16) [226,324,327].

[1] although they did not use wtFhuA but D336C FhuA, which they claimed to behave identical to wtFhuA, referencing [313]

The studies from the Movileanu group underline that ΔcΔ5L and TL-FhuA are amenable for protein engineering. Furthermore, they claimed that purified and denatured FhuA scaffolds can easily be refolded into functional beta-barrels via rapid dilution into detergent solutions [255,325]. Other variants constructed by the Schwaneberg group, for instance FhuA Δ1-160 variants with increased pore size [328] are not conceptualized as stochastic biosensors but as improved catalysts for organic chemistry [306,329] and chiral separators [330].

Table 16 *Compilation of studies that successfully used FhuA variants as biosensors.*

FhuA variant	Analyte / Event detection	Publications
TL-FhuA	Barstar (RNase barnase inhibitor)	[324,327]
TL-FhuA	Anti-His antibody	[226]
ΔcΔ5L	Positively charged polypeptide	[228,323]
ΔcΔ5L	Interaction between HIV-1 Nucleocapsid NCp7 and DNA aptamer	[323]
ΔcΔ5L	IgG digestion by pepsin	[323]
FhuA Δ1-160 variants with increased pore size	PEG derivates	[328]

1.4 Interlude – Addressing Bilayer Instability

As outlined, transmembrane proteins are promising biosensor scaffolds due to their excellent specificity. Yet, their dependence on lipid bilayers is a drawback regarding their incorporation in miniaturized sensing devices, as lipid bilayers are dynamic and limited in their electrical, mechanical and temporal stability [217]. Thus, alternatives for and stabilized versions of lipid bilayers have been developed. For instance, lipid bilayers tethered to a surface *via* long aliphatic linkers show better stability and storability [331]. Other approaches include photo-polymerization [217,332], gel encapsulation [271], scaffolding *via* actin-filaments [333], substitution of the lipid bilayer with polymers [64] and alternative electrolytes [270].

A promising yet challenging concept is the combination of lipid-embedded biological nanopores with solid-state nanopores (SSNs). Since early studies with small biological channels and polymer membranes [334], platforms for highly parallelized membrane protein characterization have been realized [335]. It remains to be seen if the fabrication and readout process can be further optimized to enable construction of reliable point-of-care devices.

1.5 Perspectives

The success of nanopore sequencing underlines the potential of stochastic sensing. Researchers continue to find and characterize whole new nanopore families, for example the actinoporins [336]. New nanopore scaffolds continue to emerge, both via the top-down and bottom-up approaches, that will ultimately lead to improved design for miniaturized devices.

During my thesis, I focused on the FhuA ΔcΔ5L scaffold from the Movileanu group. Firstly, the published purification pipeline was reproduced and applied to ΔcΔ5L variants carrying terminal peptide tags. Following the rationale of modularity, these responsive tags were conceptualized

as recruiting and attachment points for specific secondary protein receptors. By this strategy, a set of novel stochastic sensors was envisioned based on the robust transmembrane scaffold ΔcΔ5L. Two responsive tags were tested: SnoopTag (described in section 3.2.2, Chapter 1) and SmBiT86. SnoopTag showed the best performance and allowed irreversible capturing of a SnoopCatcher fusion protein. A third tag, SpyTag, was tested by Sebastian Schaupp during his Master Thesis, but respective ΔcΔ5L variants inserted very poorly into lipid bilayers, if at all.

2. Methods

Standard methods are described in section 2.1, Chapter 2.

2.1 Purification of soluble proteins

LgBiT and SnoopCatcher-NB_{GFP} were purified *via* their respective StrepTagII. In case of LgBiT, *E. coli* BL21(DE3) were transformed with the corresponding pET32-Strep-LgBiT plasmid. An overnight culture was used to inoculate 1.5 l LB medium to OD_{600}=0.1. At OD_{600}=0.4, 0.5 mM IPTG (final concentration) was added to induce expression. Expression was performed for 4 h at 37 °C. In case of SnoopCatcher-NB_{GFP}, an overnight BL21(DE3) culture carrying pET24-SnoopCatcher-^{GGSSG}-NB_{GFP}-strep was used to inoculate 2x 1 l LB medium to OD_{600}=0.1. At OD_{600}=0.48, 0.5 mM IPTG was added to induce expression. Expression was performed for 16 h at 24 °C. Further downstream purification was the same as described in section 2.6, Chapter 2, with the exception that KCl was used instead of NaCl for all buffers.

2.2 Purification of insoluble proteins / inclusion bodies

E. coli BL21(DE3)omp8 (kindly provided by Klaus Hantke, Universität Thübingen) [337] or BL21(DE3) cells were transformed with the respective FhuA and ΔcΔ5L variants in pET32 (Table 17). A 100 ml O/N culture was inoculated with a single colony. On the next day, transformed cells were grown at 37 °C in a larger volume (1-2 L) LB +100 μg/ml ampicillin until an OD_{600} of 0.5-0.6 was reached, after which they were induced with 0.5 mM IPTG. After 4 h of expression at 37 °C, cells were harvested via centrifugation and stored at -20 °C. For purification of ΔcΔ5L variants from inclusion bodies, an adapted protocol from Thakur *et al.* [226] was used. Briefly, cells were resuspended in 300 mM KCl, 50 mM Tris-Cl pH=8, 5 mM EDTA, lysed by four passes through an Emulsiflex (Avestin) at 1500-2000 bar and centrifuged at 4000 xg and 4 °C for 20 min. Pellets were washed two times with 300 mM KCl, 50 mM Tris-Cl pH 8, 5 mM EDTA, followed by two washes with 300 mM KCl, 50 mM Tris-Cl pH=8, 5 mM EDTA, 0.5 % (v/v) Triton X-100 and one wash with 50 mM Tris-Cl pH=8. After each wash step, a centrifugation step (11200 xg, 4 °C, 20 min) was performed. Afterwards, the inclusion bodies were dissolved in 500 mM KCl, 50 mM Tris-Cl pH=8, 8 M Urea and incubated for 2 h at room temperature. Aggregates were removed by centrifugation. The remaining supernatant was filtered (0.2 μm) and applied onto a Ni-NTA column equilibrated in 500 mM KCl, 50 mM Tris-Cl pH=8, 8 M Urea. After a 5 CV washing step with the same buffer plus 10 mM Imidazole, protein was eluted over a 10 mM – 200 mM Imidazole gradient in the same buffer. Purified proteins were dialyzed against 5 l of ddH_2O overnight with one buffer exchange, flash-frozen and lyophilized overnight (Alpha 2-4 LD plus, Christ). Sealed, lyophilized samples were stored at 4 °C until refolding.

Table 17 *Relevant plasmid list for FhuA related experiments*

Plasmid	Used for	Acknowledgements
pASK-IBA3-ColicinM(D226A)-sfGFP-strep	Microscopy	
pET24-wtFhuA	Microscopy	
pET32-ΔcΔ5L^{6xHis}	Lipid bilayer studies	
pET32-Strep-LgBiT	Lipid bilayer studies	Constructed by Claudia Kreher
pET32 $^{+sig}$ΔcΔ5L^{6xHis}	Lipid bilayer studies	
pET32 $^{+sig}$ΔcΔ5L-SmBiT86^{6xHis}	Lipid bilayer studies	
pET32 ^{6xHis}SnoopTag-$^{+sig}$ΔcΔ5L	Lipid bilayer studies	Constructed by Sebastian Schaupp
pET32-^{6xHis}SnoopTag-10Link-ΔcΔ5L	Lipid bilayer studies	Constructed by Philipp Kemp and Marco Bechtel
pET32 $^{+sig}$ΔcΔ5L-2Link-SnoopTag^{6xHis}	Lipid bilayer studies	Constructed by Sebastian Schaupp
pET32 $^{+sig}$ΔcΔ5L-10Link-SnoopTag^{6xHis}	Lipid bilayer studies	Constructed by Philipp Kemp and Marco Bechtel
pET24 SnoopCatcher-^{GGSSG}-NB$_{GFP}$-strep	Lipid bilayer studies	Constructed by Sebastian Schaupp

2.3 Protein refolding

Lyophilized proteins were dissolved in 200 mM KCl, 50 mM Tris-Cl pH=8, 8 M Urea to a final concentration of ≈ 4 mg/ml. After incubation for 2 h at RT, they were diluted fortyfold into cold refolding buffer (200 mM KCl, 50 mM Tris pH=8, 0.5 % (w/v) DDM) and incubated for about 48 h at 4 °C. Protein aggregates were removed by centrifugation at 16000 ×g at 4 °C for 10 min. An aliquot was directly used for bilayer experiments, while the others were flash frozen and stored at -80 °C.

2.4 Vertical lipid bilayer experiments

Electrical recordings were carried out at the Plant Membrane Biophysics group headed by Prof. Thiel with a workbench setup described in [338]. The chamber setup is schematically depicted in **Figure *22***. Briefly, two custom made polytetrafluorethylene (PTFE) chambers, each holding 2.5 ml, were separated by a 25-μm-thick PTFE membrane having a central aperture of about 100 μm. ≈ 2 μl of a 1% hexadecane in *n*-hexane solution was applied to the rim of the hole from both sides. 800 μl of buffer solution was filled into each chamber, followed by 35 μl of 15 mg/ml 1,2-diphytanoyl-*sn*-glycero-3-phosphocholine (DPhPC, Avanti Polar Lipids) in *n*-pentane. After about 5 min the chambers were filled up to 2.5 ml with buffer solution. The bilayer was formed via the pseudo painting/air bubble technique [339]. After a stable bilayer was formed, protein was added to the *trans* chamber (grounded in all experiments) starting at a chamber concentration of 0.1 μg/ml which was increased over time if no protein inserted. In all bilayer experiments, Ag/AgCl electrodes were used. The current between both chambers in response to applied voltages was recorded with an L/M-EPC7 (List-Medical) patch clamp amplifier connected to a preamplifier with a gain of 5 mV/pA and low-pass filtered at 1 kHz. After digitalization on a 16-bit LIH 1600 A/D converter (HEKA) the signal was recorded on a personal computer employing the PATCHMASTER software (HEKA) and a LIH 8+8 data acquisition

device [340]. Recorded current traces were analysed with Nest-o-Patch [341] and PATCHMASTER software (HEKA) and visualized with Prism 7 (GraphPad).

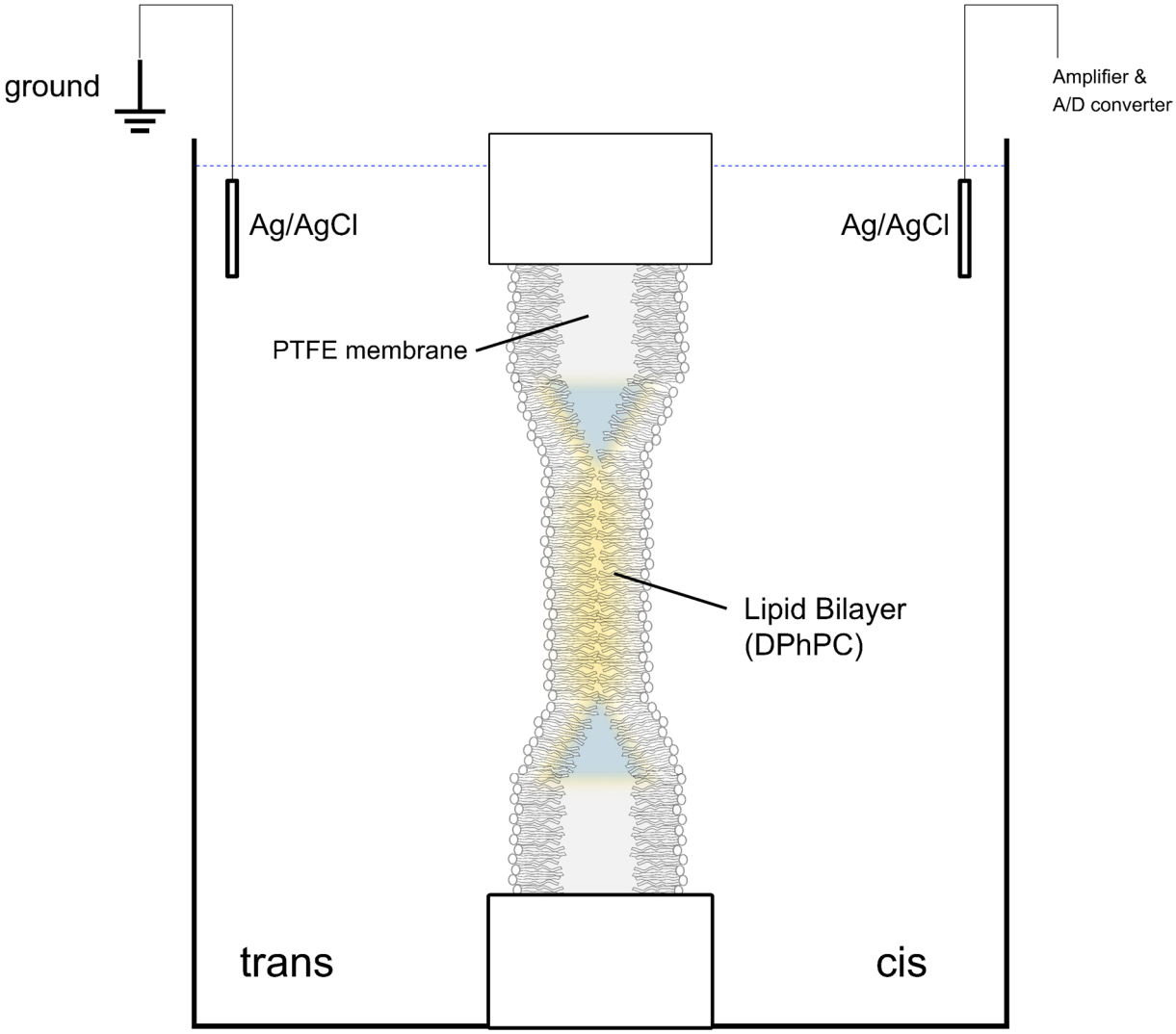

Figure 22 *Schematic drawing of the lipid bilayer measurement chamber setup (not to scale). Two chambers, trans and cis, are separated by a PTFE membrane (25 μm thickness) with a ≈ 100 μm aperture. A DPhPC lipid bilayer is drawn over the aperture by the pseudo painting/air bubble technique [339]. Protein was always added to the grounded trans chamber.*

3. Results

3.1 Visualization of wtFhuA

A first step towards thorough understand of a protein is to visualize it in its natural context. wtFhuA was overexpressed in BL21(DE3) cells (NEB) and incubated with the purified fusion protein Colicin M(D226A)-sfGFP (superfolder GFP, [342]) while observed under the confocal laser scanning microscope (CLSM). The Colicin M D226A mutant employed here still binds to the cork of wtFhuA but is catalytically inactive [343,344]. In a control experiment with cells overexpressing corkless FhuA, no binding of Colicin M(D226A)-sfGFP was observed, whereas the latter accumulated at membranes with wtFhuA as seen by local fluorescence increase (Figure 23). This small experiment enabled an indirect visualisation of the FhuA scaffold and proved the functionality of its 33-*aa* signal sequence.

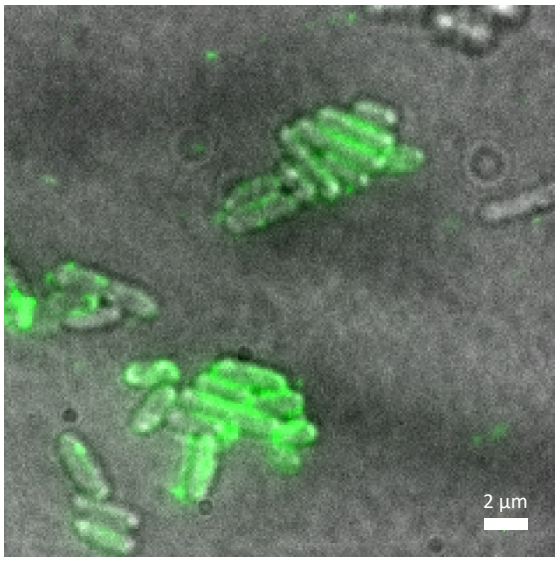

Figure 23 *Imaging of wtFhuA at the outer membrane of BL21(DE3) E. coli by binding of Colicin M(D226A)-sfGFP. Shown are the merged images of bright light and (blue light fluorescence) channel. I acknowledge Wadim Weber for CLSM handling and image recording.*

3.2 Setting up a purification pipeline for FhuA variants

3.2.1 FhuA purification in the literature

Since its crystal structure was solved in 1998, many purification protocols for FhuA and its variants have been described. Briefly, these protocols can be divided into two approaches: The outer membrane extraction method and the inclusion body purification.

Membrane-extraction using detergents is the original method of choice and is still used in some groups to date [304,315,345]. For this procedure, it is necessary to use *E. coli* strains that lack major outer membrane proteins like LamB, OmpA and OmpF [337], as these are otherwise co-purified. The strains mainly used are AW740 [346,347] and BL21(DE3)omp8 or omp9 [255,337]. Incorporation into the outer membrane is reduced in FhuA variants that lack the cork domain (e.g. FhuAΔ5-160) [319,348].

When overexpressed in *E. coli*, a large portion of translated FhuA forms inclusion bodies, especially if the signal sequence is omitted [317]. Thus, FhuA purification via refolding from inclusion bodies was proposed in 2011 by both the Schwaneberg [349] and the Movileanu

group [255] as an alternative to membrane extraction. Both groups pointed out that the inclusion body refolding method improves protein yield considerably while being technically and experimentally less challenging than the membrane extraction method [255,349]. Importantly, the use of BL21(DE3) instead of BL21(DE3)omp8 leads to higher yields [349]. Nevertheless, the Schwaneberg group still employs the outer membrane extraction [350–352] as inclusion body purification is incompatible with FhuA variants that contain single free cysteines, a feature important for applications in organic chemistry catalysis projects [353].

Straightforward inclusion body purification and refolding protocols have been established by the Movileanu group [228,255]. They introduced a rapid-dilution method for FhuA refolding using the mild detergent n-Dodecyl-β-D-maltosid (DDM) [323] derived from an OmpA refolding study [354]. Other refolding detergents have been investigated, but along with 1-lauroyl-2-hydroxy-sn-glycero-3-phosphocholine (LysoFos), DDM is favoured as it does not interact with FhuA [325].

3.2.2 FhuA purification pipeline in the Stein lab

During my doctoral studies, various inclusion body purification methods for FhuA variants were tested. Considering the aim (creation of a nanopore-based biosensor scaffold), outer membrane extraction was not pursued due to the above-mentioned reasons:

- Corkless variants show poor incorporation into outer membranes
- The 33-*aa* signal sequence (+sig) would constitute a mandatory N-terminal feature
- Outer membrane extraction is technically and experimentally more challenging and time-consuming while yielding less protein

The inclusion body purification protocol described by Wolfe *et al.* [228] proved to be reliable for most corkless FhuA variants. Optimization efforts that focused on small detergent screens, pursued by Sebastian Schaupp in his Master thesis, did not yield considerable improvements.

3.2.3 Expression and Purification Results

FhuA and ΔcΔ5L variants were successfully overexpressed in T7 polymerase-based vectors pET32 and pET24 (Sup Fig 4). Washed inclusion bodies were resolubilized in 8 M Urea and purified *via* 6xHis-Tag (Figure 24). After dialysis against water, samples were lyophilized and stored as solid powder at 4 °C in reagent tubes additionally sealed with Parafilm M. Except for SpyTagged variants (Master Thesis Sebastian Schaupp), yields were in the range of 3-8 mg per l culture.

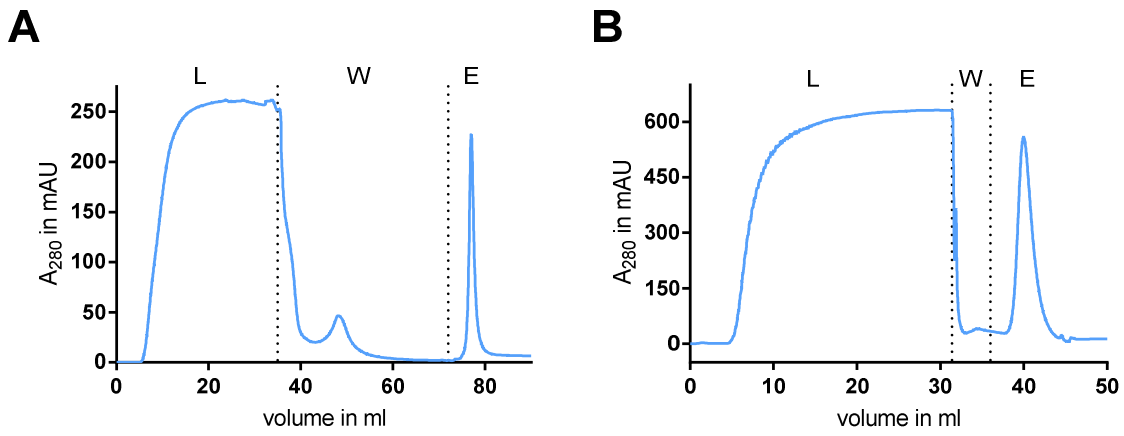

Figure 24 *Example chromatogram of ΔcΔ5L inclusion body His-Tag ÄKTApure purification. L, W and E denote Load, Wash and Elution parts, respectively. A: $^{+sig}$ΔcΔ5L-SmBiT86^{6xHis} run via 5 ml HisTrap column. B: $^{+sig}$ΔcΔ5L-10Link-SnoopTag^{6xHis} run via 1 ml HisTrap column.*

3.2.4 Protein refolding with DDM

All purified ΔcΔ5L variants were refolded by rapid dilution into buffer containing DDM [323]. Circular dichroism (CD)-spectroscopy under these detergent solvation conditions confirmed successful refolding of tagged ΔcΔ5L variants (Figure 25). The spectrum shows a clear minimum at ≈ 218 nm, confirming the beta-barrel structure of the protein (in this case: ^{6xHis}SnoopTag-$^{+sig}$ΔcΔ5L) [355]. The buffer affects the spectrum at wavelengths below 210 nm, which is a known phenomenon caused by high chloride concentrations (200 mM KCl) [356].

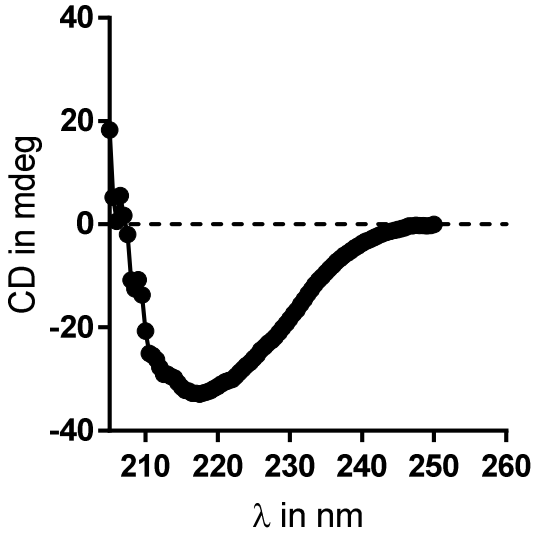

Figure 25 *CD spectrum of ^{6xHis}SnoopTag-$^{+sig}$ΔcΔ5L. ≈ 150 nM of protein was measured in refolding buffer (200 mM KCl, 50 mM Tris pH=8, 0.5 % (w/v) DDM). I acknowledge Philipp Czechowski for performing the measurement at research group Reggelin.*

3.3 Bilayer investigations of ΔcΔ5L

3.3.1 Insertion efficiency

It must be emphasized that the process of membrane protein bilayer insertion *in vivo* is fundamentally different from the insertion of purified transmembrane proteins into artificial bilayers (see section 1.2.5.1). While insertion of DDM-refolded ΔcΔ5L variants into the bilayer occurred spontaneously in some cases, insertion was often facilitated by short (10-20 s) high-voltage pulses (e.g. -160 mV / 160 mV). This approach of "pushing" membrane proteins or peptides into lipid bilayers has been described in the literature, not only for FhuA variants [312,315] but also for cWza, where the authors applied +100 mV to promote peptide insertion [243].

Nevertheless, no universally reproducible success route could be derived. This contrasts statements from the Movileanu group [323]. In general, the chance of insertion increased with higher protein concentration in the chamber, although this led to higher instability of the DPhPC bilayer, likely due to higher DDM concentration. As soon as a protein inserted, the high-voltage pulse was interrupted, and measurements were started. ΔcΔ5L variants inserted as monomers and in an oriented manner (with the lipopolysaccharide-facing side first), in agreement with literature [226,323,324]. Once inserted, ΔcΔ5L variants were stable at applied voltages between -80 mV / +80 mV and increasingly noisy at higher voltages, especially at higher electrolyte concentrations. Altogether, ΔcΔ5L bilayer insertion at vertical PTFE chamber setups [338] is a laborious procedure that is only briefly discussed in the literature, if at all [228,255].

3.3.2 Control: ΔcΔ5L^{6xHis}

As a control, the minimalized ΔcΔ5L^{6xHis} protein was tested. ΔcΔ5L^{6xHis} lacks the 33-*aa* signal sequence and has a GSGLE$(H)_6$-tag at its C-terminus. The current trace of ΔcΔ5L^{6xHis} shows an open state corresponding to a conductivity of ≈ 2.3 nS in 500 mM KCl, 25 mM Tris-Cl pH=8, in agreement with literature (Figure 26) [228,357]. The observation of long blocking events also underlines that even a small tag like the GSGLE$(H)_6$-tag is able to block the pore for time periods in the range of seconds. The distinct open state current was also observed for the other ΔcΔ5L variants, hence it was possible to discriminate inserted protein from detergent pores and artefacts.

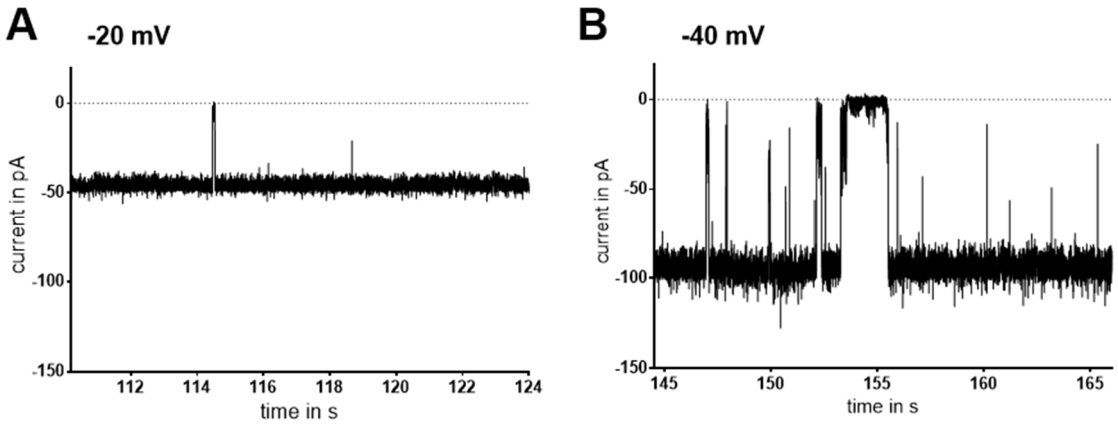

Figure 26 *Example trace of ΔcΔ5L^{6xHis} at A -20 mV and B -40 mV in 500 mM KCl, 25 mM Tris-Cl pH=8.*

3.3.3 Blocking behaviour of the signal sequence: $^{+sig}\Delta c\Delta 5L^{6xHis}$

In general, the addition of the 33-*aa* signal sequence to the scaffold improved the insertion probability of ΔcΔ5L scaffolds. Yet, in the case of the minimal $\Delta c\Delta 5L^{6xHis}$, +sig rendered the nanopore more blocked at voltages beyond ± 20 mV. While the trace was comparable to $\Delta c\Delta 5L^{6xHis}$ for -20 mV and while the inserted protein showed the expected conductivity (≈ 4.5 nS in 1 M KCl, 10 mM KH_2PO_4 pH=7.4), current blockades were more frequent e.g. at -40 mV (Figure 27). As $^{+sig}\Delta c\Delta 5L^{6xHis}$ was only measured once, these results are shown to give a qualitative overview of the blocking behaviour of +sig.

Nanopore blocking by the signal sequence (+sig) at negative applied voltages was also frequently observed during recordings of other ΔcΔ5L variants. The most straightforward explanation for this phenomenon is the positive net charge of +sig (+5 e & N-terminal amino-group) at the given pH (7.4 or 8). In the natural context, such positive charges – especially near the N-terminus – are conserved motifs of outer-membrane protein signal sequences and recruit unfolded proteins to the lipid membrane for translocation [290] (see section 1.2.5.1). In the context of artificial bilayer measurements, this explains the improved insertion efficiency. Moreover, the blocking properties of the +sig feature elucidate the actual orientation of ΔcΔ5L inside the bilayer, as depicted in (Figure 28). The investigation on +sig contrasts observations from a publication by the Movileanu group where the authors claimed that +sig addition to the nanopore scaffold has little effect on its conductive behaviour [228]. Their statement must be relativized, as it only holds true for positive applied voltages.

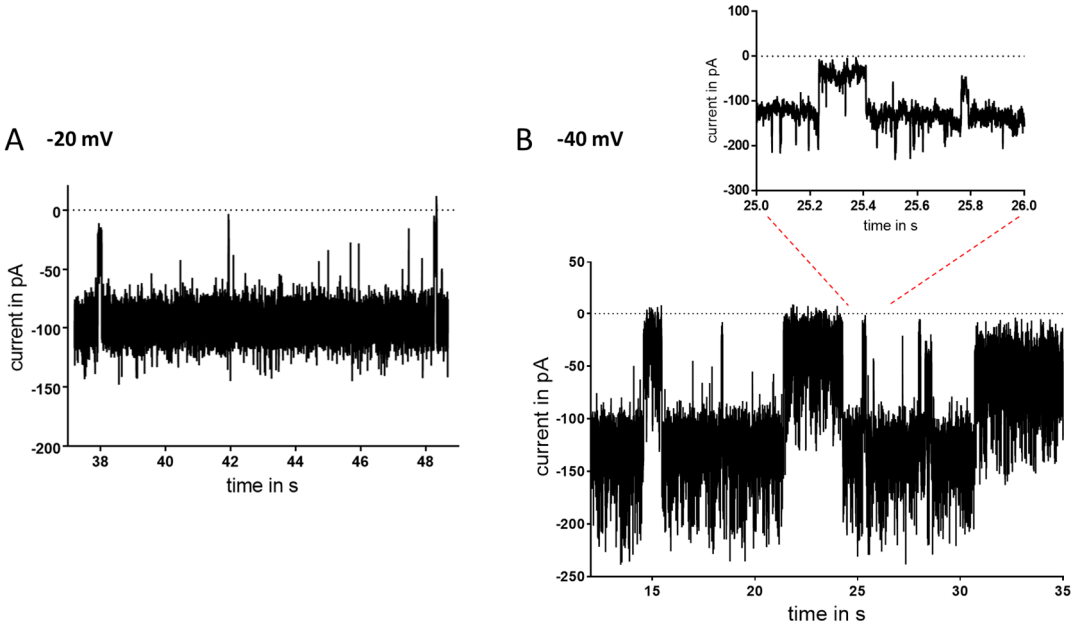

Figure 27 *Representative current traces of $^{+sig}\Delta c\Delta 5L^{6xHis}$ at -20 mV (A) and -40 mV (B), respectively. The inset in B shows a short closing and opening event and a short partially blocked state. Measurements were performed in 1 M KCl, 10 mM KH_2PO_4 pH=7.4.*

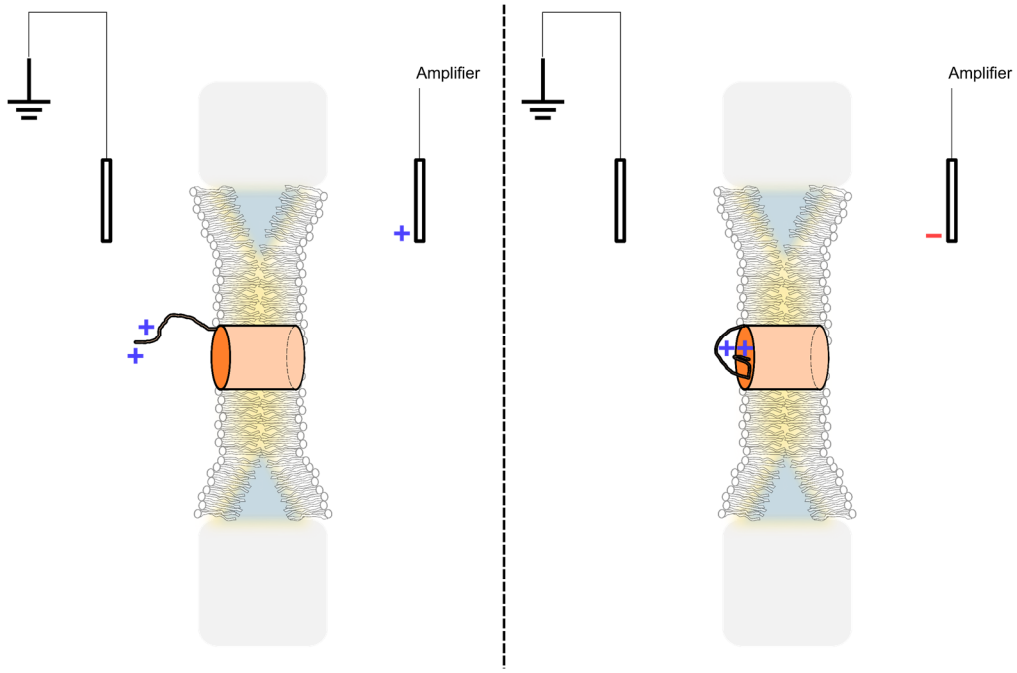

Figure 28 *ΔcΔ5L orientation is elucidated by +sig transient blocking. Termini are oriented towards the grounded chamber. At an applied positive voltage (left), positively charged +sig is mainly moving outside the ΔcΔ5L lumen, whereas +sig is occluding the pore at negative applied voltages (right). The drawing is schematic and not to scale.*

3.3.4 $^{+sig}$ΔcΔ5L-SmBiT^{6xHis}

With the ΔcΔ5L scaffold showing an expected behaviour, the investigation focused on the attachment of tags that could serve as anchor site for a second (receptor) protein. In principle, such second protein can be attached covalently or non-covalently. Both methods have advantages and disadvantages; for instance, while covalent attachment is more stable, it may impact the structural stability of the membrane protein inside a bilayer to a greater extent.

SmBiT86 was chosen as a tag that enables non-covalent attachment of a second protein to the nanopore. SmBiT86 is a 11-*aa* small subunit of the engineered split luciferase NanoBiT and binds with high affinity (K_D = 0.7 nM) to its larger partner LgBiT (18 kDa) [358]. The SmBiT86/LgBiT interaction was chosen due to the small size of both interaction partners.

$^{+sig}$ΔcΔ5L-SmBiT86^{6xHis}, carrying a C-terminal SmBiT86-tag, inserted into DPhPC bilayers in 150 mM KCl, 10 mM KH_2PO_4 pH=7.4 with the aid of an applied voltage. The protein showed a voltage dependent open probability (Figure 29, Figure 30). At a positive voltage up to +80 mV, the nanopore occupies an open state with a conductivity of 0.49 ± 0.05 nS (N=3), while the pore was often transiently blocked by the tags at negative voltages, as observed before for $^{+sig}$ΔcΔ5L.

In multiple cases, either the SmBiT86^{6xHis}-tag, the +sig or a combination of both tags blocked the ΔcΔ5L lumen nearly irreversibly, decreasing the open probability for both positive and negative applied voltages drastically (Figure 31). In contrast to other ΔcΔ5L variants, this blocking persisted for minutes even at positive voltages. Another explanation for this phenomenon – apart from tag-blocking – might be a collapse of the ΔcΔ5L transmembrane beta-barrel due to applied voltages beyond a certain threshold. Such instability has been observed for other engineered FhuA variants (Δc/Δ7L-30N in [228]). Altogether, these blocking events complicated the identification of LgBiT interactions, as discussed in the following paragraph.

To bilayer inserted $^{+sig}$ΔcΔ5L-SmBiT86^{6xHis}, purified LgBiT (final concentration: 0.5 μM) was added to probe if it shows an interaction with the SmBiT86 tag. Multiple (N=3) measurements where the current trace appeared to respond to the addition of LgBiT yielded inconsistent and unreproducible results, hence the hypothesis that LgBiT interaction should result in distinct changes in nanopore behaviour remained inconclusive. In one experiment, an increased open probability (0.75 in contrast to 0.21) at +40 mV over the course of two (± LgBiT) 15 min traces hinted towards a binding of LgBiT, with the rationale that the SmBiT86-tag is "captured" outside the pore lumen and thus prevented from blocking the pore (Sup Fig 5). Yet, these findings could not be reproduced with a second inserted $^{+sig}$ΔcΔ5L-SmBiT86^{6xHis}. Moreover, the inherent property of the tags to block the nanopore complicate a clear differentiation between LgBiT-caused and intrinsic events.

In conclusion, the behaviour of bilayer-inserted $^{+sig}$ΔcΔ5L-SmBiT86^{6xHis} was recorded, showing a high open probability at positive applied voltages similar to the other ΔcΔ5L variants. The mechanism of intrinsic blocking could not be elucidated and is likely caused by persistent tag blocking or membrane protein distortion at higher applied voltages. Recruitment of LgBiT by the SmBiT86 module of the membrane protein could not be distinguished from background events.

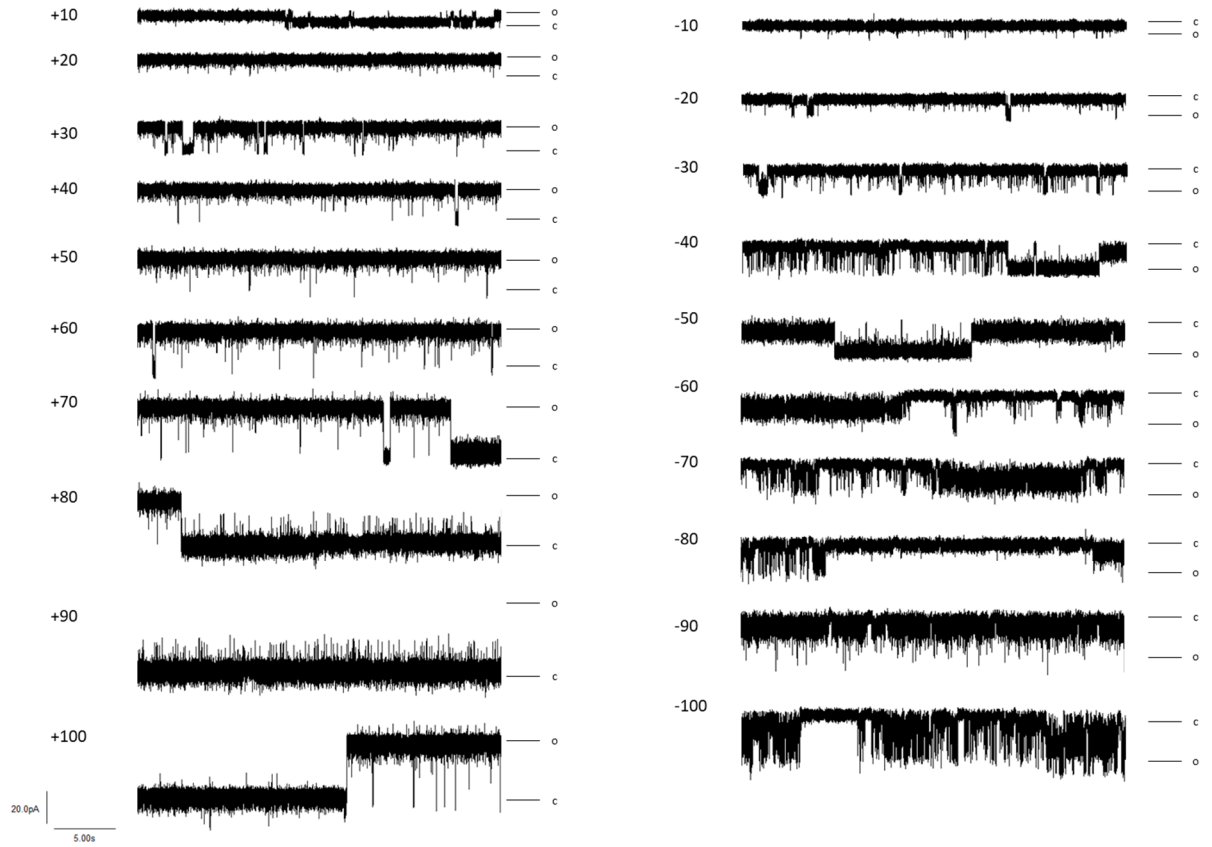

Figure 29 *Representative current traces of $^{+sig}$ΔcΔ5L-SmBiT86^{6xHis} at positive (left) and negative (right) voltages in 150 mM KCl, 10 mM KH_2PO_4 pH=7.4. Numbers correspond to applied voltages in mV. O: Fully open state; C: Fully closed state. Notice that the presence of only one open and closed state for ΔcΔ5L variants is an idealized assumption; for instance, sub-states appear at -60 mV and -80 mV.*

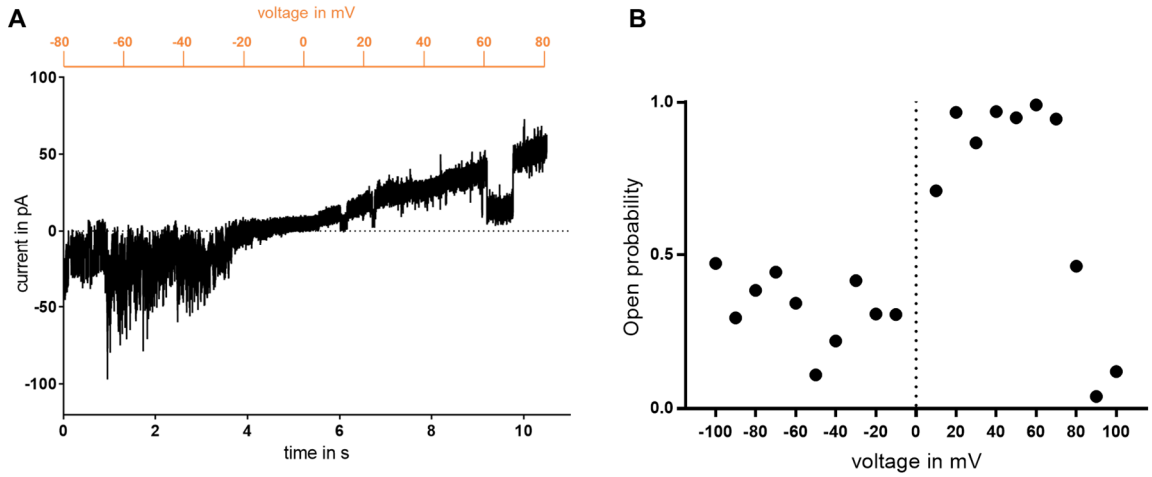

Figure 30 *A: -80 mV/+80 mV voltage ramp of $^{+sig}$ΔcΔ5L-SmBiT86^{6xHis} in 150 mM KCl, 10 mM KH_2PO_4 pH=7.4. B: Open probability of the inserted nanopore calculated via NestoPatch [341]. For calculation, all states not fully closed were treated as open.*

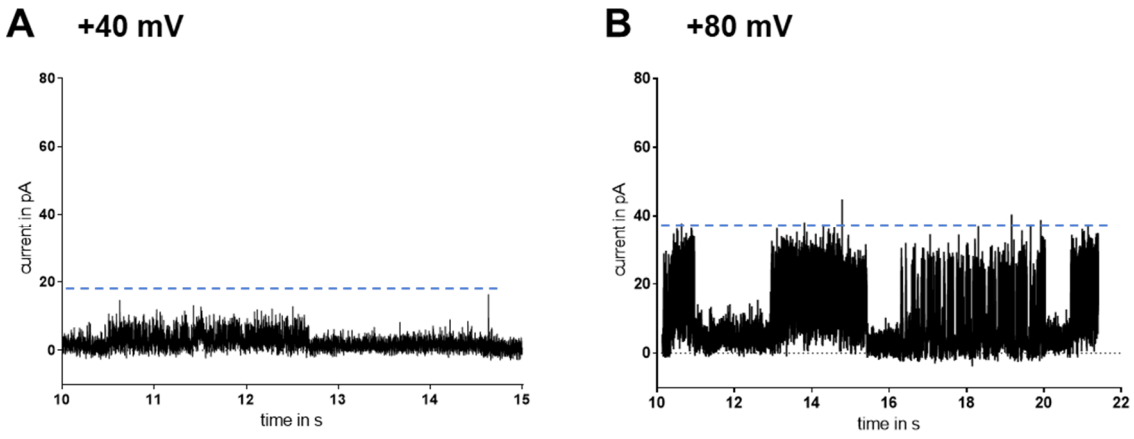

Figure 31 *Constitutively and partially blocked $^{+sig}$ΔcΔ5L-SmBiT86^{6xHis} pore in 150 mM KCl, 10 mM KH_2PO_4 pH=7.4 at applied voltages of +40 mV (left) and +80 mV (right). Blue dashed line represents the expected open state current at the applied voltage.*

3.3.5 Towards covalent attachment: SnoopTag-ΔcΔ5L variants

The $^{+sig}$ΔcΔ5L-SmBiT86^{6xHis} investigation in the artificial lipid bilayer context outlined that the discrimination of protein interactions at the single molecule level is challenging, in particular if a specific binding event relies on the presence of flexible tags. However, such discrimination should become easier if the interaction results in covalent attachment, as this should change the nanopore behaviour irreversibly. Thus, ^{6xHis}SnoopTag-$^{+sig}$ΔcΔ5L was investigated, a variant with +sig separating an N-terminal SnoopTag and the ΔcΔ5L scaffold. SnoopTag can form an isopeptide bond with SnoopCatcher and thus should enable covalent attachment (see section 3.2.2, Chapter 1)

^{6xHis}SnoopTag-$^{+sig}$ΔcΔ5L showed a conductivity of 4.4 ± 1.3 nS (N=10) in 1 M KCl, 50 mM Tris-Cl pH=8 and 0.85 ± 0.14 nS (N=3) in 150 mM KCl, 10 mM KH_2PO_4 pH=7.4, with the same open probability bias towards positive voltages as $^{+sig}$ΔcΔ5L and $^{+sig}$ΔcΔ5L-SmBiT86^{6xHis} (Figure 32, Figure 33). As discussed, the transient blockages at negative voltages are caused by positively charged flexible tags, in this case the long N-terminal tag with a net charge of +6. Importantly, these blockages were only transient, as the fully open state occurred occasionally (Figure 34, Sup Fig 6). Interestingly, the ^{6xHis}SnoopTag-$^{+sig}$ΔcΔ5L nanopore reproducibly opened again if positive voltages were applied deliberately (Figure 35). This phenomenon was also observed for $^{+sig}$ΔcΔ5L-SmBiT86^{6xHis}, albeit less pronounced.

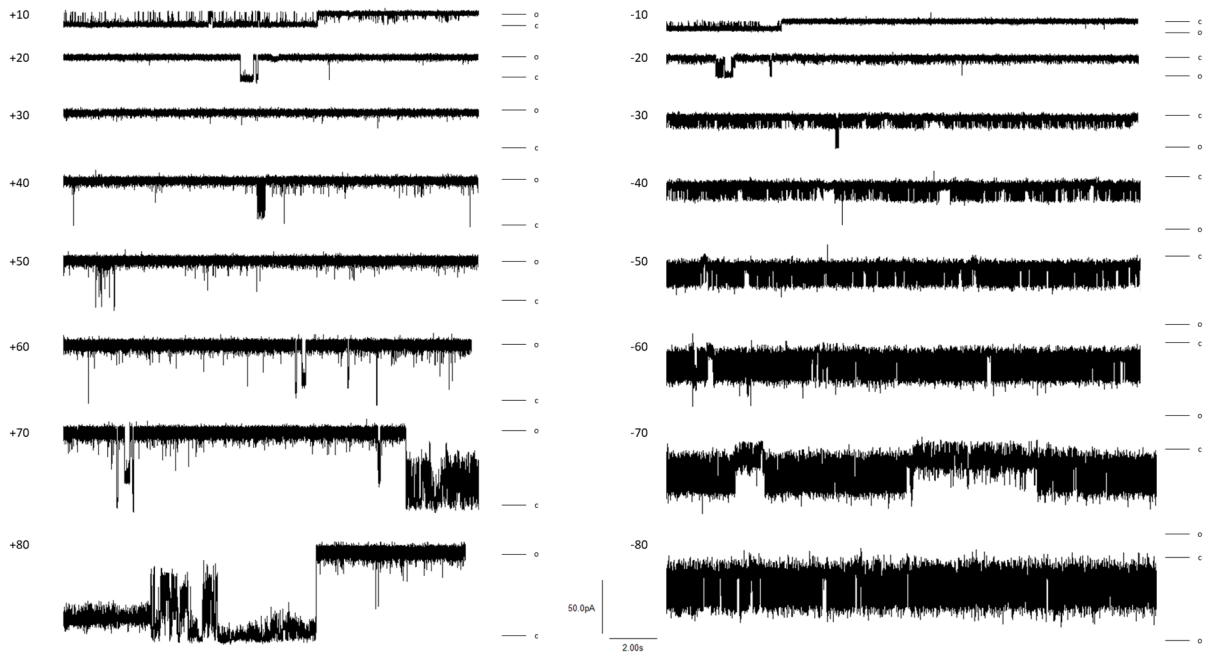

Figure 32 *Representative current traces of ^{6xHis}SnoopTag-$^{+sig}$ΔcΔ5L at positive (left) and negative (right) voltages in 150 mM KCl, 10 mM KH_2PO_4 pH=7.4. Numbers correspond to applied voltages in mV. O: Fully open state; C: Fully closed state. Notice that the presence of only one open and closed state for ΔcΔ5L variants is an idealized assumption; for instance, sub-states appear at +80 mV and -70 mV. Representative current traces from measurements in 1 M KCl, 50 mM Tris-Cl pH=8 are attached to the supplement (Sup Fig 7).*

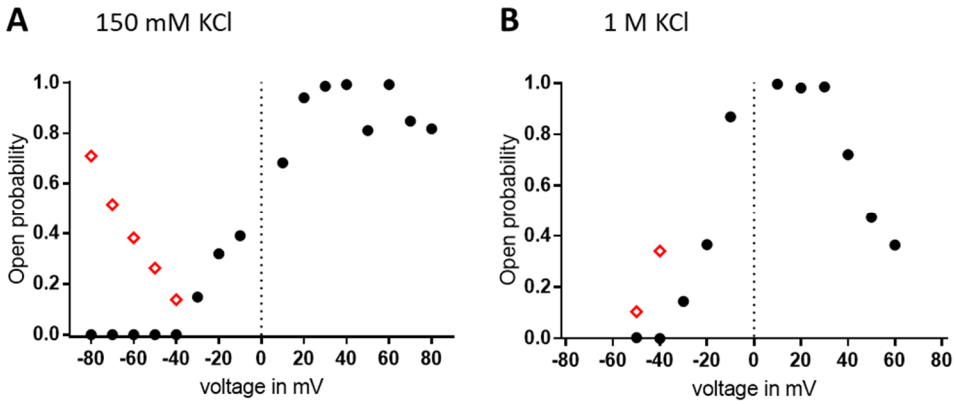

Figure 33 *Representative open probabilities of bilayer inserted ^{6xHis}SnoopTag-$^{+sig}$ΔcΔ5L nanopores in different buffers, calculated via NestoPatch [341] over all recorded current traces of distinct single nanopores. A: 150 mM KCl, 10 mM KH_2PO_4 pH=7.4; B: 1 M KCl 50 mM Tris-Cl pH=8. Red diamonds represent the open probability if partially blocked states that frequently occur at the respective applied voltages are treated as open.*

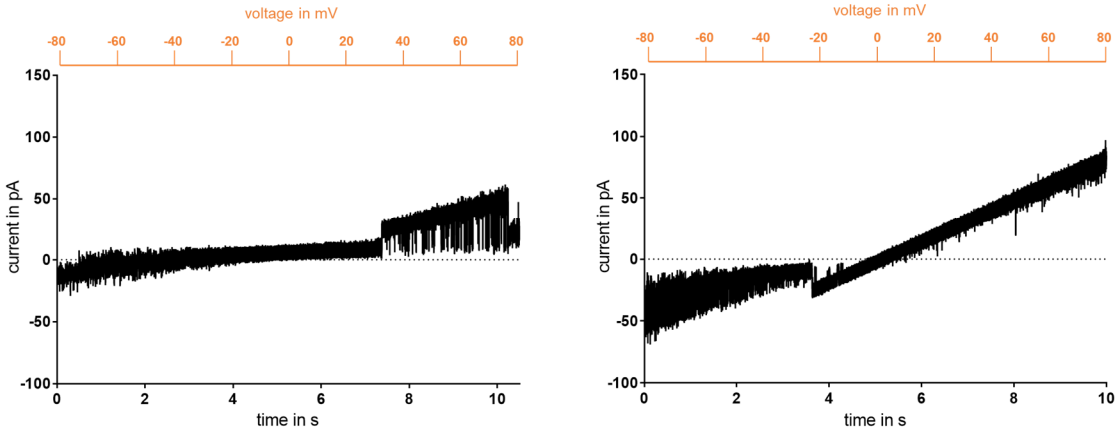

Figure 34 *A: Representative -80 mV/+80 mV voltage ramps of ^{6xHis}SnoopTag-$^{+sig}$ΔcΔ5L in 150 mM KCl, 10 mM KH_2PO_4 pH=7.4. On the left, the nanopore is blocked and partially blocked by its tag with exceptions at positive applied voltages; on the right, the nanopore is only partially blocked at negative applied voltages.*

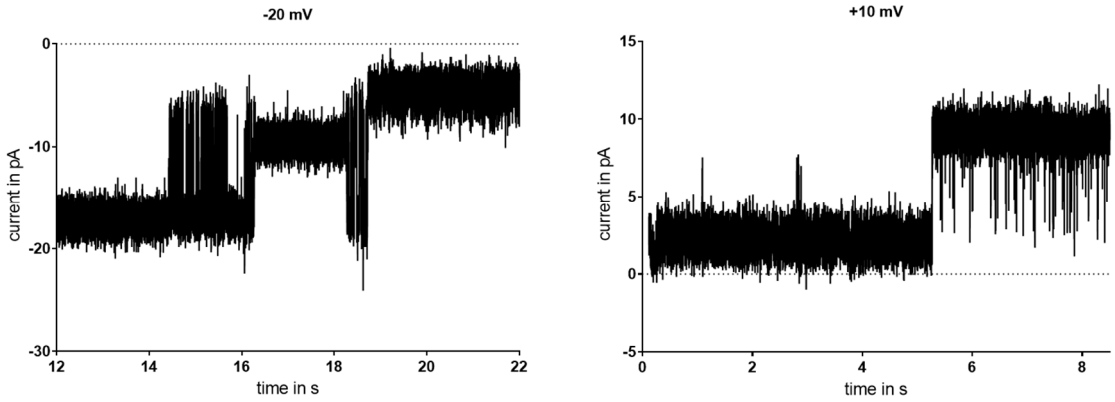

Figure 35 *Representative current traces of ^{6xHis}SnoopTag-$^{+sig}$ΔcΔ5L demonstrating the response of the N-terminal tag to voltage reversal. After applying a negative voltage, the current amplitude drops as the tag becomes arrested inside the pore lumen, whereas shortly after applying a positive voltage, the blocking is abolished. This phenomenon is comparable to the one described in Figure 28. Shown traces were measured in 150 mM KCl, 10 mM KH_2PO_4 pH=7.4.*

The behaviour of the long N-terminal tag was further elucidated by two homology models of ^{6xHis}SnoopTag-$^{+sig}$ΔcΔ5L based on a wtFhuA crystal structure, both created by Patrick Kunzmann from the Computational Biology and Simulation group (details on modelling in Sup Text 2). If the tag was aligned with the cork of wtFhuA, it folded into a compact, cork-like structure (Figure 36 B). However, if the tag was not aligned with the cork, it stretched away from the transmembrane barrel (Figure 36 A). This finding underlines the high flexibility of the tag and its ability to occupy different conformational states. Yet, further simulation attempts did not yield sufficient data to confirm the proposed blocking role of the tag *in silico*.

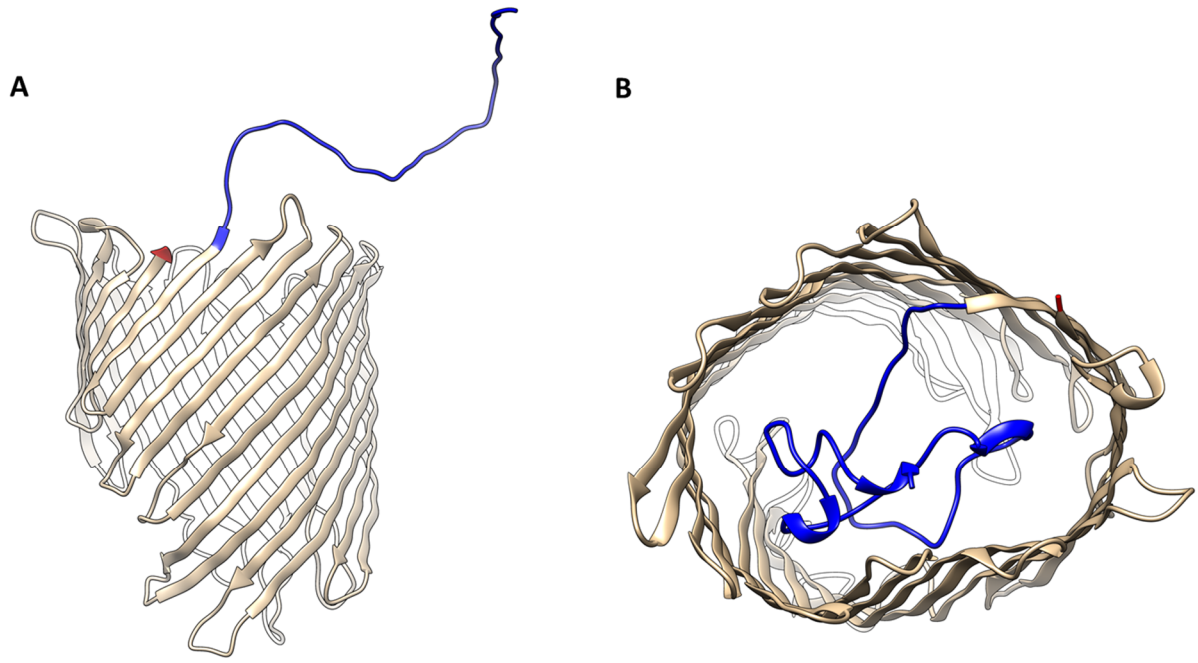

Figure 36 *Homology models of ^{6xHis}SnoopTag-$^{+sig}$ΔcΔ5L. N-terminal tag is colored in blue, C-terminus indicated in red. Model A: The N-terminal tag is freely moving outside the pore lumen; Model B: The N-terminal tag is arrested inside the nanopore lumen. Images were generated via UCSF Chimera [120]. I acknowledge Patrick Kunzmann for the creation of the models. Details are given in Sup Text 2.*

The ability to control the tag behaviour of ΔcΔ5L variants by voltage changes encouraged further investigations. Exchanging the +sig part of the N-terminal tag by a shorter, uncharged 10-*aa* linker (SGSGASGGSG) rendered the nanopore less blocked, especially at negative voltages (Figure 37). The same correlation of tag length and open probability was observed for two C-terminally tagged variants, $^{+sig}$ΔcΔ5L-2Link-SnoopTag^{6xHis} and $^{+sig}$ΔcΔ5L-10Link-SnoopTag^{6xHis} (Sup Fig 8, Sup Fig 9, Sup Fig 10). In summary, the propensity of ΔcΔ5L scaffolds to be intrinsically blocked is directly correlated to the tag length and charge. Yet, a charged tag gives the researcher control over the tag behaviour, at least to a certain degree.

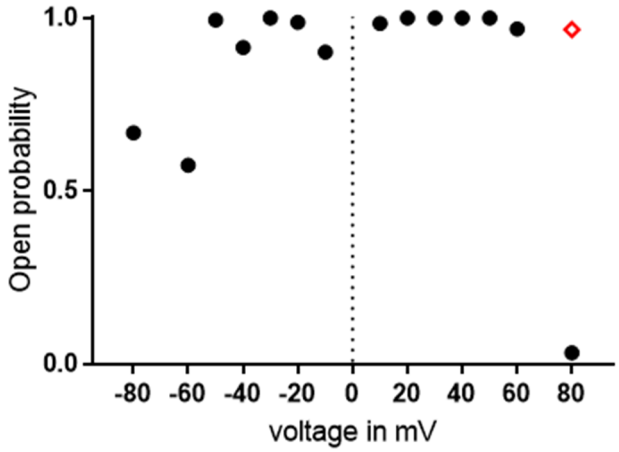

Figure 37 *Representative open probabilities of bilayer inserted ^{6xHis}SnoopTag-10Link-ΔcΔ5L nanopore in 1 M KCl, 50 mM Tris-Cl pH=8 calculated via NestoPatch [341]. Red diamond represents the open probability if partially blocked states are treated as open.*

Thus, it was probed if the various SnoopTag-ΔcΔ5L variants can irreversibly catch a SnoopCatcher-fusion protein while embedded inside the lipid bilayer. Despite multiple attempts, neither nanopore variant that contained small linkers between SnoopTag and ΔcΔ5L – namely $^{+sig}$ΔcΔ5L-2Link-SnoopTag^{6xHis}, $^{+sig}$ΔcΔ5L-10Link-SnoopTag^{6xHis} and ^{6xHis}SnoopTag-10Link-ΔcΔ5L – showed a distinct, irreversible change in either conductivity or blocking frequency upon addition of SnoopCatcher-NB$_{GFP}$ to the measurement chamber. There are several possible reasons for this lack of recognition. For instance, the SnoopCatcher protein or the SnoopTag might interact unspecifically with DPhPC lipids of bilayer. Yet, considering the role of linker length in fusion proteins (section 1.1.2 in Chapter 2), the respective SnoopTags of all these variants may not be sterically accessible to the large SnoopCatcher moiety.

This hypothesis is supported by the reproducible response of bilayer-inserted ^{6xHis}SnoopTag-$^{+sig}$ΔcΔ5L to SnoopCatcher. While this variant is unfavourable in terms of intrinsic blocking, the very long spacer between ΔcΔ5L and the N-terminal SnoopTag (36 *aa*) apparently provided the necessary conditions for a successful isopeptide bond formation between the interaction partners. Precisely, the reaction lead to irreversible current blockades that were distinct to the ones created by SnoopTag and +sig alone (Figure 39, Sup Fig 11). Additionally, no irreversible conductivity changes or blocking states were observed when SpyCatcher-NB$_{GFP}$ was added to ^{6xHis}SnoopTag-$^{+sig}$ΔcΔ5L. The SpyCatcher fusion protein was employed as an additional negative control because the SpyCatcher and SnoopCatcher system do not cross-react [43]. Altogether, these observations underline the importance of the linker length between the transmembrane (actuator) part and the soluble (receptor) part. This further emphasizes the role of linkers in fusion proteins, as discussed in detail in Chapter 2.

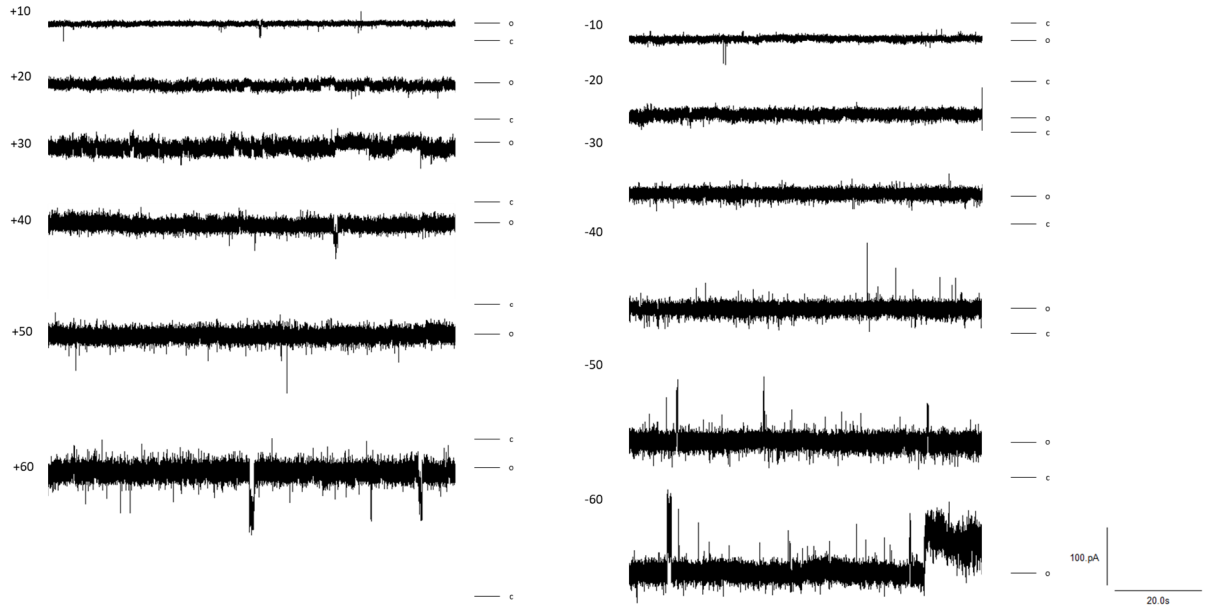

Figure 38 *Representative current traces of ^{6xHis}SnoopTag-10Link-ΔcΔ5L at positive (left) and negative (right) voltages in 1 M KCl 50 mM Tris-Cl pH=8. Numbers correspond to applied voltages in mV. O: Fully open state; C: Fully closed state. Notice that the presence of only one open and closed state for ΔcΔ5L variants is an idealized assumption; for instance, partially blocked sub-states appear at -60 mV.*

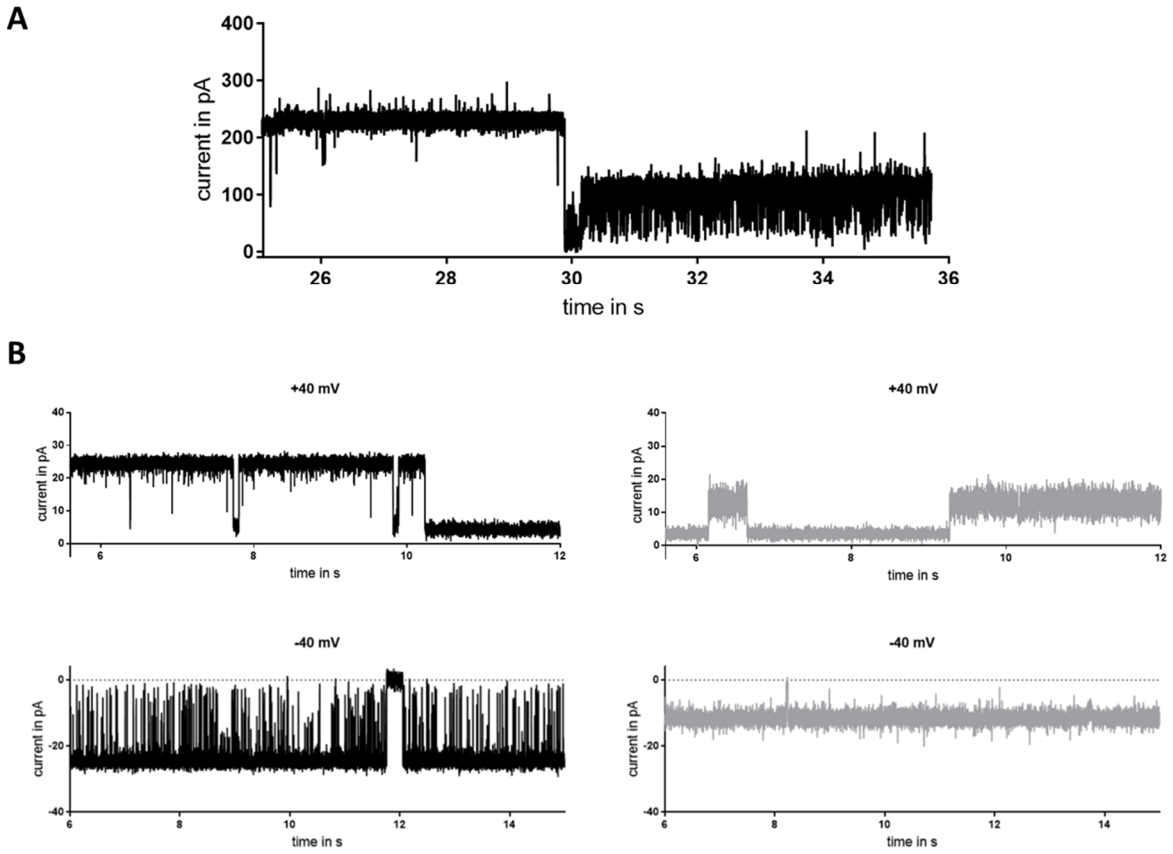

Figure 39 *A: Live event of SnoopCatcher-NB reaction with ^{6xHis}SnoopTag-$^{+sig}$ΔcΔ5L, recorded in 1 M KCl 50 mM Tris-Cl pH=8 at an applied voltage of 50 mV. B: Representative current traces of ^{6xHis}SnoopTag-$^{+sig}$ΔcΔ5L before (black) and after (grey) reaction, measured in 150 mM KCl 10 mM KPO_4 pH=7.4. For better comparability, time scales of ± Catcher traces were normalized to each other.*

3.3.6 Conclusion and Perspectives

In the light of all bilayer experiments that were conducted during my PhD studies, the ΔcΔ5L nanopore scaffold is *per se* reliable and offers various target points of specific fine-tuning. ΔcΔ5L variants respond specifically to (small) changes in terminally attached peptide tags, in accordance with studies from the Movileanu lab [226,324,327]. This ability allows detailed investigation of charge and length impact on protein nanopore conductivity and blocking at the single molecule level. In this regard, the +sig sequence is both blessing and curse, as it facilitates protein insertion and specifically responds to applied voltages but is prone to become arrested inside the nanopore lumen (Figure 36).

Multiple aspects complicate quantitative protein interaction studies using ΔcΔ5L variants. Small and robust receptor modules can be fused to the nanopore on the genetic level [324,327], yet, post-translational capturing of a second receptor has limitation and requires linker optimization, as shown here for SnoopCatcher-NB_{GFP}. With more modules attached to the ΔcΔ5L scaffold, discrimination between multiple unspecific blocking events and actual ligand interaction becomes elusive. In one recent study, the attachment of an additional adaptor polypeptide was necessary to identify protein interactions outside the nanopore [324]. The only purpose of this adaptor was to transform the interaction into a detectable current change, underlining the complexity of single molecule nanopore biosensing. Considering this, the best option of equipping ΔcΔ5L with a specific sensing function apparently is a genetic fusion to either N- or C-terminus. Yet, this is limited to small domains that are robust to inclusion body purification and refolding.

The ΔcΔ5L scaffold is still far from optimized to allow integration into a bilayer-based biosensor platform or device. ΔcΔ5L is a stable monomer with exceptionally high conductivity, yet, its refolding and insertion process, together with its broad conductivity spectrum [357], complicate reproducible measurements especially in labile lipid bilayer environments. For instance, residual DDM molecules still attached to the beta-barrel are likely responsible for observed conductance outliers [325]. Generally, stabilized lipid bilayers [270,271] or lipid alternatives like diblock copolymers [64] also tested by the Schwaneberg group [359–361], could achieve better reliability of membrane protein-based biosensor devices.

Without gathering data of other membrane proteins, it is difficult to predict if other scaffolds are better suited as modular stochastic biosensors. Judging from their structure and recent publications, either ClyA or MspA might be promising alternatives, as both are stable monomers and show calm current traces (section 1.2.3.1 and 1.2.4.1). However, considering the depth of current industrial nanopore scaffold screening [263] and the large patent landscape [362], finding the “perfect” nanopore for a certain application is difficult to say the least.

To conclude, FhuA based membrane protein nanopores are stable, tunable and enable real-time detection of single-molecule interaction events. Thus, most of the important biosensor requirements mentioned in the following chapter are met. FhuA based biosensing, as pioneered by the Movileanu group, will undoubtedly become a reliable platform if the current drawbacks are overcome. Currently, these include protein handling, long-term stability of bilayer systems and unspecific responses of attached tags. The high sensitivity of the system towards charges could in principle be used to probe charged peptide ligands, for instance the Alzheimer related amyloid-β (1-40) and (1-42) peptides with a net charge of -3 e [363]. In this regard, future studies should focus on the robustness of the platform towards biofluids [327]. The inspiring success of nanopore-based DNA sequencing [57] serves as an encouraging example of nanopore biosensing and highlights its potential for real world applications.

4. Supplement Chapter 3

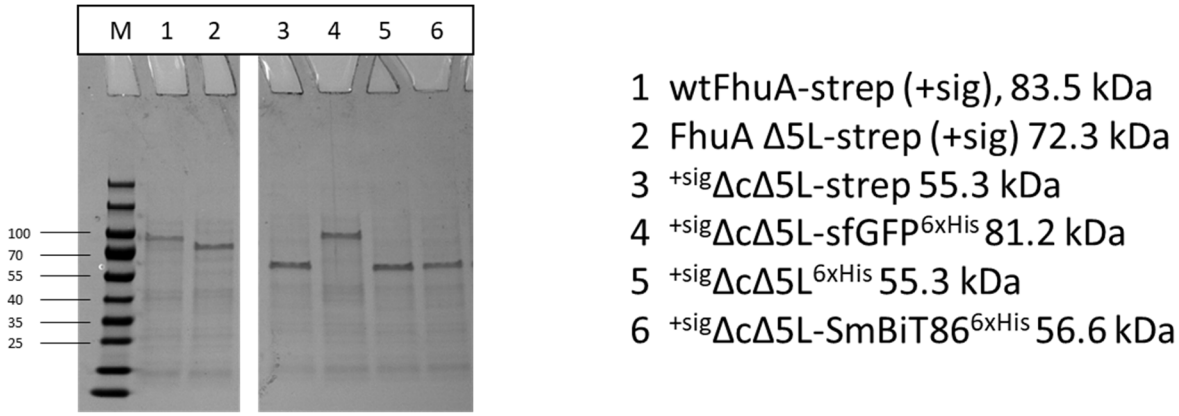

Sup Fig 4 *SDS-PAGE of selected FhuA variants. Shown are samples of lysed BL21(DE3) cells after overexpression of the respective FhuA variants. M: BlueStar prestained protein Marker (Nippon Genetics).*

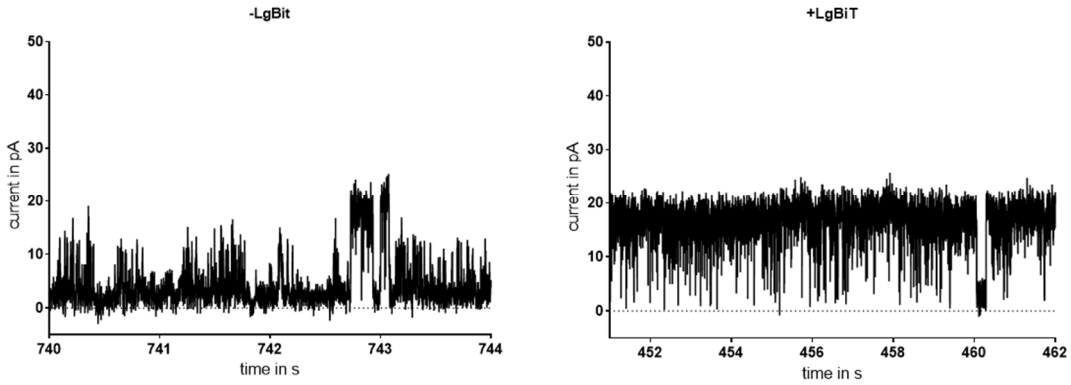

Sup Fig 5 *Possible LgBiT interaction with $^{+sig}$ΔcΔ5L-SmBiT86^{6xHis}, observed at +40 mV in 150 mM KCl, 10 mM KH_2PO_4 pH=7.4.*

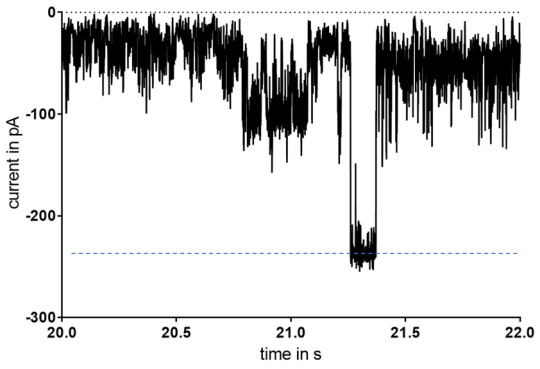

Sup Fig 6 *Example trace showing a fully open event of ^{6xHis}SnoopTag-$^{+sig}$ΔcΔ5L during partially blocked substates at an applied voltage of -50 mV in 1 M KCl, 50 mM Tris-Cl pH=8. The conductivity of this specific pore is 4.6 nS.*

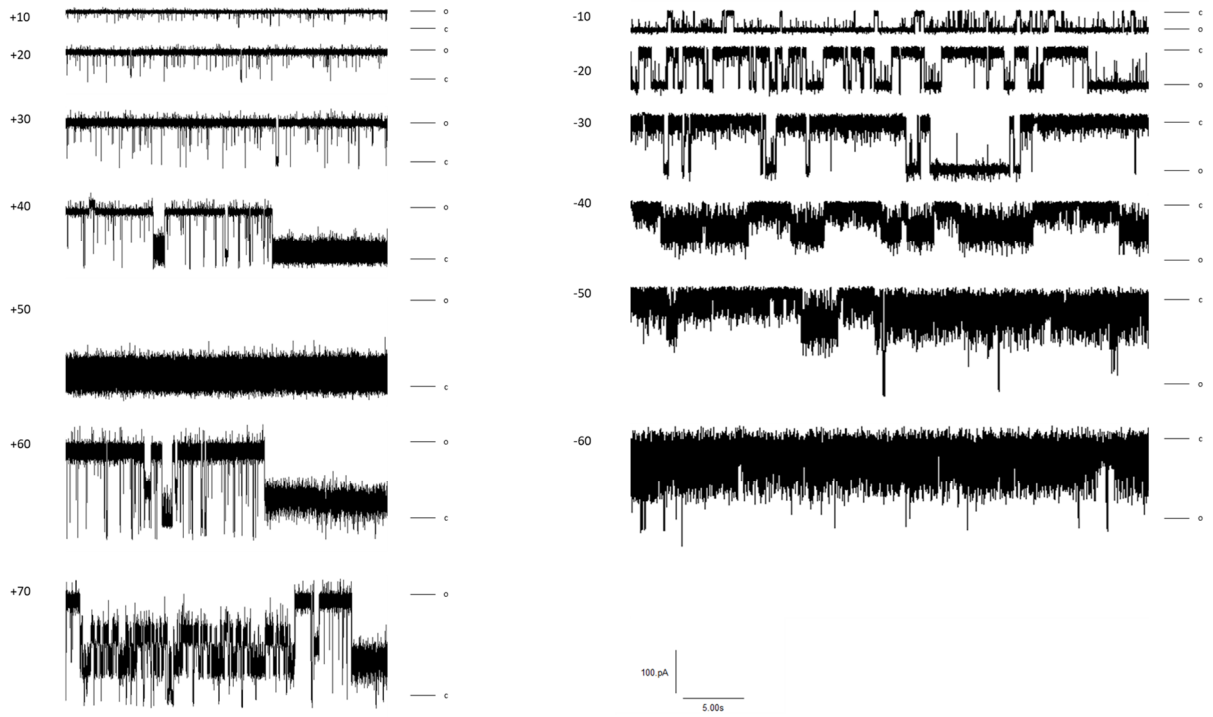

Sup Fig 7 *Representative current traces of ^{6xHis}SnoopTag-$^{+sig}$ΔcΔ5L at positive (left) and negative (right) voltages in 1 M KCl, 50 mM Tris-Cl pH=8. Numbers correspond to applied voltages in mV. O: Fully open state; C: Fully closed state. Notice that the presence of only one open and closed state for ΔcΔ5L variants is an idealized assumption; for instance, sub-states appear at +70 mV and -50 mV.*

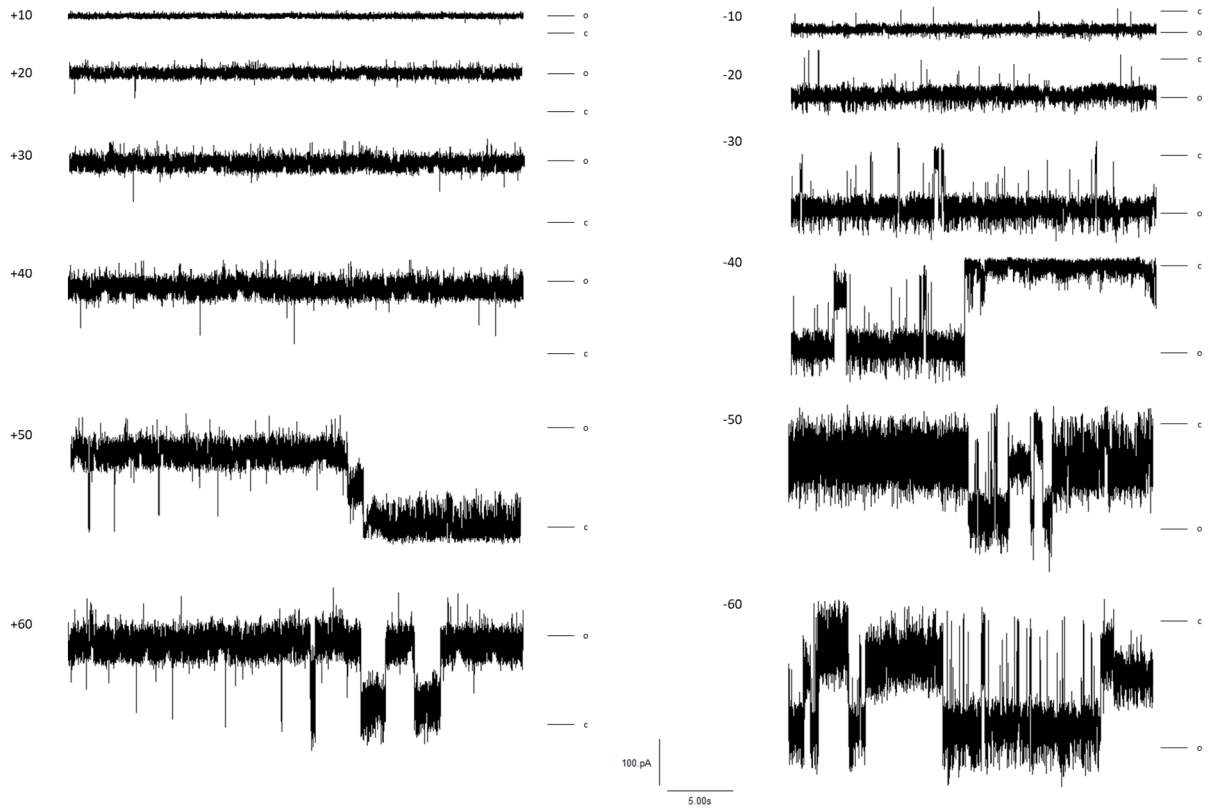

Sup Fig 8 *Representative current traces of $^{+sig}$ΔcΔ5L-2Link-SnoopTag^{6xHis} at positive (left) and negative (right) voltages in 1 M KCl 50 mM Tris-Cl pH=8. Numbers correspond to applied voltages in mV. O: Fully open state; C: Fully closed*

state. Notice that the presence of only one open and closed state for ΔcΔ5L variants is an idealized assumption; for instance, blocked sub-states appear at +50 mV and -60 mV. Shown measurements were performed by Sebastian Schaupp during his Master Studies.

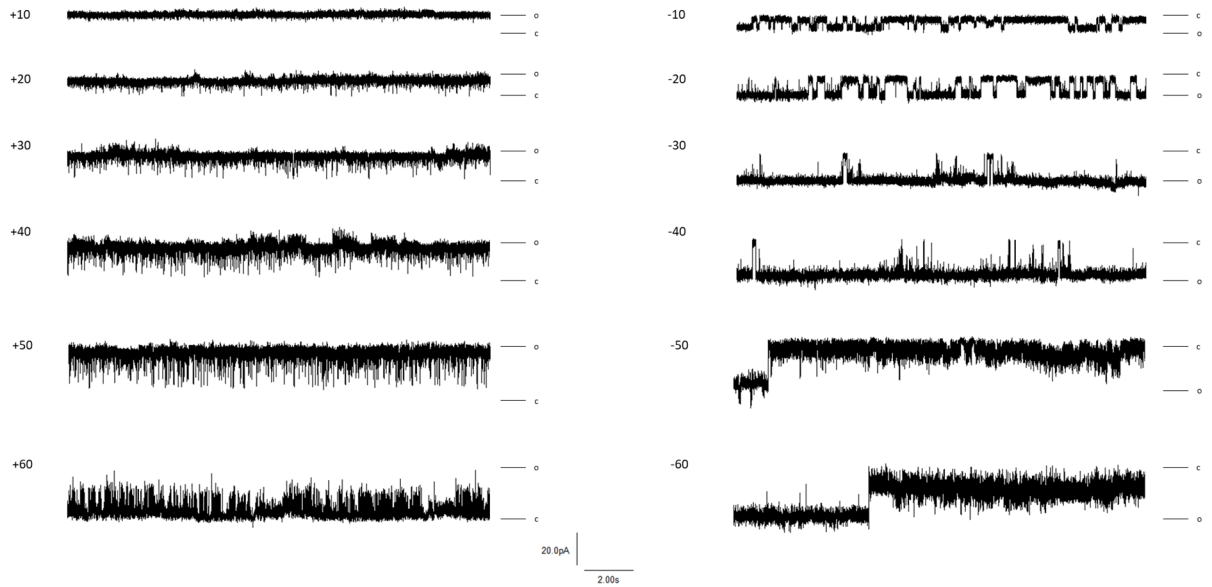

Sup Fig 9 *Representative current traces of $^{+sig}$ΔcΔ5L-10Link-SnoopTag^{6xHis} at positive (left) and negative (right) voltages in 150 mM KCl, 10 mM KH_2PO_4 pH=7.4. Numbers correspond to applied voltages in mV. O: Fully open state; C: Fully closed state. Notice that the presence of only one open and closed state for ΔcΔ5L variants is an idealized assumption; for instance, blocked sub-states appear at -50 mV.*

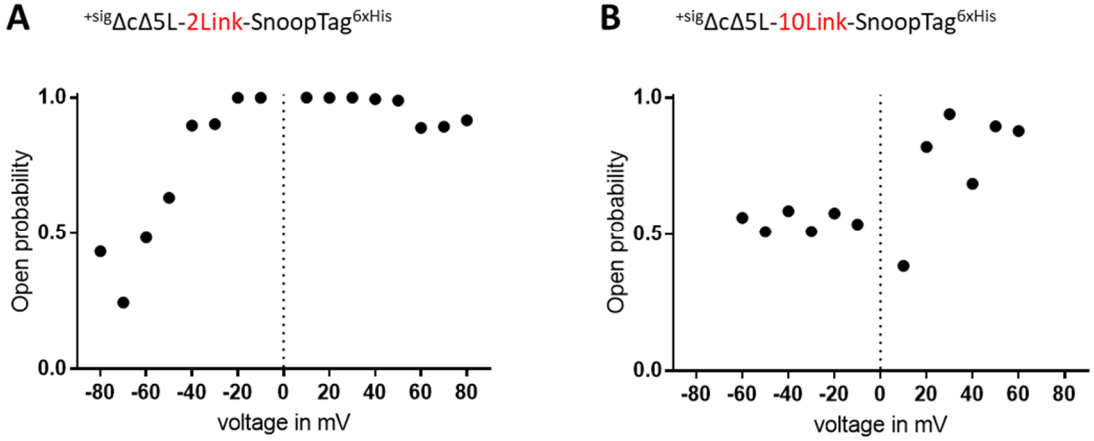

Sup Fig 10 *Representative open probability of $^{+sig}$ΔcΔ5L variants with C-terminal SnoopTags. A: $^{+sig}$ΔcΔ5L-2Link-SnoopTag^{6xHis} in 1 M KCl, 50 mM Tris-Cl pH=8; B: $^{+sig}$ΔcΔ5L-10Link-SnoopTag^{6xHis} in 150 M KCl, 10 mM KH_2PO_4 pH=7.4. The buffer difference is intended for comparison purposes, as in 1 M KCl, $^{+sig}$ΔcΔ5L-10Link-SnoopTag^{6xHis} was constitutively partially blocked.*

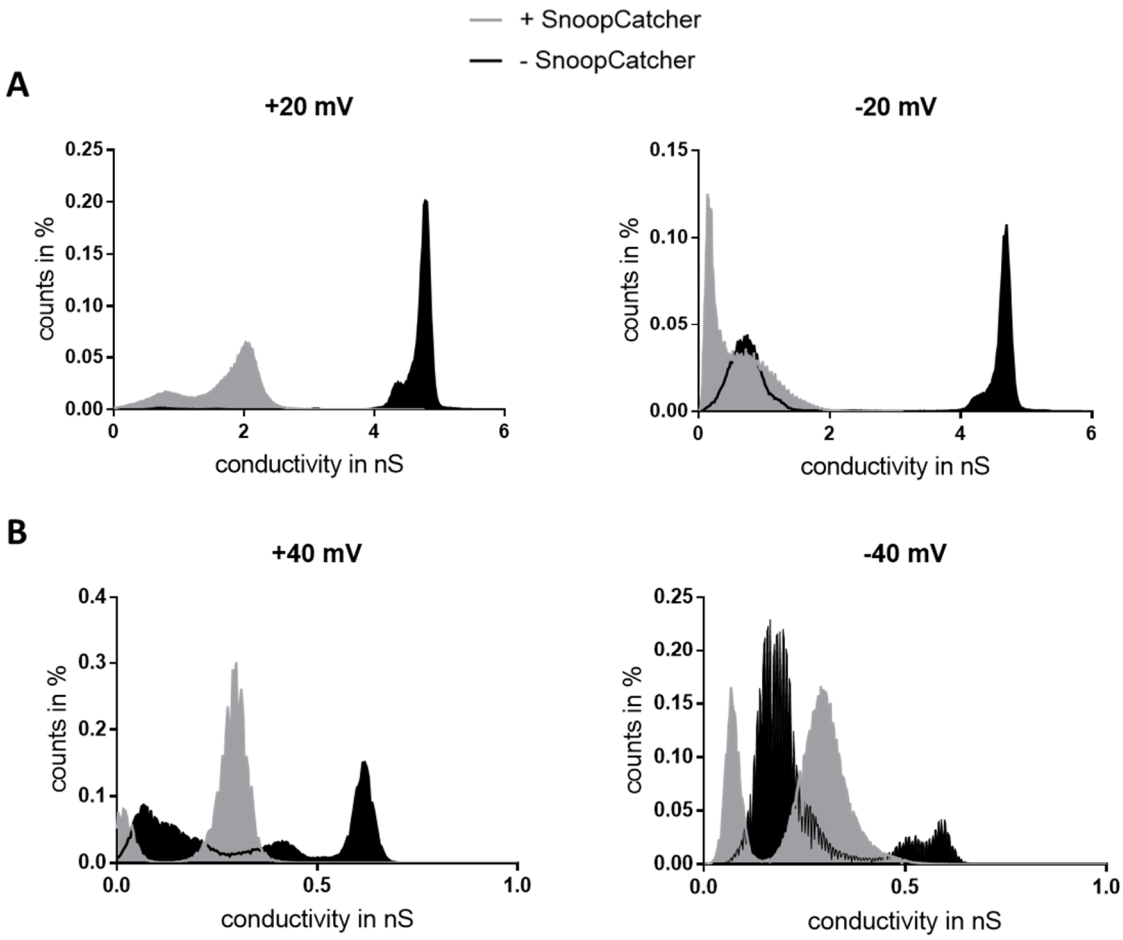

Sup Fig 11 *Change in conductivity of* ^{6xHis}*SnoopTag-*$^{+sig}$*ΔcΔ5L after SnoopCatcher/Tag reaction in different buffers. Shown are overlaid conductivity frequency histograms of* ^{6xHis}*SnoopTag-*$^{+sig}$*ΔcΔ5L before (black) and after (grey) the addition of SnoopCatcher-NB.* ***A****: Buffer was 1 M KCl, 50 mM Tris-Cl pH=8.* ***B****: Buffer was 150 mM KCl, 10 mM* KPO_4*, pH=7.4*

Sup text 2: In silico modelling of ^{6xHis}SnoopTag-$^{+sig}$ΔcΔ5L (Patrick Kunzmann, pers. comm.)

Homology modelling (performed by Patrick Kunzmann)

Both models were built with the *Modeller* software and its *loopmodel* functionality [364,365]. As template for both models, the PDB file 4CU4 [307] was chosen, representing a 2.3 Å resolution crystal structure of wtFhuA. Model A was created by aligning the long N-terminal tag with the cork domain, while model B was deliberately avoiding this alignment. The Snakemake software [366] enabled a reliable workflow.

Chapter 4
Bio-Functionalized Solid-State Nanopores

1. Introduction & Background

As discussed in the previous chapters, biosensors are powerful tools for a plethora of applications. Yet, one of the key challenges is the embedding of molecular switches in some sort of device, so they can be applied beyond academics and research. An ideal device must fulfil multiple requirements: Easy production and handling, robust performance, and simple, yet quick read-out, to name the most important.

Thus, the symbiosis of Life Sciences and Material Science offers great opportunities in health monitoring, point-of-care diagnosis and biosensing in general. Both disciplines rely on each other: Life Scientists identify and characterize biomarkers, while Material Scientists provide solutions to improve and simplify detection. At the core of this symbiosis lies the ability to link biochemical events to readily detectable electrical readouts. Electrical current is a superior output for multiple reasons: It happens on the millisecond scale, is highly sensitive and supporting electronics are generally smaller and more common than excitation sources or photodetectors, leading to better portability [367,368].

In this regard, miniaturization is a key technology. Especially microfluidic platforms have pushed biosensing approaches forward. Such miniaturized systems or microsystems offer many advantages. For instance, they allow parallel operation, save samples and material and can be produced at large scale [369]. Among these biosensing microsystems, **solid-state** or **"synthetic" nanopores (SSNs)** have emerged as powerful tools. During fabrication, their characteristics like material, geometry and surface charge can be precisely tuned to the desired application. Modification of the raw pores with specific receptor molecules introduces a sensing capability. Generally, the readout is based on changes in ionic current or rectification behaviour upon analyte binding [370–372].

In this chapter, fabrication and modification techniques of SSNs are discussed, with focus on modification with biochemical receptors and biosensing technologies. In cooperation with Ivana Duznovic from the Materials Analysis group at TU Darmstadt, a strategy for biofunctionalized SSNs was developed and tested. Specifically, I constructed and characterized an optimized immobilization peptide and multiple fusion proteins that allow oriented bioconjugation. As proof of concept, the biosensing platform was evaluated with nanobodies for the stress biomarker α-amylase and two fluorescent proteins.

1.1 Fabrication and properties of raw solid-state nanopores

The size and diameter of SSNs is highly variable. Depending on the application, preferred diameters lie in the range of 1-100 nm [55,373]. Based on IUPAC recommendation, the term nanopore is only suited for pores with diameters ≤ 100 nm [374]. Analytical SSNs have been implemented in a large variety of materials [55]. The most common include silicon materials, mainly silicon nitride [55,373,375] and glass [55,376], and polymer materials like poly(ethylene terephthalate) (PET) [370,377–379].

The choice of material dictates the adequate fabrication pipeline. For instance, nanopores in PET membranes are generated by firstly penetrating them with energetic heavy ions. This can be achieved at facilities like the UNILAC (Universal Linear Accelerator) in Darmstadt, Germany or the GANIL (Grand Accélérateur National d'Ions Lourds) in Caen, France [378,380]. The initial nanopores in the prepared polymer membranes serve as raw material for the generation of pores with desired geometries. The choice of adjustment method depends again on the material. For SiO_2- based nanopores, precise tuning is possible by using defocused electron beams [55]. For common PET membranes, chemical etching with NaOH is an inexpensive procedure and allows fabrication of various geometries, depending on the etching technique [55,381,382].

The geometry has a strong impact on the electrical behaviour of a nanopore. Due to the formation of an electrical double layer at the surface of the pores, conical SSNs show a diode-like behaviour, strongly reducing the current flow in one direction when a voltage is applied (Figure 40) [382,383].

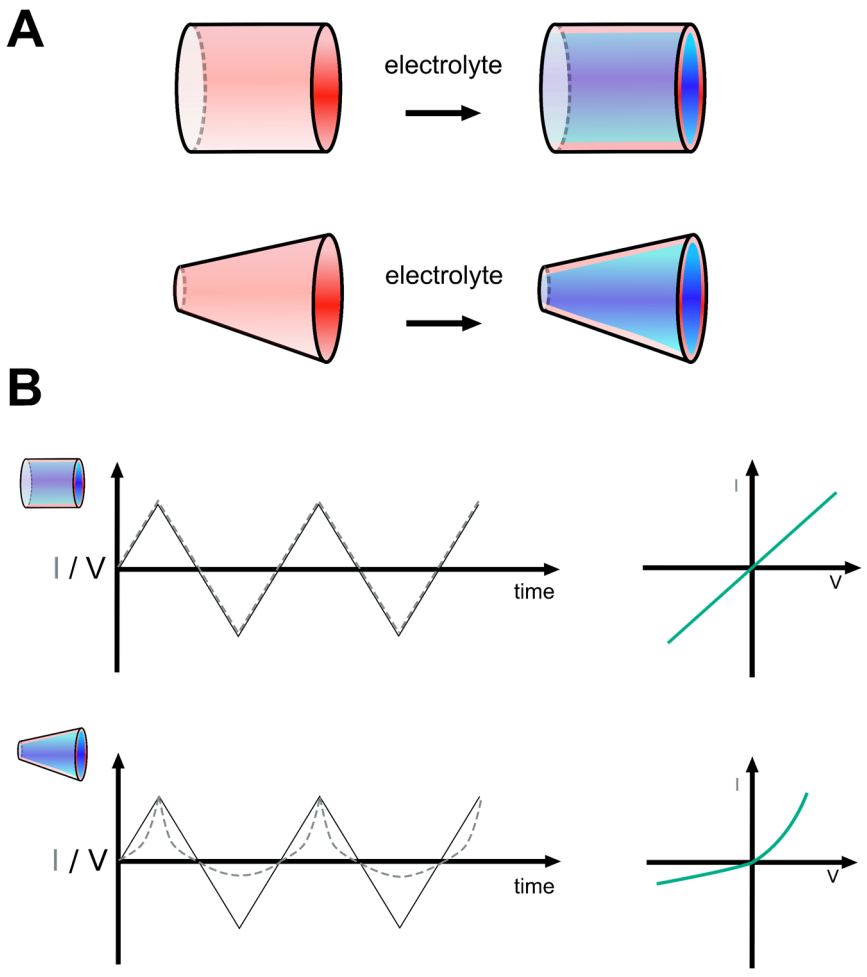

Figure 40 *Schematic depiction of electrical double layers inside SSNs and rectification behaviour. A: Cylindrical or conical pores PET pores with a layer of negative charges (red) develop an electrical layer of positive charges (blue) at the surface when exposed to electrolyte solution, rendering the pores anion-specific. B: The electrical double layer leads to a non-linear I-V behaviour in case of conical pores. The shown current profile (grey dotted line) is obtained if the electrode near the large aperture is grounded.*

This effect is quantified by the rectification factor *RF* via

$$RF = \frac{|I(+V)|}{|I(-V)|}, \tag{2}$$

where *I(-V)* and *I(+V)* are currents at equal voltage magnitudes but at opposite polarity [378,384]. Changes in *RF* are correlated to changes in the nanopore environment, hence *RF* is a useful factor for characterization of binding processes in SSNs [377,385,386].

“Blank” fabricated and etched SSNs interact only unspecifically with the surrounding solution, for instance via charge attraction or repulsion, thus they do not have any intrinsic sensing abilities [55]. While this is useful for certain applications that rely on distinguishable current blockades, like DNA translocation [387] or glycan and polysaccharide profiling [375], SSNs can be modified with nearly any type of receptor moiety.

Nonetheless, the surface groups of etched nanopores – e.g. the carboxylic acid groups of PET – are amenable for direct modification. This feature enabled development of simple ion and small molecule sensors [386,388,389]. However, by applying an additional layer of reactive groups, SSNs can be converted into a highly modular immobilization and sensing platform for complex analytes.

1.2 Immobilization techniques

For reasons of clarity, only techniques that allow receptor immobilization on non-porous surfaces or inside SSNs are covered in the following. Completely (meso)porous surfaces – including (protein) hydrogels [46,47,390], silica gels [391] and polymer meshes [392] – are omitted here. A respective review is found in [393].

1.2.1 Activated esters

Amino groups present in proteins or peptides have nucleophilic character. Thus, they will form an amide bond with activated esters. A straightforward approach to couple proteins or peptides to surfaces is therefore to activate the surface with an activated ester. A common choice for the generation of such activated ester is the consecutive treatment of the surface with 1-ethyl-3-(3-dimethylaminopropyl)-carbodiimide (EDC) and N-hydroxysuccinimide (NHS) or pentafluorophenol (PFP) [377,394]. As activation reagent, PFP is preferred as the reactivity of the formed pentafluorophenyl esters is an order of magnitude higher than that of NHS esters [395,396]. An alternative is the use of N,N′-disuccinimidyl carbonate (NDC) and 4-dimethylaminopyridine (DMAP) [397].

1.2.2 Self-assembled monolayers (SAM)

A well-studied way of rendering an inorganic (metallic) surface an organic one relies on spontaneous self-assembly of distinct molecules at the respective inorganic surface [398]. One of the best studied examples is the high affinity of alkanethiols to gold. When the alkanethiols bind to a gold surface, they self-assemble into an organized monolayer (SAM) [398]. By deliberately using mixtures of different alkanethiol head groups, various receptor moieties can be presented on the surface (Figure 41) [373,399]. These receptors can either serve as direct sensing moiety or as attachment point for proteins or peptides. Importantly, the alkanethiols

function as a useful spacer, thereby reducing unspecific protein binding and fouling (see remarks in section 1.4).

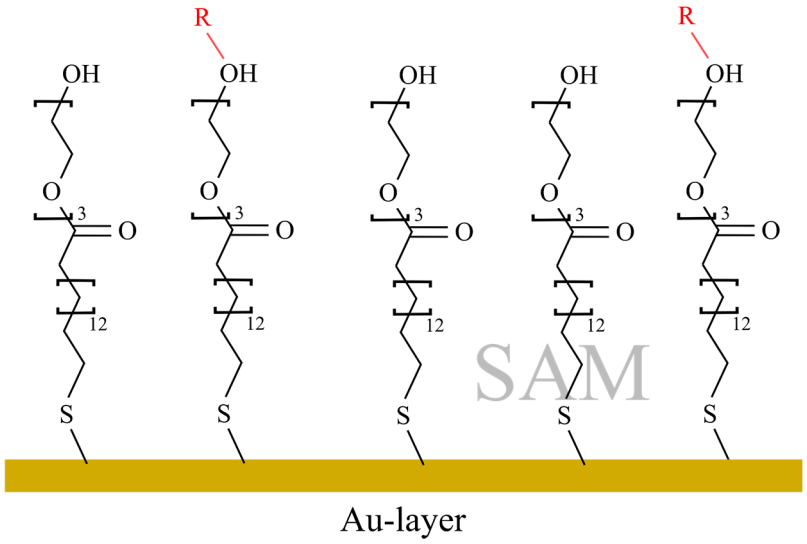

Figure 41 *Concept of self-assembled monolayers (SAM) in the form used by [373]. Triethylene glycol alkylthiols attach to a gold surface and self-assemble into structured monolayers. Attached head groups (R) provide specific binding sites. Modified after [373].*

1.2.3 Enzyme-mediated immobilization

Immobilization *via* enzymatic reactions has the advantage of being site-specific. In many cases, this is crucial to ensure that the protein is correctly oriented and thus active [400]. Useful enzymes include Sortase A [35,401,402], self-labeling tags like the SNAP-tag [401] and the engineered SpyTag/SpyCatcher system [403,404]. However, these techniques demand distinct modifications of the target protein coding sequence. This complicates matters for difficult-to-purify proteins like antibodies and may be one of the reasons that enzyme-mediated immobilization is less common compared to other techniques.

1.2.4 Click-chemistry

Another approach for site-specific immobilization relies on abiotic, bioorthogonal chemical groups. The Cu(I)-catalyzed and strain-promoted azide-alkyne cycloadditions (CuAAC and SPAAC, respectively) are the most prominent examples for biocompatible click-chemistry [401] (Figure 42). While SPAAC does not need copper as catalyst and therefore prevents possible denaturation reactions [405], the CuAAC method proceeds faster [401]. Both reactions work in aqueous solution at neutral pH and room temperature, although higher temperature can improve the CuAAC reaction [406].

If proteins or peptides are to be immobilized *via* click-chemistry, they must be modified to present one of the reactive groups. This is achieved for example by incorporation of unnatural *aa* that carry the bioorthogonal group [401].

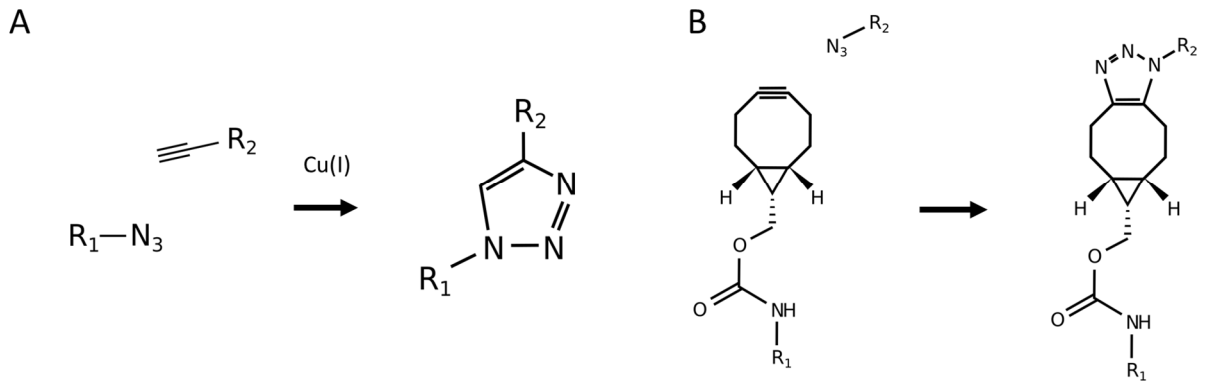

Figure 42 *Common biocompatible click chemistry reactions. A: Cu(I)-catalyzed azide-alkyne cycloaddition (CuAAC); B: Strain promoted azide-alkyne cycloaddition (SPAAC), here with a bicyclononye derivate. R_1 and R_2 are variable attachments and/or surfaces. Derived from [401].*

1.2.5 Unusual techniques

A rather harsh approach to combine a biological channel with SSNs was described by Balme *et al.* [407]. The authors added a solution of gramicidin A, a channel selective towards monovalent cations, to track-etched PVP membranes and impregnated the protein for 6 h at 72 °C. Thereby, they generated K^+ permeable, but H^+ impermeable membranes that could potentially be used for water purification. Other studies used similar approaches to combine biological channels with solid-state membranes [408]. Such studies have generally proof-of-concept character. Their reproduction is difficult, as the structure of the protein does not resemble the one of its actual natural context. Importantly, simple adhesion or impregnation will not work for every protein – especially considering surface fouling and orientation problems (see remarks in section 1.4).

1.3 Biomolecule functionalization of SSNs

Many biomolecules have evolved to bind specific ligands or analytes with high affinity. A famous example is the recognition of biotin by avidin, an interaction with a K_D of 10^{-15} M [22]. Immobilization of such specific receptors on or in SSNs – using the outlined techniques – has led to sensor designs for ions, *aa* and small molecules. Selected key publications are described in the following; for an extensive review see [409].

The described high affinity of avidin to biotin was exploited to test a PET single-nanopore system. When biotin was attached to the pore walls *via* EDC/PFP coupling, binding of streptavidin resulted in decreased currents that was not observed with control molecules [410]. Based on this approach, the Ensinger group at TU Darmstadt developed a variety of biochemical sensors [371,377,385,386,388,389,411].

One study combined the SAM concept with nanopores [373]. Immobilization of NTA-Ni^{2+} chelates on gold-covered silicon nitride allowed discrimination of his-tagged IgG-antibody subclasses while simultaneously revealing cooperative binding effects. To enable stochastic sensing, it was crucial to prevent receptor overloading of the pore.

In many cases – especially for complex analytes – immobilized antibodies are the receptors of choice. Respective early examples include the detection of ricin [412] and poly γ-D-glutamic

acid [394], followed by the detection of the cancer biomarker glycoprotein CA15-3 [413] and cSNAP-25, a cleavage product from botulinum type A [379]. These SSN-sensing studies have paved the way for ultrasensitive biosensor devices that can detect analytes even in complex samples. One nanofluidic device presented by Liu *et al.* uses nanoslits instead of nanopores (Figure 43) [372]. The authors demonstrate specific detection of Troponin T at concentrations down to 300 fM in human serum samples. Furthermore, they claim that fabrication of the nanoslit devices is straightforward. A drawback of the sensor is that it is not reusable in its presented form.

Other immobilized biological receptors include enzymes [414], bacterial substrate binding proteins [415] and DNA [416]. SSN designs based on immobilized DNA scaffolds were able to detect miRNA and DNA with sensitivity as low as 10 fM [417,418] and allowed the construction of a double-gated nanopore [416]. Regarding sequencing, sensors based on engineered biological nanochannels are leading, as briefly discussed in Chapter 3.

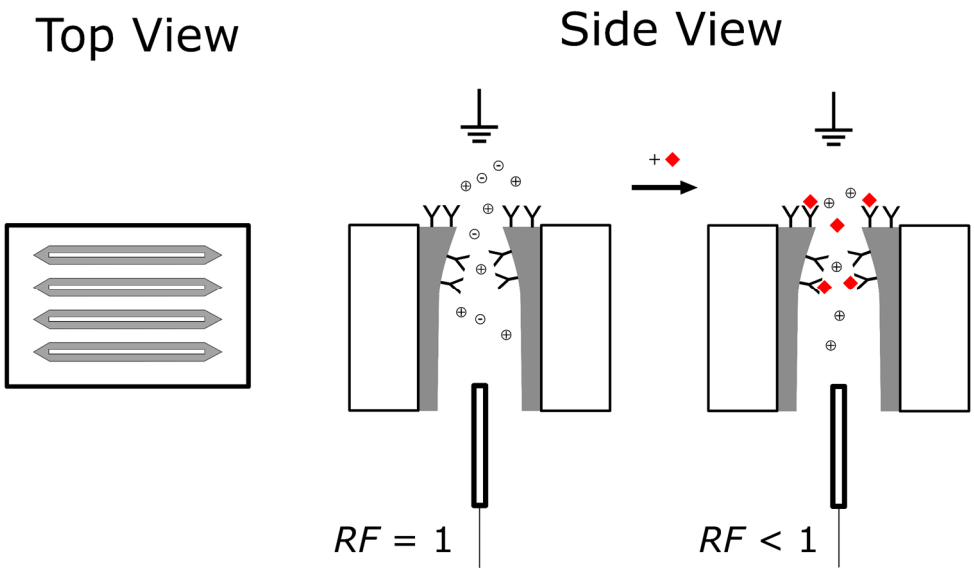

Figure 43 *Nanoslit-setup from Liu et al. [372]. Antibodies (Y) are immobilized on a triangular glass surface (grey). Presence of the corresponding analyte (red diamonds) – possessing a negative surface charge – results in concentration-dependent rectification factor (RF) changes. Figure adapted from [372]*

1.4 General considerations and challenges in SSN biosensing

The combination of protein biosensors with SSNs is demanding due to the following aspects:

- **Fouling**
- **Orientation**
- **Nanoconfinement**
- **Storability**

Most proteins are flexible, soluble molecules that become conformationally unstable when brought close to a surface, due to unspecific adhesion and absorption [398]. Such protein misfolding or denaturation poses a fundamental problem, not only in SSN sensing but in all research areas and applications that rely on protein immobilization. To prevent this **fouling**, installation of a spacer between the inorganic surface and the biological moiety is critical to

retain the functionality of the latter, especially if sensing requires conformational changes. Importantly, spacing does not only prevent fouling but also reduces steric clashes between immobilized proteins [393]. In this regard, spacing is similar important in multidomain fusion proteins, as discussed in Chapter 2.

In SSN biosensing, the installation of a spacer is most often achieved during surface preparation. For instance, the SAM method allows adjustment of the alkanethiol length to provide a proper spacing, and mixtures with "inactive" alkanethiol linkers even ensure spacing between the proteins themselves [373,398,419]. In the case of other coupling methods like EDC/(NHS or PFP), polymers represent by far the most common spacer [393,415], but peptides have also been used [420].

While spacing ensures that the immobilized protein is functional, it does not automatically account for correct **orientation**. A poorly oriented binding site may not be accessible to analytes or substrates, thus impeding the intended biosensing or enzymatic process [400,421]. In this regard, coupling *via* activated esters has the drawback of being unspecific, as all surface-exposed primary amines of proteins, e.g. lysine ε-amino groups, qualify for the coupling reaction [415].

In short, receptor coupling must proceed site-specific to ensure correct orientation. The SAM method allows this, as alkanethiols with specific head groups can be employed [373,398]. If applicable, the properties of the protein can be altered to allow enzymatic coupling. Recent examples include modification with a Sortase A tag, attachment of a bioorthogonal group for click-chemistry [401] or isopeptide bond formation systems [403]. Interestingly, these methods have been used for flat surface modification but not (yet) for SSN modification.

Much effort has been dedicated to interrogating the circumstances in **nanoconfinement**. Phenomena include altered isoelectric points, enrichment or depletion of ions [422]. Forming of additional fluidic phases is possible and affects the behaviour of flux and therefore biosensing in general [422]. The results of induced changes in the nano-environment are difficult to predict and subject of mathematical modeling [423]. Of special concern is the occurrence of elevated electrical fields that can lead to protein unfolding in narrow nanopores [424]. In short, the conditions inside nanopores are fundamentally different to those in solution [425]. This does not imply that nanoconfinement is generally unfavorable, on the contrary, it can also be beneficial [426]. Nevertheless, the presence of nanoconfinement adds another layer of complexity to SSN biosensing.

Considering that the success of a biosensor is evaluated by its specificity, sensitivity, stability, reproducibility and linearity [427], it is noteworthy that little work has been published with regard to **storability** and reusability of SSN biosensors. Exceptions are already commercially available systems that use biological nanopores, for example products from Oxford Nanopore Technologies [428]. While protein-catching surfaces can have a shelf life of multiple months [429], it is unclear to date if this could also be achieved for protein-modified SSNs.

1.5 Perspectives

Specific molecular interactions have become easily detectable *via* the simple readout of current changes. Advances in solid-state nanopore (SSN) fabrication, growing understanding of the processes in confined environments and tackling of electrical noise problems [430] further

strengthened the platform for combination with highly specific but “delicate” biological receptors.

Importantly, research at the interface of Life Sciences and Material Science is highly interdisciplinary. In this context, the boarders between both become more and more blurred. For instance, nanopore scaffolds are not limited to polymer- or glass materials, but can be achieved with biological molecules as well, for instance with DNA [431] or peptides [432]. One of the remaining key challenges is the integration of SSN biosensors into microfluidic devices. Progress is growing [433,434], and if reliable large scale production becomes feasible, such Lab-on-a-chip technologies could potentially revolutionize point-of-care diagnostics.

2. Methods

Standard methods are described in section 2.1, Chapter 2.

2.1 Protein Methods

Important properties of the proteins used in this chapter are summarized in Table 18.

Table 18 *Properties of proteins used in SSN experiments. Listed are sizes in kDa (and amino acids), theoretical pI and netto charge in e. Unless stated otherwise, values of theoretical pIs and netto charges were calculated via ProtParam [435]. It must be noted that the netto charge may not resemble the actual surface charge of a given protein but gives an approximation.*

Protein / Peptide	Size in kDa (*aa*)	Theoretical pI	netto charge in e at pH=7
Tether Peptide	7.5 (72)	10.2	+6
- As MBP fusion	50 (459)	5.6	-6
NB_{GFP}-$(GGS)_2$-SpyCatcher002	27.3 (256)	5.0	-9
$NB_{mCherry}$-$(GGS)_2$-SpyCatcher002	27.9 (265)	5.1	-7
$NB_{Amylase}$-$(GGS)_2$-Spycatcher002	27.6 (261)	4.7	-9
sfGFP-6xHis	27.8 (248)	6.2	-3 *
mCherry-strep	29.0 (260)	5.6	-7
α-amylase (porcine pancreas), glycosylated	51-54 (≈ 475)	6.4/7.5[436]	-3 **

*according to [437]
** not including glycosylation

2.1.1 Expression and Purification

The *E. coli* BL21(DE3)-RIL/pRK793 strain carrying the TEV protease (the autoinactivation-resistent mutant S219V [438]) was kindly provided by the Kolmar research group (TU Darmstadt). Expression and purification of TEV mainly followed published protocols. A 50 ml preculture was used to inoculate 1 l LB medium with 100 μg/ml ampicillin and 25 μg/ml chloramphenicol in a 3 l shaking flask to a starting OD_{600} = 0.05. When OD_{600} reached 0.3, 0.5 mM IPTG was added. Expression was performed for 3 h at 30 °C, and the culture was harvested *via* centrifugation and pellets stored at -20 °C. At the day of purification, cells were resuspended in buffer W (150 mM NaCl, 100 mM Tris-Cl pH=8) and crushed *via* four passes through an Emulsiflex C3 (Avestin). After centrifugation for 1 h at 14500 xg and 4 °C, the supernatant was sonicated for 30 s on ice *via* a sonicator (Qsonica) to destroy residual DNA. The sample was filtered through a 0.45 μm syringe filter. An ÄKTApure system and a 1 ml HisTrap HP column was used to purify TEV protease. Elution was performed in steps of 10 %, 20 %, 50 % and 100 % elution buffer (buffer W with 500 mM imidazole). Protein containing fractions were pooled and dialyzed against 3 l of 50 mM Tris-Cl pH=8, 50 mM NaCl, 1 mM EDTA and 1 mM DTT using 10 kDa MWCO Slide-A-Lyzer (Thermo Fisher Scientific) for 2 h at 4 °C. Protein purity was validated *via* SDS-PAGE. After centrifugation for 10 min at 16000 xg and 4 °C, 50 % glycerol was added to reach a final glycerol concentration of 20 %, and aliquots

with a protein concentration of about 1 mg/ml were flash frozen in liquid nitrogen and stored at -80 °C.

Sortase A5M, mCherry, NB_{GFP}-$(GGS)_2$-SpyCatcher002 and $NB_{mCherry}$-$(GGS)_2$-SpyCatcher002 were produced in *E. coli* BL21(DE3) transformed with the corresponding plasmid (pET24-SortaseA5M-strep, pFLinkC-XE-T7-mCherry-strep-LPETGG, pFLinkC-XE-T7-NB_{GFP}-$(GGS)_2$-SpyCatcher002-GASPAG-strep and pFLinkC-XE-T7-$NB_{mCherry}$-$(GGS)_2$-SpyCatcher002-GASPAG-strep, respectively). In all cases, a preculture was used to inoculate 800 ml of LB medium containing ampicillin (90 μg/ml) in a 3 l shaking flask, starting at OD_{600} = 0.1. Protein expression was induced with 0.5 μM IPTG at OD_{600} = 0.6 and performed for 4 h at 25 °C, except for Sortase A5M (30 °C). Cultures were harvested *via* centrifugation and washed once with buffer W before stored at -20 °C until used. At the day of purification, the cells were resuspended in 40 ml of buffer W each (150 mM NaCl, 100 mM Tris-Cl pH=8) and crushed *via* four passes through an Emulsiflex C3 (Avestin). After centrifugation at 25000 xg for 1 h at 4 °C, the sample was filtered through a 0.45 μm syringe filter. An ÄKTApure system and a 1 ml StrepTrap HP column was used to purify the proteins (8 CV equilibration, 8 CV wash, 5 CV elution). The protein was eluted in buffer E (150 mM NaCl, 100 mM Tris-Cl, 2.5 mM desthiobiotin, pH=8) and the concentration estimated *via* nanodrop. After a final buffer exchange to 100 mM KCl and 10 mM Tris-Cl pH=8 *via* PD 10 columns, protein aliquots were flash frozen in $N_{2(l)}$ and stored at -80 °C until needed.

SpyTag containing Tether Peptide was produced as MBP-fusion protein in *E. coli* BL21(DE3) transformed with the plasmid pET24-MBP-Tether-Peptide-LPETGG. A preculture was used to inoculate 2 l of LB medium containing kanamycin (50 μg/ml) in a 5 l shaking flask, starting at OD_{600} = 0.1. Protein expression was induced with 0.5 μM IPTG at OD_{600} = 0.5 and performed for 4.5 h at 30 °C. Cultures were harvested *via* centrifugation and stored at -20°C overnight. The next day, the cells were resuspended in 70 ml of buffer W (150 mM NaCl, 100 mM Tris-Cl pH=8) and crushed *via* four passes through an Emulsiflex C3 (Avestin). After centrifugation at 25000 xg for 1 h at 4 °C, the supernatant was sonicated for 30s on ice *via* a sonicator (Qsonica) to destroy residual DNA. The sample was filtered through a 0.45 μm syringe filter. An ÄKTApure system and a 5 ml StrepTrap HP column was used to purify the protein (8 CV equilibration, 8 CV wash, 5 CV elution). The protein was eluted in buffer E (150 mM NaCl, 100 mM Tris-Cl, 2.5 mM desthiobiotin, pH=8) and the concentration estimated *via* nanodrop. Protein aliquots were flash frozen in $N_{2(l)}$ and stored at -80 °C until needed.

sfGFP, GFP(-30) and Sortase A7M were produced in *E. coli* BL21(DE3) transformed with the corresponding plasmid (pACYCT2-sfGFP-6xHis, pET29-6xHis-(-30)GFP (Addgene #62936) and pET24-SortaseA7M-6xHis). Respective main cultures were induced with 0.5 mM IPTG and expression performed for 4 h at 37 °C. Cultures were harvested *via* centrifugation and stored at -20°C overnight. The next day, cells were resuspended in cold His-Tag equilibration buffer (500 mM NaCl, 20 mM $NaPO_4$, 20 mM Imidazole pH=7.4) supplemented with a protease inhibitor tablet and crushed *via* four passes through an Emulsiflex C3 (Avestin). After centrifugation at 25000 xg for 1 h at 4 °C, the respective sample was filtered through a 0.45 μm syringe filter and applied on a 1 ml HisTrap HP column that was equilibrated with 10 CV His-Tag equilibration buffer. Sample was loaded and the column was washed with 8 CV of His-Tag equilibration buffer at 5 % elution buffer (500 mM NaCl, 20 mM $NaPO_4$, 300 mM Imidazole pH=7.4), before protein was eluted over a 10 CV gradient, starting at 5 % elution buffer and ending at 100 %. Protein containing fractions were pooled and buffers exchanged *via* PD 10 columns to His-Tag storage buffer (150 mM NaCl, 20 mM $NaPO_4$ pH=7.4), and with the

exception of sfGFP (which was stored at 4°C), purified proteins were flash frozen in $N_{2(l)}$ and stored at -80 °C until needed.

2.1.2 Azp-coupling and TEV-cleavage

Purified proteins were thawed on ice. Azp-coupling reactions were performed in 100 μl reactions in 1.5 ml reaction tubes in 100 mM NH_4HCO_3 buffer. Azp was added from a 1 M stock (acetic acid) to a final concentration of 100 mM. Sortase A7M or Sortase A5M was added to a final concentration of 10 μM (as estimated *via* nanodrop) and MBP-Tether-Peptide of about 60 μM. Azp-coupling reaction was performed for 3 h (Sortase A7M) or 1 h (Sortase A5M) at 37 °C. Subsequently, the reactions were stopped by addition of 0.2 % formic acid (in case of Sortase A7M) or 20 mM EDTA (in case of Sortase A5M) and buffer was exchanged to 50 mM Tris-Cl, 2 mM DTT, pH=8 *via* a Vivaspin 20 filtration unit (Sartorius).

Purified TEV protease was added to a final concentration of 30 μg/ml. TEV cleavage was performed at 18 °C over night under slight shaking. On the following day, successfully cleaved peptide was separated from the larger components (TEV, Sortase A7M or A5M, MBP) *via* centrifugation through a Vivaspin 500 (10 kDa MWCO) at 10000 xg in a tabletop centrifuge. Peptide purity in the filtrate was examined by a 4-12 % SDS-PAGE analysis.

2.1.3 *In vitro* verification of Azp-coupling

To verify the Azp-tagging of MBP-Tether-Peptide, a copper click-reaction was performed to attach a 5-FAM-alkyne to the protein containing the azide-moiety. 15 μM 5-FAM-alkyne and about 5 μM MBP-Tether-Peptide were coupled in 100 mM HEPES-KOH pH=7, 0.1 mM $CuSO_4$, 5 mM sodium ascorbate for 1 h at RT under slight shaking. The reaction was stopped by addition of an excess of EDTA relatively to $CuSO_4$. Copper and unreacted 5-FAM-alkyne were separated from the sample *via* Vivaspin 500. An aliquot of the retentate was treated with TVMVp in 100 mM HEPES-KOH pH=7, 2 mM DTT, and SDS-PAGE was performed.

2.1.4 *In vitro* verification of SpyTag-SpyCatcher reaction

5-FAM-tagged MBP-Tether-Peptide was subjected to a SpyTag-SpyCatcher reaction. NB_{GFP}-SpyCatcher002 and 5-FAM-tagged MBP-Tether-Peptide were mixed at an approximately 1:1 molar ratio in either 100 mM HEPES pH=7 or buffer W and incubated either at 4 °C for 14 h or at RT for 1 h, directly followed by SDS-PAGE analysis.

2.1.5 Fluorescent SDS-PAGE

Protein samples containing fluorophores were semi-denaturated with heat (10 min 72 °C) and loaded on polyacrylamide gels. After the run, fluorescence was recorded at a Gel Imager AI600 (Amersham).

2.1.6 Microscale Thermophoresis

For each measurement, a dilution series of NB_{GFP}-SpyCatcher (2 μM – 0.24 nM) in buffer W (150 mM KCl, 100 mM Tris-Cl pH=8) supplemented with 0.05 % Tween 20 to prevent unspecific binding was prepared. After mixing with the fluorophore (which concentration was

kept constant), capillaries were filled with the respective solutions and inserted into the instrument (Monolith NT.115). Measurements were analysed with NT analysis software.

2.2 I-V Measurements

The setup used for the I-V measurements at the Materials Analysis group, TU Darmstadt, is described in [439]. The I-V curves were recorded by applying a scanning triangle voltage ranging from -1 to +1 V for three periods, each with 80 data points (1150 ms per point). As discussed, the type of the nanopore (cylindrical or conical) impacts the shape of the resulting I-V curve (Figure 40 B). All measurements were performed in 0.1 M KCl in 1x PBS, pH=7 unless stated otherwise. All measurements were performed by Ivana Duznovic and co-workers. I included their data in my thesis for clarity and to allow discussion.

3. Results

3.1 Conceptualization

As discussed in section 3.1 of Chapter 1, nanobinders like V_HHs or nanobodies offer many advantages. Despite these advantages, a combination of solid-state nanopores (SSNs) with nanobodies as receptors has not been reported to date, in contrast to antibody-functionalized SSNs [412,413]. Thus, an immobilization concept was developed in cooperation with Ivana Duznovic from the Materials Analysis group with the aim of investigating the feasibility of nanobody-SSN biosensor scaffolds.

Regarding the nanobodies, we chose to test three different nanobodies: An anti-GFP nanobody (NB_{GFP}) [440], an anti-mCherry nanobody ($NB_{mCherry}$, LaM-4 from [441]) and an anti-α-amylase nanobody ($NB_{Amylase}$, AMD9 from [25]). The first two bind to green and red fluorescent proteins GFP [442] and mCherry [443] with K_Ds of 1.4 nM and 0.2 nM, respectively, while the $NB_{Amylase}$ binds the stress biomarker α-amylase with a K_D of 3.5 nM. The advantage of using fluorescent proteins is that an evaluation of the platform *via* microscopy becomes accessible, whereas α-amylase is an important biomarker worth detecting in clinics as increased levels may hint towards pancreatic diseases [444].

Regarding the molecular design, spacing and orientation were deemed pivotal. Firstly, a proper spacing between the nanobody and the SSN surface will ensure protein flexibility and prevent fouling. Secondly, a correct orientation of the nanobody towards the lumen of the pore is needed to enable binding of analytes. To ensure both, we introduced a multifunctional spacing peptide ("tether") that gets coupled to the SSN surface *via* strain-promoted cycloaddition (SPAAC). Apart from flexible linker sequences, this Tether Peptide contains the following features from N- to C-terminus:

1. SH3-recognition motif
2. SpyTag002
3. TVMV protease cleavage site
4. StrepTagII for purification
5. Sortase A motif

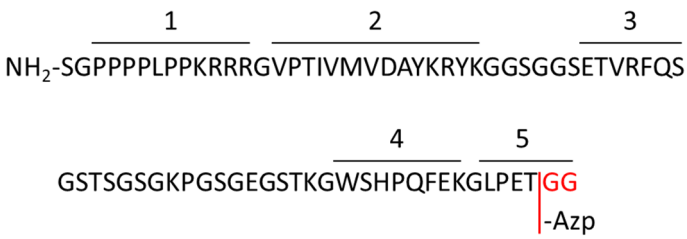

Figure 44 *Tether Peptide amino acid sequence. Numbers correspond to listed features. Sortase A motif is LPETGG; the terminal glycines (red) are exchanged by azidopropanamine (Azp) during Sortase reaction.*

A crucial part of this Tether Peptide is the SpyTag002 motif that can form an isopeptide bond with a SpyCatcher002 fusion protein [44]. As the fusion partner of SpyCatcher002 is modularly exchangeable on the genetic level, this approach accelerates screening of suitable receptors and the biosensor development pipeline in general.

The C-terminal LPETGG motif enables enzymatic attachment of a bioorthogonal functional group, for example an azide, *via* improved Sortase A variants [39,445]. Thereby, the Tether Peptide can be immobilized site-specifically at its C-terminus, for example *via* Strain-promoted azide-alkinyl cycloaddition (SPAAC) to a dibenzocyclooctyne-amine (DBCO)-functionalized surface [446].

A C-terminal immobilization was deemed superior to an N-terminal immobilization due to favored orientation of the proteins: When SpyTag002 is coupled to the nanopore surface *via* its

C-terminus, both N-termini of SpyTag002 and SpyCatcher002 point away from the surface after isopeptide bond formation (design A, Figure 45). This implies that a fusion domain at the N-terminus of SpyCatcher002 will also point away from the surface. Thereby, the chance of unspecific surface absorption that could lead to protein fouling is reduced. In contrast, N-terminal coupling of SpyTag002 and C-terminal domain fusion to SpyCatcher002 will likely lead to unfavorable crowding at the nanopore surface, hampering analyte recognition (design B, Figure 45). Moreover, the SpyTag002/SpyCatcher002 complex in design A serves as additional spacing element between the receptor and the pore wall.

During preparation of the SSN membrane, the chemical functionalization proceeds unspecifically, meaning not only inside the nanopore but also near the aperture at the polymer surface. However, specific immobilization of receptors only inside the nanopore would reduce background signals and thus improve the biosensing qualities of the scaffold. Following this rationale, the TVMV protease (TVMVp) cleavage site and the SH3-recognition motif were included in the Tether Peptide sequence. A fusion protein consisting of TVMVp and an SH3 domain should be able to remove excess receptors on the polymer surface after immobilization, while receptors inside the SSN should be less accessible. SH3 acts as an recruiting domain that enhances cleavage rates by increasing the local concentration of TVMVp at its substrate [28].

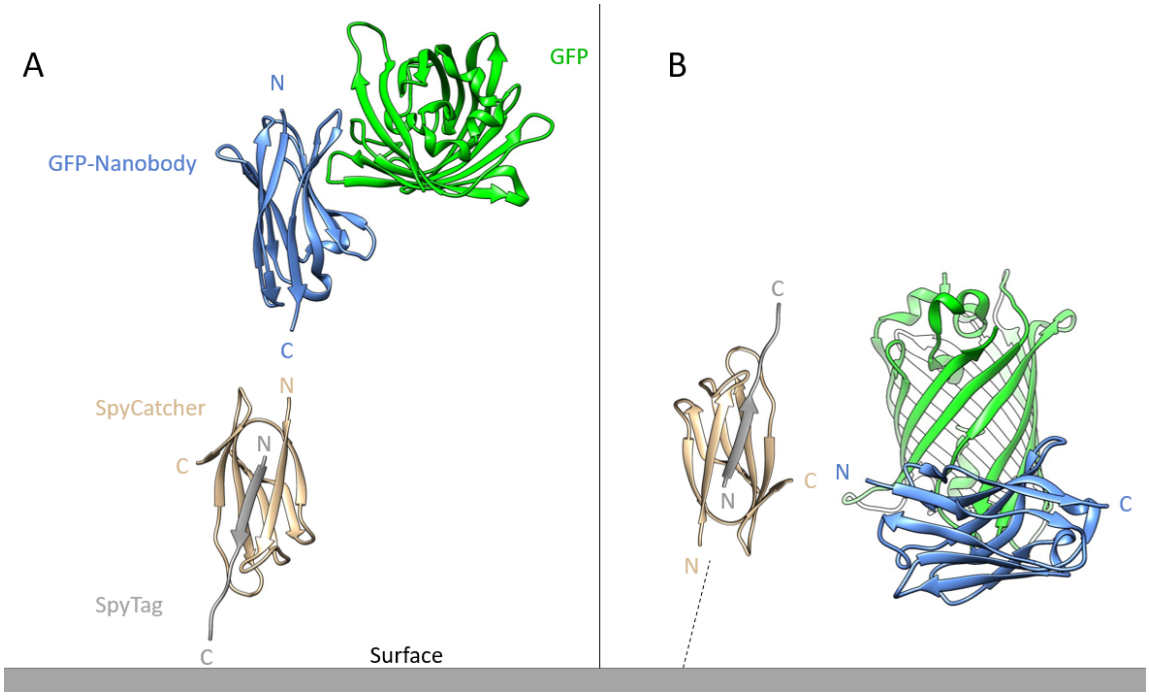

Figure 45 *Molecular design for oriented immobilization inside solid-state nanopores, exemplified with NB_{GFP}. A) Design A: C-terminal immobilization of SpyTag combined with N-terminal attachment of GFP-Nanobody (NB_{GFP}) to SpyCatcher (favorable); B) Design B: N- or C-terminal immobilization of SpyTag combined with C-terminal attachment of NB_{GFP} to SpyCatcher (unfavorable). Proteins were visualized with UCSF Chimera [120] using PDB entries 3K1K & 4MLS.*

3.2 Protein purification and characterization

Typically, protein purification by 6xHis-Tag or StrepTagII yielded 2-4 mg purified protein per l culture as depicted in Table 19. Variations are likely a results of used expression vectors, experimental conditions and / or protein in general. Due to its small sized (7.5 kDa), Tether Peptide was expressed and purified as MBP-fusion (section 2.1.1).

Table 19 *Typical yields of proteins used in the SSN project. NB with subscript denotes specific nanobodies.*

Protein	Size (kDa / AA)	Expression vector	Purification	Typical yield of pure protein (per l culture)
Tether Peptide (expressed as MBP-fusion)	7.5 / 72	pET24	Strep-Tag	5-8 mg
Sortase A7M	17.9 / 156	pET24	His-Tag	3-4 mg
Sortase A5M	18 / 158	pET24	Strep-Tag	1-2 mg
$NB_{Amylase}$-$(GGS)_2$-SpyCatcher002	27.6 / 261	pFlink-XE	Strep-Tag	2-3 mg
NB_{GFP}-$(GGS)_2$-SpyCatcher002	27.3 / 256	pFlink-XE	Strep-Tag	4-5 mg
$NB_{mCherry}$-$(GGS)_2$-SpyCatcher002	27.9 / 265	pFlink-XE	Strep-Tag	2-3 mg
SH3-sFv2linker-TVMVp*	35.5 / 322	pFlink-XE	Strep-Tag	2-4 mg

* self-cleaving variant MBP-$TVMV_{site}$-SH3-^{sFv2link}-TVMVp-strep. sFv2link: GSEGSTSGSGGGGSGAGSTKG

Following a published protocol from [39], an azidopropanamine (Azp) was attached to purified MBP-Tether Peptide *via* Sortase A7M. To verify the reaction success, the product was incubated with 5-Fluorescein-alkyne (FAM-alkyne) *via* copper-catalyzed azide-alkyne cycloaddition (CuAAC) [406]. Excess FAM-alkyne was depleted *via* Vivaspin 500 concentrator. As can be concluded by SDS-PAGE (Figure 46), both Sortase coupling and CuAAC were successful. Importantly, when the modified Tether Peptide was cleaved from the MBP *via* TEV protease, the large MBP domain lost its fluorescence (lane 3), meaning that Sortase A7M specifically attached Azp to the LPETGG motif *via* C-terminal transpeptidation. The FAM-modified MBP-Tether Peptide was employed to verify the SpyTag002-SpyCatcher002 coupling reaction. SDS-PAGE confirmed successful isopeptide bond formation between the modified protein and NB_{GFP}-$(GGS)_2$-SpyCatcher002 for various conditions (Figure 47).

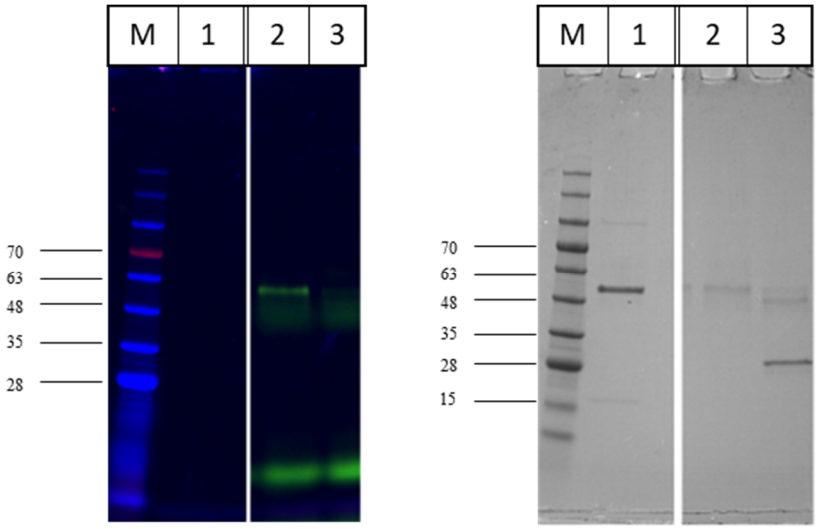

Figure 46 *In vitro verification of Azp-coupling. Left: Fluorescent image of the performed SDS-PAGE. Right: Bright light image of the same SDS-PAGE. M Marker BlueStar Prestained (Nippon Genetics), label in kDa; 1 MBP-Peptide-Azp before Copper-Click reaction with FAM-Alkyne; 2 Coupled MBP-Peptide-FAM, visible as a green fluorescent band; 3 TEV protease cleaved MBP-Peptide. TEV appears at about 27 kDa.*

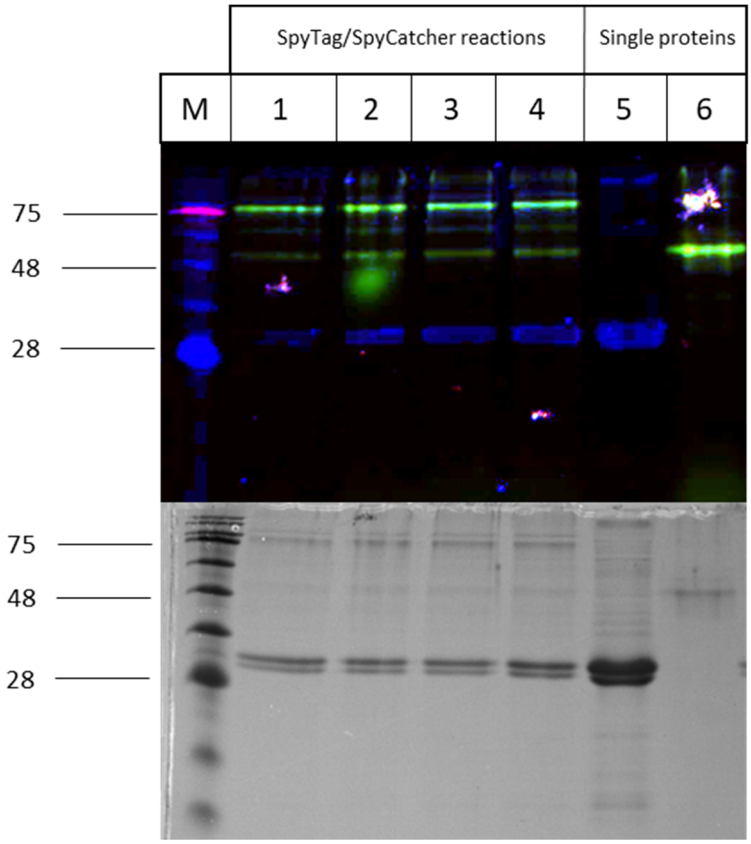

Figure 47 *In vitro verification of SpyTag-SpyCatcher reaction. Top: Fluorescent image of the performed SDS-PAGE; Bottom: Bright light image of the same SDS-PAGE after Coomassie staining. M Marker BlueStar (Nippon Genetics); 1-4) SpyTag-SpyCatcher reactions under different conditions. 1) 4 °C O/N in HEPES-KOH pH=7; 2) 4 °C O/N in buffer W pH=8; 3) RT 1 h in HEPES-KOH pH=7; 4) RT 1 h in buffer W pH=8; 5 NB_{GFP}-$(GGS)_2$-SpyCatcher002; 6) MBP-Peptide-FAM. Expected sizes: MBP-Tether Peptide 50 kDa; NB_{GFP}-$(GGS)_2$-SpyCatcher002: 27 kDa; Both together: 77 kDa. Obtained double and multi-bands result from semi-denaturation of NB_{GFP} proteins that contain disulfide bonds.*

As an alternative to the Ca^{2+} independent Sortase A7M, the pentamutant Sortase A5M was tested. This mutant has a 140-fold higher activity than wt Sortase [38]. As Sortase A5M requires Ca^{2+} as a cofactor, it can be inactivated by EDTA addition. Sortase A5M proved superior to Sortase A7M regarding Azp coupling efficiency (Figure 48). Moreover, no unspecific cleavage products were observed in contrast to the Sortase A7M batch reaction. These may result from cleavage at aspartyl residues due to the use of 0.2 % formic acid as deactivation agent [447].

Finally, the general functionality of purified nanobodies was verified in solution by a simple pulldown assay (Figure 49). MBP-eGFP^{6xHis} (71 kDa, final concentration 9 μM, kindly provided by Wadim Weber) was mixed with a GST-NB_{GFP} fusion protein (42 kDa, final concentration 22 μM), diluted in 300 mM NaCl, 50 mM $NaPO_4$ pH=8 and applied onto a prepacked Ni-IDA column. The column was washed two times with the same buffer (W1 & W2) and the proteins were eluted in two steps with 300 mM NaCl, 300 mM Imidazole, 50 mM $NaPO_4$ pH=8 (E1 & E2). As the GST-NB_{GFP} protein did not contain a 6xHis-tag, it remained coupled to MBP-GFP-6xHis during the pulldown assay, verifying the functionality of the nanobody.

Although the proteins in this assay are not the same as the ones used for SSN modification, the pulldown assay demonstrates that the purification pipeline of the lab yielded correctly folded, active nanobodies. In an additional experiment with a supercharged GFP variant, a microscale thermophoresis experiment further verified correct binding of sfGFP by purified NB_{GFP} (see section 3.5).

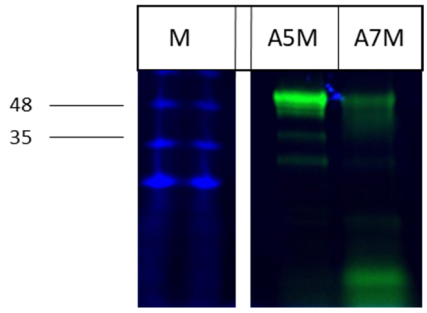

Figure 48 *Comparison of Sortase A5M and Sortase A7M via fluorescent SDS-PAGE. M: Protein Marker BlueStar Prestained (Nippon Genetics), sizes in kDa. Sortase A5M shows higher coupling efficiency and less side product formation than Sortase A7M.*

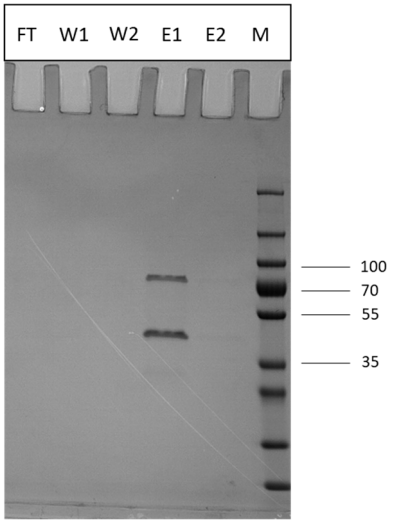

Figure 49 *Pulldown assay validates the functionality of purified GFP-nanobody fusion protein. FT: Flowthrough; W1 & W2: Wash 1 & 2; E1 & E2: Elution 1 & 2. Samples were analyzed on a Mini-PROTEAN^{TM} TGX precast gel (Bio-Rad). M: Protein Marker BlueStar Prestained (Nippon Genetics), sizes in kDa. GST-NB_{GFP} coelutes with MBP-eGFP^{6xHis}.*

3.3 Downstream Processing of Tether Peptide

With purified and active proteins at hand, Tether Peptide was prepared for coupling to solid-state nanopores (SSNs). Following Azp attachment *via* Sortase, MBP was cleaved with TEV protease and, together with the Sortase, separated from the small 7.5 kDa peptide *via* 10 kDa

MWCO concentrators (Figure 50). As the downstream process involves multiple buffer exchange and concentration steps (see section 3.2), ≈ 1.5 mg MBP-Tether Peptide were used for each downstream batch to achieve sufficient amount of modified peptide. The Tether Peptide (in 50 mM TRIS-Cl, pH = 8) was then given to Ivana Duznovic and stored at 4 °C until coupled to DBCO-functionalized PET SSNs.

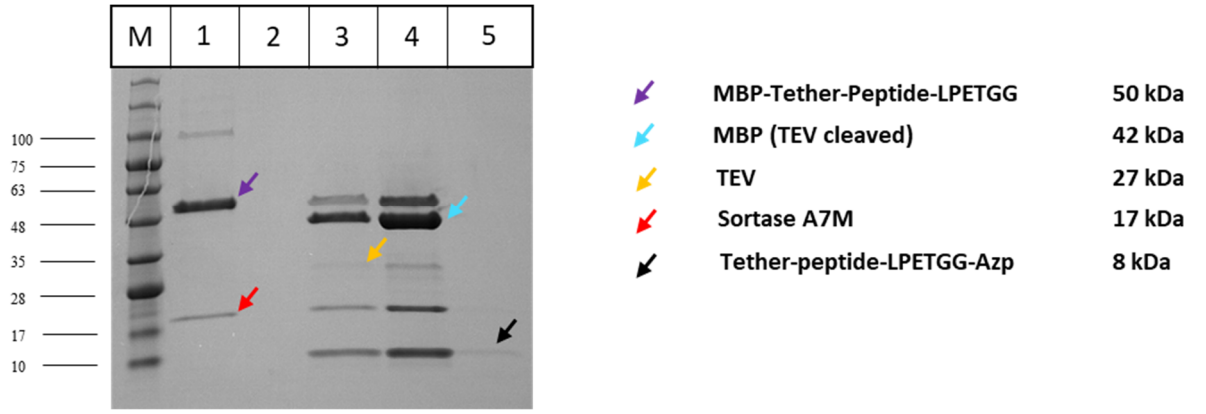

Figure 50 *Tether Peptide downstream processing. A precast TGX gradient gel (Bio-Rad) was used. M Marker BlueStar (Nippon Genetics), sizes in kDa; 1 Reaction mix after Sortase A7M reaction; 2 Flowthrough 10 kDa MWCO concentrator (step: depletion of residual Azp); 3 After TEV-cleavage (O/N 18 °C); 4 Retentate after TEV cleavage; 5 Filtrate after TEV cleavage, containing the desired Tether Peptide.*

3.4 Solid-state nanopore modification

All immobilization experiments and I-V measurements were carried out by Ivana Duznovic and co-workers in the Materials Analysis group laboratories. The workflow was divided into four consecutive steps:

1. Asymmetrical pore etching of irradiated PET foils
2. DBCO coupling *via* EDC/PFP chemistry
3. Tether Peptide coupling *via* SPAAC
4. Nanobody coupling *via* SpyTag/SpyCatcher isopeptide bond

The general feasibility and robustness of the workflow was analyzed both with conical single pores and multipore membranes ($>10^4$ pores / cm^2).

3.4.1 Single pore membranes

After each modification step and extensive washing, I-V curves were measured in 0.1 M KCl. The results of single pore experiments are shown in Figure 51 and Table 20. Attachment of uncharged DBCO led to an expected lower ionic conductance, but also to an unexpected rectification factor (*RF*, equation 1) slightly lower than 1. This phenomenon is most likely caused by cation-π interactions between the C-C triple bond of DBCO and K^+, leading to an apparent positive layer und thus rendering the pore weakly anion selective [448,449]. In the next step, coupling of Tether Peptide led to increased conductivity, while the *RF* remained < 1 due to the peptides net charge of +6 e at the given pH (= 7). The following attachment of SpyCatcher002-NBs with net charges between -6/-8 e resulted in *RF*s > 1. Importantly, while the size of the tip diameter (A: ≈ 45 nm, B: ≈ 26 nm, evaluated by Ivana Duznovic *via* scanning

electron microscopy) impacted the overall conductivity and the nanopores response to attachment, the trend regarding rectification remained similar for both geometries. The final rectification behaviour thus implies an internal quality control for the success of SSN biofunctionalization.

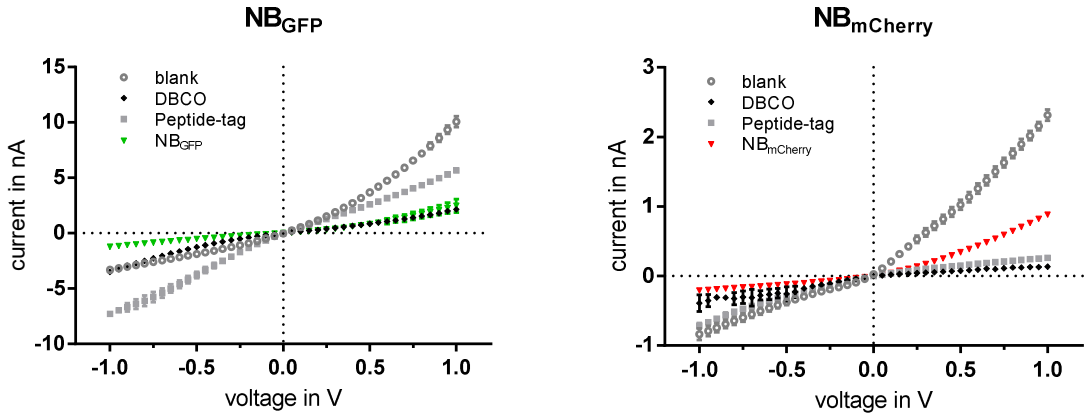

Figure 51 *I-V curves during the modification process of SSNs. Rectification behaviour and conductivity change with modifications. A: Tip diameter ≈ 45 nm, coupling protein: NB$_{GFP}$-(GGS)$_2$-SpyCatcher002; B: Tip diameter ≈ 26 nm, coupling protein: NB$_{GFP}$-(GGS)$_2$-SpyCatcher002. Mean values and error bars result from 3 periods of triangular voltage recordings (section 2.2). Data were acquired by Ivana Duznovic and her students.*

Table 20 *Rectification factors (RF) at ± 1 V of the respective I-V single pore measurements in Figure 51. Errors calculated via Gaussian error propagation.*

Pore modification	*RF* pore 1 (tip d ≈ 45 nm)	*RF* pore 2 (tip d ≈ 26 nm)
Blank	3.04 ± 0.16	2.76 ± 0.30
DBCO	0.61 ± 0.05	0.34 ± 0.14
Tether Peptide	0.77 ± 0.01	0.37 ± 0.03
NB-SpyCatcher chimera	2.00 ± 0.50 (NB$_{GFP}$)	4.22 ± 0.20 (NB$_{mCherry}$)

3.4.2 Specificity

The chambers separated by NB-functionalized SSNs were consecutively filled with different dilutions of analyte protein (ranging from 10^{-15} to 10^{-6} M in logarithmic manner) in 1x PBS buffer, and I-V curves were recorded. Specific current responses correlated to the binding of NBs to their cognate protein-epitopes were observed (Figure 52). The data could be fitted to distinct sigmoidal binding curves, with the best fit of the GFP-NB$_{GFP}$ interaction data resembling the expected dose-response curve. Importantly, the NB-functionalized nanopores were selective towards their analyte, as the respective correlation between concentration and conductivity was not observed for other analytes (section 3.5). Altogether, this demonstrates the potential of the setup to discriminate specific analytes.

In case of sfGFP/NB$_{GFP}$, the RF value increased about 30 %, while it did not deviate more than ≈ 11 % for the other cases (Sup Fig 12). However, it is important to notice that in all cases the specific interaction between the immobilized nanobodies and their respective analytes resulted in a conductivity increase instead of a decrease. This implies that a higher local concentration of the analytes – due to specific binding – influences the charge density near the pore aperture and thus the conductivity of the pore.

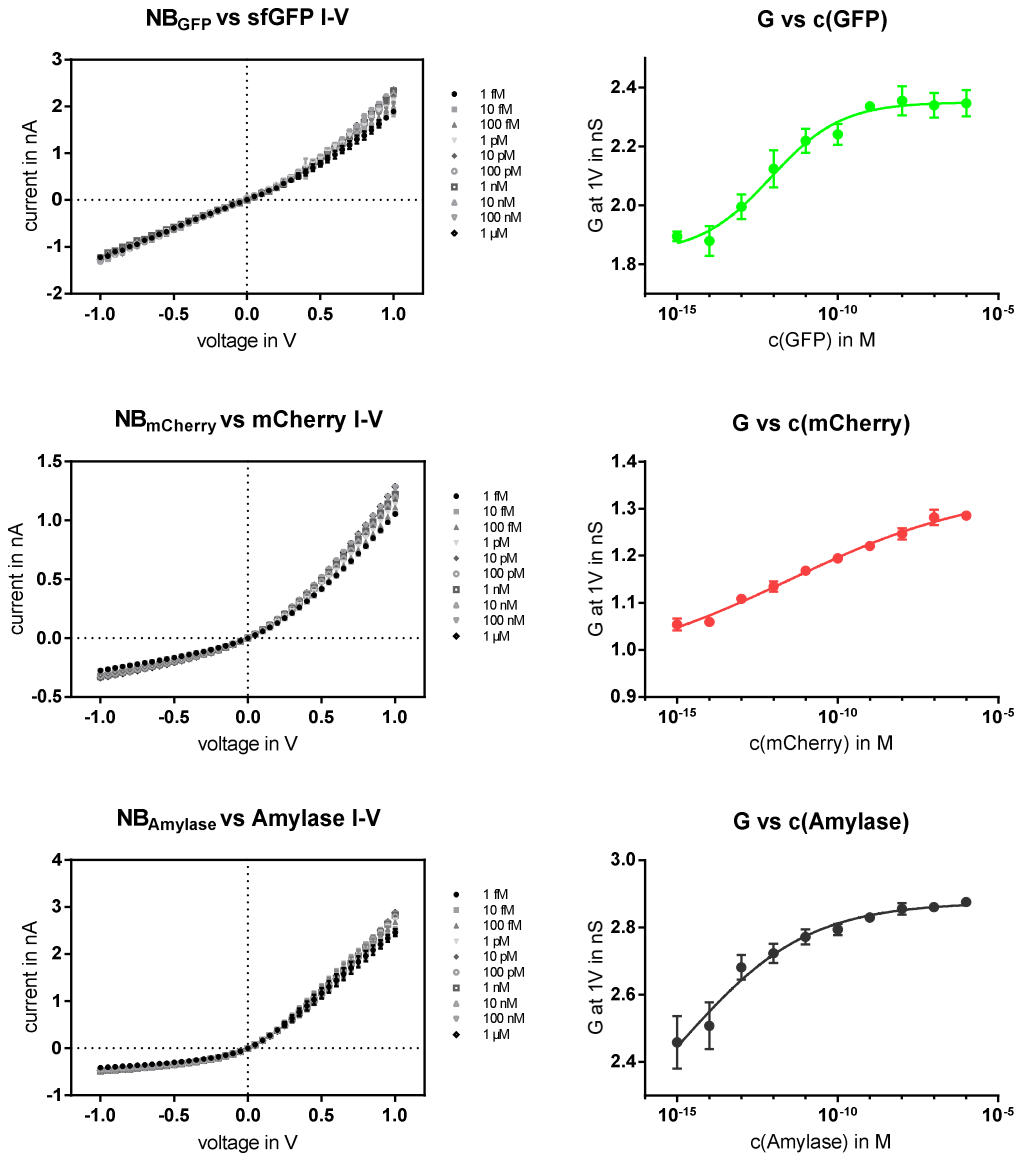

Figure 52 *Specific recognition of analytes via nanobody-nanopore-sensors. Shown are I-V curves (left) and corresponding conductivity plots (right) recorded with respective NB-modified single pore membranes. The concentrations refer to the respective analyte. Scales of* G vs analyte *graphs are logarithmic. Data were fitted with a sigmoidal dose-response-like equation in Prism 7 (Graphpad) (details in Sup Table 2).*

3.4.3 Multipore membranes

Modification experiments on multipore membranes (pore density ≥ 10^4 / cm^2) yielded results comparable to the single pore experiments. The *RF*s at ± 1 V showed the same trends, with exception of NB$_{GFP}$-(GGS)$_2$-SpyCatcher002 coupling that did not result in an inversion of rectification (Table 21), albeit in an increase in *RF*. This suggests that SpyCatcher/SpyTag coupling does not proceed consistently over the whole membrane and that a larger number of Tether Peptides remain uncoupled to the fusion protein compared to the single pore setup.

A small increase (≈ 26 %) in the *RF* value was observed upon addition of the analyte sfGFP to the NB$_{GFP}$-(GGS)$_2$-SpyCatcher002 functionalized multipore membrane. This agrees with the single pore experiment (RF increase ≈ 30 %). In contrast to the latter, however, a loss of

conductivity (“blocking”) was observed in the multipore setup (data not shown). Possible reasons for this finding are discussed in the following paragraph on SSN control experiments (section 3.5).

Table 21 *Rectification factors (RF) at ± 1 V for measurements on a multipore membrane. Errors calculated via Gaussian error propagation.*

Pore modification	*RF* of the membrane
Blank	3.33 ± 0.22
DBCO	0.71 ± 0.07
Tether Peptide	0.66 ± 0.12
NB-SpyCatcher chimera	0.83 ± 0.03
sfGFP addition	1.04 ± 0.06

The use of multipore membranes together with fluorescent analytes allowed an additional analysis of the specific nanobody – target interaction *via* a confocal laser scanning microscope (CLSM). A specific binding of sfGFP or mCherry to their respective nanobodies should result in an increased local concentration inside the pores if the biofunctionalization was successful.

Precisely, analyte dilutions (at ≈ 1 μM) were added to NB-functionalized membranes that were fixed on coverslips with 0.5 % agarose solution. After incubation and rinsing (2 times with 1x PBS buffer), the samples were analyzed *via* top view and scanning mode (performed by Wadim Weber). Strong fluorescent signals were observed inside both conical and cylindrical nanopores (Figure 53 A&C), but only if the respective analyte was incubated with its corresponding nanobody (Figure 54). For instance, if sfGFP was incubated with $NB_{mCherry}$ modified nanopores, only marginal spots of fluorescence were visible, in contrast to bright fluorescence in NB_{GFP} pores. sfGFP also showed accumulation in unfunctionalized membrane areas (Figure 53 B), likely due to non-specific interactions and/or rinsing limitations, however at much lower intensities compared to NB_{GFP} areas. For mCherry, such unspecific accumulation may be hidden due to its smaller quantum yield [342,443]. Additional images are provided in the supplement (Sup Fig 13). Altogether, the images demonstrate that the extraordinary specificity of the nanobodies is preserved when immobilized inside the nanopore confinement.

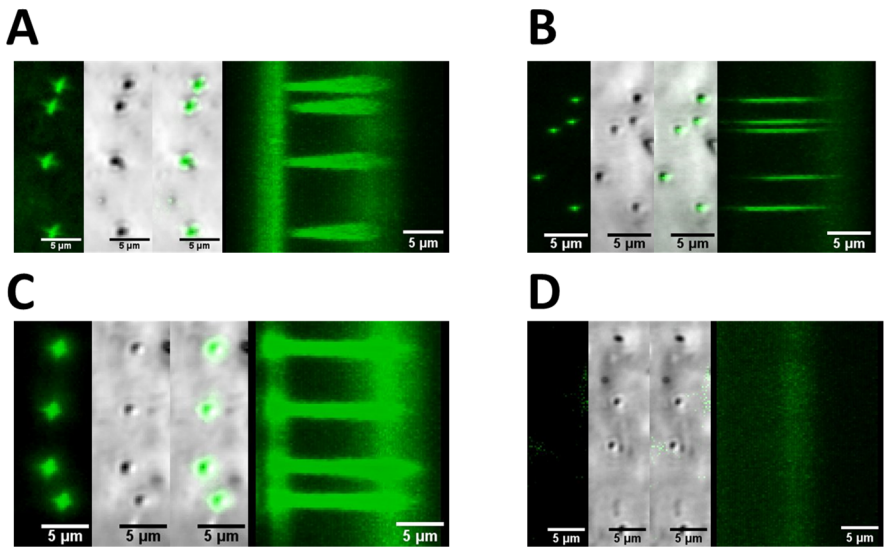

Figure 53 *CLSM images of multipore membranes with different geometry and/or modification exposed to sfGFP. A: Conical pores modified with* NB_{GFP}*; B: Unfunctionalized membrane (PET surface); C: Cylindrical pores modified with* NB_{GFP}*; D: Cylindrical pores modified with* $NB_{mCherry}$*. CLSM images were recorded, merged and aligned by Wadim Weber.*

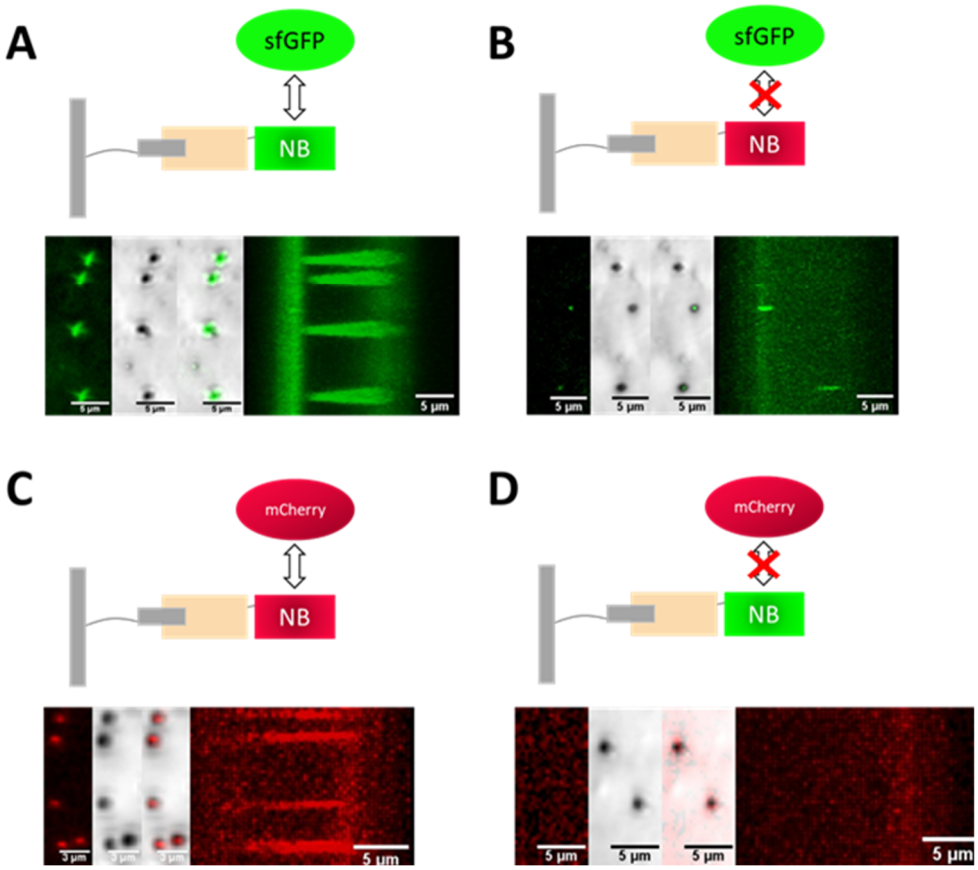

Figure 54 *CLSM-images of multipore membranes (*10^7 *pores/cm*^{2}*) modified with specific nanobinders* NB_{GFP} *and* $NB_{mCherry}$*. Protein solutions were added on top of the respective membranes, incubated for 30 min and rinsed two times with 1x PBS. The respective NB/analyte combination in the respective frame (A-D) is depicted schematically. CLSM images were recorded, merged and aligned by Wadim Weber.*

3.5 SSN control experiments

Multiple unpredicted phenomena appeared during the development of the SSN-nanobody platform and during the measurements – observations that need careful examination. With two track-etched PET membranes never being identical – especially after chemical etching –, reproduction of the same measurement is limited to qualitative statements with respect to I-V correlation and *RF* values. Nonetheless, the gathered data from the following control experiments underline that the principle idea of biosensing with NB-functionalized SSNs is valid and reliable.

It is important to note that charge interactions can have significant effects on the conductive behaviour of SSNs. In fact, many studies use charge interactions as a biosensing concept or for immobilization approaches [379,450]. Such charge interaction is probably the cause of unspecific adsorption of sfGFP and mCherry to Tether Peptide modified SSN lacking any NB moiety (Figure 55). The Tether Peptide having a net charge of +6 e at pH=7 attracts both sfGFP (formal net charge -3 e) and mCherry (formal net charge -7 e). Moreover, the experiment showed that a considerable proportion of analyte remained electrostatically bound to the surface despite washing, as the experiment was performed on the same foil but sfGFP was tested first. To a certain degree this “memory effect” or clogging was also observed in control experiments on cross-reactivity that were performed on single pores (Figure 56). These experiments proved that the NBs do not bind to other analytes, however, the conductivity-concentration correlation for the matching analyte was considerably less pronounced compared to Figure 52, likely due to the memory effect caused by measuring the mismatching analytes before the matching one. In fact, a correlation for α-amylase recognition by the $NB_{Amylase}$ functionalized membrane was barely seen in the cross-reactivity experiment (Figure 56 B).

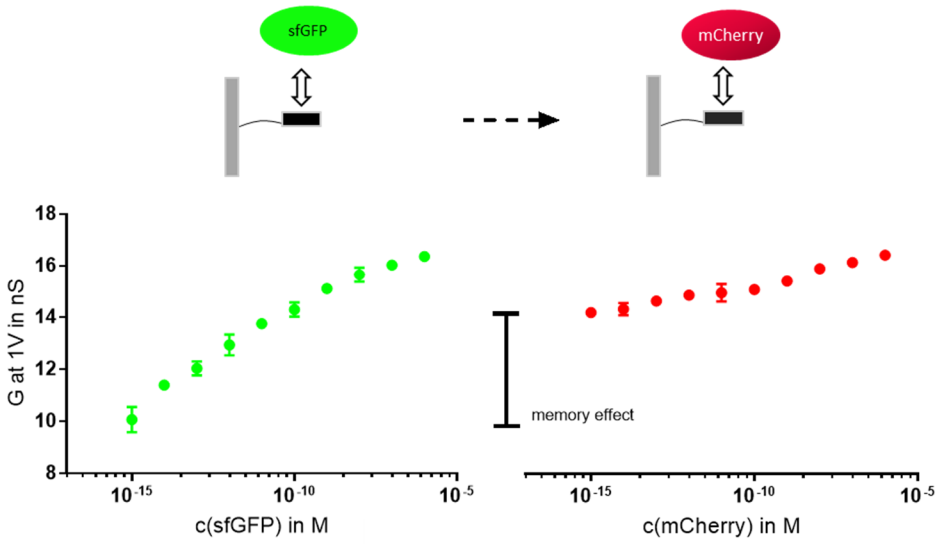

Figure 55 *Unspecific interaction of sfGFP and mCherry with immobilized Tether Peptide. After measuring sfGFP interaction, the foil was rinsed extensively, followed by mCherry testing. Despite washing, a memory effect was observed, likely due to strong electrostatic interaction between positively charged Tether Peptide and negatively charged sfGFP.*

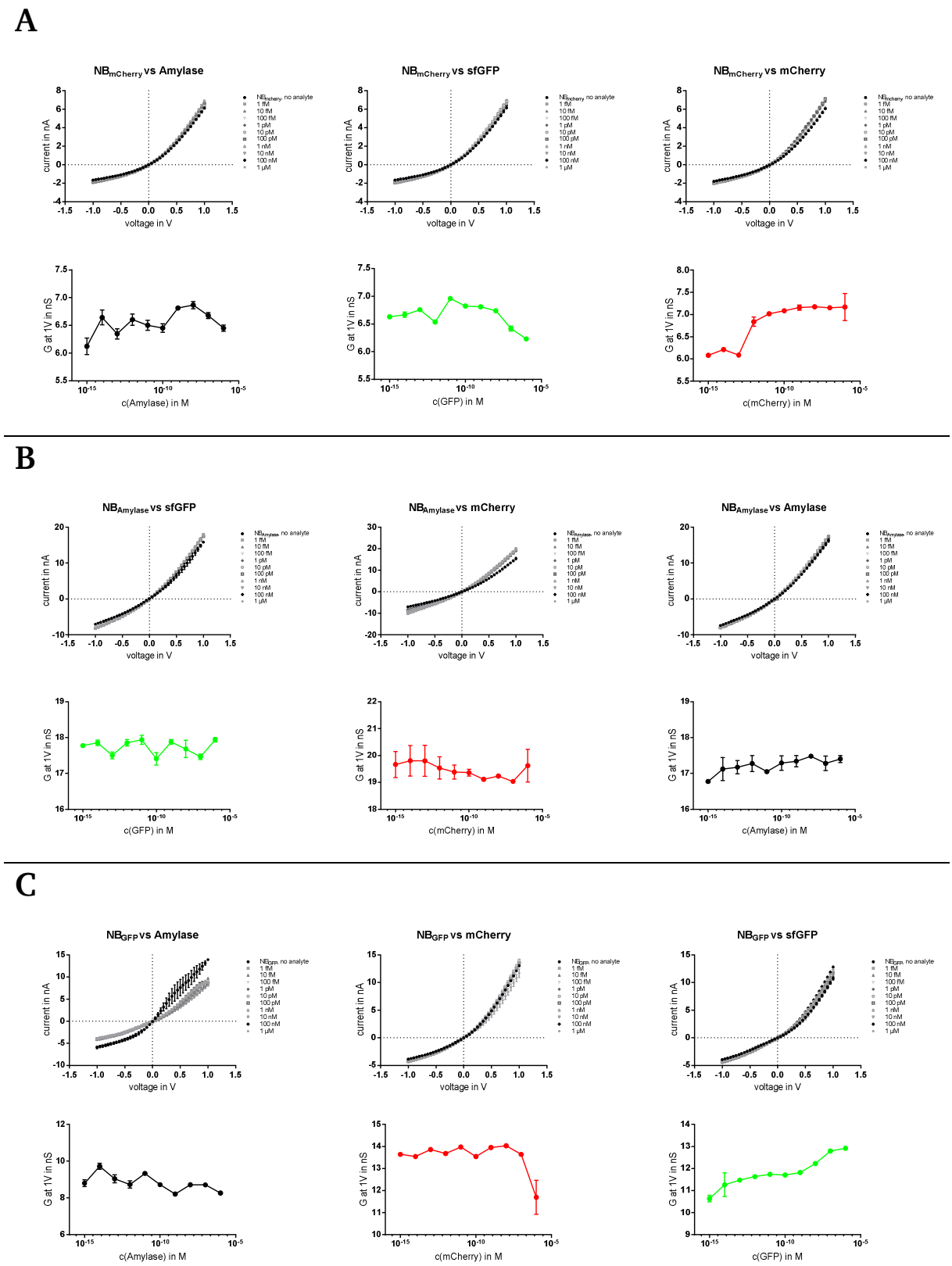

Figure 56 *Cross-reactivity measurements on single pore membranes. A: $NB_{mCherry}$ vs. analytes; B: $NB_{Amylase}$ vs. analytes; C: NB_{GFP} vs. analytes. Each I-V measurement is paired with a graph showing the corresponding conductivity at 1 V. In A, B and C, the same foil was exposed to two unspecific analytes before being exposed to the correct one; the order from left to right corresponds to the time coordinate. The selectivities of the NBs to their respective analyte are preserved after exposure to other analytes, although memory effects adversely affect the recognition efficiency (compare to Figure 52).*

To elucidate the role of protein charge inside SSNs better, sfGFP was compared to a negatively supercharged GFP, GFP(-30). From available supercharged GFP variants [451], GFP(-30) was chosen because the residues involved in the nanobody interaction are not changed in contrast to e.g. GFP(+9) [452], as determined by structure based *in silico* analysis with UCSF Chimera [120,440]. To validate that GFP(-30) is bound by NB_{GFP}, a microscale thermophoresis (MST) experiment was performed on a Monolith NT.115. When GFP(-30) was titrated with NB_{GFP}-$(GGS)_2$-SpyCatcher002, the raw fluorescence values of GFP(-30) increased for NB_{GFP} concentrations above a certain threshold, similar to an MST experiment with sfGFP. This increase was expected, as the used NB_{GFP} protein has also fluorescence enhancing properties and was named GFP-enhancer in one study [440,453].

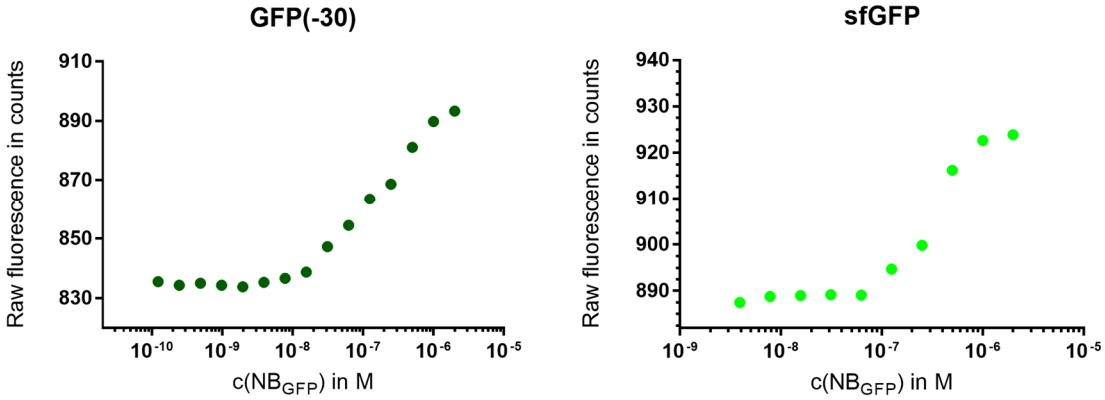

Figure 57 *MST experiments with GFP(-30) and sfGFP. Raw fluorescence of the GFP proteins, held at constant 78 nM (GFP(-30)) and 44 nM (sfGFP), respectively, increases when bound by* NB_{GFP}.

Subsequently, GFP(-30) was assayed on SSNs with immobilized NB_{GFP}-$(GGS)_2$-SpyCatcher002 on multipore membranes (10^4 pores / cm^2) and compared to sfGFP in order to understand the role of charge interaction in the SSN biofunctionalization context. Both experiments resulted in a slight loss of conductivity as observed before for multipores, however, the *RF* value during sfGFP binding only increases slightly (≈ 15 %) over seven orders of magnitude whereas it increased drastically in case of GFP(-30) (≈ 66 %) (Figure 58).

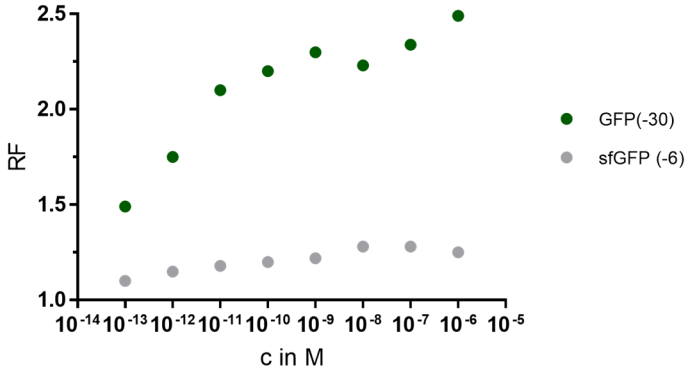

Figure 58 *RF values as a function of analyte concentration. Upon* NB_{GFP} *binding of GFP(-30), RF increases 66 % between seven orders of magnitude, while RF is nearly unaffected in case of sfGFP binding.*

To conclude, the surface charge of the analyte affects the rectification behaviour of biofunctionalized SSNs. This has both advantages and disadvantages for the proposed biosensor platform. Changes in rectification are considered a reliable readout in the nanopore field [372,379,454]. However, the recruitment of charges to the aperture of the nanopore changes its conductive behaviour. Thereby current changes upon specific analyte binding may be considerably masked by charge effects, leading to a bias in conductivity readout and a hampered sensitivity of the system.

Taking both effects account, it is possible to explain the observed conductivity differences between biofunctionalized single pores and multipores. In the multipore context, nanopore blocking *via* binding of analytes outweighs the effect of charges on conductivity, unless an analyte with high surface charge is bound (Figure 57). In this case, the considerable *RF* changes may serve as a readout. In the single pore context, the charge changes near the only aperture outweigh this blocking and lead to an increase in conductivity if the corresponding analyte is present. To assess how strong the charge affects the final current signal is not trivial and should be examined in future studies.

3.6 Conclusion and Perspectives

Both single pore measurements and CLSM data proved the specificity of the nanobody-analyte interaction in nanoconfined SSN environments. Two main variables are affecting the detection range: Charge interactions and blocking. While blocking outweighs in multipore setups, charge interactions play a dominant role in the single pore context. Importantly, considerable differences between analytes were observed regarding the correlation between conductivity and concentration (Figure 52), underlining the sensitivity of the system towards charge and size differences.

Considering the high modularity with respect to available nanobodies, the results encourage further development of nanobody-nanopore devices for biosensing approaches. Remaining challenges are reproducible fabrication of the SSN membranes as well as elucidation of the interaction between charge, blocking and conductive behaviour. An important aspect concerns the stability of proteins in nanoconfinement and electrical fields [424]. Protein engineering could address this issue by construction of stabilized receptors.

For example, receptor stability may be enhanced by a shielding PASylation layer (see section 1.1.1, Chapter 2) if this strategy does not impact analyte recognition. Regarding SSNs, evaluation of other pore geometries (e.g. cylindrical or cigar-shaped [382]) could lead to an improved signal-to-noise ratio. In this context, adjusting the properties of the Tether Peptide sequence is another promising strategy. For instance, introduction of additional charges in the spacing region could reduce any unspecific surface adsorption or intermolecular aggregation of the peptide [455], leading to an improved nanobody-labeling of the pore interior. Moreover, further experiments with SH3-TVMV protease to specifically deplete protein outside the nanopore could render the platform more sensitive. First experiments with the protease did not yield considerable results, thus the data were not included in this work.

The qualitative data gathered in this work demonstrate the feasibility and potential of the modular nanobody-nanopore platform. Further optimization will allow precise and quantitative analyte sensing. Importantly, the combination of both Material and Life Science pursued here represents one of the most promising roads to customizable point-of-care biosensors.

4. Supplement Chapter 4

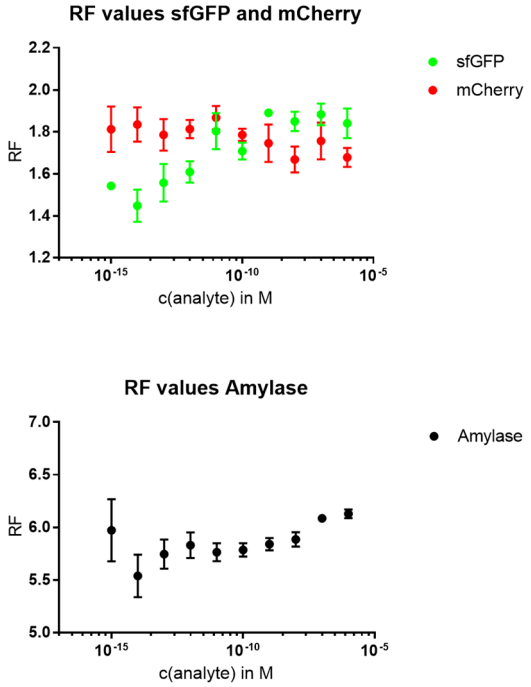

Sup Fig 12 *Rectification Factor (RF) values of direct coupling on single pores (corresponding I-V curves in Figure 52).*

Sup Table 2 *Fit parameters for specificity SSN measurements depicted in Figure 52.*

Fit function for all data	$y = \frac{A - B}{1 + (\frac{x}{z})^p} + B$
Sigmoidal fit parameters	
sfGFP	
A	1.837 ± 0.04783
B	2.35 ± 0.01849
z	8.097e-013 ± 5.539e-013
p	0.3943 ± 0.09171
mCherry	
A	0.9541 ± 0.08357
B	1.344 ± 0.04893
z	3.21e-012 ± 6.242e-012
p	0.1427 ± 0.05681
α-amylase	
A	2.062 ± 0.5864
B	2.875 ± 0.0279
z	1.669e-015 ± 1.022e-014
p	0.2246 ± 0.1003

Sup Fig 13: *Complete CLSM image set of multipore membranes with different geometry and/or modification, exposed to sfGFP or mCherry. The leftmost images constitute the fluorescent images, the middle ones the bright light images and the rightmost the merged images. Rectangles denote the sections shown in Figure 53 or Figure 54, respectively. A: Cylindrical pores modified with NB_{GFP}, exposed to sfGFP; B: Cylindrical pores modified with $NB_{mCherry}$, exposed to sfGFP; C: Conical pores modified with NB_{GFP}, exposed to sfGFP; D: Conical pores modified with $NB_{mCherry}$, exposed to sfGFP; E: Cylindrical pores modified with $NB_{mCherry}$, exposed to mCherry; F: Cylindrical pores modified with NB_{GFP}, exposed to mCherry; G: Unfunctionalized membrane area, exposed to sfGFP. CLSM images were recorded, merged, and aligned by Wadim Weber.*

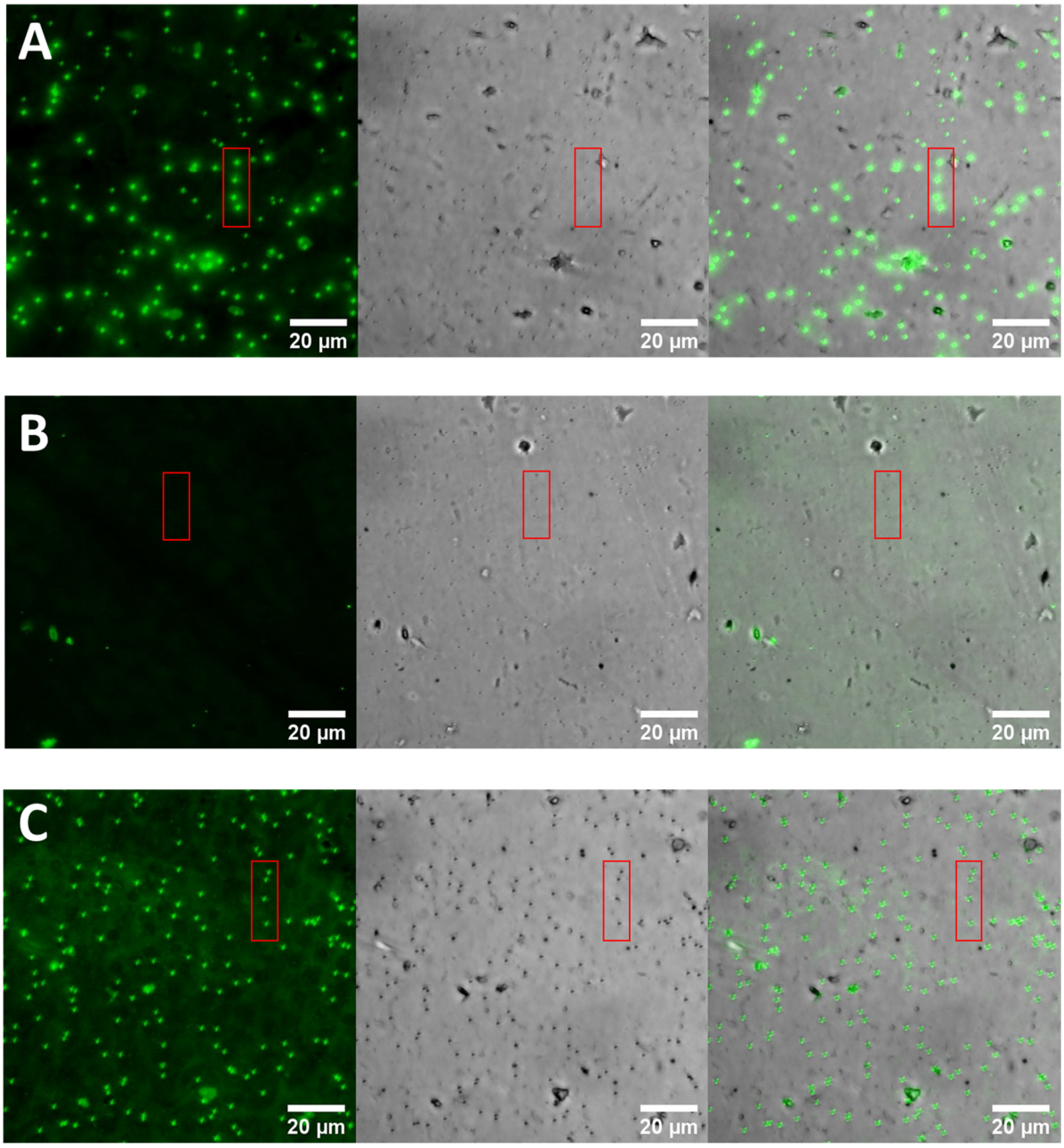

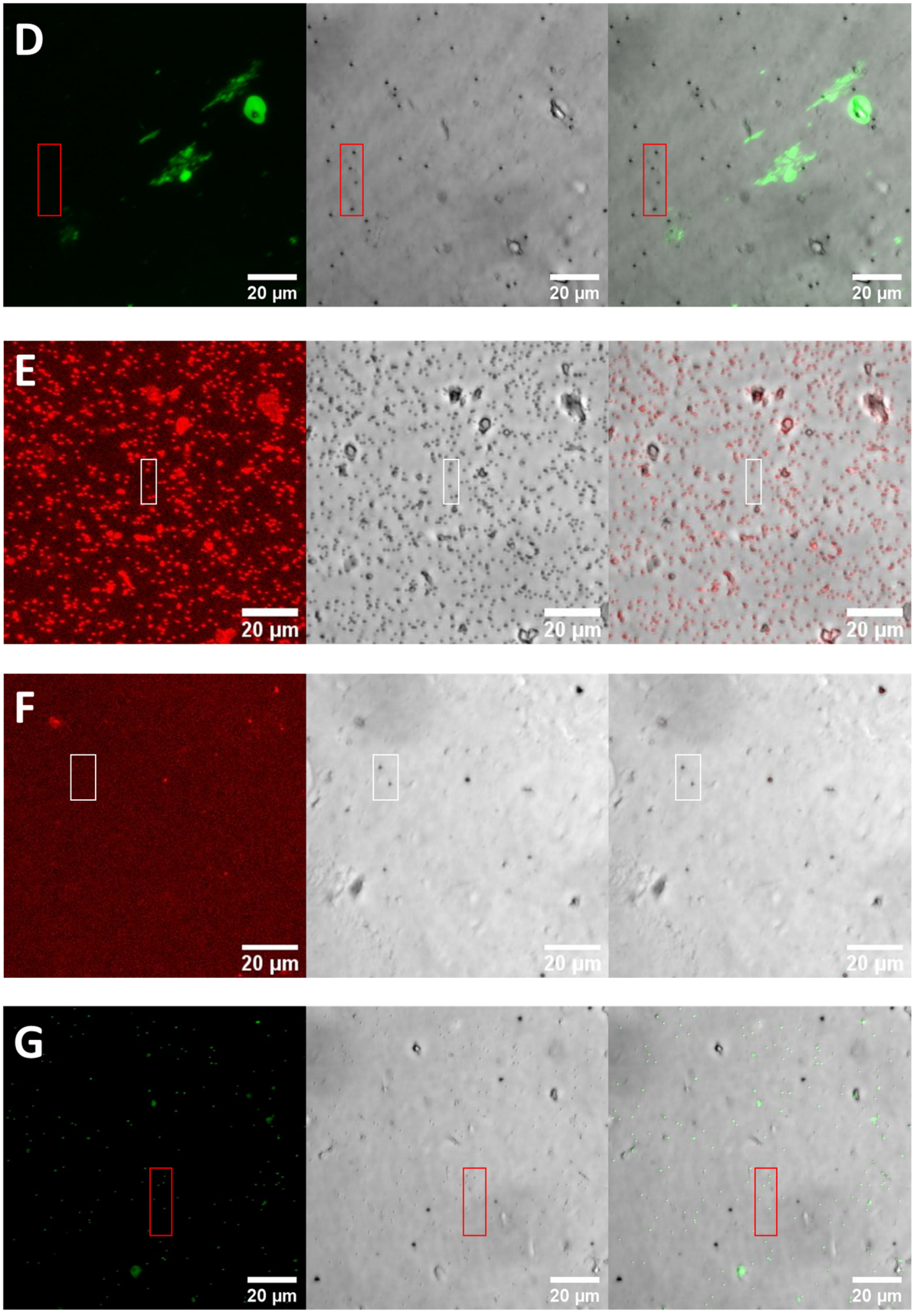
D
20 µm
20 µm
20 µm
E
20 µm
20 µm
20 µm
F
20 µm
20 µm
20 µm
G
20 µm
20 µm
20 µm

Material

iFLinkC plasmid cards are available via addgene (www.addgene.org), all other plasmid cards and primer sequences are saved on the AG Stein server. Primer oligos were purchased at Sigma Aldrich or IDT; gBlocks and longer DNA parts were purchased at IDT or GenScript. All restriction enzymes, DNA ladders, DNA loading dyes, PCR buffers and restriction buffers were purchased from New England Biolabs (NEB). All standard chemicals used in this work were purchased from Carl Roth with exceptions listed in Table 22.

Table 22 *Standard chemicals from Suppliers other than Carl Roth*

Chemical	Supplier
Imidazole (>= 99%)	Sigma Aldrich
HABA	Sigma Aldrich
D(+)Lactose 1-hydrate	AppliChem
DPhPC	Avanti Polar Lipids (Otto Nordwald)
Bio-Ethanol	Richter Chemie
Desthiobiotin	IBA Life Sciences
Copper(II)sulfate	AppliChem
Boric acid	AppliChem
Zinc sulfate	AppliChem
Hexadecane	Sigma Aldrich
n-hexane	Sigma Aldrich
n-pentane	Sigma Aldrich

Table 23 *Laboratory equipment used in this work.*

Instrument	Model	Manufacturer
Agarose gel chamber	Perfectblue Gelsystem Mini M	VWR
Amplifier	L/M-EPC7	List Medical
Block heater	Touch Screen Block Heater	Thermo Fisher Scientific
Blue LED table	FastGene LED Illuminator	Nippon Genetics
Centrifuge	Microstar 17	VWR
Centrifuge	Minispin plus	Eppendorf
Centrifuge	Allegra X-30R Centrifuge	Beckman Coulter
Electroporator	Gene Pulser II in combination with Pulse Controller Plus and Capacitance Extender Plus	Bio-Rad

Gel documentation imaging system	Amersham Imager 600 RGB	GE Healthcare
	Vilbert E-BOX-CX5.TS + TFS-20.Skylite Blaulicht LED-PAD	Vilber
Gel documentation imaging system	Gel Imager AI600	Amersham
Homogenizer for cell suspension	EmulsiFlex-C3	Avestin Europe GmbH
Incubator for microtiter plates	Titramax 1000 & Inkubator 1000	Heidolph
Lyophyll	Alpha 2-4 LD plus	Christ
Magnet spinner	Magnetrührer VWR LabDisc S040	VWR
Microtiter plate reader	Spark	Tecan
Microvolume UV-VIS spectrophotometer	NanoDrop-1000 Spectrophotometer	Peqlab
Microwellplate shaker	Titramax 1000 & Inkubator 1000	Heidolph
Monolith for Microscale Thermophoresis	Monolith NT.115	NanoTemper
OD measuring device	Ultrospex® 10 CELL DENSITY METER	Biochrom
PCR cycler	Labcycler 48 Basic 230V	Sensoquest
pH-Meter	pH-Meter VWR pHenomenal pH1102	VWR
Pipettes	Research Plus	Eppendorf
Power Supply for agarose and SDS gels	PowerPac Basic	Bio-Rad
Protein purification system	ÄKTApure	GE Healthcare
Shaking incubator	HT Ecotron	Infors
Shaking incubator	HT Unitron	Infors
Sonicator	Qsonica Q125 (125 W Sonicator, 1/8” probe) + Sound Enclosure	Qsonica
Thermal shaker	Cooling Thermal Shaker Touch	VWR
Tumbler	Taumelschüttler Rocker 3D	VWR
Vortex	Vortex VWR mixer mini	VWR

Table 24 *Genotypes of Escherichia coli strains used in this work.*

Strain	Genotype	Reference
BL21(DE3)	*fhuA2 [lon] ompT gal (λ DE3) [dcm] ΔhsdS λ DE3 = λ sBamHIo ΔEcoRI-B int::(lacI::PlacUV5::T7 gene1) i21 Δnin5*	New England Biolabs (NEB)
BL21(DE3) omp8	*B* F- *hsdSB* (rB-, mB-) *gal dcm ompT λ*(DE3) Δ*lamB ompF::Tn5* Δ*ompA* Δ*ompC*	[337], provided by Klaus Hantke
DH10B	Δ(*ara-leu*) 7697 *araD139 fhuA* ΔlacX74 galK16 galE15 e14- ϕ80 Δ(*lacZ*)M15 *recA1 relA1 endA1 nupG rpsL (StrR) rph spoT1* Δ(*mrr-hsdRMS-mcrBC*)	New England Biolabs (NEB)

Table 25 *Relevant consumables used in this work*

Consumables	Denotion	Manufacturer (Supplier)
96-well plates	BRANDplates	Brand
Aluminium Foil	Aluminium Foil	VWR
Buffer exchange columns	PD 10 Desalting columns	GE Healthcare (VWR)
Centrifugal Concentrator	Vivaspin 500 & Vivaspin 20 10000 kDa MWCO PES	Sartorius
Cuvettes	Cuvettes 10x4x45 mm	Sarstedt
Dialysis cartridges	10 kDa MWCO Slide-A-Lyzer	Thermo Fisher Scientific (VWR)
Disposable hypodermic needle	100 Sterican® Gr.1	B. Braun
Disposal Bags	Disposal Bags 200x300 mm	Carl Roth
DNA stain for Agarose gel electrophoresis	Midori Green Advance	Nippon Genetics
Falcons	15 & 50 ml	Sarstedt & VWR
Gel and PCR cleanup	NulceoSpin Gel and PCR Clean-up	Macherey-Nagel
Gibson Assembly Mastermix	Gibson Assembly® Master Mix	NEB
Microscale Thermophoresis Capillaries	Monolith™ NT.115 Series (1000)	NanoTemper
Midi-Prep Kit	NucleoBond® Xtra Midi	Macherey-Nagel
Mini-Prep Kit	NucleoSpin® Plasmid (NoLid)	Macherey-Nagel

Nitrile Gloves	StarGuard Comfort	StarLab
Parafilm	Parafilm M, 100mm Wide x 75 mm Length	Bemis (StarLab)
PCR tubes	Multiply®-μStripPro Biosphere®	Sarstedt
PET membranes	Hostaphan RN12® (12 μm thickness)	Hoechst
Pipette Tips	TipOne 10/20 μl XL Graduated Tip (Refill)	StarLab
	TipOne 200 μl Yellow Bevelled Tip (Refill)	StarLab
	TipOne 1000 μl Blue Graduated Tip (Refill)	StarLab
	5000 μl Eppendorf-Type Graduated Macro Tip, Loose	StarLab
Plastic Syringes	Omnifix® Luer Lock 10, 20 & 50 ml; Injekt®-F 1ml	B. Braun
Precast polyacrylamide gels	Mini-PROTEAN™ TGX (4-20%)	Bio-Rad
Protease inhibitor tablets	cOmplete protease inhibitor tablets	Roche (Sigma Aldrich)
Protein Ladder	BlueStar Prestained Protein Marker	Nippon Genetics
Protein Stain for SDS PAGEs	Roti®Blue 5x	Carl Roth
	FastGene® Qstain	Nippon Genetics
Purification columns	HisTrap FF & HP, 1 ml & 5 ml	GE Healthcare (VWR)
	StrepTrap HP 1ml & 5ml	GE Healthcare (VWR)
Reaction /Micro tubes	1.5 ml & 2 ml	Sarstedt
Round filters for bottles	Cellulose Acetate Filter 0.45 μm (1106-47-N)	Sartorius
Syringe filters	Rotilabo® CME sterile. 0.22 μm & 0.45 μm, outer diameter 33 mm	Carl Roth

Table 26 *Composition of standard buffers used in this work*

Buffer	composition
Buffer W	150 mM NaCl, 100 mM Tris-Cl pH=8
Refolding buffer	200 mM KCl, 50 mM Tris-Cl pH=8, 0.5% (w/v) n-dodecyl β-D-maltoside (DDM).
SDS Loading Dye	200 mM $NaPO_4$ pH=7.5, 4% (w/v) SDS, 20%(v/v) Glycerol, 0.002% (w/v) bromphenolblue
Buffer E	Buffer W with 2.5 mM Desthiobiotin
Inclusion body wash buffer	300 mM KCl, 50 mM Tris-Cl pH=8, 5 mM EDTA
Triton wash buffer	Inclusion body wash buffer with 0.5 %(v/v) Triton X-100
Inclusion body denaturing buffer	500 mM KCl, 50 mM Tris-Cl pH=8, 8 M Urea
Trace element solution	3 nM $(NH_4)_6Mo_7O_{24}$, 0.4 μM H_3BO_3, 30 nM $CoCl_2$, 10 nM $CuSO_4$, 80 nM $MnCl_2$, 10 nM $ZnSO_4$, 1 mM $MgSO_4$, 100 μM $CaCl_2$, 1 μM $FeSO_4$
Antibiotic stocks (1000x)	100 mg/ml ampicillin, 50 mg/ml kanamycin
His-Tag equilibration buffer	500 mM NaCl, 20 mM $NaPO_4$, 20 mM Imidazole pH=7.4
His-Tag Elution buffer	500 mM NaCl, 20 mM $NaPO_4$, 300 mM Imidazole pH=7.4
His-Tag Storage buffer	150 mM NaCl, 20 mM $NaPO_4$ pH=7.4
Inducer (1000x)	500 mM IPTG
SDS PAGE running buffer (10x)	250 mM Tris, 1.92 M Glycine, 1% (w/w) SDS pH=8.8
StrepTrap Regeneration buffer	1 mM HABA in buffer W
TAE-buffer (50x)	2 M Tris, 1 M Acetic acid, 50 mM EDTA, pH=8.5
TB buffer	250 mM KCl, 15 mM $CaCl2_2$, 10 mM PIPES pH=6.7, 55 mM $MnCl_2$ (add final), sterile filtered

Table 27 *Composition of standard media used in this work*

Medium	composition
LB	10 g/l NaCl, 10 g/l Peptone, 5g/l yeast extract, pH=7.4
LB agar	LB supplemented with 1.5% (w/v) agar-agar
SOB	10 mM NaCl, 2.5 mM KCl, 10 mM $MgCl_2$, 20 mM $MgSO_4$, 0.5 % (w/v) yeast extract, 2 % (w/v) peptone, pH=7.5
SOC	SOB medium supplemented with 20 mM Glucose
N-5052 autoinduction medium [202] with modifications	0.6% (w/v) Na_2PO_4, 0.3% (w/v) KH_2PO_4, 0.05% (w/v) NaCl, 0.1% (w/v) NH_4Cl supplemented with 0.5% (v/v) Glycerol, 0.05% (w/v) Glucose, 0.2% (w/v) Lactose and trace element solution after autoclaving

Protein sequences

MBP-(TEV_{site})-strep-AI_{TVMV}

KIEEGKLVIWINGDKGYNGLAEVGKKFEKDTGIKVTVEHPDKLEEKFPQVAATGDGPDIIFWAHDRF
GGYAQSGLLAEITPDKAFQDKLYPFTWDAVRYNGKLIAYPIAVEALSLIYNKDLLPNPPKTWEEIPALD
KELKAKGKSALMFNLQEPYFTWPLIAADGGYAFKYENGKYDIKDVGVDNAGAKAGLTFLVDLIKNKH
MNADTDYSIAEAAFNKGETAMTINGPWAWSNIDTSKVNYGVTVLPTFKGQPSKPFVGVLSAGINAA
SPNKELAKEFLENYLLTDEGLEAVNKDKPLGAVALKSYEEELVKDPRIAATMENAQKGEIMPNIPQM
SAFWYAVRTAVINAASGRQTVDEALKDAQTNSSSENLYFQSSGWSHPQFEKSGGREYVRFAP*

TVMV protease

SKALLKGVRDFNPISACVCLLENSSDGHSERLFGIGFGPYIIANQHLFRRNNGELTIKTMHGEFKVKN
STQLQMKPVEGRDIIVIKMAKDFPPFPQKLKFRQPTIKDRVCMVSTNFQQKSVSSLVSESSHIVHKED
TSFWQHWITTKDGQCGSPLVSIIDGNILGIHSLTHTTNGSNYFVEFPEKFVATYLDAADGWCKNWK
FNADKISWGSFTLVEDAPED*

FKBP12

VQVETISPGDGRTFPKRGQTCVVHYTGMLEDGKKFDSSRDRNKPFKFMLGKQEVIRGWEEGVAQM
SVGQRAKLTISPDYAYGATGHPGIIPPHATLVFDVELLKLE*

FRB

ILWHEMWHEGLEEASRLYFGERNVKGMFEVLEPLHAMMERGPQTLKETSFNQAYGRDLMEAQEW
CRKYMKSGNVKDLTQAWDLYYHVFRRI*

ePDZ-b1

SPELGFSISGGVGGRGNPFRPDDDGIFVTRVQPEGPASKLLQPGDKIIQANGYSFINIEHGQAVSLLK
TFQNTVELIIVREVGNGAKQEIRVRVEKDG*

FN3

GVSSVPTNLEVVAATPTSLLISWDAYRELPVSYYRITYGETGGNSPVQEFTVPGSKSTATISGLKPGVD
YTITVYAHYNYHYYSSPISINYR*

AG6

MGDRGPEFMKIEEGKLVIWINGDKGYNGLAEVGKKFEKDTGIKVTVEHPDKLEEKFPQVAATGDGP
DIIFWAHDRFGGYAQSGLLAEITPDKAFQDKLYPFTWDAVRYNGKLIAYPIAVEALSLIYNKDLLPNPP
KTWEEIPALDKELKAKGKSALMFNLQEPYFTWPLIAADGGYAFKYENGKYDIKDVGVDNAGAKAGL
TFLVDLIKNKHMNADTDYSIAEAAFNKGETAMTINGPWAWSNIDTSKVNYGVTVLPTFKGQPSKPF
VGVLSAGINAASPNKELAKEFLENYLLTDEGLEAVNKDKPLGAVALKSYEEELVKDPRIAATMENAQK
GEIMPNIPQMSAFWYAVRTAVINAASGRQTVDEALKDAQTNSSSENLYFQSSGWSHPQFEKSGGR
EYVRFAPGPGASVQVETISPGDGRTFPKRGQTCVVHYTGMLEDGKKFDSSRDRNKPFKFMLGKQEV

IRGWEEGVAQMSVGQRAKLTISPDYAYGATGHPGIIPPHATLVFDVELLKLEGLGGGSGGGSGGGSE
TILWHEMWHEGLEEASRLYFGERNVKGMFEVLEPLHAMMERGPQTLKETSFNQAYGRDLMEAQE
WCRKYMKSGNVKDLTQAWDLYYHVFRRISGGRGSSKALLKGVRDFNPISACVCLLENSSDGHSERL
FGIGFGPYIIANQHLFRRNNGELTIKTMHGEFKVKNSTQLQMKPVEGRDIIVIKMAKDFPPFPQKLKF
RQPTIKDRVCMVSTNFQQKSVSSLVSESSHIVHKEDTSFWQHWITTKDGQCGSPLVSIIDGNILGIH
SLTHTTNGSNYFVEFPEKFVATYLDAADGWCKNWKFNADKISWGSFTLVEDAPEDDFMAKKTVAAI
MDGGSHHHHHH*

FKBP-FRB protease switch 2_B3

MGKIEEGKLVIWINGDKGYNGLAEVGKKFEKDTGIKVTVEHPDKLEEKFPQVAATGDGPDIIFWAHD
RFGGYAQSGLLAEITPDKAFQDKLYPFTWDAVRYNGKLIAYPIAVEALSLIYNKDLLPNPPKTWEEIPA
LDKELKAKGKSALMFNLQEPYFTWPLIAADGGYAFKYENGKYDIKDVGVDNAGAKAGLTFLVDLIKN
KHMNADTDYSIAEAAFNKGETAMTINGPWAWSNIDTSKVNYGVTVLPTFKGQPSKPFVGVLSAGIN
AASPNKELAKEFLENYLLTDEGLEAVNKDKPLGAVALKSYEEELVKDPRIAATMENAQKGEIMPNIPQ
MSAFWYAVRTAVINAASGRQTVDEALKDAQTNSSSENLYFQSSGWSHPQFEKSGGREYVRFAPGP
GVQVETISPGDGRTFPKRGQTCVVHYTGMLEDGKKFDSSRDRNKPFKFMLGKQEVIRGWEEGVAQ
MSVGQRAKLTISPDYAYGATGHPGIIPPHATLVFDVELLKLEGPPPPPPPGILWHEMWHEGLEEASR
LYFGERNVKGMFEVLEPLHAMMERGPQTLKETSFNQAYGRDLMEAQEWCRKYMKSGNVKDLTQA
WDLYYHVFRRIGPGSKALLKGVRDFNPISACVCLLENSSDGHSERLFGIGFGPYIIANQHLFRRNNGE
LTIKTMHGEFKVKNSTQLQMKPVEGRDIIVIKMAKDFPPFPQKLKFRQPTIKDRVCMVSTNFQQKSV
SSLVSESSHIVHKEDTSFWQHWITTKDGQCGSPLVSIIDGNILGIHSLTHTTNGSNYFVEFPEKFVAT
YLDAADGWCKNWKFNADKISWGSFTLVEDAPEDGIA*

CyPet-FKBP-TVMV$_{site}$-FRB-Ypet

MGDRGPEFMSKGEELFGGIVPILVELEGDVNGHKFSVSGEGEGDATYGKLTLKFICTTGKLPVPWPT
LVTTLTWGVQCFSRYPDHMKQHDFFKSVMPEGYVQERTIFFKDDGNYKTRAEVKFEGDTLVNRIEL
KGIDFKEDGNILGHKLEYNYISHNVYITADKQKNGIKANFKARHNITDGSVQLADHYQQNTPIGDGP
VILPDNHYLSTQSALSKDPNEKRDHMVLLEFVTAAGITHGMDELYKGPGASVQVETISPGDGRTFPK
RGQTCVVHYTGMLEDGKKFDSSRDRNKPFKFMLGKQEVIRGWEEGVAQMSVGQRAKLTISPDYAY
GATGHPGIIPPHATLVFDVELLKLEGGTSETVRFQSKLGGILWHEMWHEGLEEASRLYFGERNVKG
MFEVLEPLHAMMERGPQTLKETSFNQAYGRDLMEAQEWCRKYMKSGNVKDLTQAWDLYYHVFR
RISGGRGSSMVSKGEELFTGVVPILVELDGDVNGHKFSVSGEGEGDATYGKLTLKLLCTTGKLPVPW
PTLVTTLGYGVQCFARYPDHMKQHDFFKSAMPEGYVQERTIFFKDDGNYKTRAEVKFEGDTLVNRI
ELKGIDFKEDGNILGHKLEYNYNSHNVYITADKQKNGIKANFKIRHNIEDGGVQLADHYQQNTPIGD
GPVLLPDNHYLSYQSALFKDPNEKRDHMVLLEFLTAAGITEGMNELYKGGHHHHHH*

wtFhuA-strep

MARSKTAQPKHSLRKIAVVVATAVSGMSVYAQAAVEPKEDTITVTAAPAPQESAWGPAATIAARQS
ATGTKTDTPIQKVPQSISVVTAEEMALHQPKSVKEALSYTPGVSVGTRGASNTYDHLIIRGFAAEGQS
QNNYLNGLKLQGNFYNDAVIDPYMLERAEIMRGPVSVLYGKSSPGGLLNMVSKRPTTEPLKEVQFK
AGTDSLFQTGFDFSDSLDDDGVYSYRLTGLARSANAQQKGSEEQRYAIAPAFTWRPDDKTNFTFLS
YFQNEPETGYYGWLPKEGTVEPLPNGKRLPTDFNEGAKNNTYSRNEKMVGYSFDHEFNDTFTVRQ
NLRFAENKTSQNSVYGYGICSDPANAYSKQCAALAPADKGHYLARKYVVDDEKLQNFSVDTQLQSK
FATGDIDHTLLTGVDFMRMRNDINAWFGYDDSVPLLNLYNPVNTDFDFNAKDPANSGPYRILNKQ
KQTGVYVQDQAQWDKVLVTLGGRYDWADQESLNRVAGTTDKRDDKQFTWRGGVNYLFDNGVTP

YFSYSESFEPSSQVGKDGNIFAPSKGKQYEVGVKYVPEDRPIVVTGAVYNLTKTNNLMADPEGSFFSV
EGGEIRARGVEIEAKAALSASVNVVGSYTYTDAEYTTDTTYKGNTPAQVPKHMASLWADYTFFDGP
LSGLTLGTGGRYTGSSYGDPANSFKVGSYTVVDALVRYDLARVGMAGSNVALHVNNLFDREYVASC
FNTYGCFWGAERQVVATATFRFGSGGWSHPQFEK*

SnoopCatcher-^{GGSSG}-NB$_{GFP}$-strep

MKPLRGAVFSLQKQHPDYPDIYGAIDQNGTYQNVRTGEDGKLTFKNLSDGKYRLFENSEPAGYKPV
QNKPIVAFQIVNGEVRDVTSIVPQDIPATYEFTNGKHYITNEPIPPKGGSSGQVQLVESGGALVQPGG
SLRLSCAASGFPVNRYSMRWYRQAPGKEREWVAGMSSAGDRSSYEDSVKGRFTISRDDARNTVYL
QMNSLKPEDTAVYYCNVNVGFEYWGQGTQVTVSSKGGSWSHPQFEK*

$^{+sig}$ΔcΔ5L-2Link-SnoopTag^{6xHis}

MARSKTAQPKHSLRKIAVVVATAVSGMSVYAQALKEVQFKAGTDSLFQTGFDFSDSLDDDGVYSYR
LTGLARSANAQQKGSEEQRYAIAPAFTWRPDDKTNFTFLSYFQNEPETGNSEGSTYSRNEKMVGYS
FDHEFNDTFTVRQNLRFAENKTSQNSVYGNSEGSRKYVVDDEKLQNFSVDTQLQSKFATGDIDHTL
LTGVDFMRMRNDINAWFGYNSEGSSGPYRILNKQKQTGVYVQDQAQWDKVLVTLGGRYDWADQ
ESLNRVAGTTDKRDDKQFTWRGGVNYLFDNGVTPYFSYSESFEPSSQVGKDGNIFAPSKGKQYEVG
VKYVPEDRPIVVTGAVYNLTKTNNLMADPEGSFFSVEGGEIRARGVEIEAKAALSASVNVVGSYTYTD
AEYTTDTTYKGNTPAQVPKHMASLWADYTFFDGPLSGLTLGTGGRYTNSEGSYTVVDALVRYDLAR
VGMAGSNVALHVNSEGSQVVATATFRFGSKLGDIEFIKVNKLEHHHHHH*

$^{+sig}$ΔcΔ5L-10Link-SnoopTag^{6xHis}

MARSKTAQPKHSLRKIAVVVATAVSGMSVYAQALKEVQFKAGTDSLFQTGFDFSDSLDDDGVYSYR
LTGLARSANAQQKGSEEQRYAIAPAFTWRPDDKTNFTFLSYFQNEPETGNSEGSTYSRNEKMVGYS
FDHEFNDTFTVRQNLRFAENKTSQNSVYGNSEGSRKYVVDDEKLQNFSVDTQLQSKFATGDIDHTL
LTGVDFMRMRNDINAWFGYNSEGSSGPYRILNKQKQTGVYVQDQAQWDKVLVTLGGRYDWADQ
ESLNRVAGTTDKRDDKQFTWRGGVNYLFDNGVTPYFSYSESFEPSSQVGKDGNIFAPSKGKQYEVG
VKYVPEDRPIVVTGAVYNLTKTNNLMADPEGSFFSVEGGEIRARGVEIEAKAALSASVNVVGSYTYTD
AEYTTDTTYKGNTPAQVPKHMASLWADYTFFDGPLSGLTLGTGGRYTNSEGSYTVVDALVRYDLAR
VGMAGSNVALHVNSEGSQVVATATFRFGSSGASGGSGKLGDIEFIKVNKLEHHHHHH*

^{6xHis}SnoopTag-10Link-ΔcΔ5L

MHHHHHHSGKLGDIEFIKVNKLSGSGASGGSGLKEVQFKAGTDSLFQTGFDFSDSLDDDGVYSYRL
TGLARSANAQQKGSEEQRYAIAPAFTWRPDDKTNFTFLSYFQNEPETGNSEGSTYSRNEKMVGYSF
DHEFNDTFTVRQNLRFAENKTSQNSVYGNSEGSRKYVVDDEKLQNFSVDTQLQSKFATGDIDHTLL
TGVDFMRMRNDINAWFGYNSEGSSGPYRILNKQKQTGVYVQDQAQWDKVLVTLGGRYDWADQE
SLNRVAGTTDKRDDKQFTWRGGVNYLFDNGVTPYFSYSESFEPSSQVGKDGNIFAPSKGKQYEVGV
KYVPEDRPIVVTGAVYNLTKTNNLMADPEGSFFSVEGGEIRARGVEIEAKAALSASVNVVGSYTYTD
AEYTTDTTYKGNTPAQVPKHMASLWADYTFFDGPLSGLTLGTGGRYTNSEGSYTVVDALVRYDLAR
VGMAGSNVALHVNSEGSQVVATATFRF*

ΔcΔ5L^{6xHis}

MLKEVQFKAGTDSLFQTGFDFSDSLDDDGVYSYRLTGLARSANAQQKGSEEQRYAIAPAFTWRPD
DKTNFTFLSYFQNEPETGNSEGSTYSRNEKMVGYSFDHEFNDTFTVRQNLRFAENKTSQNSVYGNS
EGSRKYVVDDEKLQNFSVDTQLQSKFATGDIDHTLLTGVDFMRMRNDINAWFGYNSEGSSGPYRIL
NKQKQTGVYVQDQAQWDKVLVTLGGRYDWADQESLNRVAGTTDKRDDKQFTWRGGVNYLFDN
GVTPYFSYSESFEPSSQVGKDGNIFAPSKGKQYEVGVKYVPEDRPIVVTGAVYNLTKTNNLMADPEG
SFFSVEGGEIRARGVEIEAKAALSASVNVVGSYTYTDAEYTTDTTYKGNTPAQVPKHMASLWADYTF
FDGPLSGLTLGTGGRYTNSEGSYTVVDALVRYDLARVGMAGSNVALHVNSEGSQVVATATFRFGSG
LEHHHHHH*

^{6xHis}SnoopTag-$^{+sig}$ΔcΔ5L

MHHHHHHSGKLGDIEFIKVNKLSGMARSKTAQPKHSLRKIAVVVATAVSGMSVYAQALKEVQFKA
GTDSLFQTGFDFSDSLDDDGVYSYRLTGLARSANAQQKGSEEQRYAIAPAFTWRPDDKTNFTFLSY
FQNEPETGNSEGSTYSRNEKMVGYSFDHEFNDTFTVRQNLRFAENKTSQNSVYGNSEGSRKYVVD
DEKLQNFSVDTQLQSKFATGDIDHTLLTGVDFMRMRNDINAWFGYNSEGSSGPYRILNKQKQTGV
YVQDQAQWDKVLVTLGGRYDWADQESLNRVAGTTDKRDDKQFTWRGGVNYLFDNGVTPYFSYS
ESFEPSSQVGKDGNIFAPSKGKQYEVGVKYVPEDRPIVVTGAVYNLTKTNNLMADPEGSFFSVEGGE
IRARGVEIEAKAALSASVNVVGSYTYTDAEYTTDTTYKGNTPAQVPKHMASLWADYTFFDGPLSGLT
LGTGGRYTNSEGSYTVVDALVRYDLARVGMAGSNVALHVNSEGSQVVATATFRF*

$^{+sig}$ΔcΔ5L-SmBiT86^{6xHis}

MARSKTAQPKHSLRKIAVVVATAVSGMSVYAQALKEVQFKAGTDSLFQTGFDFSDSLDDDGVYSYR
LTGLARSANAQQKGSEEQRYAIAPAFTWRPDDKTNFTFLSYFQNEPETGNSEGSTYSRNEKMVGYS
FDHEFNDTFTVRQNLRFAENKTSQNSVYGNSEGSRKYVVDDEKLQNFSVDTQLQSKFATGDIDHTL
LTGVDFMRMRNDINAWFGYNSEGSSGPYRILNKQKQTGVYVQDQAQWDKVLVTLGGRYDWADQ
ESLNRVAGTTDKRDDKQFTWRGGVNYLFDNGVTPYFSYSESFEPSSQVGKDGNIFAPSKGKQYEVG
VKYVPEDRPIVVTGAVYNLTKTNNLMADPEGSFFSVEGGEIRARGVEIEAKAALSASVNVVGSYTYTD
AEYTTDTTYKGNTPAQVPKHMASLWADYTFFDGPLSGLTLGTGGRYTNSEGSYTVVDALVRYDLAR
VGMAGSNVALHVNSEGSQVVATATFRFGSVSGWRLFKKISLEHHHHHH*

Strep-LgBiT

MWSHPQFEKVFTLEDFVGDWEQTAAYNLDQVLEQGGVSSLLQNLAVSVTPIQRIVRSGENALKIDI
HVIIPYEGLSADQMAQIEEVFKVVYPVDDHHFKVILPYGTLVIDGVTPNMLNYFGRPYEGIAVFDGKK
ITVTGTLWNGNKIIDERLITPDGSMLFRVTINS*

Colicin M(D226A)-sfGFP-strep

METLTVHAPSPSTNLPSYGNGAFSLSAPHVPGAGPLLVQVVYSFFQSPNMCLQALTQLEDYIKKHGA
SNPLTLQIISTNIGYFCNADRNLVLHPGISVYDAYHFAKPAPSQYDYRSMNMKQMSGNVTTPIVALA
HYLWGNGAERSVNIANIGLKISPMKINQIKDIIKSGVVGTFPVSTKFTHATGDYNVITGAYLGNITLKT
EGTLTISANGSWTYNGVVRSYDAKYDFNASTHRGIIGESLTRLGAMFSGKEYQILLPGEIHIKESGKR
GSGGMRKGEELFTGVVPILVELDGDVNGHKFSVRGEGEGDATNGKLTLKFICTTGKLPVPWPTLVTT

LTYGVQCFARYPDHMKQHDFFKSAMPEGYVQERTISFKDDGTYKTRAEVKFEGDTLVNRIELKGIDF
KEDGNILGHKLEYNFNSHNVYITADKQKNGIKANFKIRHNVEDGSVQLADHYQQNTPIGDGPVLLP
DNHYLSTQSVLSKDPNEKRDHMVLLEFVTAAGITHGMDELYKLEVDLQGDHGLSAWSHPQFEK*

$^{+sig}$ΔcΔ5L^{6xHis}

MARSKTAQPKHSLRKIAVVVATAVSGMSVYAQALKEVQFKAGTDSLFQTGFDFSDSLDDDGVYSYR
LTGLARSANAQQKGSEEQRYAIAPAFTWRPDDKTNFTFLSYFQNEPETGNSEGSTYSRNEKMVGYS
FDHEFNDTFTVRQNLRFAENKTSQNSVYGNSEGSRKYVVDDEKLQNFSVDTQLQSKFATGDIDHTL
LTGVDFMRMRNDINAWFGYNSEGSSGPYRILNKQKQTGVYVQDQAQWDKVLVTLGGRYDWADQ
ESLNRVAGTTDKRDDKQFTWRGGVNYLFDNGVTPYFSYSESFEPSSQVGKDGNIFAPSKGKQYEVG
VKYVPEDRPIVVTGAVYNLTKTNNLMADPEGSFFSVEGGEIRARGVEIEAKAALSASVNVVGSYTYTD
AEYTTDTTYKGNTPAQVPKHMASLWADYTFFDGPLSGLTLGTGGRYTNSEGSYTVVDALVRYDLAR
VGMAGSNVALHVNSEGSQVVATATFRFGSGLEHHHHHH*

MBP-TVMV$_{site}$-TVMVp

MKIEEGKLVIWINGDKGYNGLAEVGKKFEKDTGIKVTVEHPDKLEEKFPQVAATGDGPDIIFWAHDR
FGGYAQSGLLAEITPDKAFQDKLYPFTWDAVRYNGKLIAYPIAVEALSLIYNKDLLPNPPKTWEEIPAL
DKELKAKGKSALMFNLQEPYFTWPLIAADGGYAFKYENGKYDIKDVGVDNAGAKAGLTFLVDLIKNK
HMNADTDYSIAEAAFNKGETAMTINGPWAWSNIDTSKVNYGVTVLPTFKGQPSKPFVGVLSAGINA
ASPNKELAKEFLENYLLTDEGLEAVNKDKPLGAVALKSYEEELVKDPRIAATMENAQKGEIMPNIPQ
MSAFWYAVRTAVINAASGRQTVDEALKDAQTNSSSNNNNNNNNNNLGIEGRISHMSMGGRETVR
FQSSKALLKGVRDFNPISACVCLLENSSDGHSERLFGIGFGPYIIANQHLFRRNNGELTIKTMHGEFK
VKNSTQLQMKPVEGRDIIVIKMAKDFPPFPQKLKFRQPTIKDRVCMVSTNFQQKSVSSLVSESSHIVH
KEDTSFWQHWITTKDGQCGSPLVSIIDGNILGIHSLTHTTNGSNYFVEFPEKFVATYLDAADGWCK
NWKFNADKISWGSFTLVEDAPEDDFMAKKTVAAIMDGGSHHHHHH*

TEV protease expression strain *E. coli* BL21(DE3)-RIL/pRK793, originating from David S. Waugh lab [438], and kindly provided by the Kolmar research group (TU Darmstadt).

TEV-protease (as self-cleaving MBP-fusion):

MKTEEGKLVIWINGDKGYNGLAEVGKKFEKDTGIKVTVEHPDKLEEKFPQVAATGDGPDIIFWAHD
RFGGYAQSGLLAEITPDKAFQDKLYPFTWDAVRYNGKLIAYPIAVEALSLIYNKDLLPNPPKTWEEIPA
LDKELKAKGKSALMFNLQEPYFTWPLIAADGGYAFKYENGKYDIKDVGVDNAGAKAGLTFLVDLIKN
KHMNADTDYSIAEAAFNKGETAMTINGPWAWSNIDTSKVNYGVTVLPTFKGQPSKPFVGVLSAGIN
AASPNKELAKEFLENYLLTDEGLEAVNKDKPLGAVALKSYEEELAKDPRIAATMENAQKGEIMPNIPQ
MSAFWYAVRTAVINAASGRQTVDEALKDAQTNSSSNNNNNNNNNNLGIEGRGENLYFQGHHHH
HHHGESLFKGPRDYNPISSTICHLTNESDGHTTSLYGIGFGPFIITNKHLFRRNNGTLLVQSLHGVFK
VKNTTTLQQHLIDGRDMIIIRMPKDFPPFPQKLKFREPQREERICLVTTNFQTKSMSSMVSDTSCTFP
SSDGIFWKHWIQTKDGQCGSPLVSTRDGFIVGIHSASNFTNTNNYFTSVPKNFMELLTNQEAQQW
VSGWRLNADSVLWGGHKVFMVKPEEPFQPVKEATQLMNRRRRR*

SH3-TVMVp (as self-cleaving MBP-fusion)

MGKIEEGKLVIWINGDKGYNGLAEVGKKFEKDTGIKVTVEHPDKLEEKFPQVAATGDGPDIIFWAHD
RFGGYAQSGLLAEITPDKAFQDKLYPFTWDAVRYNGKLIAYPIAVEALSLIYNKDLLPNPPKTWEEIPA
LDKELKAKGKSALMFNLQEPYFTWPLIAADGGYAFKYENGKYDIKDVGVDNAGAKAGLTFLVDLIKN
KHMNADTDYSIAEAAFNKGETAMTINGPWAWSNIDTSKVNYGVTVLPTFKGQPSKPFVGVLSAGIN
AASPNKELAKEFLENYLLTDEGLEAVNKDKPLGAVALKSYEEELVKDPRIAATMENAQKGEIMPNIPQ
MSAFWYAVRTAVINAASGRQTVDEALKDAQTNSSSGGETVRFQSGGSGTGGAEYVRALFDFNGND
EEDLPFKKGDILRIRDKPEEQWWNAEDSEGKRGMIPVPYVEKYGSEGSTSGSGGGGSGAGSTKGSK
ALLKGVRDFNPISACVCLLENSSDGHSERLFGIGFGPYIIANQHLFRRNNGELTIKTMHGEFKVKNST
QLQMKPVEGRDIIVIKMAKDFPPFPQKLKFRQPTIKDRVCMVSTNFQQKSVSSLVSESSHIVHKEDTS
FWQHWITTKDGQCGSPLVSIIDGNILGIHSLTHTTNGSNYFVEFPEKFVATYLDAADGWCKNWKFN
ADKISWGSFTLVEDAPEDGGSWSHPQFEKGIA*

GST-strep-NB_{GFP} (used for pulldown experiment)

MSPILGYWKIKGLVQPTRLLLEYLEEKYEEHLYERDEGDKWRNKKFELGLEFPNLPYYIDGDVKLTQS
MAIIRYIADKHNMLGGCPKERAEISMLEGAVLDIRYGVSRIAYSKDFETLKVDFLSKLPEMLKMFEDR
LCHKTYLNGDHVTHPDFMLYDALDVVLYMDPMCLDAFPKLVCFKKRIEAIPQIDKYLKSSKYIAWPL
QGWQATFGGGDHPPKSDLEVLFQGPLGSGWSHPQFEKSGSMAQVQLVESGGALVQPGGSLRLSC
AASGFPVNRYSMRWYRQAPGKEREWVAGMSSAGDRSSYEDSVKGRFTISRDDARNTVYLQMNSL
KPEDTAVYYCNVNVGFEYWGQGTQVTVSSKLERPHRD*

MBP-$eGFP^{6xHis}$ (used for pulldown experiment, kindly provided by Wadim Weber)

MKIEEGKLVIWINGDKGYNGLAEVGKKFEKDTGIKVTVEHPDKLEEKFPQVAATGDGPDIIFWAHDR
FGGYAQSGLLAEITPDKAFQDKLYPFTWDAVRYNGKLIAYPIAVEALSLIYNKDLLPNPPKTWEEIPAL
DKELKAKGKSALMFNLQEPYFTWPLIAADGGYAFKYENGKYDIKDVGVDNAGAKAGLTFLVDLIKNK
HMNADTDYSIAEAAFNKGETAMTINGPWAWSNIDTSKVNYGVTVLPTFKGQPSKPFVGVLSAGINA
ASPNKELAKEFLENYLLTDEGLEAVNKDKPLGAVALKSYEEELAKDPRIAATMENAQKGEIMPNIPQ
MSAFWYAVRTAVINAASGRQTVDEALKDAQTNSSSNNNNNNNNNNEFGGSETVRFQSGSVSKGE
ELFTGVVPILVELDGDVNGHKFSVSGEGEGDATYGKLTLKFICTTGKLPVPWPTLVTTLTYGVQCFSR
YPDHMKQHDFFKSAMPEGYVQERTIFFKDDGNYKTRAEVKFEGDTLVNRIELKGIDFKEDGNILGH
KLEYNYNSHNVYIMADKQKNGIKVNFKIRHNIEDGSVQLADHYQQNTPIGDGPVLLPDNHYLSTQS
ALSKDPNEKRDHMVLLEFVTAAGITLGMDELYKGTSGGHHHHHH*

NB_{GFP}-SpyCatcher002

MGQVQLVESGGALVQPGGSLRLSCAASGFPVNRYSMRWYRQAPGKEREWVAGMSSAGDRSSYED
SVKGRFTISRDDARNTVYLQMNSLKPEDTAVYYCNVNVGFEYWGQGTQVTVSSGGSGGSGVTTLS
GLSGEQGPSGDMTTEEDSATHIKFSKRDEDGRELAGATMELRDSSGKTISTWISDGHVKDFYLYPG
KYTFVETAAPDGYEVATAITFTVNEQGQVTVNGEATKGDAHTGGASPAGGWSHPQFEKGIA*

$NB_{mCherry}$-SpyCatcher002

MGQVQLVESGGSLVQPGGSLRLSCAASGRFAESSSMGWFRQAPGKEREFVAAISWSGGATNYADS
AKGRFTLSRDNTKNTVYLQMNSLKPDDTAVYYCAANLGNYISSNQRLYGYWGQGTQVTVSSGGSG
GSGVTTLSGLSGEQGPSGDMTTEEDSATHIKFSKRDEDGRELAGATMELRDSSGKTISTWISDGHV
KDFYLYPGKYTFVETAAPDGYEVATAITFTVNEQGQVTVNGEATKGDAHTGGASPAGGWSHPQFE
KGIA*

$NB_{Amylase}$-SpyCatcher002

MGQVQLVESGGGSVQAGGSLSLSCAASTYTDTVGWFRQAPGKEREGVAAIYRRTGYTYSADSVKG
RFTLSQDNNKNTVYLQMNSLKPEDTGIYYCATGNSVRLASWEGYFYWGQGTQVTVSSGGSGGSGV
TTLSGLSGEQGPSGDMTTEEDSATHIKFSKRDEDGRELAGATMELRDSSGKTISTWISDGHVKDFYL
YPGKYTFVETAAPDGYEVATAITFTVNEQGQVTVNGEATKGDAHTGGASPAGGWSHPQFEKGIA*

Tether Peptide (As MBP fusion)

MGDRGPEFMKIEEGKLVIWINGDKGYNGLAEVGKKFEKDTGIKVTVEHPDKLEEKFPQVAATGDGP
DIIFWAHDRFGGYAQSGLLAEITPDKAFQDKLYPFTWDAVRYNGKLIAYPIAVEALSLIYNKDLLPNPP
KTWEEIPALDKELKAKGKSALMFNLQEPYFTWPLIAADGGYAFKYENGKYDIKDVGVDNAGAKAGL
TFLVDLIKNKHMNADTDYSIAEAAFNKGETAMTINGPWAWSNIDTSKVNYGVTVLPTFKGQPSKPF
VGVLSAGINAASPNKELAKEFLENYLLTDEGLEAVNKDKPLGAVALKSYEEELVKDPRIAATMENAQK
GEIMPNIPQMSAFWYAVRTAVINAASGRQTVDEALKDAQTNSSSENLYFQSGPPPPLPPKRRRGVP
TIVMVDAYKRYKGGSGGSETVRFQSGSTSGSGKPGSGEGSTKGWSHPQFEKGLPETGG*

Immobilized Tether Peptide from N- to C-terminus:

SGPPPPLPPKRRRGVPTIVMVDAYKRYKGGSGGSETVRFQSGSTSGSGKPGSGEGSTKGWSHPQFE
KGLPET-Azidopropanamin(Azp)

sfGFP-6xHis

MSKGEELFTGVVPILVELDGDVNGHKFSVRGEGEGDATNGKLTLKFICTTGKLPVPWPTLVTTLTYG
VQCFSRYPDHMKRHDFFKSAMPEGYVQERTISFKDDGTYKTRAEVKFEGDTLVNRIELKGIDFKEDG
NILGHKLEYNFNSHNVYITADKQKNGIKANFKIRHNVEDGSVQLADHYQQNTPIGDGPVLLPDNHY
LSTQSVLSKDPNEKRDHMVLLEFVTAAGITHGMDELYKGTSGGHHHHHH*

Addgene plasmid #62936 for expression of GFP(-30) was kindly provided by Markus Langhans.

6xHis-GFP(-30)

MGHHHHHHGGASKGEELFDGVVPILVELDGDVNGHEFSVRGEGEGDATEGELTLKFICTTGELPVP
WPTLVTTLTYGVQCFSDYPDHMDQHDFFKSAMPEGYVQERTISFKDDGTYKTRAEVKFEGDTLVN
RIELKGIDFKEDGNILGHKLEYNFNSHDVYITADKQENGIKAEFEIRHNVEDGSVQLADHYQQNTPIG
DGPVLLPDDHYLSTESALSKDPNEDRDHMVLLEFVTAAGIDHGMDELYK*

mCherry-strep

MGVSKGEEDNMAIIKEFMRFKVHMEGSVNGHEFEIEGEGEGRPYEGTQTAKLKVTKGGPLPFAWDI
LSPQFMYGSKAYVKHPADIPDYLKLSFPEGFKWERVMNFEDGGVVTVTQDSSLQDGEFIYKVKLRG
TNFPSDGPVMQKKTMGWEASSERMYPEDGALKGEIKQRLKLKDGGHYDAEVKTTYKAKKPVQLPG
AYNVNIKLDITSHNEDYTIVEQYERAEGRHSTGGMDELYKGGASPAGGWSHPQFEKGLPETGG*

Sortase A7M-6xHis

MQAKPQIPKDKSKVAGYIEIPDADIKEPVYPGPATREQLNRGVSFAKENQSLDDQNISIAGHTFIDRP
NYQFTNLKAAKKGSMVYFKVGNETRKYKMTSIRNVKPTAVEVLDEQKGKDKQLTLITCDDYNEETG
VWETRKIFVATEVKLEHHHHHH*

Sortase A5M-strep

MQAKPQIPKDKSKVAGYIEIPDADIKEPVYPGPATREQLNRGVSFAEENESLDDQNISIAGHTFIDRP
NYQFTNLKAAKKGSMVYFKVGNETRKYKMTSIRNVKPTAVEVLDEQKGKDKQLTLITCDDYNEETG
VWETRKIFVATEVKLEWSHPQFEK*

Abbreviations

Abbreviation	Meaning
(v/v)	Volume per volume
(w/v)	Weight per volume
(w/w)	Weight per weight
+sig	33-*aa* Omp signal sequence of wtFhuA
°C	Degree Celsius
μ	Micro (as unit prefix)
1D	One dimensional
2D	Two dimensional
3D	Three dimensional
6xHis	6x Histidine (purification tag)
A	Ampere (as unit)
Å	Ångström; 10^{-10} m
A/D	Analog/digital
aa	Amino acid
aHL	α-hemolysin
AI_{TVMV}	Autoinhibitory domain of TVMV protease
ANA-peptide	Quenched TVMV protease substrate, see section 2.10 Chapter 1
AU	Absorbance unit
Azp	Azidopropanamine
BAM	Beta-barrel assembly machinery
bp	basepair
cAMP	Cyclic adenosine monophosphate
CD-spectroscopy	Circular dichroism spectroscopy
CfaN	N-terminal part of a split-intein (Consensus from alignment) [456]
CFP	Cyan Fluorescent Protein
CLSM	Confocal Laser Scanning microscope
Cryo-EM	Cryo electron microscopy
CuAAC	Cu(I)-catalyzed azide-alkyne cycloadditions
CV	Column volume
DBCO	Dibenzocyclooctyne amin
DDM	n-Dodecyl-β-D-maltosid
DMSO	Dimethyl sulfoxide
DNA	Desoxyribonucleic acid
dNTPs	Desoxynucleoside triphospates
DPhPC	1,2-diphytanoyl-*sn*-glycero-3-phosphocholine
dsDNA	Double stranded DNA

DTT	Dithiothreitol
e	Charge of a proton
E. coli	*Escherichia coli*
EDC	1-Ethyl-3-(3-dimethylaminopropyl)- carbodiimide
EDTA	ethylenediaminetetraacetic acid
ePDZ-b1	Enhanced PDZ domain [204]
ExoIII	Exonuclease III
F	Farad (as unit)
f	femto (as unit prefix)
FAM	5-Fluorescein
FD	Functional domain
FhuA	Ferrihydroxamate uptake component A
FKBP	FKBP12, 12-kDa FK506 binding protein
FN3	10^{th} fibronectin type III domain of human Fibronectin
FRB	FKBP12-rapamycin binding domain
FRET	Förster resonance energy transfer
G	Conductance (used in SSN context)
GC buffer	PCR buffer from New England biolabs
GFP	Green Fluorescent Protein
GluSnFR	Glutamate sensing fluorescent reporter
GST	Glutathione S-Transferase from *Schistosoma japonicum*
h	hours
HIV	Human immunodeficiency virus
i	position
iFLinkC	Iterative functional linker cloning
IgG	Immunoglobulin G
IPTG	isopropyl-β-D-thiogalactopyranosid
ITC	Isothermal titration calorimetry
IUPAC	International Union of Pure and Applied Chemistry
I-V	Current-Voltage
K_D	Equilibrium dissociation constant
K_i	Equilibrium dissociation constant of inhibitor
K_M	Michaelis constant
kDa	kilo Dalton
kEV	Kilo electron volt
kJ	Kilo Joule
l	liter
L1, L2, L3	Linker position 1, 2, 3

LCR	Ligase cycling reaction / Cycled ligation assembly
LgBiT	Large subunit of engineered split luciferase NanoBiT
M	Molar (as unit)
m	Milli (as unit prefix) or meter (as unit)
max.	maximum
MBP	Maltose binding protein
mdeg	Millidegree, measure for ellipticity in CD-measurements
min	Minutes
min.	minimum
mol	Amount of substance (unit)
mRFP	Monomeric red fluorescent protein
MspA	*Mycobacterium smegmatis* porin A
MST	Microscale thermophoresis
n	Number or nano (as unit prefix)
N	Number for independent experiments, e.g. N=3
$N_{2(l)}$	Liquid nitrogen
NB	nanobody
$NB_{subscript}$	Nanobody specifically binding the analyte indicated in the subsript
NHS	N-Hydroxysuccinimide
Nia	Nuclear Inclusion protein A
NTA	nitrilotriacetic acid
O/N	overnight
OD_{600}	Optical density at 600 nm
Omp	Outer membrane protein
ori	Origin of replication
p	pico (as unit prefix)
PAGE	Polyacrylamide gel electrophoresis
PCR	Polymerase Chain Reaction
PDB	Protein data bank
PDZ	Erbin PDZ domain
PEG	Poly(ethylene glucol)
PET	Poly(ethylene therephtalat)
pET32/pET24	Refers to specific DNA plasmids
pers. comm.	Personal communication
PFP	Pentafluorophenol
pH	Measure for acidity or basicity of an aqueous solution
PhD	Doctor of Philosophy
pI	Isoelectric point
PPII helix	Poly-proline type II helix

PTFE	Polytetrafluorethylene (Teflon)
PVP	Polyvinylpyrrolidone
R^2	Coefficient of determination
RF	Rectification Factor (definition in section 1.1, Chapter 4)
RFU	Relative fluorescence units
RNA	Ribonucleic acid
rpm	Rounds per minute
rSAP	Recombinant shrimp alkaline phosphatase
RT	Room temperature (≈ 24 °C)
s	Seconds
S	Siemens (as unit)
SAM	Self-assembled monolayer
SDS	Sodium dodecylsulfate
sfGFP	Superfolder GFP [342]
sFvs	Single chain variable fragments
SmBiT86	Small subunit of engineered split luciferase NanoBiT (variant 86)
SOC	Scaffold oligo connector
SPAAC	Strain-promoted azide-alkyne cycloadditions
SSNs	Solid-state nanopores
Strep	StrepTag II (purification tag)
Tether Peptide	Immobilization peptide with the sequence SGPPPPLPPKRRRGVPTIVMVDAYKRYKGGS GGSETVRFQSGSTSGSGKPGSGEGSTKGWSHPQFEKGLPETGG
TEV	Tobacco etch virus
TL-FhuA	Tagless FhuA
Tris	Tris(hydroxymethyl)-aminomethan
TU	Technical University
TVMV	Tobbaco vein mottling virus
TVMVp	Tobacco vein mottling virus protease
$TVMV_{site}$	Cleavage site of TVMV protease
V	Volt (as unit)
V_HH	Engineered single-domain antibody from camelids
V_{NAR}	Engineered single-domain antibody from Chondrichthyes
W	Watt
wt	Wildtype
xg	times g-force
YFP	Yellow Fluorescent Protein
Δ	Difference (as unit prefix)
ΔcΔ5L	FhuA variant with deleted cork and 5 main loops
ΔH	Enthalpy difference

λ	Wavelength
Ω	Ohm

Amino acid code

Code	Amino acid
A	Alanine
C	Cysteine
D	Aspartic acid
E	Glutamic acid
F	Phenylalanine
G	Glycine
H	Histidine
I	Isoleucine
K	Lysine
L	Leucine
M	Methionine
N	Asparagine
P	Proline
Q	Glutamine
R	Arginine
S	Serine
T	Threonine
V	Valine
W	Tryptophan
Y	Tyrosine

References

1. Luisi PL, Stano P. Synthetic biology: minimal cell mimicry. Nat Chem. 2011; 3:755–6. doi: 10.1038/nchem.1156 PMID: 21941243.
2. Chen Z, Kibler RD, Hunt A, Busch F, Pearl J, Jia M, et al. De novo design of protein logic gates. Science. 2020; 368:78–84. doi: 10.1126/science.aay2790 PMID: 32241946.
3. Wagner HJ, Engesser R, Ermes K, Geraths C, Timmer J, Weber W. Synthetic biology-inspired design of signal-amplifying materials systems. Materials Today. 2019; 22:25–34. doi: 10.1016/j.mattod.2018.04.006.
4. Opgenorth P, Costello Z, Okada T, Goyal G, Chen Y, Gin J, et al. Lessons from Two Design-Build-Test-Learn Cycles of Dodecanol Production in Escherichia coli Aided by Machine Learning. ACS Synth Biol. 2019; 8:1337–51. doi: 10.1021/acssynbio.9b00020 PMID: 31072100.
5. Stein V, Alexandrov K. Protease-based synthetic sensing and signal amplification. Proc Natl Acad Sci U S A. 2014; 111:15934–9. doi: 10.1073/pnas.1405220111 PMID: 25355910.
6. Kuhlman B, Jacobs T, Linskey T. Computational Design of Protein Linkers. Methods Mol Biol. 2016; 1414:341–51. doi: 10.1007/978-1-4939-3569-7_20 PMID: 27094301.
7. Kuhlman B, Bradley P. Advances in protein structure prediction and design. Nat Rev Mol Cell Biol. 2019; 20:681–97. doi: 10.1038/s41580-019-0163-x PMID: 31417196.
8. Guntas G, Mansell TJ, Kim JR, Ostermeier M. Directed evolution of protein switches and their application to the creation of ligand-binding proteins. Proceedings of the National Academy of Sciences. 2005; 102:11224–9. doi: 10.1073/pnas.0502673102 PMID: 16061816.
9. National Center for Biotechnology Information. PubMed® Central [cited 18 Jul 2020]. Available from: https://pubmed.ncbi.nlm.nih.gov/.
10. Wu Y, Jiang S, Ying T. Single-Domain Antibodies As Therapeutics against Human Viral Diseases. Front Immunol. 2017; 8:1802. doi: 10.3389/fimmu.2017.01802 PMID: 29326699.
11. Ren H, Zhu S, Zheng G. Nanoreactor Design Based on Self-Assembling Protein Nanocages. Int J Mol Sci. 2019; 20. doi: 10.3390/ijms20030592 PMID: 30704048.
12. Henrich E, Dötsch V, Bernhard F. Screening for lipid requirements of membrane proteins by combining cell-free expression with nanodiscs. Meth Enzymol. 2015; 556:351–69. doi: 10.1016/bs.mie.2014.12.016 PMID: 25857790.
13. Krishnamurthy S, Muthukumaran P, Jayakumar MKG, Lisse D, Masurkar ND, Xu C, et al. Surface protein engineering increases the circulation time of a cell membrane-based nanotherapeutic. Nanomedicine. 2019; 18:169–78. doi: 10.1016/j.nano.2019.02.024 PMID: 30853651.
14. Hall MP, Unch J, Binkowski BF, Valley MP, Butler BL, Wood MG, et al. Engineered luciferase reporter from a deep sea shrimp utilizing a novel imidazopyrazinone substrate. ACS Chem Biol. 2012; 7:1848–57. doi: 10.1021/cb3002478 PMID: 22894855.
15. Arai R. Hierarchical design of artificial proteins and complexes toward synthetic structural biology. Biophys Rev. 2018; 10:391–410. doi: 10.1007/s12551-017-0376-1 PMID: 29243094.
16. Stranges PB, Palla M, Kalachikov S, Nivala J, Dorwart M, Trans A, et al. Design and characterization of a nanopore-coupled polymerase for single-molecule DNA sequencing by synthesis on an electrode array. Proc Natl Acad Sci U S A. 2016. doi: 10.1073/pnas.1608271113 PMID: 27729524.
17. Chandrasekaran AR, MacIsaac M, Dey P, Levchenko O, Zhou L, Andres M, et al. Cellular microRNA detection with miRacles: microRNA- activated conditional looping of engineered switches. Sci Adv. 2019; 5:eaau9443. doi: 10.1126/sciadv.aau9443 PMID: 30891499.
18. Vecchioni S, Capece MC, Toomey E, Le Nguyen, Ray A, Greenberg A, et al. Construction and characterization of metal ion-containing DNA nanowires for synthetic biology and nanotechnology. Sci Rep. 2019; 9:6942. doi: 10.1038/s41598-019-43316-1 PMID: 31061396.
19. Cosert KM, Castro-Forero A, Steidl RJ, Worden RM, Reguera G. Bottom-Up Fabrication of Protein Nanowires via Controlled Self-Assembly of Recombinant Geobacter Pilins. mBio. 2019; 10. doi: 10.1128/mBio.02721-19 PMID: 31822587.
20. Battigelli A, Kim JH, Dehigaspitiya DC, Proulx C, Robertson EJ, Murray DJ, et al. Glycosylated Peptoid Nanosheets as a Multivalent Scaffold for Protein Recognition. ACS Nano. 2018; 12:2455–65. doi: 10.1021/acsnano.7b08018 PMID: 29512997.
21. Vidarsson G, Dekkers G, Rispens T. IgG subclasses and allotypes: from structure to effector functions. Front Immunol. 2014; 5:520. doi: 10.3389/fimmu.2014.00520 PMID: 25368619.
22. Nelson DL, Cox MM, Lehninger AL, Beginnen K. Lehninger Biochemie. Mit 40 Tabellen. 3rd ed. Berlin: Springer; 2005.
23. Zielonka S, Weber N, Becker S, Doerner A, Christmann A, Christmann C, et al. Shark Attack: high affinity binding proteins derived from shark vNAR domains by stepwise in vitro affinity maturation. J Biotechnol. 2014; 191:236–45. doi: 10.1016/j.jbiotec.2014.04.023 PMID: 24862193.
24. Uchański T, Zögg T, Yin J, Yuan D, Wohlkönig A, Fischer B, et al. An improved yeast surface display platform for the screening of nanobody immune libraries. Sci Rep. 2019; 9:382. doi: 10.1038/s41598-018-37212-3 PMID: 30674983.
25. Desmyter A, Spinelli S, Payan F, Lauwereys M, Wyns L, Muyldermans S, et al. Three camelid VHH domains in complex with porcine pancreatic alpha-amylase. Inhibition and versatility of binding topology. J Biol Chem. 2002; 277:23645–50. doi: 10.1074/jbc.M202327200 PMID: 11960990.
26. Wang X, Chen Q, Sun Z, Wang Y, Su B, Zhang C, et al. Nanobody affinity improvement: Directed evolution of the anti-ochratoxin A single domain antibody. International Journal of Biological Macromolecules. 2020; 151:312–21. doi: 10.1016/j.ijbiomac.2020.02.180 PMID: 32084462.
27. Cao J, Zhong N, Wang G, Wang M, Zhang B, Fu B, et al. Nanobody-based sandwich reporter system for living cell sensing influenza A virus infection. Sci Rep. 2019; 9:15899. doi: 10.1038/s41598-019-52258-7 PMID: 31685871.

28. Stein V, Nabi M, Alexandrov K. Ultrasensitive Scaffold-Dependent Protease Sensors with Large Dynamic Range. ACS Synth Biol. 2017; 6:1337–42. doi: 10.1021/acssynbio.6b00370 PMID: 28291337.

29. Buchfellner A, Yurlova L, Nüske S, Scholz AM, Bogner J, Ruf B, et al. A New Nanobody-Based Biosensor to Study Endogenous PARP1 In Vitro and in Live Human Cells. PLoS One. 2016; 11:e0151041. doi: 10.1371/journal.pone.0151041 PMID: 26950694.

30. Pan D, Li G, Hu H, Xue H, Zhang M, Zhu M, et al. Direct Immunoassay for Facile and Sensitive Detection of Small Molecule Aflatoxin B1 based on Nanobody. Chemistry. 2018; 24:9869–76. doi: 10.1002/chem.201801202 PMID: 29766584.

31. Li G, Zhu M, Ma L, Yan J, Lu X, Shen Y, et al. Generation of Small Single Domain Nanobody Binders for Sensitive Detection of Testosterone by Electrochemical Impedance Spectroscopy. ACS Appl Mater Interfaces. 2016; 8:13830–9. doi: 10.1021/acsami.6b04658 PMID: 27196036.

32. Rasmussen SGF, Choi H-J, Fung JJ, Pardon E, Casarosa P, Chae PS, et al. Structure of a nanobody-stabilized active state of the β (2) adrenoceptor. Nature. 2011; 469:175–80. doi: 10.1038/nature09648 PMID: 21228869.

33. Hui JZ, Tamsen S, Song Y, Tsourkas A. LASIC: Light Activated Site-Specific Conjugation of Native IgGs. Bioconjug Chem. 2015; 26:1456–60. doi: 10.1021/acs.bioconjchem.5b00275 PMID: 26057140.

34. Marraffini LA, Dedent AC, Schneewind O. Sortases and the art of anchoring proteins to the envelopes of gram-positive bacteria. Microbiol Mol Biol Rev. 2006; 70:192–221. doi: 10.1128/MMBR.70.1.192-221.2006 PMID: 16524923.

35. Clow F, Fraser JD, Proft T. Immobilization of proteins to biacore sensor chips using Staphylococcus aureus sortase A. Biotechnol Lett. 2008; 30:1603–7. doi: 10.1007/s10529-008-9718-1 PMID: 18414796.

36. Parthasarathy R, Subramanian S, Boder ET. Sortase A as a novel molecular "stapler" for sequence-specific protein conjugation. Bioconjug Chem. 2007; 18:469–76. doi: 10.1021/bc060339w PMID: 17302384.

37. Hirakawa H, Ishikawa S, Nagamune T. Design of Ca2+-independent Staphylococcus aureus sortase A mutants. Biotechnol Bioeng. 2012; 109:2955–61. doi: 10.1002/bit.24585 PMID: 22729808.

38. Chen I, Dorr BM, Liu DR. A general strategy for the evolution of bond-forming enzymes using yeast display. Proc Natl Acad Sci U S A. 2011; 108:11399–404. doi: 10.1073/pnas.1101046108 PMID: 21697512.

39. Glasgow JE, Salit ML, Cochran JR. In Vivo Site-Specific Protein Tagging with Diverse Amines Using an Engineered Sortase Variant. J Am Chem Soc. 2016; 138:7496–9. doi: 10.1021/jacs.6b03836 PMID: 27280683.

40. Kang HJ, Baker EN. Intramolecular isopeptide bonds: protein crosslinks built for stress. Trends Biochem Sci. 2011; 36:229–37. doi: 10.1016/j.tibs.2010.09.007 PMID: 21055949.

41. Reddington SC, Howarth M. Secrets of a covalent interaction for biomaterials and biotechnology: SpyTag and SpyCatcher. Curr Opin Chem Biol. 2015; 29:94–9. doi: 10.1016/j.cbpa.2015.10.002 PMID: 26517567.

42. Zakeri B, Fierer JO, Celik E, Chittock EC, Schwarz-Linek U, Moy VT, et al. Peptide tag forming a rapid covalent bond to a protein, through engineering a bacterial adhesin. Proc Natl Acad Sci U S A. 2012; 109:E690-7. doi: 10.1073/pnas.1115485109 PMID: 22366317.

43. Veggiani G, Nakamura T, Brenner MD, Gayet RV, Yan J, Robinson CV, et al. Programmable polyproteams built using twin peptide superglues. Proc Natl Acad Sci U S A. 2016; 113:1202–7. doi: 10.1073/pnas.1519214113 PMID: 26787909.

44. Keeble AH, Banerjee A, Ferla MP, Reddington SC, Anuar INAK, Howarth M. Evolving Accelerated Amidation by SpyTag/SpyCatcher to Analyze Membrane Dynamics. Angew Chem Int Ed Engl. 2017; 56:16521–5. doi: 10.1002/anie.201707623 PMID: 29024296.

45. Liu Y, Liu D, Yang W, Wu X-L, Lai L, Zhang W-B. Tuning SpyTag–SpyCatcher mutant pairs toward orthogonal reactivity encryption. Chem. Sci. 2017; 32:506. doi: 10.1039/C7SC02686B.

46. Sun F, Zhang W-B, Mahdavi A, Arnold FH, Tirrell DA. Synthesis of bioactive protein hydrogels by genetically encoded SpyTag-SpyCatcher chemistry. Proc Natl Acad Sci U S A. 2014; 111:11269–74. doi: 10.1073/pnas.1401291111 PMID: 25049400.

47. Gao X, Fang J, Xue B, Fu L, Li H. Engineering Protein Hydrogels Using SpyCatcher-SpyTag Chemistry. Biomacromolecules. 2016; 17:2812–9. doi: 10.1021/acs.biomac.6b00566 PMID: 27477779.

48. Wan X, Volpetti F, Petrova E, French C, Maerkl SJ, Wang B. Cascaded amplifying circuits enable ultrasensitive cellular sensors for toxic metals. Nat Chem Biol. 2019; 15:540–8. doi: 10.1038/s41589-019-0244-3 PMID: 30911179.

49. Akter F, Yokobayashi Y. RNA signal amplifier circuit with integrated fluorescence output. ACS Synth Biol. 2015; 4:655–8. doi: 10.1021/sb500314r PMID: 25354355.

50. Lebar T, Bezeljak U, Golob A, Jerala M, Kadunc L, Pirš B, et al. A bistable genetic switch based on designable DNA-binding domains. Nat Comms. 2014; 5:5007. doi: 10.1038/ncomms6007 PMID: 25264186.

51. Gao XJ, Chong LS, Kim MS, Elowitz MB. Programmable protein circuits in living cells. Science. 2018; 361:1252–8. doi: 10.1126/science.aat5062 PMID: 30237357.

52. Gräwe A, Ranglack J, Weber W, Stein V. Engineering artificial signalling functions with proteases. Curr Opin Biotechnol. 2020; 63:1–7. doi: 10.1016/j.copbio.2019.09.017 PMID: 31698156.

53. Zheng N, Pérez JdJ, Zhang Z, Domínguez E, Garcia JA, Xie Q. Specific and efficient cleavage of fusion proteins by recombinant plum pox virus NIa protease. Protein Expr Purif. 2008; 57:153–62. doi: 10.1016/j.pep.2007.10.008 PMID: 18024078.

54. Sun P, Austin BP, Tözsér J, Waugh DS. Structural determinants of tobacco vein mottling virus protease substrate specificity. Protein Sci. 2010; 19:2240–51. doi: 10.1002/pro.506 PMID: 20862670.

55. Howorka S, Siwy Z. Nanopore analytics: sensing of single molecules. Chem Soc Rev. 2009; 38:2360–84. doi: 10.1039/b813796j PMID: 19623355.

56. Braha O, Walker B, Cheley S, Kasianowicz JJ, Song L, Gouaux JE, et al. Designed protein pores as components for biosensors. Chem Biol. 1997; 4:497–505.

57. Bayley H. Nanopore sequencing. From imagination to reality. Clin Chem. 2015; 61:25–31. doi: 10.1373/clinchem.2014.223016 PMID: 25477535.

58. Mongan AE, Tuda JSB, Runtuwene LR. Portable sequencer in the fight against infectious disease. J Hum Genet. 2020; 65:35–40. doi: 10.1038/s10038-019-0675-4 PMID: 31582773.
59. Faria NR, Sabino EC, Nunes MRT, Alcantara LCJ, Loman NJ, Pybus OG. Mobile real-time surveillance of Zika virus in Brazil. Genome Med. 2016; 8:97. doi: 10.1186/s13073-016-0356-2 PMID: 27683027.
60. Shin SC, Kim H, Lee JH, Kim H-W, Park J, Choi B-S, et al. Nanopore sequencing reads improve assembly and gene annotation of the Parochlus steinenii genome. Sci Rep. 2019; 9:5095. doi: 10.1038/s41598-019-41549-8 PMID: 30911035.
61. Schmidt J. Stochastic sensors. J Mater Chem. 2005; 15:831. doi: 10.1039/b414551h.
62. Bayley H, Cremer PS. Stochastic sensors inspired by biology. Nature. 2001; 413:226–30. doi: 10.1038/35093038 PMID: 11557992.
63. Pham B, Eron SJ, Hill ME, Li X, Fahie MA, Hardy JA, et al. A Nanopore Approach for Analysis of Caspase-7 Activity in Cell Lysates. Biophys J. 2019; 117:844–55. doi: 10.1016/j.bpj.2019.07.045 PMID: 31427065.
64. Morton D, Mortezaei S, Yemenicioglu S, Isaacman MJ, Nova IC, Gundlach JH, et al. Tailored Polymeric Membranes for Mycobacterium Smegmatis Porin A (MspA) Based Biosensors. J Mater Chem B Mater Biol Med. 2015; 3:5080–6. doi: 10.1039/C5TB00383K PMID: 26413301.
65. Bülow L, Ljungcrantz P, Mosbach K. Preparation of a Soluble Bifunctional Enzyme by Gene Fusion. Bio/Technology. 1985; 3:821 EP -. doi: 10.1038/nbt0985-821.
66. Bird RE, Hardman KD, Jacobson JW, Johnson S, Kaufman BM, Lee SM, et al. Single-chain antigen-binding proteins. Science. 1988; 242:423–6. doi: 10.1126/science.3140379 PMID: 3140379.
67. Hires SA, Zhu Y, Tsien RY. Optical measurement of synaptic glutamate spillover and reuptake by linker optimized glutamate-sensitive fluorescent reporters. Proc Natl Acad Sci U S A. 2008; 105:4411–6. doi: 10.1073/pnas.0712008105 PMID: 18332427.
68. Mitchell JA, Whitfield JH, Zhang WH, Henneberger C, Janovjak H, O'Mara ML, et al. Rangefinder: A Semisynthetic FRET Sensor Design Algorithm. ACS Sens. 2016; 1:1286–90. doi: 10.1021/acssensors.6b00576.
69. Deuschle K, Okumoto S, Fehr M, Looger LL, Kozhukh L, Frommer WB. Construction and optimization of a family of genetically encoded metabolite sensors by semirational protein engineering. Protein Sci. 2005; 14:2304–14. doi: 10.1110/ps.051508105 PMID: 16131659.
70. Lobanov MY, Garbuzynskiy SO, Galzitskaya OV. Statistical analysis of unstructured amino acid residues in protein structures. Biochemistry Mosc. 2010; 75:192–200. doi: 10.1134/s0006297910020094 PMID: 20367606.
71. Torres Pazmiño DE, Riebel A, Lange J de, Rudroff F, Mihovilovic MD, Fraaije MW. Efficient biooxidations catalyzed by a new generation of self-sufficient Baeyer-Villiger monooxygenases. Chembiochem. 2009; 10:2595–8. doi: 10.1002/cbic.200900480 PMID: 19795432.
72. Whitlow M, Bell BA, Feng S-L, Filpula D, Hardman KD, Hubert SL, et al. An improved linker for single-chain Fv with reduced aggregation and enhanced proteolytic stability. Protein Eng Des Sel. 1993; 6:989–95. doi: 10.1093/protein/6.8.989.
73. Kaczmarski JA, Mitchell JA, Spence MA, Vongsouthi V, Jackson CJ. Structural and evolutionary approaches to the design and optimization of fluorescence-based small molecule biosensors. Curr Opin Struct Biol. 2019; 57:31–8. doi: 10.1016/j.sbi.2019.01.013 PMID: 30825845.
74. Chen X, Zaro JL, Shen W-C. Fusion protein linkers. Property, design and functionality. Adv Drug Deliv Rev. 2013; 65:1357–69. doi: 10.1016/j.addr.2012.09.039 PMID: 23026637.
75. Liu C, Chin JX, Lee D-Y. SynLinker: an integrated system for designing linkers and synthetic fusion proteins. Bioinformatics. 2015; 31:3700–2. doi: 10.1093/bioinformatics/btv447 PMID: 26227144.
76. Papaleo E, Saladino G, Lambrughi M, Lindorff-Larsen K, Gervasio FL, Nussinov R. The Role of Protein Loops and Linkers in Conformational Dynamics and Allostery. Chem Rev. 2016; 116:6391–423. doi: 10.1021/acs.chemrev.5b00623 PMID: 26889708.
77. Ruiz DM, Turowski VR, Murakami MT. Effects of the linker region on the structure and function of modular GH5 cellulases. Sci Rep. 2016; 6:28504. doi: 10.1038/srep28504 PMID: 27334041.
78. George RA, Heringa J. An analysis of protein domain linkers. Their classification and role in protein folding. Protein Eng. 2002; 15:871–9.
79. Argos P. An investigation of oligopeptides linking domains in protein tertiary structures and possible candidates for general gene fusion. J Mol Biol. 1990; 211:943–58. doi: 10.1016/0022-2836(90)90085-Z.
80. Ramachandran GN, Sasisekharan V. Conformation of Polypeptides and Proteins. In: Anfinsen CB, editor. Advances in protein chemistry. New York, London: Academic Press; 1968. pp. 283–437.
81. Robinson CR, Sauer RT. Optimizing the stability of single-chain proteins by linker length and composition mutagenesis. Proceedings of the National Academy of Sciences. 1998; 95:5929–34. doi: 10.1073/pnas.95.11.5929.
82. Das RK, Ruff KM, Pappu RV. Relating sequence encoded information to form and function of intrinsically disordered proteins. Curr Opin Struct Biol. 2015; 32:102–12. doi: 10.1016/j.sbi.2015.03.008 PMID: 25863585.
83. Kavoosi M, Creagh AL, Kilburn DG, Haynes CA. Strategy for selecting and characterizing linker peptides for CBM9-tagged fusion proteins expressed in Escherichia coli. Biotechnol Bioeng. 2007; 98:599–610. doi: 10.1002/bit.21396 PMID: 17394253.
84. Norris JL, Hughes RM. protaTETHER - a method for the incorporation of variable linkers in protein fusions reveals impacts of linker flexibility in a PKAc-GFP fusion protein. FEBS Open Bio. 2018; 8:1029–42. doi: 10.1002/2211-5463.12414 PMID: 29928581.
85. Evers TH, van Dongen EMWM, Faesen AC, Meijer EW, Merkx M. Quantitative understanding of the energy transfer between fluorescent proteins connected via flexible peptide linkers. Biochemistry. 2006; 45:13183–92. doi: 10.1021/bi061288t PMID: 17073440.
86. Violin JD, Zhang J, Tsien RY, Newton AC. A genetically encoded fluorescent reporter reveals oscillatory phosphorylation by protein kinase C. J Cell Biol. 2003; 161:899–909. doi: 10.1083/jcb.200302125 PMID: 12782683.

87. van Rosmalen M, Krom M, Merkx M. Tuning the Flexibility of Glycine-Serine Linkers To Allow Rational Design of Multidomain Proteins. Biochemistry. 2017; 56:6565–74. doi: 10.1021/acs.biochem.7b00902 PMID: 29168376.
88. Aper SJA, den Hamer A, Wouters SFA, Lemmens LJM, Ottmann C, Brunsveld L, et al. Protease-Activatable Scaffold Proteins as Versatile Molecular Hubs in Synthetic Signaling Networks. ACS Synth Biol. 2018; 7:2216–25. doi: 10.1021/acssynbio.8b00217 PMID: 30125482.
89. Feng J, Jester BW, Tinberg CE, Mandell DJ, Antunes MS, Chari R, et al. A general strategy to construct small molecule biosensors in eukaryotes. Elife. 2015; 4. doi: 10.7554/eLife.10606 PMID: 26714111.
90. Huang J, Makabe K, Biancalana M, Koide A, Koide S. Structural basis for exquisite specificity of affinity clamps, synthetic binding proteins generated through directed domain-interface evolution. J Mol Biol. 2009; 392:1221–31. doi: 10.1016/j.jmb.2009.07.067 PMID: 19646997.
91. Selgrade DF, Lohmueller JJ, Lienert F, Silver PA. Protein scaffold-activated protein trans-splicing in mammalian cells. J Am Chem Soc. 2013; 135:7713–9. doi: 10.1021/ja401689b PMID: 23621664.
92. Reddy Chichili VP, Kumar V, Sivaraman J. Linkers in the structural biology of protein-protein interactions. Protein Sci. 2013; 22:153–67. doi: 10.1002/pro.2206 PMID: 23225024.
93. Zhang Z, Wang Y, Ding Y, Hattori M. Structure-based engineering of anti-GFP nanobody tandems as ultra-high-affinity reagents for purification. Sci Rep. 2020; 10:6239. doi: 10.1038/s41598-020-62606-7 PMID: 32277083.
94. Greineder CF, Villa CH, Walsh LR, Kiseleva RY, Hood ED, Khoshnejad M, et al. Site-Specific Modification of Single-Chain Antibody Fragments for Bioconjugation and Vascular Immunotargeting. Bioconjug Chem. 2018; 29:56–66. doi: 10.1021/acs.bioconjchem.7b00592 PMID: 29200285.
95. Ibraheem A, Yap H, Ding Y, Campbell RE. A bacteria colony-based screen for optimal linker combinations in genetically encoded biosensors. BMC Biotechnol. 2011; 11:105. doi: 10.1186/1472-6750-11-105 PMID: 22074568.
96. Rose JC, Huang P-S, Camp ND, Ye J, Leidal AM, Goreshnik I, et al. A computationally engineered RAS rheostat reveals RAS-ERK signaling dynamics. Nat Chem Biol. 2017; 13:119–26. doi: 10.1038/nchembio.2244 PMID: 27870838.
97. Komatsu N, Aoki K, Yamada M, Yukinaga H, Fujita Y, Kamioka Y, et al. Development of an optimized backbone of FRET biosensors for kinases and GTPases. Mol Biol Cell. 2011; 22:4647–56. doi: 10.1091/mbc.E11-01-0072 PMID: 21976697.
98. Jones AM, Danielson JA, Manojkumar SN, Lanquar V, Grossmann G, Frommer WB. Abscisic acid dynamics in roots detected with genetically encoded FRET sensors. Elife. 2014; 3:e01741. doi: 10.7554/eLife.01741 PMID: 24737862.
99. Sørensen CS, Jendroszek A, Kjaergaard M. Linker Dependence of Avidity in Multivalent Interactions between Disordered Proteins. J Mol Biol. 2019. doi: 10.1016/j.jmb.2019.09.001 PMID: 31518611.
100. Sørensen CS, Kjaergaard M. Effective concentrations enforced by intrinsically disordered linkers are governed by polymer physics. Proc Natl Acad Sci U S A. 2019. doi: 10.1073/pnas.1904813116 PMID: 31659043.
101. Oma Y, Kino Y, Toriumi K, Sasagawa N, Ishiura S. Interactions between homopolymeric amino acids (HPAAs). Protein Sci. 2007; 16:2195–204. doi: 10.1110/ps.072955307 PMID: 17766374.
102. Albà MM, Tompa P, Veitia RA. Amino acid repeats and the structure and evolution of proteins. Genome Dyn. 2007; 3:119–30. doi: 10.1159/000107607 PMID: 18753788.
103. Yushchenko T, Deuerling E, Hauser K. Insights into the Aggregation Mechanism of PolyQ Proteins with Different Glutamine Repeat Lengths. Biophys J. 2018; 114:1847–57. doi: 10.1016/j.bpj.2018.02.037 PMID: 29694863.
104. Oma Y, Kino Y, Sasagawa N, Ishiura S. Intracellular localization of homopolymeric amino acid-containing proteins expressed in mammalian cells. J Biol Chem. 2004; 279:21217–22. doi: 10.1074/jbc.M309887200 PMID: 14993218.
105. Lilliu E, Villeri V, Pelassa I, Cesano F, Scarano D, Fiumara F. Polyserine repeats promote coiled coil-mediated fibril formation and length-dependent protein aggregation. J Struct Biol. 2018; 204:572–84. doi: 10.1016/j.jsb.2018.09.001 PMID: 30194983.
106. Yang C-G, Lang M-F, Fu X, Lin H, Zhang L-C, Ge G-S, et al. Application of short hydrophobic elastin-like polypeptides for expression and purification of active proteins. 3 Biotech. 2020; 10:334. doi: 10.1007/s13205-020-2139-0.
107. Krieger F, Möglich A, Kiefhaber T. Effect of proline and glycine residues on dynamics and barriers of loop formation in polypeptide chains. J Am Chem Soc. 2005; 127:3346–52. doi: 10.1021/ja042798i PMID: 15755151.
108. Wriggers W, Chakravarty S, Jennings PA. Control of protein functional dynamics by peptide linkers. Biopolymers. 2005; 80:736–46. doi: 10.1002/bip.20291 PMID: 15880774.
109. Tooke L, Duitch L, Measey TJ, Schweitzer-Stenner R. Kinetics of the self-aggregation and film formation of poly-L-proline at high temperatures explored by circular dichroism spectroscopy. Biopolymers. 2010; 93:451–7. doi: 10.1002/bip.21361 PMID: 19998404.
110. Adzhubei AA, Sternberg MJE, Makarov AA. Polyproline-II helix in proteins. Structure and function. J Mol Biol. 2013; 425:2100–32. doi: 10.1016/j.jmb.2013.03.018 PMID: 23507311.
111. Schuler B, Lipman EA, Steinbach PJ, Kumke M, Eaton WA. Polyproline and the "spectroscopic ruler" revisited with single-molecule fluorescence. Proc Natl Acad Sci U S A. 2005; 102:2754–9. doi: 10.1073/pnas.0408164102 PMID: 15699337.
112. Griss R, Schena A, Reymond L, Patiny L, Werner D, Tinberg CE, et al. Bioluminescent sensor proteins for point-of-care therapeutic drug monitoring. Nat Chem Biol. 2014; 10:598–603. doi: 10.1038/nchembio.1554 PMID: 24907901.
113. Xue L, Yu Q, Griss R, Schena A, Johnsson K. Bioluminescent Antibodies for Point-of-Care Diagnostics. Angew Chem Int Ed Engl. 2017; 56:7112–6. doi: 10.1002/anie.201702403 PMID: 28510347.
114. Kolossov VL, Spring BQ, Sokolowski A, Conour JE, Clegg RM, Kenis PJA, et al. Engineering redox-sensitive linkers for genetically encoded FRET-based biosensors. Exp Biol Med (Maywood). 2008; 233:238–48. doi: 10.3181/0707-RM-192 PMID: 18222979.
115. Haga T, Hirakawa H, Nagamune T. Fine tuning of spatial arrangement of enzymes in a PCNA-mediated multienzyme complex using a rigid poly-L-proline linker. PLoS One. 2013; 8:e75114. doi: 10.1371/journal.pone.0075114 PMID: 24040392.
116. Dagliyan O, Shirvanyants D, Karginov AV, Ding F, Fee L, Chandrasekaran SN, et al. Rational design of a ligand-controlled protein conformational switch. Proc Natl Acad Sci U S A. 2013; 110:6800–4. doi: 10.1073/pnas.1218319110 PMID: 23569285.

117. Ude S, Lassak J, Starosta AL, Kraxenberger T, Wilson DN, Jung K. Translation elongation factor EF-P alleviates ribosome stalling at polyproline stretches. Science. 2013; 339:82–5. doi: 10.1126/science.1228985 PMID: 23239623.

118. Wilson RH, Morton SK, Deiderick H, Gerth ML, Paul HA, Gerber I, et al. Engineered DNA ligases with improved activities in vitro. Protein Eng Des Sel. 2013; 26:471–8. doi: 10.1093/protein/gzt024 PMID: 23754529.

119. Zhao HL, Yao XQ, Xue C, Wang Y, Xiong XH, Liu ZM. Increasing the homogeneity, stability and activity of human serum albumin and interferon-alpha2b fusion protein by linker engineering. Protein Expr Purif. 2008; 61:73–7. doi: 10.1016/j.pep.2008.04.013 PMID: 18541441.

120. Pettersen EF, Goddard TD, Huang CC, Couch GS, Greenblatt DM, Meng EC, et al. UCSF Chimera--a visualization system for exploratory research and analysis. J Comput Chem. 2004; 25:1605–12. doi: 10.1002/jcc.20084 PMID: 15264254.

121. Klement M, Liu C, Loo BLW, Choo AB-H, Ow DS-W, Lee D-Y. Effect of linker flexibility and length on the functionality of a cytotoxic engineered antibody fragment. J Biotechnol. 2015; 199:90–7. doi: 10.1016/j.jbiotec.2015.02.008 PMID: 25697559.

122. Caparco AA, Bommarius AS, Champion JA. Effect of peptide linker length and composition on immobilization and catalysis of leucine zipper-enzyme fusion proteins. AIChE J. 2018; 64:2934–46. doi: 10.1002/aic.16150.

123. Gräwe A, Ranglack J, Weyrich A, Stein V. iFLinkC: an iterative functional linker cloning strategy for the combinatorial assembly and recombination of linker peptides with functional domains. Nucleic Acids Res. 2020; 48:e24. doi: 10.1093/nar/gkz1210 PMID: 31925441.

124. Kong Y, Tong Y, Gao M, Chen C, Gao X, Yao W. Linker engineering for fusion protein construction. Improvement and characterization of a GLP-1 fusion protein. Enzyme Microb Technol. 2016; 82:105–9. doi: 10.1016/j.enzmictec.2015.09.001 PMID: 26672455.

125. Hiblot J, Yu Q, Sabbadini MDB, Reymond L, Xue L, Schena A, et al. Luciferases with Tunable Emission Wavelengths. Angew Chem Int Ed Engl. 2017; 56:14556–60. doi: 10.1002/anie.201708277 PMID: 28941028.

126. Schlapschy M, Binder U, Börger C, Theobald I, Wachinger K, Kisling S, et al. PASylation. A biological alternative to PEGylation for extending the plasma half-life of pharmaceutically active proteins. Protein Eng Des Sel. 2013; 26:489–501. doi: 10.1093/protein/gzt023 PMID: 23754528.

127. Lerchner A, Daake M, Jarasch A, Skerra A. Fusion of an alcohol dehydrogenase with an aminotransferase using a PAS linker to improve coupled enzymatic alcohol-to-amine conversion. Protein Eng Des Sel. 2016; 29:557–62. doi: 10.1093/protein/gzw039 PMID: 27578886.

128. Jevsevar S, Kunstelj M, Porekar VG. PEGylation of therapeutic proteins. Biotechnol J. 2010; 5:113–28. doi: 10.1002/biot.200900218 PMID: 20069580.

129. Aghaabdollahian S, Ahangari Cohan R, Norouzian D, Davami F, Asadi Karam MR, Torkashvand F, et al. Enhancing bioactivity, physicochemical, and pharmacokinetic properties of a nano-sized, anti-VEGFR2 Adnectin, through PASylation technology. Sci Rep. 2019; 9:2978. doi: 10.1038/s41598-019-39776-0 PMID: 30814652.

130. Ahmadpour S, Hosseinimehr SJ. PASylation as a Powerful Technology for Improving the Pharmacokinetic Properties of Biopharmaceuticals. Curr Drug Deliv. 2018; 15:331–41. doi: 10.2174/1567201814666171120122352 PMID: 29165076.

131. Grashoff C, Hoffman BD, Brenner MD, Zhou R, Parsons M, Yang MT, et al. Measuring mechanical tension across vinculin reveals regulation of focal adhesion dynamics. Nature. 2010; 466:263–6. doi: 10.1038/nature09198 PMID: 20613844.

132. Nick Pace C, Martin Scholtz J. A Helix Propensity Scale Based on Experimental Studies of Peptides and Proteins. Biophys J. 1998; 75:422–7. doi: 10.1016/S0006-3495(98)77529-0.

133. Arai R, Wriggers W, Nishikawa Y, Nagamune T, Fujisawa T. Conformations of variably linked chimeric proteins evaluated by synchrotron X-ray small-angle scattering. Proteins. 2004; 57:829–38. doi: 10.1002/prot.20244 PMID: 15390267.

134. Arai R, Ueda H, Kitayama A, Kamiya N, Nagamune T. Design of the linkers which effectively separate domains of a bifunctional fusion protein. Protein Eng. 2001; 14:529–32. doi: 10.1093/protein/14.8.529 PMID: 11579220.

135. Marqusee S, Baldwin RL. Helix stabilization by Glu-…Lys+ salt bridges in short peptides of de novo design. Proceedings of the National Academy of Sciences. 1987; 84:8898–902. doi: 10.1073/pnas.84.24.8898 PMID: 3122208.

136. Swanson CJ, Sivaramakrishnan S. Harnessing the unique structural properties of isolated α-helices. J Biol Chem. 2014; 289:25460–7. doi: 10.1074/jbc.R114.583906 PMID: 25059657.

137. Doig AJ, Baldwin RL. N- and C-capping preferences for all 20 amino acids in alpha-helical peptides. Protein Sci. 1995; 4:1325–36. doi: 10.1002/pro.5560040708 PMID: 7670375.

138. Wu Y-J, Fan C-Y, Li Y-K. Protein purification involving a unique auto-cleavage feature of a repeated EAAAK peptide. J Chromatogr B Analyt Technol Biomed Life Sci. 2009; 877:4015–21. doi: 10.1016/j.jchromb.2009.10.009 PMID: 19858001.

139. Zhang WH, Herde MK, Mitchell JA, Whitfield JH, Wulff AB, Vongsouthi V, et al. Monitoring hippocampal glycine with the computationally designed optical sensor GlyFS. Nat Chem Biol. 2018; 14:861–9. doi: 10.1038/s41589-018-0108-2 PMID: 30061718.

140. Belal ASF, Sell BR, Hoi H, Davidson MW, Campbell RE. Optimization of a genetically encoded biosensor for cyclin B1-cyclin dependent kinase 1. Mol Biosyst. 2014; 10:191–5. doi: 10.1039/c3mb70402e PMID: 24281384.

141. Li G, Huang Z, Zhang C, Dong B-J, Guo R-H, Yue H-W, et al. Construction of a linker library with widely controllable flexibility for fusion protein design. Appl Microbiol Biotechnol. 2016; 100:215–25. doi: 10.1007/s00253-015-6985-3 PMID: 26394862.

142. Liu B, Åberg C, van Eerden FJ, Marrink SJ, Poolman B, Boersma AJ. Design and Properties of Genetically Encoded Probes for Sensing Macromolecular Crowding. Biophys J. 2017; 112:1929–39. doi: 10.1016/j.bpj.2017.04.004 PMID: 28494963.

143. Arts R, den Hartog I, Zijlema SE, Thijssen V, van der Beelen SHE, Merkx M. Detection of Antibodies in Blood Plasma Using Bioluminescent Sensor Proteins and a Smartphone. Anal Chem. 2016; 88:4525–32. doi: 10.1021/acs.analchem.6b00534 PMID: 27018236.

144. Golynskiy MV, Rurup WF, Merkx M. Antibody detection by using a FRET-based protein conformational switch. Chembiochem. 2010; 11:2264–7. doi: 10.1002/cbic.201000143 PMID: 20928879.

145. Soleimani M, Mahnam K, Mirmohammad-Sadeghi H, Sadeghi-Aliabadi H, Jahanian-Najafabadi A. Theoretical design of a new chimeric protein for the treatment of breast cancer. Res Pharm Sci. 2016; 11:187–99.

146. Sivaramakrishnan S, Spudich JA. Systematic control of protein interaction using a modular ER/K α-helix linker. Proc Natl Acad Sci U S A. 2011; 108:20467–72. doi: 10.1073/pnas.1116066108 PMID: 22123984.

147. Baker EG, Bartlett GJ, Crump MP, Sessions RB, Linden N, Faul CFJ, et al. Local and macroscopic electrostatic interactions in single α-helices. Nat Chem Biol. 2015; 11:221–8. doi: 10.1038/nchembio.1739 PMID: 25664692.

148. Malik RU, Ritt M, DeVree BT, Neubig RR, Sunahara RK, Sivaramakrishnan S. Detection of G protein-selective G protein-coupled receptor (GPCR) conformations in live cells. J Biol Chem. 2013; 288:17167–78. doi: 10.1074/jbc.M113.464065 PMID: 23629648.

149. Gupte TM, Ritt M, Dysthe M, Malik RU, Sivaramakrishnan S. Minute-scale persistence of a GPCR conformation state triggered by non-cognate G protein interactions primes signaling. Nat Commun. 2019; 10:4836. doi: 10.1038/s41467-019-12755-9 PMID: 31645561.

150. Liu EJ, Sinclair A, Keefe AJ, Nannenga BL, Coyle BL, Baneyx F, et al. EKylation. Addition of an Alternating-Charge Peptide Stabilizes Proteins. Biomacromolecules. 2015; 16:3357–61. doi: 10.1021/acs.biomac.5b01031 PMID: 26407134.

151. Wolny M, Batchelor M, Bartlett GJ, Baker EG, Kurzawa M, Knight PJ, et al. Characterization of long and stable de novo single alpha-helix domains provides novel insight into their stability. Sci Rep. 2017; 7:44341. doi: 10.1038/srep44341 PMID: 28287151.

152. Simm D, Kollmar M. Waggawagga-CLI. A command-line tool for predicting stable single α-helices (SAH-domains), and the SAH-domain distribution across eukaryotes. PLoS One. 2018; 13:e0191924. doi: 10.1371/journal.pone.0191924 PMID: 29444145.

153. Lissandron V, Terrin A, Collini M, D'alfonso L, Chirico G, Pantano S, et al. Improvement of a FRET-based indicator for cAMP by linker design and stabilization of donor-acceptor interaction. J Mol Biol. 2005; 354:546–55. doi: 10.1016/j.jmb.2005.09.089 PMID: 16257413.

154. Steffen V, Otten J, Engelmann S, Radek A, Limberg M, Koenig BW, et al. A Toolbox of Genetically Encoded FRET-Based Biosensors for Rapid l-Lysine Analysis. Sensors (Basel). 2016; 16:1604. doi: 10.3390/s16101604 PMID: 27690044.

155. Höfig H, Otten J, Steffen V, Pohl M, Boersma AJ, Fitter J. Genetically Encoded Förster Resonance Energy Transfer-Based Biosensors Studied on the Single-Molecule Level. ACS Sens. 2018; 3:1462–70. doi: 10.1021/acssensors.8b00143 PMID: 29979038.

156. Gonçalves F, Silva C, Ribeiro A, Cavaco-Paulo A. 1-Aminoanthracene Transduction into Liposomes Driven by Odorant-Binding Protein Proximity. ACS Appl Mater Interfaces. 2018; 10:27531–9. doi: 10.1021/acsami.8b10158 PMID: 30040883.

157. Liu N, Hui N, Davis JJ, Luo X. Low Fouling Protein Detection in Complex Biological Media Supported by a Designed Multifunctional Peptide. ACS Sens. 2018; 3:1210–6. doi: 10.1021/acssensors.8b00318 PMID: 29771110.

158. Cui M, Wang Y, Jiao M, Jayachandran S, Wu Y, Fan X, et al. Mixed Self-Assembled Aptamer and Newly Designed Zwitterionic Peptide as Antifouling Biosensing Interface for Electrochemical Detection of alpha-Fetoprotein. ACS Sens. 2017; 2:490–4. doi: 10.1021/acssensors.7b00103 PMID: 28723181.

159. Klein JS, Jiang S, Galimidi RP, Keeffe JR, Bjorkman PJ. Design and characterization of structured protein linkers with differing flexibilities. Protein Eng Des Sel. 2014; 27:325–30. doi: 10.1093/protein/gzu043 PMID: 25301959.

160. Inobe T, Nukina N. Rapamycin-induced oligomer formation system of FRB-FKBP fusion proteins. J Biosci Bioeng. 2016; 122:40–6. doi: 10.1016/j.jbiosc.2015.12.004 PMID: 26777239.

161. Choi JH, Laurent AH, Hilser VJ, Ostermeier M. Design of protein switches based on an ensemble model of allostery. Nat Commun. 2015; 6:6968. doi: 10.1038/ncomms7968 PMID: 25902417.

162. Różycki B, Cazade P-A, O'Mahony S, Thompson D, Cieplak M. The length but not the sequence of peptide linker modules exerts the primary influence on the conformations of protein domains in cellulosome multi-enzyme complexes. Phys Chem Chem Phys. 2017; 19:21414–25. doi: 10.1039/c7cp04114d PMID: 28758665.

163. Lučić I, Truebestein L, Leonard TA. Novel Features of DAG-Activated PKC Isozymes Reveal a Conserved 3-D Architecture. J Mol Biol. 2016; 428:121–41. doi: 10.1016/j.jmb.2015.11.001 PMID: 26582574.

164. Ikonomova SP, Le MT, Kalla N, Karlsson AJ. Effect of linkers on immobilization of scFvs with biotin-streptavidin interaction. Biotechnol Appl Biochem. 2018; 65:580–5. doi: 10.1002/bab.1645 PMID: 29377386.

165. Aalbers F, Fraaije M. Enzyme fusions in biocatalysis - Coupling reactions by pairing enzymes. Chembiochem. 2018. doi: 10.1002/cbic.201800394 PMID: 30178909.

166. Younger AKD, Su PY, Shepard AJ, Udani SV, Cybulski TR, Tyo KEJ, et al. Development of novel metabolite-responsive transcription factors via transposon-mediated protein fusion. Protein Eng Des Sel. 2018; 31:55–63. doi: 10.1093/protein/gzy001 PMID: 29385546.

167. Chu P-H, Tsygankov D, Berginski ME, Dagliyan O, Gomez SM, Elston TC, et al. Engineered kinase activation reveals unique morphodynamic phenotypes and associated trafficking for Src family isoforms. Proc Natl Acad Sci U S A. 2014; 111:12420–5. doi: 10.1073/pnas.1404487111 PMID: 25118278.

168. Marvin JS, Shimoda Y, Magloire V, Leite M, Kawashima T, Jensen TP, et al. A genetically encoded fluorescent sensor for in vivo imaging of GABA. Nat Methods. 2019; 16:763–70. doi: 10.1038/s41592-019-0471-2 PMID: 31308547.

169. Lobas MA, Tao R, Nagai J, Kronschläger MT, Borden PM, Marvin JS, et al. A genetically encoded single-wavelength sensor for imaging cytosolic and cell surface ATP. Nat Commun. 2019; 10:711. doi: 10.1038/s41467-019-08441-5 PMID: 30755613.

170. Suzuki K, Kimura T, Shinoda H, Bai G, Daniels MJ, Arai Y, et al. Five colour variants of bright luminescent protein for real-time multicolour bioimaging. Nat Commun. 2016; 7:13718. doi: 10.1038/ncomms13718 PMID: 27966527.

171. Levy Y. Protein Assembly and Building Blocks. Beyond the Limits of the LEGO Brick Metaphor. Biochemistry. 2017; 56:5040–8. doi: 10.1021/acs.biochem.7b00666 PMID: 28809494.

172. Arviv O, Levy Y. Folding of multidomain proteins. Biophysical consequences of tethering even in apparently independent folding. Proteins. 2012; 80:2780–98. doi: 10.1002/prot.24161 PMID: 22890725.
173. Vishwanath S, Brevern AG de, Srinivasan N. Same but not alike. Structure, flexibility and energetics of domains in multi-domain proteins are influenced by the presence of other domains. PLoS Comput Biol. 2018; 14:e1006008. doi: 10.1371/journal.pcbi.1006008 PMID: 29432415.
174. Lua LHL, Fan Y, Chang C, Connors NK, Middelberg APJ. Synthetic biology design to display an 18 kDa rotavirus large antigen on a modular virus-like particle. Vaccine. 2015; 33:5937–44. doi: 10.1016/j.vaccine.2015.09.017 PMID: 26387437.
175. Williams SJ, Ve T, Kobe B. A linker strategy for the production and crystallization of Toll/interleukin-1 receptor/resistance protein domain complexes. Protein Eng Des Sel. 2015; 28:137–45. doi: 10.1093/protein/gzv013 PMID: 25777769.
176. Yu K, Liu C, Kim B-G, Lee D-Y. Synthetic fusion protein design and applications. Biotechnol Adv. 2015; 33:155–64. doi: 10.1016/j.biotechadv.2014.11.005 PMID: 25450191.
177. Fink T, Lonzarić J, Praznik A, Plaper T, Merljak E, Leben K, et al. Design of fast proteolysis-based signaling and logic circuits in mammalian cells. Nat Chem Biol. 2019; 15:115–22. doi: 10.1038/s41589-018-0181-6 PMID: 30531965.
178. Leriche G, Chisholm L, Wagner A. Cleavable linkers in chemical biology. Bioorg Med Chem. 2012; 20:571–82. doi: 10.1016/j.bmc.2011.07.048 PMID: 21880494.
179. Ma B, Tsai C-J, Haliloğlu T, Nussinov R. Dynamic allostery. Linkers are not merely flexible. Structure. 2011; 19:907–17. doi: 10.1016/j.str.2011.06.002 PMID: 21742258.
180. Kumawat A, Chakrabarty S. Hidden electrostatic basis of dynamic allostery in a PDZ domain. Proc Natl Acad Sci U S A. 2017; 114:E5825-E5834. doi: 10.1073/pnas.1705311114 PMID: 28634294.
181. Liu J, Nussinov R. Energetic redistribution in allostery to execute protein function. Proc Natl Acad Sci U S A. 2017; 114:7480–2. doi: 10.1073/pnas.1709071114 PMID: 28696318.
182. Stein V, Alexandrov K. Synthetic protein switches: design principles and applications. Trends Biotechnol. 2015; 33:101–10. doi: 10.1016/j.tibtech.2014.11.010 PMID: 25535088.
183. Adamson H, Ajayi MO, Campbell E, Brachi E, Tiede C, Tang AA, et al. Affimer-Enzyme-Inhibitor Switch Sensor for Rapid Wash-free Assays of Multimeric Proteins. ACS Sens. 2019; 4:3014–22. doi: 10.1021/acssensors.9b01574 PMID: 31578863.
184. Kirubakaran P, Pfeiferová L, Boušová K, Bednarova L, Obšilová V, Vondrášek J. Artificial proteins as allosteric modulators of PDZ3 and SH3 in two-domain constructs. A computational characterization of novel chimeric proteins. Proteins. 2016; 84:1358–74. doi: 10.1002/prot.25082 PMID: 27273513.
185. Jeong WH, Lee H, Song DH, Eom J-H, Kim SC, Lee H-S, et al. Connecting two proteins using a fusion alpha helix stabilized by a chemical cross linker. Nat Commun. 2016; 7:11031. doi: 10.1038/ncomms11031 PMID: 26980593.
186. Fahie MA, Yang B, Pham B, Chen M. Tuning the selectivity and sensitivity of an OmpG nanopore sensor by adjusting ligand tether length. ACS Sens. 2016; 1:614–22. doi: 10.1021/acssensors.6b00014 PMID: 27500277.
187. Einav T, Yazdi S, Coey A, Bjorkman PJ, Phillips R. Harnessing Avidity: Quantifying the Entropic and Energetic Effects of Linker Length and Rigidity for Multivalent Binding of Antibodies to HIV-1. Cell Syst. 2019; 9:466-474.e7. doi: 10.1016/j.cels.2019.09.007 PMID: 31668801.
188. Krishnamurthy VM, Semetey V, Bracher PJ, Shen N, Whitesides GM. Dependence of effective molarity on linker length for an intramolecular protein-ligand system. J Am Chem Soc. 2007; 129:1312–20. doi: 10.1021/ja066780e PMID: 17263415.
189. Rotem D, Jayasinghe L, Salichou M, Bayley H. Protein detection by nanopores equipped with aptamers. J Am Chem Soc. 2012; 134:2781–7. doi: 10.1021/ja2105653 PMID: 22229655.
190. Shetty RP, Endy D, Knight TF. Engineering BioBrick vectors from BioBrick parts. J Biol Eng. 2008; 2:5. doi: 10.1186/1754-1611-2-5 PMID: 18410688.
191. Anderson JC, Dueber JE, Leguia M, Wu GC, Goler JA, Arkin AP, et al. BglBricks. A flexible standard for biological part assembly. J Biol Eng. 2010; 4:1. doi: 10.1186/1754-1611-4-1 PMID: 20205762.
192. Scior A, Preissler S, Koch M, Deuerling E. Directed PCR-free engineering of highly repetitive DNA sequences. BMC Biotechnol. 2011; 11:1–9. doi: 10.1186/1472-6750-11-87.
193. Weber E, Birkenfeld J, Franz J, Gritzan U, Linden L, Trautwein M. Modular Protein Expression Toolbox (MoPET), a standardized assembly system for defined expression constructs and expression optimization libraries. PLoS One. 2017; 12:e0176314. doi: 10.1371/journal.pone.0176314 PMID: 28520717.
194. Engler C, Kandzia R, Marillonnet S. A one pot, one step, precision cloning method with high throughput capability. PLoS One. 2008; 3:e3647. doi: 10.1371/journal.pone.0003647 PMID: 18985154.
195. McDaniel JR, Mackay JA, Quiroz FG, Chilkoti A. Recursive directional ligation by plasmid reconstruction allows rapid and seamless cloning of oligomeric genes. Biomacromolecules. 2010; 11:944–52. doi: 10.1021/bm901387t PMID: 20184309.
196. Ohlendorf R, Schumacher CH, Richter F, Möglich A. Library-Aided Probing of Linker Determinants in Hybrid Photoreceptors. ACS Synth Biol. 2016; 5:1117–26. doi: 10.1021/acssynbio.6b00028 PMID: 27002379.
197. Gibson DG, Young L, Chuang R-Y, Venter JC, Hutchison CA, Smith HO. Enzymatic assembly of DNA molecules up to several hundred kilobases. Nat Methods. 2009; 6:343–5. doi: 10.1038/nmeth.1318 PMID: 19363495.
198. Laemmli UK. Cleavage of structural proteins during the assembly of the head of bacteriophage T4. Nature. 1970; 227:680–5. doi: 10.1038/227680a0 PMID: 5432063.
199. Kok S de, Stanton LH, Slaby T, Durot M, Holmes VF, Patel KG, et al. Rapid and reliable DNA assembly via ligase cycling reaction. ACS Synth Biol. 2014; 3:97–106. doi: 10.1021/sb4001992 PMID: 24932563.
200. Roth TL, Milenkovic L, Scott MP. A rapid and simple method for DNA engineering using cycled ligation assembly. PLoS One. 2014; 9:e107329. doi: 10.1371/journal.pone.0107329 PMID: 25226397.
201. Xu S-Y, Zhu Z, Zhang P, Chan S-H, Samuelson JC, Xiao J, et al. Discovery of natural nicking endonucleases Nb.BsrDI and Nb.BtsI and engineering of top-strand nicking variants from BsrDI and BtsI. Nucleic Acids Res. 2007; 35:4608–18. doi: 10.1093/nar/gkm481 PMID: 17586812.
202. Studier FW. Protein production by auto-induction in high density shaking cultures. Protein Expr Purif. 2005; 41:207–34. doi: 10.1016/j.pep.2005.01.016 PMID: 15915565.

203. Santos-Aberturas J, Dörr M, Bornscheuer UT. Normalized Screening of Protein Engineering Libraries by Split-GFP Crude Cell Extract Quantification. In: Bornscheuer UT, Höhne M, editors. Protein engineering. Methods and protocols. New York, NY: Springer New York; 2018. pp. 157–70.
204. Huang J, Koide A, Makabe K, Koide S. Design of protein function leaps by directed domain interface evolution. Proc Natl Acad Sci U S A. 2008; 105:6578–83. doi: 10.1073/pnas.0801097105 PMID: 18445649.
205. Banaszynski LA, Liu CW, Wandless TJ. Characterization of the FKBP.rapamycin.FRB ternary complex. J Am Chem Soc. 2005; 127:4715–21. doi: 10.1021/ja043277y PMID: 15796538.
206. Sun P, Tropea JE, Waugh DS. Enhancing the Solubility of Recombinant Proteins in Escherichia coli by Using Hexahistidine-Tagged Maltose-Binding Protein as a Fusion Partner. In: Evans TC, Xu M-Q, editors. Heterologous Gene Expression in E.coli. Methods and Protocols. Totowa, NJ: Springer Science+Business Media LLC; 2011. pp. 259–74.
207. Hulme EC, Trevethick MA. Ligand binding assays at equilibrium: validation and interpretation. Br J Pharmacol. 2010; 161:1219–37. doi: 10.1111/j.1476-5381.2009.00604.x PMID: 20132208.
208. Connelly PR, Thomson JA. Heat capacity changes and hydrophobic interactions in the binding of FK506 and rapamycin to the FK506 binding protein. Proceedings of the National Academy of Sciences. 1992; 89:4781–5. doi: 10.1073/pnas.89.11.4781 PMID: 1375751.
209. McGuffee SR, Elcock AH. Diffusion, crowding & protein stability in a dynamic molecular model of the bacterial cytoplasm. PLoS Comput Biol. 2010; 6:e1000694. doi: 10.1371/journal.pcbi.1000694 PMID: 20221255.
210. Somalinga BR, Roy RP. Volume exclusion effect as a driving force for reverse proteolysis. Implications for polypeptide assemblage in a macromolecular crowded milieu. J Biol Chem. 2002; 277:43253–61. doi: 10.1074/jbc.M207974200 PMID: 12207031.
211. Trantidou T, Friddin M, Elani Y, Brooks NJ, Law RV, Seddon JM, et al. Engineering Compartmentalized Biomimetic Micro- and Nanocontainers. ACS Nano. 2017; 11:6549–65. doi: 10.1021/acsnano.7b03245 PMID: 28658575.
212. Howorka S, Cheley S, Bayley H. Sequence-specific detection of individual DNA strands using engineered nanopores. Nat Biotechnol. 2001; 19:636–9. doi: 10.1038/90236 PMID: 11433274.
213. Dekker C. Solid-state nanopores. Nat Nanotechnol. 2007; 2:209–15. doi: 10.1038/nnano.2007.27 PMID: 18654264.
214. Ramirez P, Manzanares JA, Cervera J, Gomez V, Ali M, Pause I, et al. Nanopore charge inversion and current-voltage curves in mixtures of asymmetric electrolytes. Journal of Membrane Science. 2018; 563:633–42. doi: 10.1016/j.memsci.2018.06.032.
215. Bayley H, Martin CR. Resistive-Pulse SensingFrom Microbes to Molecules. Chem Rev. 2000; 100:2575–94. doi: 10.1021/cr980099g.
216. Ji Z, Jordan M, Jayasinghe L, Guo P. Insertion of channel of phi29 DNA packaging motor into polymer membrane for high-throughput sensing. Nanomedicine. 2020:102170. doi: 10.1016/j.nano.2020.102170 PMID: 32035271.
217. Bright LK, Baker CA, Branstrom R, Saavedra SS, Aspinwall CA. Methacrylate Polymer Scaffolding Enhances the Stability of Suspended Lipid Bilayers for Ion Channel Recordings and Biosensor Development. ACS Biomater Sci Eng. 2015; 1:955–63. doi: 10.1021/acsbiomaterials.5b00205 PMID: 26925461.
218. Fahie MA, Yang B, Mullis M, Holden MA, Chen M. Selective Detection of Protein Homologues in Serum Using an OmpG Nanopore. Anal Chem. 2015; 87:11143–9. doi: 10.1021/acs.analchem.5b03350 PMID: 26451707.
219. Kukwikila M, Howorka S. Nanopore-based electrical and label-free sensing of enzyme activity in blood serum. Anal Chem. 2015; 87:9149–54. doi: 10.1021/acs.analchem.5b01764 PMID: 26305576.
220. Wang Y, Yang Q, Wang Z. The evolution of nanopore sequencing. Front Genet. 2014; 5:449. doi: 10.3389/fgene.2014.00449 PMID: 25610451.
221. Kasianowicz JJ, Brandin E, Branton D, Deamer DW. Characterization of individual polynucleotide molecules using a membrane channel. Proceedings of the National Academy of Sciences. 1996; 93:13770–3. doi: 10.1073/pnas.93.24.13770 PMID: 8943010.
222. Zhou S, Wang L, Chen X, Guan X. Label-free nanopore single-molecule measurement of trypsin activity. ACS Sens. 2016; 1:607–13. doi: 10.1021/acssensors.6b00043 PMID: 29130069.
223. Wang L, Han Y, Zhou S, Guan X. Real-time label-free measurement of HIV-1 protease activity by nanopore analysis. Biosens Bioelectron. 2014; 62:158–62. doi: 10.1016/j.bios.2014.06.041 PMID: 24997370.
224. Willems K, van Meervelt V, Wloka C, Maglia G. Single-molecule nanopore enzymology. Philos Trans R Soc Lond , B, Biol Sci. 2017; 372. doi: 10.1098/rstb.2016.0230 PMID: 28630164.
225. Fahie M, Chisholm C, Chen M. Resolved single-molecule detection of individual species within a mixture of anti-biotin antibodies using an engineered monomeric nanopore. ACS Nano. 2015; 9:1089–98. doi: 10.1021/nn506606e PMID: 25575121.
226. Thakur AK, Larimi MG, Gooden K, Movileanu L. Aberrantly large single-channel conductance of polyhistidine arm-containing protein nanopores. Biochemistry. 2017. doi: 10.1021/acs.biochem.7b00577 PMID: 28812882.
227. Wang Y, Montana V, Grubisic V, Stout RF, JR, Parpura V, Gu L-Q. Nanopore sensing of botulinum toxin type B by discriminating an enzymatically cleaved Peptide from a synaptic protein synaptobrevin 2 derivative. ACS Appl Mater Interfaces. 2015; 7:184–92. doi: 10.1021/am5056596 PMID: 25511125.
228. Wolfe AJ, Mohammad MM, Thakur AK, Movileanu L. Global redesign of a native beta-barrel scaffold. Biochim Biophys Acta. 2016; 1858:19–29. doi: 10.1016/j.bbamem.2015.10.006 PMID: 26456555.
229. Restrepo-Pérez L, Huang G, Bohländer PR, Worp N, Eelkema R, Maglia G, et al. Resolving Chemical Modifications to a Single Amino Acid within a Peptide Using a Biological Nanopore. ACS Nano. 2019; 13:13668–76. doi: 10.1021/acsnano.9b05156 PMID: 31536327.
230. Li X, Lee KH, Shorkey S, Chen J, Chen M. Different Anomeric Sugar Bound States of Maltose Binding Protein Resolved by a Cytolysin A Nanopore Tweezer. ACS Nano. 2020. doi: 10.1021/acsnano.9b07385 PMID: 31995359.
231. Pavithrra G, Rajasekaran R. Gramicidin Peptide to Combat Antibiotic Resistance. A Review. Int J Pept Res Ther. 2020; 26:191–9. doi: 10.1007/s10989-019-09828-0.

232. Li Q-Q, Chen P-G, Hu Z-W, Cao Y, Chen L-X, Chen Y-X, et al. Selective inhibition of cancer cells by enzyme-induced gain of function of phosphorylated melittin analogues. Chem. Sci. 2017; 8:7675–81. doi: 10.1039/C7SC03217J.
233. Fuertes A, Juanes M, Granja JR, Montenegro J. Supramolecular functional assemblies. Dynamic membrane transporters and peptide nanotubular composites. Chem. Commun. 2017; 53:7861–71. doi: 10.1039/C7CC02997G.
234. Ghadiri MR, Granja JR, Buehler LK. Artificial transmembrane ion channels from self-assembling peptide nanotubes. Nature. 1994; 369:301–4. doi: 10.1038/369301a0 PMID: 7514275.
235. Krauson AJ, Hall OM, Fuselier T, Starr CG, Kauffman WB, Wimley WC. Conformational Fine-Tuning of Pore-Forming Peptide Potency and Selectivity. J Am Chem Soc. 2015; 137:16144–52. doi: 10.1021/jacs.5b10595 PMID: 26632653.
236. Curnow P. Designing minimalist membrane proteins. Biochem Soc Trans. 2019; 47:1233–45. doi: 10.1042/BST20190170 PMID: 31671181.
237. Koebnik R, Krämer L. Membrane Assembly of Circularly Permuted Variants of theE. coliOuter Membrane Protein OmpA. J Mol Biol. 1995; 250:617–26. doi: 10.1006/jmbi.1995.0403.
238. Wimley WC. Application of Synthetic Molecular Evolution to the Discovery of Antimicrobial Peptides. Adv Exp Med Biol. 2019; 1117:241–55. doi: 10.1007/978-981-13-3588-4_13 PMID: 30980361.
239. Goodall MC, Urry DW. A synthetic transmembrane channel. Biochimica et Biophysica Acta (BBA) - Biomembranes. 1973; 291:317–20. doi: 10.1016/0005-2736(73)90425-2.
240. Anzai K, Hamasuna M, Kadono H, Lee S, Aoyagi H, Kirino Y. Formation of ion channels in planar lipid bilayer membranes by synthetic basic peptides. Biochim Biophys Acta. 1991; 1064:256–66.
241. Krauson AJ, He J, Wimley AW, Hoffmann AR, Wimley WC. Synthetic molecular evolution of pore-forming peptides by iterative combinatorial library screening. ACS Chem Biol. 2013; 8:823–31. doi: 10.1021/cb300598k PMID: 23394375.
242. Chen CH, Starr CG, Troendle E, Wiedman G, Wimley WC, Ulmschneider JP, et al. Simulation-Guided Rational de Novo Design of a Small Pore-Forming Antimicrobial Peptide. J Am Chem Soc. 2019; 141:4839–48. doi: 10.1021/jacs.8b11939 PMID: 30839209.
243. Mahendran KR, Niitsu A, Kong L, Thomson AR, Sessions RB, Woolfson DN, et al. A monodisperse transmembrane α-helical peptide barrel. Nature Chem. 2016. doi: 10.1038/nchem.2647.
244. Young R. Phage lysis. Do we have the hole story yet. Curr Opin Microbiol. 2013; 16:790–7. doi: 10.1016/j.mib.2013.08.008 PMID: 24113139.
245. Lella M, Mahalakshmi R. Engineering a Transmembrane Nanopore Ion Channel from a Membrane Breaker Peptide. J Phys Chem Lett. 2016; 7:2298–303. doi: 10.1021/acs.jpclett.6b00987 PMID: 27257735.
246. Rincon-Restrepo M, Mikhailova E, Bayley H, Maglia G. Controlled translocation of individual DNA molecules through protein nanopores with engineered molecular brakes. Nano Lett. 2011; 11:746–50. doi: 10.1021/nl1038874 PMID: 21222450.
247. Wloka C, Mutter NL, Soskine M, Maglia G. Alpha-Helical Fragaceatoxin C Nanopore Engineered for Double-Stranded and Single-Stranded Nucleic Acid Analysis. Angew Chem. 2016; 128:12682–6. doi: 10.1002/ange.201606742.
248. Cao C, Cirauqui N, Marcaida MJ, Buglakova E, Duperrex A, Radenovic A, et al. Single-molecule sensing of peptides and nucleic acids by engineered aerolysin nanopores. Nat Commun. 2019; 10:4918. doi: 10.1038/s41467-019-12690-9 PMID: 31664022.
249. Gu LQ, Braha O, Conlan S, Cheley S, Bayley H. Stochastic sensing of organic analytes by a pore-forming protein containing a molecular adapter. Nature. 1999; 398:686–90. doi: 10.1038/19491 PMID: 10227291.
250. Soskine M, Biesemans A, Moeyaert B, Cheley S, Bayley H, Maglia G. An engineered ClyA nanopore detects folded target proteins by selective external association and pore entry. Nano Lett. 2012; 12:4895–900. doi: 10.1021/nl3024438 PMID: 22849517.
251. Xie H, Braha O, Gu L-Q, Cheley S, Bayley H. Single-molecule observation of the catalytic subunit of cAMP-dependent protein kinase binding to an inhibitor peptide. Chem Biol. 2005; 12:109–20. doi: 10.1016/j.chembiol.2004.11.013 PMID: 15664520.
252. Zhuang T, Tamm LK. Control of the conductance of engineered protein nanopores through concerted loop motions. Angew Chem Int Ed Engl. 2014; 53:5897–902. doi: 10.1002/anie.201400400 PMID: 24777684.
253. Pittel I, Alper N, Yonai S, Basch S, Blum L, Bachur A, et al. Computational and biochemical design of a nanopore cleavable by a cancer-secreted enzyme. Chembiochem. 2015; 16:463–71. doi: 10.1002/cbic.201402378 PMID: 25581099.
254. Fahie MA, Chen M. Electrostatic Interactions between OmpG Nanopore and Analyte Protein Surface Can Distinguish between Glycosylated Isoforms. J Phys Chem B. 2015; 119:10198–206. doi: 10.1021/acs.jpcb.5b06435 PMID: 26181080.
255. Mohammad MM, Howard KR, Movileanu L. Redesign of a plugged beta-barrel membrane protein. J Biol Chem. 2011; 286:8000–13. doi: 10.1074/jbc.M110.197723 PMID: 21189254.
256. Krewinkel M, Dworeck T, Fioroni M. Engineering of an E. coli outer membrane protein FhuA with increased channel diameter. J Nanobiotechnology. 2011; 9:33. doi: 10.1186/1477-3155-9-33 PMID: 21854627.
257. Soskine M, Biesemans A, Maeyer M de, Maglia G. Tuning the size and properties of ClyA nanopores assisted by directed evolution. J Am Chem Soc. 2013; 135:13456–63. doi: 10.1021/ja4053398 PMID: 23919630.
258. Reina S, Magrì A, Lolicato M, Guarino F, Impellizzeri A, Maier E, et al. Deletion of β-strands 9 and 10 converts VDAC1 voltage-dependence in an asymmetrical process. Biochim Biophys Acta. 2013; 1827:793–805. doi: 10.1016/j.bbabio.2013.03.007 PMID: 23541892.
259. Stoddart D, Ayub M, Hofler L, Raychaudhuri P, Klingelhoefer JW, Maglia G, et al. Functional truncated membrane pores. Proc Natl Acad Sci U S A. 2014; 111:2425–30. doi: 10.1073/pnas.1312976111 PMID: 24469792.
260. Grosse W, Psakis G, Mertins B, Reiss P, Windisch D, Brademann F, et al. Structure-based engineering of a minimal porin reveals loop-independent channel closure. Biochemistry. 2014; 53:4826–38. doi: 10.1021/bi500660q PMID: 24988371.
261. Huang G, Voet A, Maglia G. FraC nanopores with adjustable diameter identify the mass of opposite-charge peptides with 44 dalton resolution. Nat Commun. 2019; 10:835. doi: 10.1038/s41467-019-08761-6 PMID: 30783102.

262. Ho C-W, van Meervelt V, Tsai K-C, Temmerman P-J de, Mast J, Maglia G. Engineering a nanopore with co-chaperonin function. Sci Adv. 2015; 1:e1500905. doi: 10.1126/sciadv.1500905 PMID: 26824063.
263. Brown CG, Clarke J. Nanopore development at Oxford Nanopore. Nat Biotechnol. 2016; 34:810–1. doi: 10.1038/nbt.3622 PMID: 27504770.
264. Wendell D, Jing P, Geng J, Subramaniam V, Lee TJ, Montemagno C, et al. Translocation of double-stranded DNA through membrane-adapted phi29 motor protein nanopores. Nat Nanotechnol. 2009; 4:765–72. doi: 10.1038/nnano.2009.259 PMID: 19893523.
265. Haque F, Li J, Wu H-C, Liang X-J, Guo P. Solid-State and Biological Nanopore for Real-Time Sensing of Single Chemical and Sequencing of DNA. Nano Today. 2013; 8:56–74. doi: 10.1016/j.nantod.2012.12.008 PMID: 23504223.
266. Haque F, Lunn J, Fang H, Smithrud D, Guo P. Real-time sensing and discrimination of single chemicals using the channel of phi29 DNA packaging nanomotor. ACS Nano. 2012; 6:3251–61. doi: 10.1021/nn3001615 PMID: 22458779.
267. Berube BJ, Bubeck Wardenburg J. Staphylococcus aureus α-toxin. Nearly a century of intrigue. Toxins (Basel). 2013; 5:1140–66. doi: 10.3390/toxins5061140 PMID: 23888516.
268. Song L, Hobaugh MR, Shustak C, Cheley S, Bayley H, Gouaux JE. Structure of staphylococcal alpha-hemolysin, a heptameric transmembrane pore. Science. 1996; 274:1859–66. doi: 10.1126/science.274.5294.1859 PMID: 8943190.
269. Hall AR, Scott A, Rotem D, Mehta KK, Bayley H, Dekker C. Hybrid pore formation by directed insertion of alpha-haemolysin into solid-state nanopores. Nat Nanotechnol. 2010; 5:874–7. doi: 10.1038/nnano.2010.237 PMID: 21113160.
270. Wang Y, Yao F, Kang X-f. Tetramethylammonium-filled protein nanopore for single-molecule analysis. Anal Chem. 2015; 87:9991–7. doi: 10.1021/acs.analchem.5b02611 PMID: 26337294.
271. Kang X-f, Cheley S, Rice-Ficht AC, Bayley H. A storable encapsulated bilayer chip containing a single protein nanopore. J Am Chem Soc. 2007; 129:4701–5. doi: 10.1021/ja068654g PMID: 17375923.
272. Osaki T, Suzuki H, Le Pioufle B, Takeuchi S. Multichannel simultaneous measurements of single-molecule translocation in alpha-hemolysin nanopore array. Anal Chem. 2009; 81:9866–70. doi: 10.1021/ac901732z PMID: 20000639.
273. Iacovache I, Carlo S de, Cirauqui N, Dal Peraro M, van der Goot FG, Zuber B. Cryo-EM structure of aerolysin variants reveals a novel protein fold and the pore-formation process. Nat Comms. 2016; 7:332. doi: 10.1038/ncomms12062.
274. Wilmsen HU, Pattus F, Buckley JT. Aerolysin, a hemolysin fromAeromonas hydrophila, forms voltage-gated channels in planar lipid bilayers. J Membr Biol. 1990; 115:71–81. doi: 10.1007/BF01869107.
275. Wang Y, Gu L-Q, Tian K. The aerolysin nanopore. From peptidomic to genomic applications. Nanoscale. 2018; 10:13857–66. doi: 10.1039/C8NR04255A.
276. Roderer D, Glockshuber R. Assembly mechanism of the α-pore-forming toxin cytolysin A from Escherichia coli. Philos Trans R Soc Lond , B, Biol Sci. 2017; 372. doi: 10.1098/rstb.2016.0211 PMID: 28630151.
277. Mueller M, Grauschopf U, Maier T, Glockshuber R, Ban N. The structure of a cytolytic alpha-helical toxin pore reveals its assembly mechanism. Nature. 2009; 459:726–30. doi: 10.1038/nature08026 PMID: 19421192.
278. Aminipour Z, Khorshid M, Bayoumi M, Losada-Pérez P, Thoelen R, Bonakdar S, et al. Formation and electrical characterization of black lipid membranes in porous filter materials. Phys Status Solidi A. 2017; 214:1700104. doi: 10.1002/pssa.201700104.
279. Biesemans A, Soskine M, Maglia G. A Protein Rotaxane Controls the Translocation of Proteins Across a ClyA Nanopore. Nano Lett. 2015; 15:6076–81. doi: 10.1021/acs.nanolett.5b02309 PMID: 26243210.
280. Soskine M, Biesemans A, Maglia G. Single-Molecule Analyte Recognition with ClyA Nanopores Equipped with Internal Protein Adaptors. J Am Chem Soc. 2015; 137:5793–7. doi: 10.1021/jacs.5b01520 PMID: 25871548.
281. Lu B, Stokes C, Fahie M, Chen M, Golovchenko JA, Hau LV. Protein Motion and Configurations in a Form-Fitting Nanopore. Avidin in ClyA. Biophys J. 2018; 115:801–8. doi: 10.1016/j.bpj.2018.07.024 PMID: 30122294.
282. Fahie MA, Liang L, Avelino AR, Pham B, Limpikirati P, Vachet RW, et al. Disruption of the open conductance in the β-tongue mutants of Cytolysin A. Sci Rep. 2018; 8:3796. doi: 10.1038/s41598-018-22009-1 PMID: 29491391.
283. Tanaka K, Caaveiro JMM, Morante K, González-Mañas JM, Tsumoto K. Structural basis for self-assembly of a cytolytic pore lined by protein and lipid. Nat Commun. 2015; 6:6337. doi: 10.1038/ncomms7337 PMID: 25716479.
284. Butler TZ, Pavlenok M, Derrington IM, Niederweis M, Gundlach JH. Single-molecule DNA detection with an engineered MspA protein nanopore. Proc Natl Acad Sci U S A. 2008; 105:20647–52. doi: 10.1073/pnas.0807514106 PMID: 19098105.
285. Derrington IM, Butler TZ, Collins MD, Manrao E, Pavlenok M, Niederweis M, et al. Nanopore DNA sequencing with MspA. Proc Natl Acad Sci U S A. 2010; 107:16060–5. doi: 10.1073/pnas.1001831107 PMID: 20798343.
286. Konovalova A, Kahne DE, Silhavy TJ. Outer Membrane Biogenesis. Annu Rev Microbiol. 2017; 71:539–56. doi: 10.1146/annurev-micro-090816-093754 PMID: 28886680.
287. Sanganna Gari RR, Chattrakun K, Marsh BP, Mao C, Chada N, Randall LL, et al. Direct visualization of the E. coli Sec translocase engaging precursor proteins in lipid bilayers. Sci Adv. 2019; 5:eaav9404. doi: 10.1126/sciadv.aav9404.
288. Denks K, Vogt A, Sachelaru I, Petriman N-A, Kudva R, Koch H-G. The Sec translocon mediated protein transport in prokaryotes and eukaryotes. Mol Membr Biol. 2014; 31:58–84. doi: 10.3109/09687688.2014.907455 PMID: 24762201.
289. Driessen AJM, Nouwen N. Protein Translocation Across the Bacterial Cytoplasmic Membrane. Annu Rev Biochem. 2008; 77:643–67. doi: 10.1146/annurev.biochem.77.061606.160747.
290. Heijne G von. The signal peptide. J Membr Biol. 1990; 115:195–201. doi: 10.1007/BF01868635 PMID: 2197415.
291. Bai L, He W, Li T, Yang C, Zhuang Y, Quan S. Chaperone-substrate interactions monitored via a robust TEM-1 beta-lactamase fragment complementation assay. Biotechnol Lett. 2017. doi: 10.1007/s10529-017-2347-9 PMID: 28492977.
292. Sklar JG, Wu T, Kahne D, Silhavy TJ. Defining the roles of the periplasmic chaperones SurA, Skp, and DegP in Escherichia coli. Genes & Development. 2007; 21:2473–84. doi: 10.1101/gad.1581007.
293. Thoma J, Burmann BM, Hiller S, Muller DJ. Impact of holdase chaperones Skp and SurA on the folding of beta-barrel outer-membrane proteins. Nat Struct Mol Biol. 2015; 22:795–802. doi: 10.1038/nsmb.3087 PMID: 26344570.

294. Robert V, Volokhina EB, Senf F, Bos MP, van Gelder P, Tommassen J. Assembly factor Omp85 recognizes its outer membrane protein substrates by a species-specific C-terminal motif. PLoS Biol. 2006; 4:e377. doi: 10.1371/journal.pbio.0040377 PMID: 17090219.
295. Paramasivam N, Habeck M, Linke D. Is the C-terminal insertional signal in Gram-negative bacterial outer membrane proteins species-specific or not. BMC Genomics. 2012; 13:510. doi: 10.1186/1471-2164-13-510.
296. Lehr U, Schütz M, Oberhettinger P, Ruiz-Perez F, Donald JW, Palmer T, et al. C-terminal amino acid residues of the trimeric autotransporter adhesin YadA of Yersinia enterocolitica are decisive for its recognition and assembly by BamA. Mol Microbiol. 2010; 78:932–46. doi: 10.1111/j.1365-2958.2010.07377.x.
297. Zhuang T, Chisholm C, Chen M, Tamm LK. NMR-based conformational ensembles explain pH-gated opening and closing of OmpG channel. J Am Chem Soc. 2013; 135:15101–13. doi: 10.1021/ja408206e PMID: 24020969.
298. Chen M, Khalid S, Sansom MSP, Bayley H. Outer membrane protein G. Engineering a quiet pore for biosensing. Proc Natl Acad Sci U S A. 2008; 105:6272–7. doi: 10.1073/pnas.0711561105 PMID: 18443290.
299. Lin M, Zhang G, Fahie M, Morgan LK, Chen M, Keiderling TA, et al. Engineering a Novel Porin OmpGF via Strand Replacement From Computational Analysis of Sequence Motif. Biochimica et Biophysica Acta (BBA) - Biomembranes. 2017. doi: 10.1016/j.bbamem.2017.03.012.
300. Perez-Rathke A, Fahie MA, Chisholm C, Liang J, Chen M. Mechanism of OmpG pH-Dependent Gating from Loop Ensemble and Single Channel Studies. J Am Chem Soc. 2018; 140:1105–15. doi: 10.1021/jacs.7b11979 PMID: 29262680.
301. Braun V. FhuA (TonA), the career of a protein. Journal of Bacteriology. 2009; 191:3431–6. doi: 10.1128/JB.00106-09 PMID: 19329642.
302. Kadner RJ, Heller K, Coulton JW, Braun V. Genetic control of hydroxamate-mediated iron uptake in Escherichia coli. Journal of Bacteriology. 1980; 143:256–64.
303. Endriss F, Braun M, Killmann H, Braun V. Mutant analysis of the Escherichia coli FhuA protein reveals sites of FhuA activity. Journal of Bacteriology. 2003; 185:4683–92. doi: 10.1128/jb.185.16.4683-4692.2003 PMID: 12896986.
304. Ferguson AD, Breed J, Diederichs K, Welte W, Coulton JW. An internal affinity-tag for purification and crystallization of the siderophore receptor FhuA, integral outer membrane protein from Escherichia coli K-12. Konstanz: Bibliothek der Universität Konstanz; 1998.
305. Locher KP, Rees B, Koebnik R, Mitschler A, Moulinier L, Rosenbusch JP, et al. Transmembrane signaling across the ligand-gated FhuA receptor: crystal structures of free and ferrichrome-bound states reveal allosteric changes. Cell. 1998; 95:771–8.
306. Philippart F, Arlt M, Gotzen S, Tenne S-J, Bocola M, Chen H-H, et al. A hybrid ring-opening metathesis polymerization catalyst based on an engineered variant of the beta-barrel protein FhuA. Chemistry. 2013; 19:13865–71. doi: 10.1002/chem.201301515 PMID: 23959581.
307. Mathavan I, Zirah S, Mehmood S, Choudhury HG, Goulard C, Li Y, et al. Structural basis for hijacking siderophore receptors by antimicrobial lasso peptides. Nat Chem Biol. 2014; 10:340–2. doi: 10.1038/nchembio.1499 PMID: 24705590.
308. Killmann H, Braun M, Herrmann C, Braun V. FhuA barrel-cork hybrids are active transporters and receptors. Journal of Bacteriology. 2001; 183:3476–87. doi: 10.1128/JB.183.11.3476-3487.2001 PMID: 11344156.
309. Mills A, Le H-T, Coulton JW, Duong F. FhuA interactions in a detergent-free nanodisc environment. Biochim Biophys Acta. 2014; 1838:364–71. doi: 10.1016/j.bbamem.2013.09.022 PMID: 24140007.
310. Pawelek PD, Croteau N, Ng-Thow-Hing C, Khursigara CM, Moiseeva N, Allaire M, et al. Structure of TonB in complex with FhuA, E. coli outer membrane receptor. Science. 2006; 312:1399–402. doi: 10.1126/science.1128057 PMID: 16741125.
311. Hickman SJ, Cooper REM, Bellucci L, Paci E, Brockwell DJ. Gating of TonB-dependent transporters by substrate-specific forced remodelling. Nat Comms. 2017; 8:14804. doi: 10.1038/ncomms14804.
312. Udho E, Jakes KS, Buchanan SK, James KJ, Jiang X, Klebba PE, et al. Reconstitution of bacterial outer membrane TonB-dependent transporters in planar lipid bilayer membranes. Proc Natl Acad Sci U S A. 2009; 106:21990–5. doi: 10.1073/pnas.0910023106 PMID: 19959664.
313. James KJ, Hancock MA, Moreau V, Molina F, Coulton JW. TonB induces conformational changes in surface-exposed loops of FhuA, outer membrane receptor of Escherichia coli. Protein Sci. 2008; 17:1679–88. doi: 10.1110/ps.036244.108.
314. Braun M, Endriss F, Killmann H, Braun V. In Vivo Reconstitution of the FhuA Transport Protein of Escherichia coli K-12. Journal of Bacteriology. 2003; 185:5508–18. doi: 10.1128/JB.185.18.5508-5518.2003.
315. Udho E, Jakes KS, Finkelstein A. TonB-dependent transporter FhuA in planar lipid bilayers: partial exit of its plug from the barrel. Biochemistry. 2012; 51:6753–9. doi: 10.1021/bi300493u PMID: 22846061.
316. Riback JA, Bowman MA, Zmyslowski AM, Knoverek CR, Jumper JM, Hinshaw JR, et al. Innovative scattering analysis shows that hydrophobic disordered proteins are expanded in water. Science. 2017; 358:238–41. doi: 10.1126/science.aan5774 PMID: 29026044.
317. Fioroni M, Dworeck T, Rodriguez-Ropero F. ß-barrel Channel Proteins as Tools in Nanotechnology. Dordrecht: Springer Netherlands; 2014.
318. Rodriguez-Ropero F, Fioroni M. Structural and dynamical analysis of an engineered FhuA channel protein embedded into a lipid bilayer or a detergent belt. J Struct Biol. 2012; 177:291–301. doi: 10.1016/j.jsb.2011.12.021 PMID: 22248453.
319. Killmann H, Benz R, Braun V. Conversion of the FhuA transport protein into a diffusion channel through the outer membrane of Escherichia coli. EMBO J. 1993; 12:3007–16.
320. Bonhivers M, Ghazi A, Boulanger P, Letellier L. FhuA, a transporter of the Escherichia coli outer membrane, is converted into a channel upon binding of bacteriophage T5. EMBO J. 1996; 15:1850–6.
321. Braun M, Killmann H, Maier E, Benz R, Braun V. Diffusion through channel derivatives of the Escherichia coli FhuA transport protein. European Journal of Biochemistry. 2002; 269:4948–59. doi: 10.1046/j.1432-1033.2002.03195.x.
322. Braun V, Killmann H, Benz R. Energy-coupled transport through the outer membrane of Escherichia coli small deletions in the gating loop convert the FhuA transport protein into a diffusion channel. FEBS Letters. 1994; 346:59–64. doi: 10.1016/0014-5793(94)00431-5.

323. Mohammad MM, Iyer R, Howard KR, McPike MP, Borer PN, Movileanu L. Engineering a rigid protein tunnel for biomolecular detection. J Am Chem Soc. 2012; 134:9521–31. doi: 10.1021/ja3043646 PMID: 22577864.
324. Thakur AK, Movileanu L. Real-time measurement of protein-protein interactions at single-molecule resolution using a biological nanopore. Nat Biotechnol. 2018. doi: 10.1038/nbt.4316 PMID: 30531896.
325. Wolfe AJ, Hsueh Y-C, Blanden AR, Mohammad MM, Pham B, Thakur AK, et al. Interrogating Detergent Desolvation of Nanopore-Forming Proteins by Fluorescence Polarization Spectroscopy. Anal Chem. 2017. doi: 10.1021/acs.analchem.7b01339 PMID: 28650154.
326. Wolfe AJ, Si W, Zhang Z, Blanden AR, Hsueh Y-C, Gugel JF, et al. Quantification of Membrane Protein-Detergent Complex Interactions. J Phys Chem B. 2017. doi: 10.1021/acs.jpcb.7b08045 PMID: 29035562.
327. Thakur AK, Movileanu L. Single-Molecule Protein Detection in a Biofluid Using a Quantitative Nanopore Sensor. ACS Sens. 2019; 4:2320–6. doi: 10.1021/acssensors.9b00848 PMID: 31397162.
328. Liu Z, Ghai I, Winterhalter M, Schwaneberg U. Engineering Enhanced Pore Sizes Using FhuA Δ1-160 from E. coli Outer Membrane as Template. ACS Sens. 2017; 2:1619–26. doi: 10.1021/acssensors.7b00481 PMID: 29052976.
329. Sauer DF, Bocola M, Broglia C, Arlt M, Zhu L-L, Brocker M, et al. Hybrid ruthenium ROMP catalysts based on an engineered variant of beta-barrel protein FhuA DeltaCVF(tev). Effect of spacer length. Chem Asian J. 2015; 10:177–82. doi: 10.1002/asia.201403005 PMID: 25425216.
330. Anand D, Dhoke GV, Gehrmann J, Garakani TM, Davari MD, Bocola M, et al. Chiral separation of d/l-arginine with whole cells through an engineered FhuA nanochannel. Chem Commun. 2019; 55:5431–4. doi: 10.1039/C9CC00154A PMID: 30916680.
331. Cranfield CG, Cornell BA, Grage SL, Duckworth P, Carne S, Ulrich AS, et al. Transient potential gradients and impedance measures of tethered bilayer lipid membranes: pore-forming peptide insertion and the effect of electroporation. Biophys J. 2014; 106:182–9. doi: 10.1016/j.bpj.2013.11.1121 PMID: 24411250.
332. Jeon T-J, Malmstadt N, Schmidt JJ. Hydrogel-encapsulated lipid membranes. J Am Chem Soc. 2006; 128:42–3. doi: 10.1021/ja056901v PMID: 16390112.
333. Burden DL, Kim D, Cheng W, Chandler Lawler E, Dreyer DR, Keranen Burden LM. Mechanically Enhancing Planar Lipid Bilayers with a Minimal Actin Cortex. Langmuir. 2018; 34:10847–55. doi: 10.1021/acs.langmuir.8b01847 PMID: 30149716.
334. Dhoke MA, Ladha PJ, Boerio FJ, Lessard LB, Malinowska DH, Cuppoletti J, et al. Porous membranes for reconstitution of ion channels. Biochim Biophys Acta. 2005; 1716:117–25. doi: 10.1016/j.bbamem.2005.09.008 PMID: 16214106.
335. Diederichs T, Nguyen QH, Urban M, Tampé R, Tornow M. Transparent Nanopore Cavity Arrays Enable Highly Parallelized Optical Studies of Single Membrane Proteins on Chip. Nano Lett. 2018; 18:3901–10. doi: 10.1021/acs.nanolett.8b01252 PMID: 29741381.
336. Alvarado-Mesén J, Solano-Campos F, Canet L, Pedrera L, Hervis YP, Soto C, et al. Cloning, purification and characterization of nigrelysin, a novel actinoporin from the sea anemone Anthopleura nigrescens. Biochimie. 2019; 156:206–23. doi: 10.1016/j.biochi.2018.07.013 PMID: 30036605.
337. Prilipov A, Phale PS, van Gelder P, Rosenbusch JP, Koebnik R. Coupling site-directed mutagenesis with high-level expression. Large scale production of mutant porins from E. coli. FEMS Microbiol Lett. 1998; 163:65–72.
338. Bartsch P, Harsman A, Wagner R. Single channel analysis of membrane proteins in artificial bilayer membranes. Methods Mol Biol. 2013; 1033:345–61. doi: 10.1007/978-1-62703-487-6_22 PMID: 23996188.
339. Braun CJ, Baer T, Moroni A, Thiel G. Pseudo painting/air bubble technique for planar lipid bilayers. J Neurosci Methods. 2014; 233:13–7. doi: 10.1016/j.jneumeth.2014.05.031 PMID: 24938397.
340. Winterstein L-M, Kukovetz K, Rauh O, Turman DL, Braun C, Moroni A, et al. Reconstitution and functional characterization of ion channels from nanodiscs in lipid bilayers. J Gen Physiol. 2018; 150:637–46. doi: 10.1085/jgp.201711904 PMID: 29487088.
341. Dr. Viatcheslav Nesterov. Nest-o-Patch.
342. Pédelacq J-D, Cabantous S, Tran T, Terwilliger TC, Waldo GS. Engineering and characterization of a superfolder green fluorescent protein. Nat Biotechnol. 2006; 24:79–88. doi: 10.1038/nbt1172 PMID: 16369541.
343. Helbig S, Braun V. Mapping functional domains of colicin M. Journal of Bacteriology. 2011; 193:815–21. doi: 10.1128/JB.01206-10 PMID: 21148729.
344. Grinter R, Walker D. Lipid II-Degrading M-Class Bacteriocins. In: Scott RA, editor. Encyclopedia of Inorganic and Bioinorganic Chemistry. Chichester, UK: John Wiley & Sons, Ltd; 2011. pp. 1–10.
345. Tenne S-J, Schwaneberg U. First insights on organic cosolvent effects on FhuA wildtype and FhuA Delta1-159. Int J Mol Sci. 2012; 13:2459–71. doi: 10.3390/ijms13022459 PMID: 22408464.
346. Moeck GS, Tawa P, Xiang H, Ismail AA, Turnbull JL, Coulton JW. Ligand-induced conformational change in the ferrichrome-iron receptor of Escherichia coli K-12. Mol Microbiol. 1996; 22:459–71. doi: 10.1046/j.1365-2958.1996.00112.x PMID: 8939430.
347. Ingham C, Buechner M, Adler J. Effect of outer membrane permeability on chemotaxis in Escherichia coli. Journal of Bacteriology. 1990; 172:3577–83. doi: 10.1128/jb.172.7.3577-3583.1990 PMID: 1694521.
348. Braun M, Killmann H, Braun V. The beta-barrel domain of FhuADelta5-160 is sufficient for TonB-dependent FhuA activities of Escherichia coli. Mol Microbiol. 1999; 33:1037–49. doi: 10.1046/j.1365-2958.1999.01546.x PMID: 10476037.
349. Dworeck T, Petri A-K, Muhammad N, Fioroni M, Schwaneberg U. FhuA deletion variant Delta1-159 overexpression in inclusion bodies and refolding with Polyethylene-Poly(ethylene glycol) diblock copolymer. Protein Expr Purif. 2011; 77:75–9. doi: 10.1016/j.pep.2010.12.006 PMID: 21168506.
350. Charan H, Kinzel J, Glebe U, Anand D, Garakani TM, Zhu L, et al. Grafting PNIPAAm from beta-barrel shaped transmembrane nanopores. Biomaterials. 2016; 107:115–23. doi: 10.1016/j.biomaterials.2016.08.033 PMID: 27614163.

351. Kinzel J, Sauer DF, Bocola M, Arlt M, Mirzaei Garakani T, Thiel A, et al. 2-Methyl-2,4-pentanediol (MPD) boosts as detergent-substitute the performance of ß-barrel hybrid catalyst for phenylacetylene polymerization. Beilstein J Org Chem. 2017; 13:1498–506. doi: 10.3762/bjoc.13.148 PMID: 28845193.
352. Nallani M, Benito S, Onaca O, Graff A, Lindemann M, Winterhalter M, et al. A nanocompartment system (Synthosome) designed for biotechnological applications. J Biotechnol. 2006; 123:50–9. doi: 10.1016/j.jbiotec.2005.10.025 PMID: 16364484.
353. Tenne S-J, Kinzel J, Arlt M, Sibilla F, Bocola M, Schwaneberg U. 2-Methyltetrahydrofuran and cyclopentylmethylether: two green solvents for efficient purification of membrane proteins like FhuA. J Chromatogr B Analyt Technol Biomed Life Sci. 2013; 937:13–7. doi: 10.1016/j.jchromb.2013.07.021 PMID: 24013125.
354. Kleinschmidt JH, Tamm LK. Time-resolved distance determination by tryptophan fluorescence quenching: probing intermediates in membrane protein folding. Biochemistry. 1999; 38:4996–5005. doi: 10.1021/bi9824644 PMID: 10213602.
355. Miles AJ, Wallace BA. Synchrotron radiation circular dichroism spectroscopy of proteins and applications in structural and functional genomics. Chem Soc Rev. 2006; 35:39–51. doi: 10.1039/b316168b PMID: 16365641.
356. Miles AJ, Wallace BA. Circular dichroism spectroscopy of membrane proteins. Chem Soc Rev. 2016; 45:4859–72. doi: 10.1039/c5cs00084j PMID: 27347568.
357. Niedzwiecki DJ, Mohammad MM, Movileanu L. Inspection of the engineered FhuA ΔC/Δ4L protein nanopore by polymer exclusion. Biophys J. 2012; 103:2115–24. doi: 10.1016/j.bpj.2012.10.008 PMID: 23200045.
358. Dixon AS, Schwinn MK, Hall MP, Zimmerman K, Otto P, Lubben TH, et al. NanoLuc Complementation Reporter Optimized for Accurate Measurement of Protein Interactions in Cells. ACS Chem Biol. 2016; 11:400–8. doi: 10.1021/acschembio.5b00753 PMID: 26569370.
359. Onaca O, Sarkar P, Roccatano D, Friedrich T, Hauer B, Grzelakowski M, et al. Functionalized nanocompartments (synthosomes) with a reduction-triggered release system. Angew Chem Int Ed Engl. 2008; 47:7029–31. doi: 10.1002/anie.200801076 PMID: 18677788.
360. Muhammad N, Dworeck T, Fioroni M, Schwaneberg U. Engineering of the E. coli outer membrane protein FhuA to overcome the hydrophobic mismatch in thick polymeric membranes. J Nanobiotechnology. 2011; 9:8. doi: 10.1186/1477-3155-9-8 PMID: 21414201.
361. Mirzaei Garakani T, Liu Z, Glebe U, Gehrmann J, Lazar J, Mertens MAS, et al. In Situ Monitoring of Membrane Protein Insertion into Block Copolymer Vesicle Membranes and Their Spreading via Potential-Assisted Approach. ACS Appl Mater Interfaces. 2019; 11:29276–89. doi: 10.1021/acsami.9b09302 PMID: 31329408.
362. KnowMade, editor. Nanopore Sequencing. Patent Landscape Analysis, February 2019. 2019. Available from: https://www.knowmade.com/wp-content/uploads/2019/02/Nanopore-sequencing-2019-Patent-Landscape-FLYER.pdf.
363. Grimaldi M, Scrima M, Esposito C, Vitiello G, Ramunno A, Limongelli V, et al. Membrane charge dependent states of the beta-amyloid fragment Abeta (16-35) with differently charged micelle aggregates. Biochim Biophys Acta. 2010; 1798:660–71. doi: 10.1016/j.bbamem.2009.12.012 PMID: 20045392.
364. Sali A, Blundell TL. Comparative protein modelling by satisfaction of spatial restraints. J Mol Biol. 1993; 234:779–815. doi: 10.1006/jmbi.1993.1626 PMID: 8254673.
365. Fiser A, Do RK, Sali A. Modeling of loops in protein structures. Protein Sci. 2000; 9:1753–73. doi: 10.1110/ps.9.9.1753 PMID: 11045621.
366. Köster J, Rahmann S. Snakemake--a scalable bioinformatics workflow engine. Bioinformatics. 2012; 28:2520–2. doi: 10.1093/bioinformatics/bts480 PMID: 22908215.
367. Anatoliy N. Sokolov, Mark E. Roberts, Zhenan Bao. Fabrication of low-cost electronic biosensors.
368. Chen L-C, Wang E, Tai C-S, Chiu Y-C, Li C-W, Lin Y-R, et al. Improving the reproducibility, accuracy, and stability of an electrochemical biosensor platform for point-of-care use. Biosensors and Bioelectronics. 2020:112111. doi: 10.1016/j.bios.2020.112111.
369. Derkus B. Applying the miniaturization technologies for biosensor design. Biosens Bioelectron. 2016; 79:901–13. doi: 10.1016/j.bios.2016.01.033 PMID: 26800206.
370. Balme S, Picaud F, Manghi M, Palmeri J, Bechelany M, Cabello-Aguilar S, et al. Ionic transport through sub-10 nm diameter hydrophobic high-aspect ratio nanopores: experiment, theory and simulation. Sci Rep. 2015; 5:10135. doi: 10.1038/srep10135 PMID: 26036687.
371. Ali M, Nasir S, Ensinger W. Bioconjugation-induced ionic current rectification in aptamer-modified single cylindrical nanopores. Chem Commun (Camb). 2015; 51:3454–7. doi: 10.1039/c5cc00257e PMID: 25627437.
372. Liu Y, Yobas L. Label-free specific detection of femtomolar cardiac troponin using an integrated nanoslit array fluidic diode. Nano Lett. 2014; 14:6983–90. doi: 10.1021/nl5032524 PMID: 25366228.
373. Wei R, Gatterdam V, Wieneke R, Tampé R, Rant U. Stochastic sensing of proteins with receptor-modified solid-state nanopores. Nat Nanotechnol. 2012; 7:257–63. doi: 10.1038/nnano.2012.24 PMID: 22406921.
374. Thommes M, Kaneko K, Neimark AV, Olivier JP, Rodriguez-Reinoso F, Rouquerol J, et al. Physisorption of gases, with special reference to the evaluation of surface area and pore size distribution (IUPAC Technical Report). Pure and Applied Chemistry. 2015; 87:1051–69. doi: 10.1515/pac-2014-1117.
375. Karawdeniya BI, Bandara YMNDY, Nichols JW, Chevalier RB, Dwyer JR. Surveying silicon nitride nanopores for glycomics and heparin quality assurance. Nat Comms. 2018; 9:3278. doi: 10.1038/s41467-018-05751-y PMID: 30115917.
376. Schibel AEP, Ervin EN. Antigen detection via the rate of ion current rectification change of the antibody-modified glass nanopore membrane. Langmuir. 2014; 30:11248–56. doi: 10.1021/la502714b PMID: 25157668.
377. Ali M, Mafe S, Ramirez P, Neumann R, Ensinger W. Logic gates using nanofluidic diodes based on conical nanopores functionalized with polyprotic acid chains. Langmuir. 2009; 25:11993–7. doi: 10.1021/la902792f PMID: 19780595.
378. Lepoitevin M, Bechelany M, Balanzat E, Janot J-M, Balme S. Non-Fluorescence label protein sensing with track-etched nanopore decorated by avidin/biotin system. Electrochimica Acta. 2016; 211:611–8. doi: 10.1016/j.electacta.2016.06.079.

379. Pérez-Mitta G, Peinetti AS, Cortez ML, Toimil-Molares ME, Trautmann C, Azzaroni O. Highly Sensitive Biosensing with Solid-State Nanopores Displaying Enzymatically Reconfigurable Rectification Properties. Nano Lett. 2018; 18:3303–10. doi: 10.1021/acs.nanolett.8b01281 PMID: 29697265.
380. Ali M, Neumann R, Ensinger W. Sequence-specific recognition of DNA oligomer using peptide nucleic acid (PNA)-modified synthetic ion channels: PNA/DNA hybridization in nanoconfined environment. ACS Nano. 2010; 4:7267–74. doi: 10.1021/nn102119q PMID: 21082785.
381. Apel PY, Korchev YE, Siwy Z, Spohr R, Yoshida M. Diode-like single-ion track membrane prepared by electro-stopping. Nuclear Instruments and Methods in Physics Research Section B: Beam Interactions with Materials and Atoms. 2001; 184:337–46. doi: 10.1016/S0168-583X(01)00722-4.
382. Apel PY, Blonskaya IV, Lizunov NE, Olejniczak K, Orelovitch OL, Sartowska BA, et al. Asymmetrical nanopores in track membranes: Fabrication, the effect of nanopore shape and electric charge of pore walls, promising applications. Russ J Electrochem. 2017; 53:58–69. doi: 10.1134/S1023193517010037.
383. Siwy ZS. Ion-Current Rectification in Nanopores and Nanotubes with Broken Symmetry. Adv Funct Mater. 2006; 16:735–46. doi: 10.1002/adfm.200500471.
384. Wen C, Zeng S, Li S, Zhang Z, Zhang S-L. On Rectification of Ionic Current in Nanopores. Anal Chem. 2019; 91:14597–604. doi: 10.1021/acs.analchem.9b03685 PMID: 31644866.
385. Ali M, Nasir S, Ensinger W. Stereoselective detection of amino acids with protein-modified single asymmetric nanopores. Electrochimica Acta. 2016; 215:231–7. doi: 10.1016/j.electacta.2016.08.067.
386. Ali M, Nasir S, Ramirez P, Cervera J, Mafe S, Ensinger W. Calcium binding and ionic conduction in single conical nanopores with polyacid chains: model and experiments. ACS Nano. 2012; 6:9247–57. doi: 10.1021/nn303669g PMID: 22978291.
387. Fologea D, Gershow M, Ledden B, McNabb DS, Golovchenko JA, Li J. Detecting single stranded DNA with a solid state nanopore. Nano Lett. 2005; 5:1905–9. doi: 10.1021/nl051199m PMID: 16218707.
388. Ali M, Ahmed I, Ramirez P, Nasir S, Cervera J, Niemeyer CM, et al. Fluoride-induced modulation of ionic transport in asymmetric nanopores functionalized with "caged" fluorescein moieties. Nanoscale. 2016; 8:8583–90. doi: 10.1039/c6nr00292g PMID: 27050623.
389. Ali M, Nguyen QH, Neumann R, Ensinger W. ATP-modulated ionic transport through synthetic nanochannels. Chem Commun (Camb). 2010; 46:6690–2. doi: 10.1039/c0cc01632b PMID: 20737089.
390. Culver HR, Clegg JR, Peppas NA. Analyte-Responsive Hydrogels: Intelligent Materials for Biosensing and Drug Delivery. Acc Chem Res. 2017; 50:170–8. doi: 10.1021/acs.accounts.6b00533 PMID: 28170227.
391. Zhao XS, Bao XY, Guo W, Lee FY. Immobilizing catalysts on porous materials. Materials Today. 2006; 9:32–9. doi: 10.1016/S1369-7021(06)71388-8.
392. Koo B, Dolan NS, Wucherer K, Munch HK, Francis MB. Site-Selective Protein Immobilization on Polymeric Supports through N-Terminal Imidazolidinone Formation. Biomacromolecules. 2019; 20:3933–9. doi: 10.1021/acs.biomac.9b01002 PMID: 31448594.
393. Kim D, Herr AE. Protein immobilization techniques for microfluidic assays. Biomicrofluidics. 2013; 7:41501. doi: 10.1063/1.4816934 PMID: 24003344.
394. Vlassiouk I, Kozel TR, Siwy ZS. Biosensing with nanofluidic diodes. J Am Chem Soc. 2009; 131:8211–20. doi: 10.1021/ja901120f PMID: 19507907.
395. Lahiri J, Ostuni E, Whitesides GM. Patterning Ligands on Reactive SAMs by Microcontact Printing. Langmuir. 1999; 15:2055–60. doi: 10.1021/la9811970.
396. Kovacs J, Mayers GL, Johnson RH, Cover RE, Ghatak UR. Rates of racemization and coupling of cysteine active ester derivatives. J Chem Soc D. 1970:53. doi: 10.1039/c29700000053.
397. Chuah K, Wu Y, Vivekchand SRC, Gaus K, Reece PJ, Micolich AP, et al. Nanopore blockade sensors for ultrasensitive detection of proteins in complex biological samples. Nat Comms. 2019; 10:2109. doi: 10.1038/s41467-019-10147-7 PMID: 31068594.
398. Frasconi M, Mazzei F, Ferri T. Protein immobilization at gold-thiol surfaces and potential for biosensing. Anal Bioanal Chem. 2010; 398:1545–64. doi: 10.1007/s00216-010-3708-6 PMID: 20414768.
399. Cheng F, Gamble LJ, Castner DG. XPS, TOF-SIMS, NEXAFS, and SPR characterization of nitrilotriacetic acid-terminated self-assembled monolayers for controllable immobilization of proteins. Anal Chem. 2008; 80:2564–73. doi: 10.1021/ac702380w PMID: 18302347.
400. Faccio G. From Protein Features to Sensing Surfaces. Sensors (Basel). 2018; 18. doi: 10.3390/s18041204 PMID: 29662030.
401. Meldal M, Schoffelen S. Recent advances in covalent, site-specific protein immobilization. F1000Res. 2016; 5. doi: 10.12688/f1000research.9002.1 PMID: 27785356.
402. Raeeszadeh-Sarmazdeh M, Parthasarathy R, Boder ET. Fine-tuning sortase-mediated immobilization of protein layers on surfaces using sequential deprotection and coupling. Biotechnol Prog. 2017; 33:824–31. doi: 10.1002/btpr.2449 PMID: 28218499.
403. Williams DM, Kaufman G, Izadi H, Gahm AE, Prophet SM, Vanderlick KT, et al. Facile Protein Immobilization Using Engineered Surface-Active Biofilm Proteins. ACS Appl Nano Mater. 2018; 1:2483–8. doi: 10.1021/acsanm.8b00520.
404. Lin Z, Lin Q, Li J, Pistolozzi M, Zhao L, Yang X, et al. Spy chemistry-enabled protein directional immobilization and protein purification. Biotechnol Bioeng. 2020. doi: 10.1002/bit.27460 PMID: 32543719.
405. van Hest JCM, van Delft FL. Protein modification by strain-promoted alkyne-azide cycloaddition. Chembiochem. 2011; 12:1309–12. doi: 10.1002/cbic.201100206 PMID: 21557431.
406. Presolski SI, Hong VP, Finn MG. Copper-Catalyzed Azide-Alkyne Click Chemistry for Bioconjugation. Curr Protoc Chem Biol. 2011; 3:153–62. doi: 10.1002/9780470559277.ch110148 PMID: 22844652.
407. Balme S, Picaud F, Kraszewski S, Dejardin P, Janot JM, Lepoitevin M, et al. Controlling potassium selectivity and proton blocking in a hybrid biological/solid-state polymer nanoporous membrane. Nanoscale. 2013; 5:3961–8. doi: 10.1039/c3nr00564j PMID: 23535870.

408. Puiggalí-Jou A, Pérez-Madrigal MM, Del Valle LJ, Armelin E, Casas MT, Michaux C, et al. Confinement of a β-barrel protein in nanoperforated free-standing nanomembranes for ion transport. Nanoscale. 2016; 8:16922–35. doi: 10.1039/c6nr04948f PMID: 27714137.
409. Ma Q, Si Z, Li Y, Wang D, Wu X, Gao P, et al. Functional solid-state nanochannels for biochemical sensing. TrAC Trends in Analytical Chemistry. 2019; 115:174–86. doi: 10.1016/j.trac.2019.04.014.
410. Ali M, Schiedt B, Neumann R, Ensinger W. Biosensing with functionalized single asymmetric polymer nanochannels. Macromol Biosci. 2010; 10:28–32. doi: 10.1002/mabi.200900198 PMID: 19685499.
411. Ali M, Ramirez P, Tahir MN, Mafe S, Siwy Z, Neumann R, et al. Biomolecular conjugation inside synthetic polymer nanopores via glycoprotein-lectin interactions. Nanoscale. 2011; 3:1894–903. doi: 10.1039/c1nr00003a PMID: 21423941.
412. Siwy Z, Trofin L, Kohli P, Baker LA, Trautmann C, Martin CR. Protein biosensors based on biofunctionalized conical gold nanotubes. J Am Chem Soc. 2005; 127:5000–1. doi: 10.1021/ja043910f PMID: 15810817.
413. La Escosura-Muñiz A de, Merkoçi A. A nanochannel/nanoparticle-based filtering and sensing platform for direct detection of a cancer biomarker in blood. Small. 2011; 7:675–82. doi: 10.1002/smll.201002349 PMID: 21294272.
414. Zhu L, Gu D, Liu Q. Hydrogen Peroxide Sensing Based on Inner Surfaces Modification of Solid-State Nanopore. Nanoscale Res Lett. 2017; 12:422. doi: 10.1186/s11671-017-2190-x PMID: 28637348.
415. Bernhard M, Diefenbach M, Biesalski M, Laube B. Electrical Sensing of Phosphonates by Functional Coupling of Phosphonate Binding Protein PhnD to Solid-State Nanopores. ACS Sens. 2020; 5:234–41. doi: 10.1021/acssensors.9b02097 PMID: 31829017.
416. Liu M, Zhang H, Li K, Heng L, Wang S, Tian Y, et al. A Bio-inspired Potassium and pH Responsive Double-gated Nanochannel. Adv Funct Mater. 2015; 25:421–6. doi: 10.1002/adfm.201401655.
417. Liu F-F, Zhao X-P, Kang B, Xia X-H, Wang C. Non-linear mass transport in confined nanofluidic devices for label-free bioanalysis/sensors. TrAC Trends in Analytical Chemistry. 2020; 123:115760. doi: 10.1016/j.trac.2019.115760.
418. Liu N, Jiang Y, Zhou Y, Xia F, Guo W, Jiang L. Two-way nanopore sensing of sequence-specific oligonucleotides and small-molecule targets in complex matrices using integrated DNA supersandwich structures. Angew Chem Int Ed Engl. 2013; 52:2007–11. doi: 10.1002/anie.201209162 PMID: 23307498.
419. Perez JB, Tyagi D, Yang M, Calvo L, Perez R, Moreno E, et al. Predicting the right spacing between protein immobilization sites on self-assembled monolayers to optimize ligand binding. Anal Biochem. 2015; 484:133–5. doi: 10.1016/j.ab.2015.05.005 PMID: 25983235.
420. Wu X, Fraser K, Zha J, Dordick JS. Flexible Peptide Linkers Enhance the Antimicrobial Activity of Surface-Immobilized Bacteriolytic Enzymes. ACS Appl Mater Interfaces. 2018; 10:36746–56. doi: 10.1021/acsami.8b14411 PMID: 30281274.
421. Luk Y-Y, Tingey ML, Dickson KA, Raines RT, Abbott NL. Imaging the binding ability of proteins immobilized on surfaces with different orientations by using liquid crystals. J Am Chem Soc. 2004; 126:9024–32. doi: 10.1021/ja0398565 PMID: 15264835.
422. Koyama A, Fukami K, Imaoka Y, Kitada A, Sakka T, Abe T, et al. Dynamic manipulation of the local pH within a nanopore triggered by surface-induced phase transition. Phys Chem Chem Phys. 2017; 19:16323–8. doi: 10.1039/c7cp01157a PMID: 28425518.
423. Kondrat S, Vasilyev OA, Kornyshev AA. Feeling Your Neighbors across the Walls: How Interpore Ionic Interactions Affect Capacitive Energy Storage. J Phys Chem Lett. 2019; 10:4523–7. doi: 10.1021/acs.jpclett.9b01623 PMID: 31318564.
424. Freedman KJ, Haq SR, Edel JB, Jemth P, Kim MJ. Single molecule unfolding and stretching of protein domains inside a solid-state nanopore by electric field. Sci Rep. 2013; 3:1638. doi: 10.1038/srep01638 PMID: 23572157.
425. Ding D, Gao P, Ma Q, Wang D, Xia F. Biomolecule-Functionalized Solid-State Ion Nanochannels/Nanopores: Features and Techniques. Small. 2019; 15:e1804878. doi: 10.1002/smll.201804878 PMID: 30756522.
426. Laucirica G, Pérez-Mitta G, Toimil-Molares ME, Trautmann C, Marmisollé WA, Azzaroni O. Amine-Phosphate Specific Interactions within Nanochannels: Binding Behavior and Nanoconfinement Effects. J Phys Chem C. 2019; 123:28997–9007. doi: 10.1021/acs.jpcc.9b07977.
427. Bhalla N, Jolly P, Formisano N, Estrela P. Introduction to biosensors. Essays Biochem. 2016; 60:1–8. doi: 10.1042/EBC20150001 PMID: 27365030.
428. Jain M, Olsen HE, Paten B, Akeson M. The Oxford Nanopore MinION: delivery of nanopore sequencing to the genomics community. Genome Biol. 2016; 17:239. doi: 10.1186/s13059-016-1103-0 PMID: 27887629.
429. Ananth A, Genua M, Aissaoui N, Díaz L, Eisele NB, Frey S, et al. Reversible Immobilization of Proteins in Sensors and Solid-State Nanopores. Small. 2018; 14:e1703357. doi: 10.1002/smll.201703357 PMID: 29611258.
430. Shekar S, Niedzwiecki DJ, Chien C-C, Ong P, Fleischer DA, Lin J, et al. Measurement of DNA Translocation Dynamics in a Solid-State Nanopore at 100 ns Temporal Resolution. Nano Lett. 2016; 16:4483–9. doi: 10.1021/acs.nanolett.6b01661 PMID: 27332998.
431. Diederichs T, Pugh G, Dorey A, Xing Y, Burns JR, Hung Nguyen Q, et al. Synthetic protein-conductive membrane nanopores built with DNA. Nat Comms. 2019; 10:5018. doi: 10.1038/s41467-019-12639-y PMID: 31685824.
432. Yu J-S, Lee J, Ju M, Cho OH, Kim H-M, Nam KT, et al. DNA translocation through a nanopore in an ultrathin self-assembled peptide membrane. Nanotechnology. 2019; 30:195602. doi: 10.1088/1361-6528/ab0488 PMID: 30721897.
433. Duan L, Yobas L. Label-Free Multiplexed Electrical Detection of Cancer Markers on a Microchip Featuring an Integrated Fluidic Diode Nanopore Array. ACS Nano. 2018; 12:7892–900. doi: 10.1021/acsnano.8b02260 PMID: 30024729.
434. Zhao Y, Chen D, Yue H, French JB, Rufo J, Benkovic SJ, et al. Lab-on-a-chip technologies for single-molecule studies. Lab Chip. 2013; 13:2183–98. doi: 10.1039/c3lc90042h PMID: 23670195.
435. SIB Swiss Institute of Bioinformatics. ExPASy ProtParam.
436. Ajandouz EH, Marchis-Mouren GJ. Subsite mapping of porcine pancreatic alpha-amylase I and II using 4-nitrophenyl-alpha-maltooligosaccharides. Carbohydr Res. 1995; 268:267–77. doi: 10.1016/0008-6215(94)00335-d PMID: 7736471.
437. Simon AJ, Zhou Y, Ramasubramani V, Glaser J, Pothukuchy A, Gollihar J, et al. Supercharging enables organized assembly of synthetic biomolecules. Nat Chem. 2019; 11:204–12. doi: 10.1038/s41557-018-0196-3 PMID: 30643229.

438. Kapust RB, Tözsér J, Fox JD, Anderson DE, Cherry S, Copeland TD, et al. Tobacco etch virus protease: mechanism of autolysis and rational design of stable mutants with wild-type catalytic proficiency. Protein Eng. 2001; 14:993–1000. doi: 10.1093/protein/14.12.993 PMID: 11809930.

439. Ali M, Ahmed I, Ramirez P, Nasir S, Cervera J, Mafe S, et al. Cesium-Induced Ionic Conduction through a Single Nanofluidic Pore Modified with Calixcrown Moieties. Langmuir. 2017; 33:9170–7. doi: 10.1021/acs.langmuir.7b02368 PMID: 28796516.

440. Kubala MH, Kovtun O, Alexandrov K, Collins BM. Structural and thermodynamic analysis of the GFP:GFP-nanobody complex. Protein Sci. 2010; 19:2389–401. doi: 10.1002/pro.519 PMID: 20945358.

441. Fridy PC, Li Y, Keegan S, Thompson MK, Nudelman I, Scheid JF, et al. A robust pipeline for rapid production of versatile nanobody repertoires. Nat Methods. 2014; 11:1253–60. doi: 10.1038/nmeth.3170 PMID: 25362362.

442. Shimomura O. The discovery of aequorin and green fluorescent protein. J Microsc. 2005; 217:1–15. doi: 10.1111/j.0022-2720.2005.01441.x PMID: 15655058.

443. Shaner NC, Campbell RE, Steinbach PA, Giepmans BNG, Palmer AE, Tsien RY. Improved monomeric red, orange and yellow fluorescent proteins derived from Discosoma sp. red fluorescent protein. Nat Biotechnol. 2004; 22:1567–72. doi: 10.1038/nbt1037 PMID: 15558047.

444. Rompianesi G, Hann A, Komolafe O, Pereira SP, Davidson BR, Gurusamy KS. Serum amylase and lipase and urinary trypsinogen and amylase for diagnosis of acute pancreatitis. Cochrane Database Syst Rev. 2017; 4:CD012010. doi: 10.1002/14651858.CD012010.pub2 PMID: 28431198.

445. Suree N, Liew CK, Villareal VA, Thieu W, Fadeev EA, Clemens JJ, et al. The structure of the Staphylococcus aureus sortase-substrate complex reveals how the universally conserved LPXTG sorting signal is recognized. J Biol Chem. 2009; 284:24465–77. doi: 10.1074/jbc.M109.022624 PMID: 19592495.

446. Kuzmin A, Poloukhtine A, Wolfert MA, Popik VV. Surface functionalization using catalyst-free azide-alkyne cycloaddition. Bioconjug Chem. 2010; 21:2076–85. doi: 10.1021/bc100306u PMID: 20964340.

447. Li A, Sowder RC, Henderson LE, Moore SP, Garfinkel DJ, Fisher RJ. Chemical cleavage at aspartyl residues for protein identification. Anal Chem. 2001; 73:5395–402. doi: 10.1021/ac010619z PMID: 11816565.

448. Nagy E, St Germain E, Cosme P, Maity P, Terentis AC, Lepore SD. Ammonium catalyzed cyclitive additions: evidence for a cation-π interaction with alkynes. Chem Commun (Camb). 2016; 52:2311–3. doi: 10.1039/c5cc08641h PMID: 26728333.

449. Hu J, Barbour LJ, Gokel GW. Solid-state evidence for pi-complexation of sodium and potassium cations by carbon-carbon triple bonds. J Am Chem Soc. 2001; 123:9486–7. doi: 10.1021/ja0112137 PMID: 11562249.

450. Ali M, Yameen B, Cervera J, Ramírez P, Neumann R, Ensinger W, et al. Layer-by-layer assembly of polyelectrolytes into ionic current rectifying solid-state nanopores: insights from theory and experiment. J Am Chem Soc. 2010; 132:8338–48. doi: 10.1021/ja101014y PMID: 20518503.

451. Lawrence MS, Phillips KJ, Liu DR. Supercharging proteins can impart unusual resilience. J Am Chem Soc. 2007; 129:10110–2. doi: 10.1021/ja071641y PMID: 17665911.

452. Liu DR. Addgene plasmid #89247. pET-6xHis-(pos9)GFP. Available from: http://n2t.net/addgene:89247.

453. Kirchhofer A, Helma J, Schmidthals K, Frauer C, Cui S, Karcher A, et al. Modulation of protein properties in living cells using nanobodies. Nat Struct Mol Biol. 2010; 17:133–8. doi: 10.1038/nsmb.1727 PMID: 20010839.

454. Zhang S, Chai H, Cheng K, Song L, Chen W, Yu L, et al. Ultrasensitive and regenerable nanopore sensing based on target induced aptamer dissociation. Biosens Bioelectron. 2020; 152:112011. doi: 10.1016/j.bios.2020.112011 PMID: 32056734.

455. Laber JR, Dear BJ, Martins ML, Jackson DE, DiVenere A, Gollihar JD, et al. Charge Shielding Prevents Aggregation of Supercharged GFP Variants at High Protein Concentration. Mol Pharm. 2017; 14:3269–80. doi: 10.1021/acs.molpharmaceut.7b00322 PMID: 28870080.

456. Stevens AJ, Brown ZZ, Shah NH, Sekar G, Cowburn D, Muir TW. Design of a Split Intein with Exceptional Protein Splicing Activity. J Am Chem Soc. 2016; 138:2162–5. doi: 10.1021/jacs.5b13528 PMID: 26854538.

Danksagung

An dieser Stelle möchte ich den vielen Menschen danken, die mich direkt oder indirekt bei meinem Promotionsvorhaben unterstützt haben.

Mein besonderer Dank gilt…

…meinem Chef und Supervisor **Prof. Dr. Viktor Stein** für die Möglichkeit, meine Promotion in dem spannenden Umfeld einer jungen Arbeitsgruppe durchführen zu können. Während der Odysse durch die verschiedensten Büro- und Laborräume und auch nach unserer endgültigen Einquartierung in B2/05 konnten wir stets ergiebige Gespräche und Diskussionen führen, sowohl über die Forschung als auch über die Anekdoten der wissenschaftlichen Laufbahn.

…meinen Kollegen **Wadim Weber** und **Jan Ranglack** für die gemeinsame Zeit. Unsere Spieleabende nach langen Labortagen waren immer spannend und entspannend, auch wenn ein gewisser Dungeon Master(and) uns das Leben oft schwergemacht hat.

…**Ivana Duznovic** für die erfolgreiche Kooperation. Danke für deine nicht enden wollende Motivation und die Möglichkeit, ein echtes interdisziplinäres Projekt zu realisieren.

…**Linda Wiesinger** und **Dr. Melanie Mikosch-Werssching**, dafür, dass ihr mich und meine Kollegen vor allem in der Anfangsphase sicher durch die nebligen Fahrwasser der universitären Bürokratie gelotst habt.

…den vielen freundlichen Mitgliedern der **AG Thiel**, die mir die Bilayer-Technik beigebracht haben und denen ich zahlreiche wertvolle Tips verdanke, wie sie sich beherrschen lässt (die Lösung: viel Geduld und eine Prise Voodoo).

…**Dr. Markus Langhans** für die zahllosen Unterstützungen in Form von Plasmiden, Enzymen und anderem Laborkram, und natürlich für die interessanten Gespräche und Diskussionen.

…**Patrick Kunzmann** für die Mühe, zwei vernünftige SnoopTag-$^{+sig}$ΔcΔ5L Homologiemodelle zu erstellen.

…meinen Masteranden und Bacheloranden **Claudia Kreher, Sebastian Schaupp, Anastasia Weyrich, Jana Anton,** und **Luca Brenker**. Ein Riesen-Dankeschön für eure Motivation und euer Durchhaltevermögen. Ohne eure Beiträge wären wichtige Eckpunkte meiner Promotion unbeleuchtet geblieben. Auch den Praktikanten **Philipp Kemp, Marco Bechtel, Lisa Gertig, Tim Maier** und **Sven Gutzeit** danke ich für die Diskussionen und die Beiträge zum FhuA und Linker-Projekt.

…den **iNAPO**-Doktorand:innen für die Einblicke in andere Forschungsfelder und erholsame und witzige Stammtischrunden.

…den Darmstädter **iGEMern**. Die unfassbare Motivation, mit denen ihr eure Projekte vorangetrieben habt, haben die Betreuung zu einer angenehmen Beschäftigung gemacht. Gebt den Spirit weiter!

…denen, die mich abseits der Labor- und Schreibarbeit vor dem Durchdrehen bewahrt haben: **Johannes Tiedje, Mark Sinzger, Ursela Barteczko, Christin Fuks** und **Matthias Bretschneider**... Vielen Dank für die vielen gemeinsamen Abende, Erlebnisse und Gespräche.

…meinen Eltern und meinem Bruder. Danke, dass ihr mir immer zur Seite standet und steht.

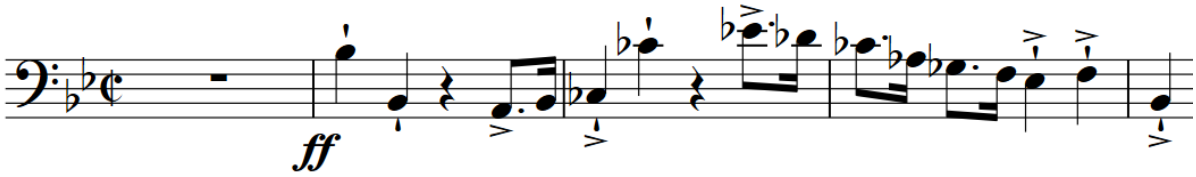

Anton Bruckner

Ehrenwörtliche Erklärung

Ich erkläre hiermit ehrenwörtlich, dass ich die vorliegende Arbeit entsprechend den Regeln guter wissenschaftlicher Praxis selbstständig und ohne unzulässige Hilfe Dritter angefertigt habe.

Sämtliche aus fremden Quellen direkt oder indirekt übernommenen Gedanken sowie sämtliche von Anderen direkt oder indirekt übernommenen Daten, Techniken und Materialien sind als solche kenntlich gemacht. Die Arbeit wurde bisher bei keiner anderen Hochschule zu Prüfungszwecken eingereicht.

Darmstadt, den ……

.....